Spring 1-1-2015

Unveiled Characteristics of Energetic Electrons and Ions: the Inner Radiation Belt, Slot Region, and Ring Current

Hong Zhao
University of Colorado at Boulder, zhaohong89@gmail.com

Unveiled Characteristics of Energetic Electrons and Ions: the Inner Radiation Belt, Slot Region, and Ring Current

by

Hong Zhao

B. S., Peking University, 2011

A thesis submitted to the

Faculty of the Graduate School of the

University of Colorado in partial fulfillment

of the requirement for the degree of

Doctor of Philosophy

Department of Aerospace Engineering Sciences

2015

This thesis entitled:

Unveiled Characteristics of Energetic Electrons and Ions: the Inner Radiation Belt, Slot Region, and Ring Current

written by Hong Zhao

has been approved for the Department of Aerospace Engineering Sciences

_____

Prof. Xinlin Li

_____

Prof. Dan Baker

_____

Prof. Howard Singer

_____

Dr. Scot Elkington

_____

Prof. Zoltan Sternovsky

Date_____

The final copy of this thesis has been examined by the signatories, and we find that both the content and the form meet acceptable presentation standards of scholarly work in the above mentioned discipline.

Hong Zhao (Ph. D., Aerospace Engineering Sciences)

Unveiled Characteristics of Energetic Electrons and Ions: the Inner Radiation Belt, Slot Region, and Ring Current

Thesis directed by Professor Xinlin Li

Earth's inner magnetosphere is a highly dynamic region consisting of various charged particle populations and current systems. Composed of relativistic electrons and protons, the radiation belt is a hazardous environment for both spacecraft and humans in space; while the variations of ring current, an electric current flowing around Earth consisting of energetic ions and electrons, can cause severe disruption of electrical systems on the ground. In the following, we focus on the dynamics of relativistic electrons (>~100 keV) in the inner radiation belt and slot region and energetic ions and electrons (>~keV) in the ring current, which are subject to influence from many different physical processes and commonly exhibit great changes on various spatial and temporal scales. Using data from SAMPEX and DEMETER satellites, we find that in the inner belt and slot region, though MeV electrons only exhibit flux enhancements during severe solar wind conditions, 100s of keV electron flux variations occur much more often. Using a radial diffusion model, a penetration event of 100s of keV electrons into the inner belt and slot region is modeled, and the results indicate that the penetration can be well explained by inward radial transport, but the radial diffusion coefficient is different from those of previous studies. Also, using data from the Van Allen Probes, we perform detailed analysis of 100s of keV electron pitch angle distributions (PADs) in the inner belt and slot region. A new type of PADs with minima at 90 °persistent near the magnetic equator is unveiled, which is contradictory to the theoretical predictions from known physical processes and shows the complexity in the inner belt dynamics. Finally, the evolution of ring current ions and electrons are investigated during geomagnetic storms using data from the Van Allen Probes. The contribution of electrons and ions to the ring current energy is calculated and intriguing results are found. Our studies on the energetic electrons and ions in the inner belt, slot region and ring current contribute to a more comprehensive picture of inner magnetosphere dynamics.

Dedication

To my parents and friends.

Acknowledgements

First and foremost, I would like to thank my advisor, Professor Xinlin Li, for encouraging me to study abroad and join CU, offering me excellent guidance on coursework and research, and giving me valuable career advice. He has always provided me insightful knowledge and inspiring ideas, which helped me overcome obstacles in my studies and research and made this thesis possible. Next I would like to thank my committee members, Prof. Dan Baker, Prof. Howard Singer, Dr. Scot Elkington, Prof. Zoltan Sternovsky, and Prof. Delores Knipp (though regretfully she is not able to attend my defense due to schedule conflict), for their valuable guidance and warm support. I would also like to thank my research mentor, Dr. Reiner Friedel, for the inspiration and direction he has provided, and also thank Ilse and Asijas for their warm encouragement. I would also like to express my thanks to fellow graduate students and our research group members - Weichao Tu, Allison Jaynes, Lauren Blum, Quintin Schiller, Sam Califf, and Theodore Sarris - for all the discussions, advice, and support. Finally, I would like to thank everyone who gave me inspirations, guidance, and suggestions for each of papers that contribute to this thesis.

Contents

Chapter

Tables

Figures

Chapter 1

Introduction

The Earth's magnetosphere is a tear-shaped cavity which is formed as the solar wind interacts with the Earth's magnetic field. Close to Earth, the Earth's inner magnetosphere is the region where the geomagnetic field resembles the dipole field. Various charged particle populations and current systems exist in the Earth's inner magnetosphere, which pose potential threats to the spacecraft and human in the space and technical systems on the ground. Energetic electrons (with energies > ~ keV) in the inner magnetosphere are subject to influence from many different physical processes and exhibit great variations on different spatial and temporal scales. Relativistic electrons (> ~ 100 keV) in the inner magnetosphere are distributed into the inner radiation belt and outer radiation belt, with the slot region in between separating the two belts; while ions and electrons with relatively lower energies (> ~ keV) flowing around Earth contribute to the ring current and waves that interact with relativistic electrons.

Many studies have focused on the dynamics of relativistic electrons in the outer radiation belt; however, the energetic electrons in the inner belt, slot region, and ring current have received little attention in the past. Understanding the characteristics of energetic electrons and ions in these regions can contribute to a comprehensive understanding and a cohesive picture of the radiation belt and ring current dynamics and thus is very important in the study of Earth's magnetosphere. This thesis mainly addresses this question and focuses on the dynamics of different charged particle populations in the inner belt, slot region and ring current.

I begin in Chapter 2 with a brief overview of the charged particles and waves in Earth's inner magnetosphere. Detailed introduction to the charged particle's motions, adiabatic invariants, diffusion processes, and wave-particle interactions are provided. Next, I introduce the radiation belts and radiation belt dynamics, including the transport, acceleration, and loss mechanisms. In particular, the dynamics of relativistic electrons in the inner radiation belt and slot region is reviewed in detail. A brief introduction of Earth's ring current, including the

formation and decay, the introduction to the geomagnetic storms and Dst index, and the Dessler-Parker-Sckopke (DPS) relation, finishes up Chapter 2.

To investigate the dynamics of energetic ions and electrons in the inner magnetosphere, this thesis mainly focuses on several important populations: MeV electrons in the slot region, 100s of keV electrons in the slot region and inner belt, and energetic ions and electrons in the ring current. In Chapter 3, using data from SAMPEX satellite, we investigate the flux enhancement of MeV electrons in the low L region. The penetration of MeV electrons into the low L region is studied and the correlation bewteen MeV electron flux enhancements in the low L region and geomagnetic activities / solar wind conditions are investigated. The sufficient and necessary solar wind conditions for MeV electron penetration into the slot region are examined, and the importance of electron flux preconditioning is revealed.

Though the penetration of MeV electrons into the slot region and inner belt is relatively rare, 100s of keV electron penetration into the low L region occurs much more often. In Chapter 4, using data from DEMETER satellite, I focus on the penetration of 100s of keV electrons into the slot region and inner belt. A specific penetration event is investigated and modeled with a radial diffusion model with diffusion coefficient as a function of solar wind parameters. The results indicate the importance of inward radial diffusion to the 100s of keV electron deep penetrations, and the radial diffusion coefficients derived from the model are also compared to those from previous studies.

Besides the radial diffusion, other physical processes also play important roles on the relativistic electron dynamics in the inner belt and slot region. The relativistic electron pitch angle distribution (PAD) is an important characteristic of radiation belt electrons and can give valued information on physical processes taking effect on relativistic electrons in a specific region. Using data from MagEIS instruments on the Van Allen Probes, 100s of keV electron PADs in the slot region and inner belt are investigated. A peculiar type of PADs with minima at 90 °pitch angle (PA) is unveiled, which is contradictory with predictions from known theories and indicates the complexity of inner belt dynamics, and possible mechanisms are suggested.

Detailed analysis on different types of electron PADs in the low L region is also performed and the underlying physical processes are revealed. This study on relativistic electron PADs in the low L region gives us insight into the physical processes in this region and helps us better understand the inner belt and slot region dynamics.

In addition to the relativistic electrons in the radiation belt, understanding energetic particles in the ring current is also essential for understanding the inner magnetospheric dynamics. Though the energetic ions in the ring current have been extensively studied, the energetic electrons have received limited attention in the past. In Chapter 6 and 7, I focus on the evolution of energetic ions and electrons in the ring current during geomagnetic storm times respectively. Using comprehensive measurements from the Van Allen Probes, the energy densities and content of ring current ions and electrons are calculated for specific geomagnetic storms and their dependence on L shell and energy of particles is investigated. The contributions of ions with different species to the ring current energy are calculated and the important role of low energy ions to the ring current buildups is shown in Chapter 6. In Chapter 7, the role of energetic electrons in the ring current dynamics is investigated and the contribution of ring current electron to the ring current energy is calculated.

Finally, Chapter 8 summarizes the conclusions from this work and discusses some possible extensions and future work. The appendices cover some additional work from previous chapters.

Chapter 2

Relevant Background

2.1 Earth's Inner Magnetosphere

Originated from the Sun, the solar wind is an outflow of tenuous plasma consisting of charged particles. As it flows past the Earth, the solar wind interacts with the Earth's magnetic field and confines it into a tear-shaped cavity, which is known as the Earth's magnetosphere. The boundary separating the solar wind and the Earth's magnetosphere is the magnetopause. It is commonly located at a geocentric distance of ~10 R_E on the dayside, but under extreme solar wind conditions it can also move below ~ 6 R_E. Inside the magnetopause, various particle populations and current systems exist and the space environment is dominated by the geomagnetic field. Figure 2.1 shows the configuration of Earth's magnetosphere and numerous current systems populated in it [Kivelson and Russell, 1995].

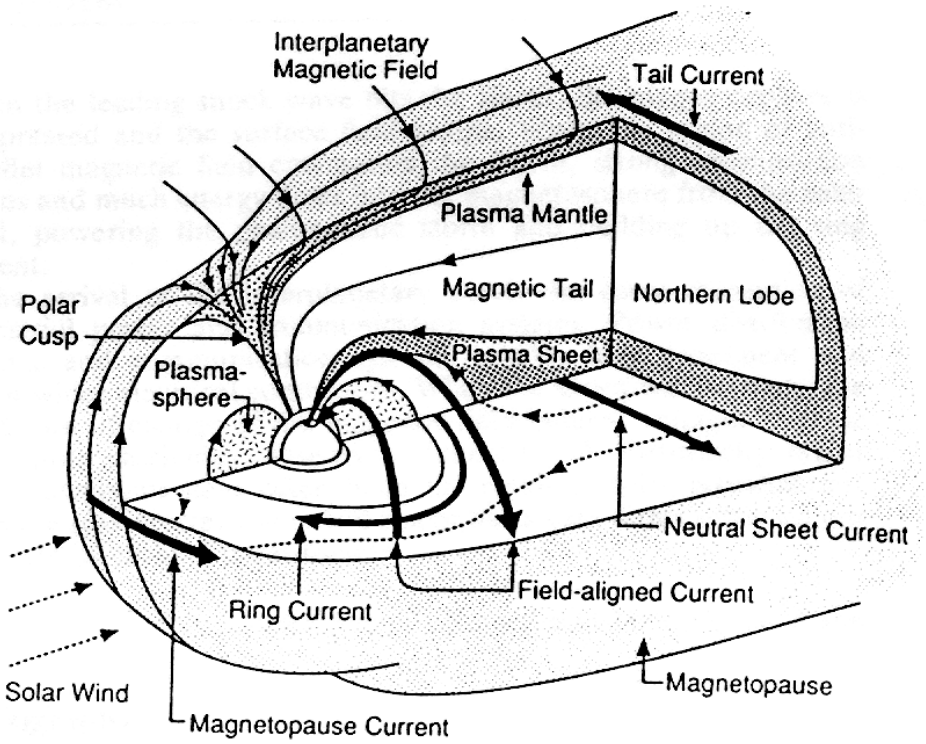

Figure 2.1: A schematic of Earth's magnetosphere. From Kivelson and Russell [1995].

Close to Earth, the Earth's inner magnetosphere is the region where the geomagnetic field resembles the dipole field. It includes the plasmasphere, radiation belts, and ring current. These overlapping regions are differentiated by charged particle populations. The charged particles and current systems existing in the Earth's inner magnetosphere pose potential threats to the spacecraft and human in the space and technical systems on the ground, and thus it is very important for us to understand their characteristics and dynamics.

2.1.1 Particle Populations in Earth's Inner Magnetosphere

The plasmasphere is a torus consisting of plasma with relatively high density (about 10 – 10^3 /cm^3) and low temperature (~ eV), which is located just above the ionosphere and extends to a geocentric distance of 2~6 R_E. It is mainly populated by H^+ and He^+, as well as a smaller portion of N^+, N^{2+}, O^+, O^{2+}, and He^{2+}. The outer boundary of plasmasphere is known as the plasmapause, which is formed as a result of the combination of charged particle motions of co-rotation and convection. The location of plasmapause is highly dynamic; it shrinks with increased geomagnetic activity and expands during geomagnetic quiet times. Under quiet solar wind conditions it often reaches the geosynchronous orbit, while during disturbed times it can get to as low as a geocentric distance of ~2 R_E.

Overlapping with the plasmasphere, the radiation belts, which are also called the Van Allen belts, are occupied by relativistic charged particles. The radiation belts include the inner radiation belt and outer radiation belt, while the region separating the two belts is called the slot region. The outer radiation belt is populated by relativistic electrons, while the inner radiation belt is populated by highly energetic protons with energies of tens of MeV and above. Recent observations also show the abundance of hundreds of keV electrons in the inner radiation belt. The slot region is usually devoid of energetic particles. However, under extreme solar wind conditions and intense geomagnetic storms, the slot region can also be filled with energetic electrons.

The ring current is a near-equatorial electric current, located between geocentric distances of ~2 R_E and ~9 R_E, flowing toroidally around Earth. It mainly consists of ions with energies of a few keV to hundreds of keV, while electrons with energies of keV to hundreds of keV also contribute to it. The main carrier of quiet time ring current is believed to be protons with energies of tens to hundreds of keV, while as the geomagnetic activity increases, heavy ions, such as O^+ and He^+, account for a significant portion of ring current energy and may even dominate under very intense geomagnetic activity.

2.1.2 Charged Particle Motion in the Geomagnetic Field

The energetic particles trapped within the Earth's inner magnetosphere execute three distinct forms of periodic motion: cyclotron motion around a magnetic field line, bounce motion between magnetic mirror points, and azimuthal drift motion around the Earth with electrons drifting eastward and ions drifting westward (see Figure 2.2).

A charged particle with mass m and charge q trapped in the geomagnetic field gyrates around the magnetic field line under the influence of $\vec{v} \times \vec{B}$ force with a gyroradius of $\frac{mv_\perp}{B|q|}$ at a frequency of $\frac{B|q|}{m}$, where $\vec{B}$ is the local magnetic field and $v_\perp$ is the component of velocity $\vec{v}$ that perpendicular to the local magnetic field. The instantaneous center of particle's gyration is known as the guiding center. Also, the gyrating charged particle travels along the magnetic field lines and bounce between two mirror points if the particle has a nonzero component of velocity that is parallel to the local magnetic field. In addition, if there is any other external forces that have perpendicular component to the local magnetic field, the charged particle will also drift at a direction perpendicular to the external force and local magnetic field at a speed of $v_d = \frac{\vec{F} \times \vec{B}}{qB^2}$. In the inner magnetosphere, the external forces can be from gravity, the electric field, or the gradient or curvature of the magnetic field. The timescales for gyration, bounce motion and drift motion are distinct. For example, for 1 MeV electrons with equatorial pitch angle of 60 °at

geosynchronous orbit, the periods of gyration is about 10^{-3} s, of bounce motion is about 0.5 s, and of azimuthal drift motion is about 10 min.

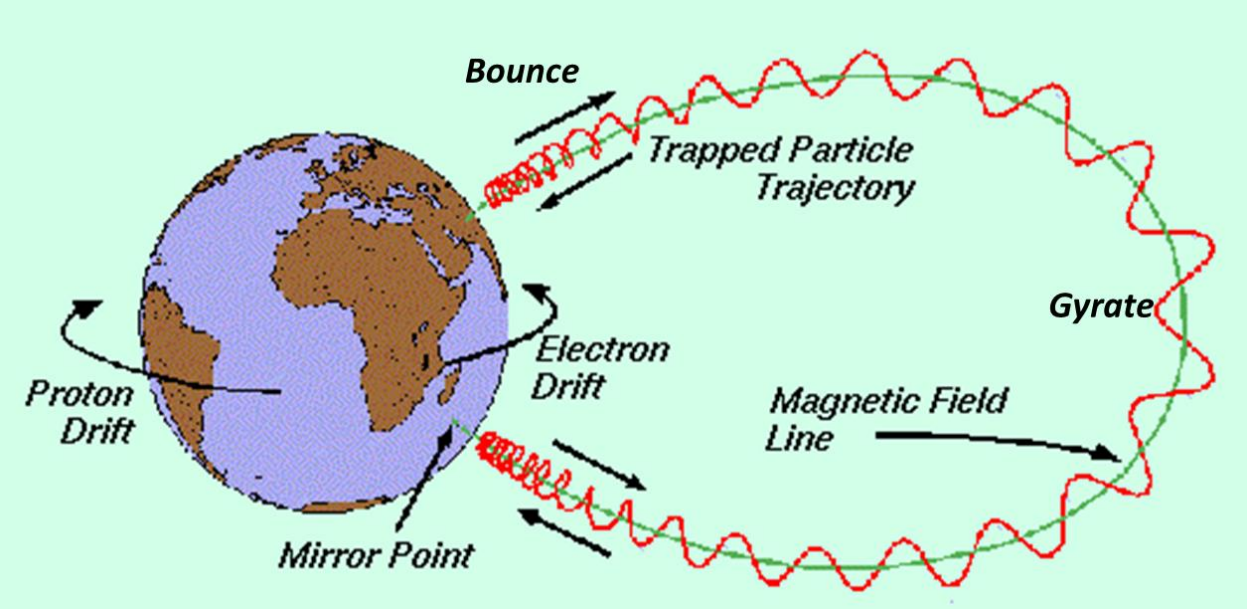

Figure 2.2: Three characteristic motions of charged particles trapped in the geomagnetic field. (Adapted from the image retrieved from http://www.spenvis.oma.be/help/background/traprad/traprad.html)

In addition, there are another two important parameters for charged particles in the geomagnetic field: the pitch angle and L shell. The pitch angle is the angle between the particle's velocity vector and the local magnetic field vector. The distribution of particle fluxes as a function of pitch angle, also called the pitch angle distribution (PAD), is an important characteristic which indicates the physical processes that are taking effect in a specific region. The L shell, also known as the drift shell, specifies a surface on which the guiding center of particle drifts around the Earth. In a dipole field, L shell is introduced as $L = \frac{r_0}{R_E}$, where r_0 is the geocentric distance of the intersection of a field line with Earth's magnetic equator. Different definitions of L shells have been used in the space physics, and the most commonly used ones are McIlwain L [McIlwain, 1961] and the Roederer L (also known as L^*) [Roederer, 1970]. The McIlwain L is defined as a function of magnetic field magnitude B and integral invariant I (which will be discussed in the following subsection) and is the analog of the radial distance of

the drift shell at the magnetic equator in a dipole field. The Roederer L is correlated with the third adiabatic invariant and will be discussed in the following subsection. It is worth mentioning that unlike the dipole L, both McIlwain L and Roederer L are dependent on the particle's equatorial pitch angle.

2.1.3 The Adiabatic Invariants and Diffusion Processes

Corresponding to three distinct motions, there are three adiabatic invariants, μ, K, and Φ, which are conserved during slow electric and magnetic field fluctuations (comparing to the periods of three motions). The first adiabatic invariant, μ, also known as the magnetic moment, can be expressed as

$$\mu = \frac{p_\perp^2}{2m_0 B}$$

where $p_\perp$is the relativistic momentum component perpendicular to the local magnetic vector, m_0 is the rest mass of particle, and B is the local magnetic field magnitude. Conservation of the first adiabatic invariant is equivalent to conservation of magnetic flux passing through the particle's orbit of cyclotron motion.

The second adiabatic invariant, J, is conserved during field changes which are slow compared to the period of particle's bounce motion. It can be written as

$$J = 2\sqrt{2m_0\mu}\int_{S_m}^{S'_m}\sqrt{B_m - B(s)}ds$$

where S_m and S'_m are mirror points at northern/southern hemisphere, B_m and $B(S)$ are the magnetic field strength of mirror points and position S respectively, and ds is the distance along the magnetic field line. Sometimes K and I are also used as invariants related to the second adiabatic invariant, which are defined as

$$K = \int_{S_m}^{S'_m}\sqrt{B_m - B(S)}ds$$

$$I = \int_{S_m}^{S'_m}\sqrt{1 - B(S)/B_m}ds$$

K and I are quantities that only related to the particle's mirror points (or equivalently, the particle's equatorial pitch angle) and the magnetic field configuration.

Corresponding to the particle's drift motion, the third adiabatic invariant Φ represents the magnetic flux encompassed by the particle's drift shell, which can be calculated as

$$\Phi = \oint \vec{A} \cdot \overrightarrow{dx}$$

where $\vec{A}$ is the magnetic vector potential and $\overrightarrow{dx}$ is a vector along a curve that lies in the particle's drift shell. The third adiabatic invariant is conserved if the field changes are slower than the particles' drift period and is also a field-related quantity which is independent of particle's charge, energy and mass. Related to the third adiabatic invariant, the Roederer L, also known as L^*, is defined as the radial distance in earth radii to the equatorial point of the shell on which the electron would be found, if all non-dipolar perturbations of the magnetic field are adiabatically turned off [Roederer, 1970], and can be calculated using the third adiabatic invariant as

$$L^* = \frac{2\pi M}{|\Phi| R_E}$$

where M is the Earth's dipole magnetic moment and R_E is the Earth's radius. It is obvious that conservation of the third adiabatic invariant is equivalent to conservation of L^*.

Related to three adiabatic invariants, another important quantity in radiation belt studies is the phase space density. The phase space density (PSD) is the distribution function of particles in six-dimension phase space and can be represented as $f(x, y, z, p_x, p_y, p_z)$. In terms of three adiabatic invariants, the PSD can also be equivalently written as $f(\mu, K, L^*, \phi_1, \phi_2, \phi_3)$, where $\phi's$ are corresponding phases of three periodic motions. In the radiation belt studies, due to limited observations, the phase-averaged PSD $f(\mu, K, L^*)$ is commonly used.

The three adiabatic invariants are conserved during slow field changes. However, if the field is changing at some frequencies near the frequencies of particle's adiabatic motions, it can violate the corresponding adiabatic invariants through resonant interaction. The violation of adiabatic invariants leads to a net diffusive process, which moves particles from high-

concentration region to low-concentration region and thus can be either a source process or a loss process. There are several distinct diffusion processes: the radial diffusion process caused by the violation of the third adiabatic invariant permits transport of the particles across field lines; while the pitch angle diffusion and energy diffusion caused by the violation of first two adiabatic invariants alters the particle pitch angle and particle energy, respectively. Figure 2.3 shows a schematic of radial diffusion and pitch angle diffusion processes. The diffusion processes can be caused by various electrostatic and electromagnetic waves in Earth's inner magnetosphere.

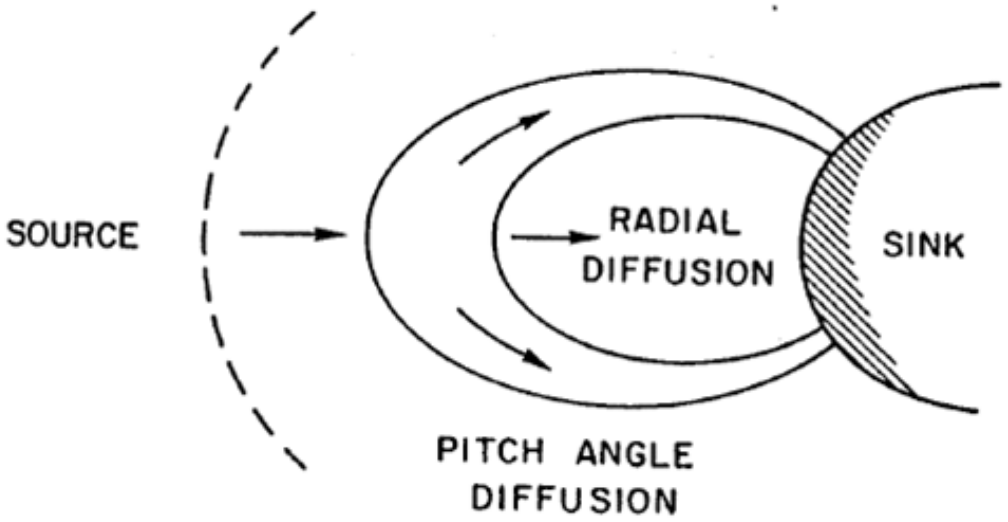

Figure 2.3: A schematic of radial diffusion and pitch angle diffusion processes. From Roederer [1970].

2.1.4 Magnetospheric Waves and Wave-Particle Interaction

Various waves exist in the inner magnetosphere, which can cause the violation of adiabatic invariants and thus the diffusion processes of charged particles in the inner magnetosphere. Figure 2.4 shows schematic wave maps under quiet and active geomagnetic activity conditions [Shprits et al., 2008]. As shown in Figure 2.4, the most common waves in the inner magnetosphere include the ULF waves, whistler mode chorus waves, plasmaspheric hiss waves, EMIC waves, lightning-generated VLF waves, VLF waves from man-made transmitters,

and, though not shown in Figure 2.4, fast magnetosonic waves. Different waves exist in different regions and take effect on different charged particle populations.

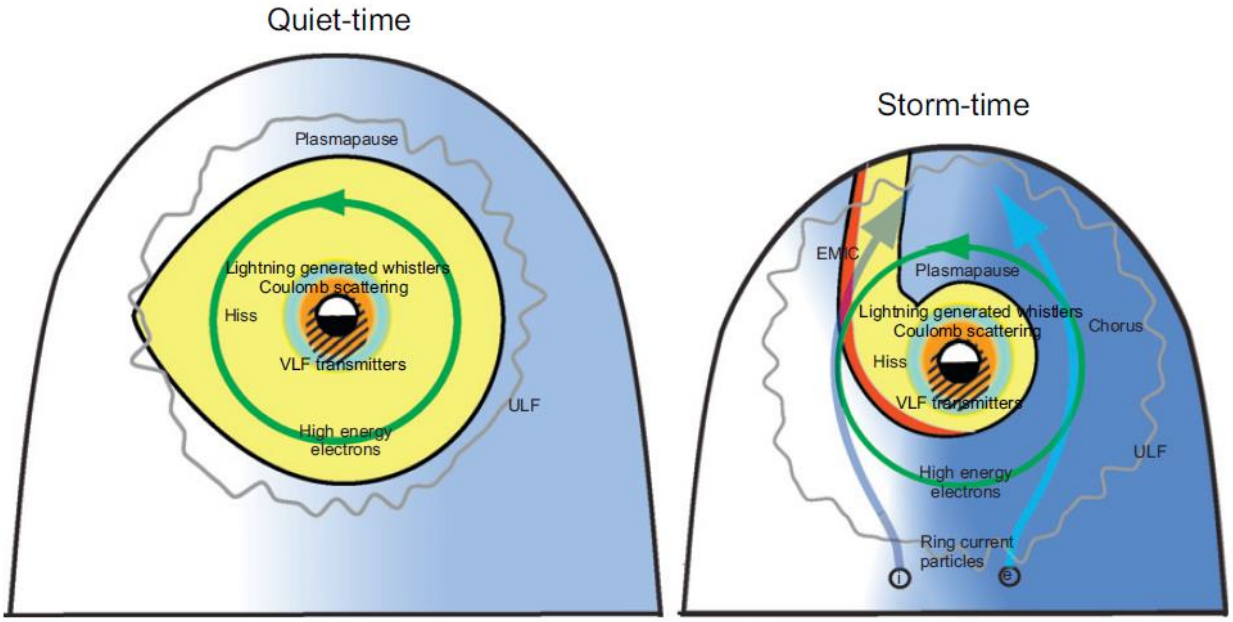

Figure 2.4: The schematics of distribution of waves in Earth's inner magnetosphere during geomagnetic quiet times and storm times. From Shprits et al. [2008].

The ULF waves, existing in the inner magnetosphere during both geomagnetic active times and quiet times, can have drift resonant interaction with charged particles and cause radial diffusion, thus are believed to play a very important role in the energization of charged particles in the inner magnetosphere [e.g., Hudson et al., 2000; Elkington et al., 1999, 2003]. The whistler mode chorus waves, existing outside the plasmasphere primarily in the dawn side, can cause the violation of first adiabatic invariant and acceleration of relativistic electrons, which is also a very important mechanism for the fast energization of radiation belt electrons [e.g., Horne and Thorne, 1998; Horne et al., 2005]. Existing inside the plasmasphere, the whistler mode hiss waves can cause pitch angle diffusion and thus loss of energetic electrons to the atmosphere (precipitation), and is considered as one of the important loss mechanisms for relativistic electrons inside the plasmasphere [e.g., Meredith et al., 2004, 2007]. EMIC waves existing primarily on the dusk sector and plasmaspheric plume can cause loss of ultra-relativistic electrons [e.g., Li et al., 2007;

Usanova et al., 2014]. Lightning-generated VLF waves and VLF waves from transmitters can interact with radiation belt electrons and cause particle precipitation [e.g., Abel and Thorne, 1998; Sauvaud et al., 2008]. Fast magnetosonic waves, also known as equatorial noise, have attracted a lot of attention recently due to the fact that they can energize relativistic electrons in a wide L range [e.g., Horne et al., 2007] and are also suggested as a mechanism for removing equatorially mirroring relativistic electrons [e.g., Chen et al., 2015]. Those waves exist in the different regions in the inner magnetosphere, occur at different times, and work as source or loss processes for the charged particles in the inner magnetosphere with distinct energies.

The magnetospheric waves can violate the adiabatic invariants through resonant interactions with particle's adiabatic motions, and violation of adiabatic invariants leads to a net diffusive process that smooth out the distributions of charged particles. The resonant interaction can occur between magnetospheric waves and three adiabatic motions of charged particles as long as the resonance condition is met. Specifically, the resonant interaction between magnetospheric waves and particle's cyclotron motion, also known as cyclotron resonance, can occur under the condition that

$$\omega - k_{\parallel} v_{\parallel} = \frac{n\Omega}{\gamma}$$

where ω is the wave frequency, $k_{\parallel}$ is the parallel component of the wave vector to the magnetic field, Ω is the gyrofrequency of the charged particle, $v_{\parallel}$ is the parallel component of the particle's velocity to the magnetic field, γ is the Lorentz factor, and n is an integer. The whistler mode chorus waves are shown to be able to energize electrons to MeV energies in the outer radiation belt through cyclotron resonance [e.g., Horne and Thorne, 1998].

2.2 Earth's Radiation Belts

The Earth's radiation belts are regions deep within the magnetosphere which consist of relativistic ions and electrons magnetically trapped by the geomagnetic field (see Figure 2.5). The outer radiation belt, which mainly consists of relativistic electrons, is highly dynamic and

exhibits great variations during geomagnetic storms. The inner radiation belt, which mainly consists of relativistic protons and electrons (with energies primarily below ~800 keV), is thought to be relatively stable. Separating the inner and outer radiation belts is a region called the slot region, which is usually devoid of relativistic electrons, while during geomagnetic active times the slot region can also be filled with relativistic electrons [e.g., Blake et al., 1992; Li et al., 1993; Baker, 2004; Zhao and Li, 2013a, 2013b; Baker et al., 2013, 2014].

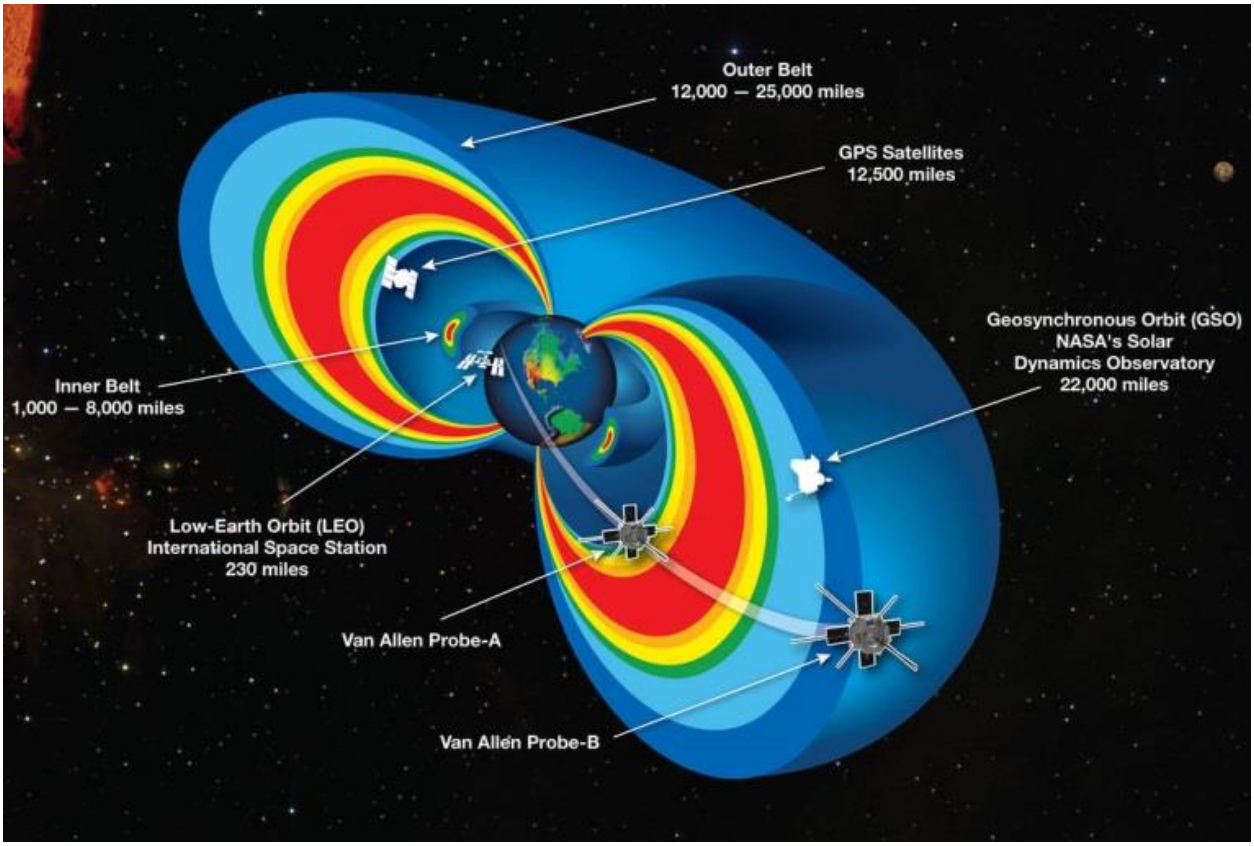

Figure 2.5: The schematic of radiation belts with locations of multiple satellites. Red color of radiation belts indicates higher flux levels of relativistic particles while blue color indicates lower flux levels. The image is retrieved from http://www.nasa.gov/mission_pages/sunearth/news/gallery/20130228-radiationbelts.html.

The radiation belts are highly dynamic regions and are subject to substantial variations, especially during geomagnetic disturbed times. Figure 2.6 shows the daily-averaged fluxes of relativistic electrons with various energies as a function of L shell and time over three years from September 2012 to October 2015, using measurements from Van Allen Probe – A. The flux

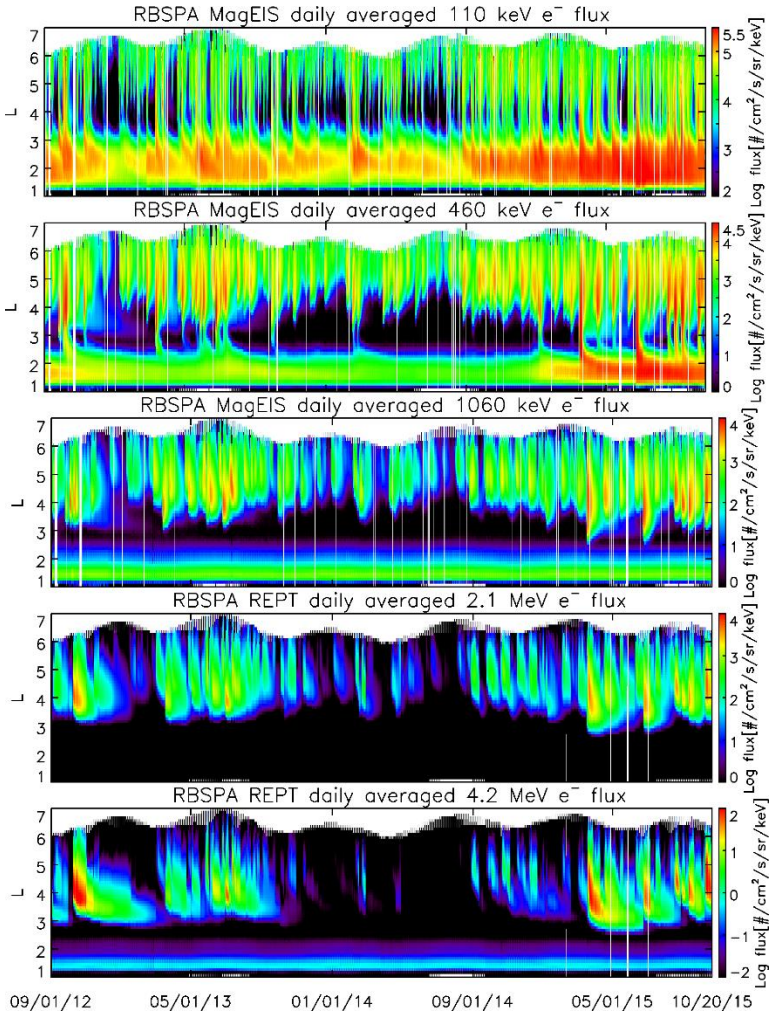

Figure 2.6: Daily-averaged fluxes of electrons with energies of ~110 keV, ~460 keV, ~1060 keV, ~2.1 MeV, and ~4.2 MeV from September 2012 to October 2015, using data from MagEIS and REPT instruments on the Van Allen Probe - A.

variations of electrons with various energies as shown in Figure 2.6 occurred frequently and are significant. In the outer radiation belt, the fluxes usually vary orders of magnitude even for ultra-relativistic electrons; while in the inner radiation belt, the fluxes of <~500 keV electrons also exhibit great changes, and those electrons frequently penetrate through the slot region. Note that the locations of slot region, where the electron fluxes are usually very low, for electrons of different energies are different: for electrons with higher energies, the slot region tends to be closer to Earth. It is also worth mentioning that in Figure 2.6 the high levels of fluxes of ~1060 keV and 4.2 MeV electrons in the inner belt are not real and likely due to the contamination from very energetic protons persistently existing in the inner belt.

The highly dynamic nature of radiation belts attracts a lot of attention and various transport, acceleration, and loss mechanisms have been proposed to explain the variations of radiation belt electrons. Some popular mechanisms are introduced in the following subsection.

2.2.1 Adiabatic Effect

Before reviewing source and loss processes of radiation belt electrons, the adiabatic effect (Dst effect) should be introduced. The adiabatic effect is a reversible process that can cause temporary decrease or increase of electron's energy. As the geomagnetic field configuration changes, which usually occurs during geomagnetic storms, due to the conservation of three adiabatic invariants electrons move inward or outward and get energized or decelerated. During a geomagnetic storm, the ring current develops and decreases the magnetic field strength inside it. As an example, for electrons with 90 °pitch angles, to conserve the third adiabatic invariant, the drift shells expand and electrons move radially outward to regions with weaker magnetic field, and thus get decelerated to conserve the first adiabatic invariant. As the ring current decays and magnetic field strength inside the current starts to recover, the drift shells of electrons move back and electrons move inward and get energized again to conserve the adiabatic invariants. It has been shown that the adiabatic effect can cause flux changes of orders of magnitude [e.g., Kim and Chan, 1997], and this effect has influence on both electrons [e.g., Li et al., 1997] and protons [e.g., Lyons and Williams, 1976]. Though the adiabatic effect involves energization or deceleration of electrons, it is not a "real" source or loss process since in the phase space the electron phase space densities do not change during this process. The adiabatic effect can cause observed flux variations but differs from source and loss processes shown in the following subsections which involve a net energy gain or loss and changes of phase space densities.

2.2.2 Acceleration Mechanisms

There are two major acceleration mechanisms of relativistic electrons in the radiation belts: inward radial diffusion and local wave heating.

The inward radial diffusion energizes electrons by moving them radially inward while conserving the first and second adiabatic invariants [e.g., Fälthammar, 1965; Schulz and Lanzerotti, 1974]. Large-scale magnetic and electric field fluctuations in the magnetosphere with periods comparable to drift period of electrons can break the third adiabatic invariant and cause the radial diffusion. The net direction of radial diffusion is determined by radial gradient of electron PSD. If the electron PSD increases as L shell increases, then such large-scale field fluctuations will tend to smooth out the radial gradient and thus cause inward radial diffusion. The electrons are brought to regions with stronger magnetic field during inward radial diffusion. As the first adiabatic invariant is conserved, perpendicular energies of electrons get preferentially energized and pitch angle distributions tend to be more peaked at 90 °. Figure 2.7 (A) shows the expected PSD profile from the inward radial diffusion. In particular, ULF waves are believed to be a major contributor to the enhanced inward radial diffusion through drift resonant interaction with electrons. Observations show strong correlation between ULF waves and MeV electron enhancements in the outer radiation belt [e.g., Baker et al., 1998a, 1998b; Nakamura et al., 2002], and MHD simulations also confirm the important role of ULF waves in accelerating relativistic electrons [e.g., Elkington et al., 1999; Hudson et al., 2000].

Another important energization mechanism for radiation belt electrons is local wave heating, which is caused by wave-particle interaction. As mentioned in the previous subsections, the cyclotron resonance of wave and charged particles can cause pitch angle diffusion and energy diffusion. With preferred conditions, electrons can be accelerated to higher energies through energy diffusion on a timescale of multiple cyclotron periods. The whistler mode chorus waves existing outside the plasmasphere are shown to be capable of energizing energetic electrons to higher energies in the outer radiation belt and play critical role in MeV electron flux

enhancements [e.g., Horne and Thorne, 1998; Horne et al., 2005]. Besides chorus waves, the fast magnetosonic waves have also been shown to be able to accelerate energetic electrons both inside and outside the plasmasphere [e.g., Horne et al., 2007]. Different from inward radial diffusion, local heating usually creates a PSD radial profile that peaks at some L shell, as shown in Figure 2.7 (B).

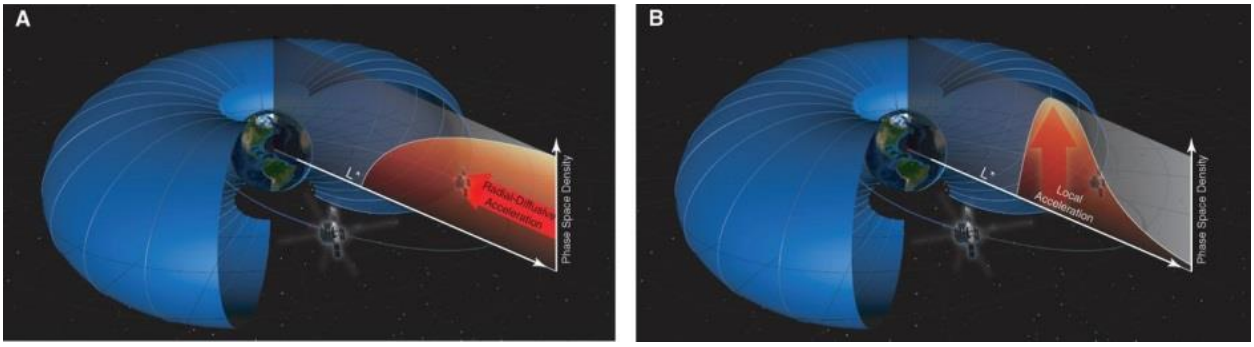

Figure 2.7: A schematic of the radial profiles of phase space density expected from (A) inward radial diffusion and (B) local wave heating. From Reeves et al. [2013].

A lot of effort has been made to identify the dominant acceleration mechanism in the outer radiation belt, and the relative importance of inward radial diffusion and local heating is still under debate [e.g., Li et al., 1997; Brautigam and Albert, 2000; Chen et al., 2007; Throne et al., 2010, 2013; Reeves et al., 2013; Jaynes et al., 2015]. Though the PSD radial profiles expected from inward radial diffusion and local wave heating are different, it is not easy to judge the most important mechanism responsible for electron acceleration just based on PSD radial profiles. This is mainly due to the lack of measurements with sufficient temporal and spatial coverage, and concurrent energization and loss processes. A local PSD peak can be generated by local wave heating, but can also be developed as a combination of inward radial diffusion and simultaneous loss in high L region. Similarly, a positive PSD radial gradient can be formed as a result of inward radial diffusion alone, but can also be expected from local heating with subsequent radial diffusion. And recently many studies focus on the combined effect of local heating and radial diffusion to radiation belt electron enhancements [e.g., Thorne et al., 2013;

Jaynes et al., 2015]. Figure 2.8 illustrates the role of chorus wave heating and radial diffusion in enhancing radiation belt electron fluxes during storm times.

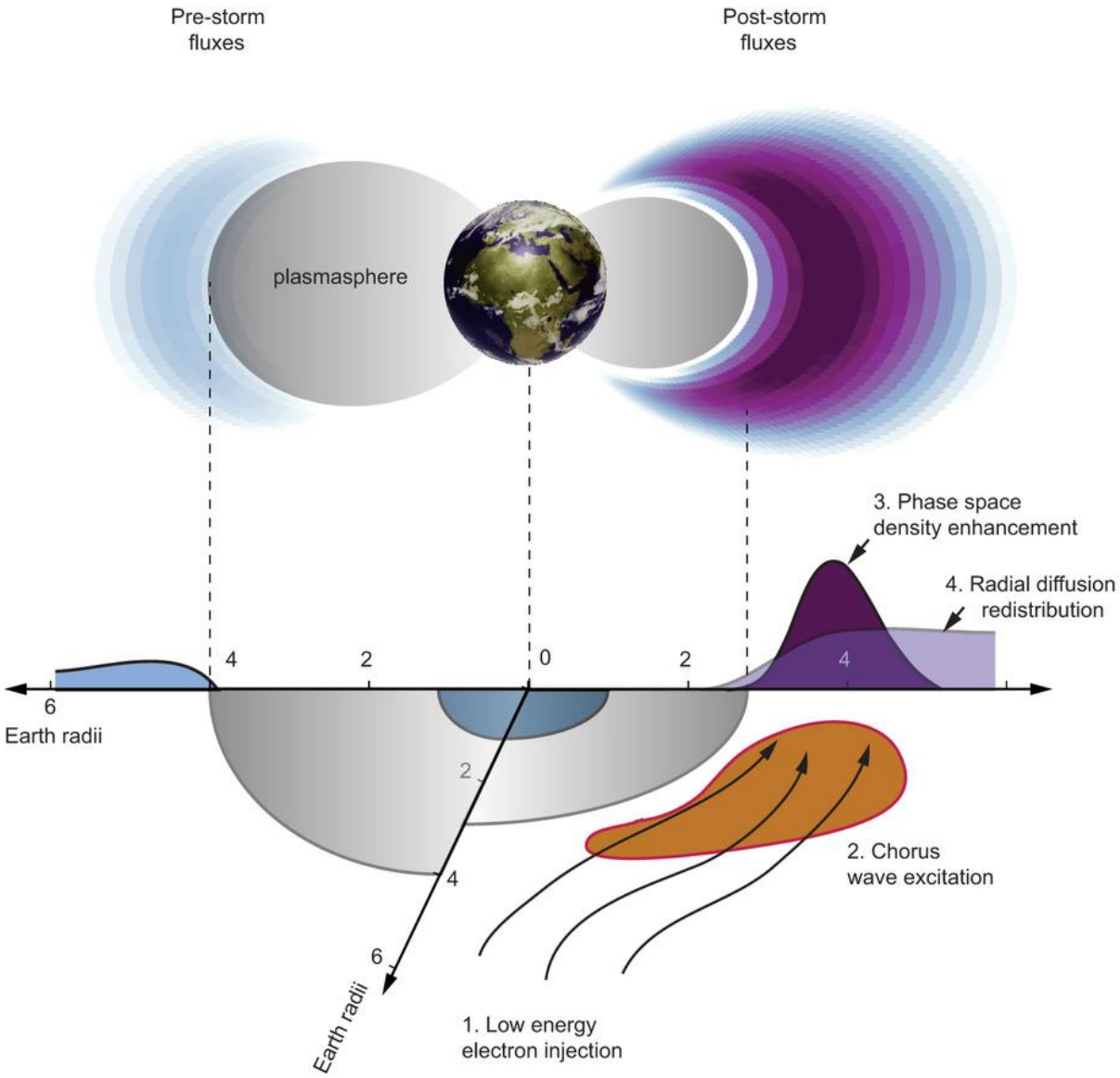

Figure 2.8: A schematic of acceleration processes for radiation belt electrons during storm times. From Thorne et al. [2013].

2.2.3 Loss Mechanisms

The ultimate sinks of radiation belt electrons are the magnetopause and atmosphere. Thus magnetopause shadowing and precipitation into the atmosphere are two of most important loss mechanisms of radiation belt electrons.

Magnetopause shadowing is a process of radiation belt electrons drifting to the magnetopause and being lost to the solar wind. During geomagnetic quiet times, generally, the magnetopause is located at a geocentric distance of ~$10R_E$ at the dayside. However, during geomagnetic disturbed times, if solar wind dynamic pressure increases, the magnetopause can be pushed into lower L shells and sometimes can even move inside of geosynchronous orbit. As the magnetopause moves in or electrons move out, electrons whose drift paths intersect the magnetopause will be lost. Magnetopause shadowing has been shown to be an effective mechanism for the loss of radiation belt electrons during storm times [e.g., West et al., 1972; Ukhorskiy et al., 2006; Turner et al., 2012].

Precipitation into the atmosphere is another important loss process of radiation belt electrons. Pitch angle diffusion caused by wave-particle interaction can scatter electrons into the loss cone and cause precipitation into the atmosphere. In the radiation belts, various waves can cause pitch angle diffusion of relativistic electrons through wave-particle interaction. The most common waves are whistler mode hiss waves, chorus waves, and EMIC waves. Responsible for pitch angle scattering inside the plasmasphere, the whistler mode hiss waves are considered to be a major contributor to the loss of relativistic electrons with a wide energy range (~10s of keV to > MeV) during both geomagnetic disturbed times and quiet times, and is thought to be responsible for the formation of the slot region [e.g., Lyons et al, 1972; Lyons and Thorne, 1973; Abel and Thorne, 1998; Meredith et al., 2006, 2007]. The wave-particle interaction caused by whistler mode chorus waves was introduced as an energization mechanism in the previous subsection, however, it can also be a loss mechanism. The chorus waves can scatter energetic electrons outside the plasmasphere and cause microbursts, which are the rapid bursts of precipitation

lasting less than 1s [e.g., Lorentzen et al., 2001; O'Brien et al., 2004; Thorne et al., 2005]. EMIC waves, existing preferentially in the dusk side and plasmasphere drainage plume, are considered to be able to cause resonant interaction and loss of ultra-relativistic electrons and are thought to be the cause of precipitation bands, which are rapid precipitations with durations of ~10s of seconds [e.g., Blum et al., 2013, 2015; Usanova et al., 2014].

On the other hand, the outward radial diffusion can also be a loss process of radiation belt electrons. Similar to inward radial diffusion which energizes electrons as they move to stronger magnetic field regions, outward radial diffusion deaccelerates electrons as electrons move to regions with weaker magnetic field and conserve the first and second adiabatic invariants. The outward radial diffusion requires a negative PSD radial profile, which usually can be produced by relativistic electron losses to the magnetopause [e.g., Shprits et al., 2006; Turner et al., 2012].

2.2.4 Electrons in the Inner Radiation Belt and Slot Region

The outer radiation belt is highly dynamic and usually attracts a lot of attention, while the inner radiation belt and slot region have been significantly neglected for the past several decades.

One reason for the neglect is that the inner radiation belt and slot region are thought to be quite stable and limited variations only happen during very intense geomagnetic storms or extreme solar wind conditions [e.g., Bostrom et al., 1970; Blake et al., 1992; Li et al., 1993; Baker et al., 2007; Li et al., 2009; Zhao and Li, 2013a; Baker and Blake, 2013; Baker et al., 2014]. However, though the inner belt and slot region are relatively stable for >MeV electrons and highly energetic protons, new observations show that they are actually quite active for 100s of keV electrons [e.g., Sauvaud et al., 2008; Selesnick et al., 2013; Zhao and Li, 2013b; Zhao et al., 2014a, 2014b].

Another reason for the lack of attention to the inner belt and slot region electrons during the past decades is data with limited quality, due to the contamination from the very energetic inner belt protons [e.g., Selesnick et al., 2014] and also from sometimes newly formed very

energetic electrons and protons in the slot region [Blake et al., 1992; Li et al., 1993; Hudson et al., 1995; Baker et al., 2004a]. Although many energetic electron flux measurements in the inner radiation belt suffer from energetic proton contamination, data from the Instrument for the Detection of Particle (IDP) onboard the Detection of Electro-Magnetic Emissions Transmitted from Earthquake Regions (DEMETER) satellite [Sauvaud et al., 2006] are believed to be relatively clean, since the energy spectrum measured by IDP shows a series of peaks at discrete energies consistent with energetic electrons interacting with VLF waves and thus confirms the effectiveness of the IDP spectrometer in the inner radiation belt [Sauvaud et al., 2006, 2008; Selesnick et al., 2013]. Furthermore, the newly available comprehensive and clean data from Van Allen Probes [Kessel et al., 2013] provide an unprecedented opportunity to study the details of relativistic electrons in the slot region and inner belt.

In addition, the source and loss processes in the inner belt and slot region were thought to be well understood, which is also a reason for the lack of attention of the inner belt and slot region over past decades. The most important source processes for the inner belt particles were recognized to be cosmic ray albedo neutron decay (CRAND) and inward radial diffusion [e.g., Walt and Farley, 1976]. CRAND was determined not to be a significant source of trapped electrons though it is an important source of relativistic protons [e.g., Kellogg, 1960; Lenchek et al., 1961; Pizzella et al., 1962]. Radial diffusion has long been considered one of the most important acceleration mechanisms for radiation belt electrons. It energizes electrons by bringing them inward where magnetic fields are stronger while conserving the first adiabatic invariant [e.g., Schulz and Lanzerotti, 1974]. The loss processes for inner belt electrons were recognized to be Coulomb collisions with atmospheric constituents and pitch angle diffusion via wave-particle interactions. Atmospheric collisions dominate energetic electron loss only for $L < 1.3$ [Walt, 1964]; while above $L = 1.3$, wave-particle interaction plays an important role in the loss of energetic electrons [e.g., Abel and Thorne, 1998]. The most important waves in the inner belt causing the loss of inner belt electrons are plasmaspheric hiss waves, VLF waves from high powered VLF transmitters, and lightning-generated VLF waves. Through the pitch angle

diffusion together with Coulomb collisions, these waves account for relativistic electron loss in the inner radiation belt. Also, the slot region is believed to form as a balance between the inward radial diffusion of electrons and pitch angle diffusion caused by wave-particle interaction [e.g., Lyons et al., 1972; Abel and Thorne, 1998; Kim et al., 2011]. Lyons et al. [1972] and Lyons and Thorne [1973] explained the formation of the slot region and predicted the pitch angle distributions in the slot region through simulation of wave-particle interaction. However, some new observations of Van Allen Probes in the inner belt and slot region, which will be discussed later in this thesis, show intriguing features of inner belt and slot region electrons which cannot be well explained by these known physical processes. These observations show the complexity of inner belt and slot region dynamics which has not been well understood and thus requires further attention.

2.3 Earth's Ring Current

The ring current is a toroidal electric current flowing around Earth (as shown in Figure 2.9). It is generally located at a geocentric distance between ~2 R_E and 9 R_E. The charged particle pressure gradient and azimuthal drift motion of charged particles in the geomagnetic field form the ring current. The main carrier of the ring current is believed to be ions with energies from ~ keV to 100s of keV [e.g., Frank, 1967a; Smith and Hoffman, 1973; Berko et al, 1975; Williams, 1981; Krimigis et al., 1985; Daglis et al., 1993], while electrons with energies from ~ keV to 10s of keV also contribute to the ring current [e.g., Frank, 1967; Deforest and McIlwain, 1971; Liu et al., 2005; Jordanova and Miyoshi, 2005; Zhao et al., 2015b]. During quiet geomagnetic activities, the ring current mainly consists of 100s of keV protons [e.g., Williams, 1981]; but during geomagnetic disturbed times, heavy ions can significantly contribute to the ring current energy and play important roles in the ring current dynamics [e.g., Krimigis et al., 1985; Hamilton et al., 1988; Roeder et al., 1996; Greenspan and Hamilton, 2000].

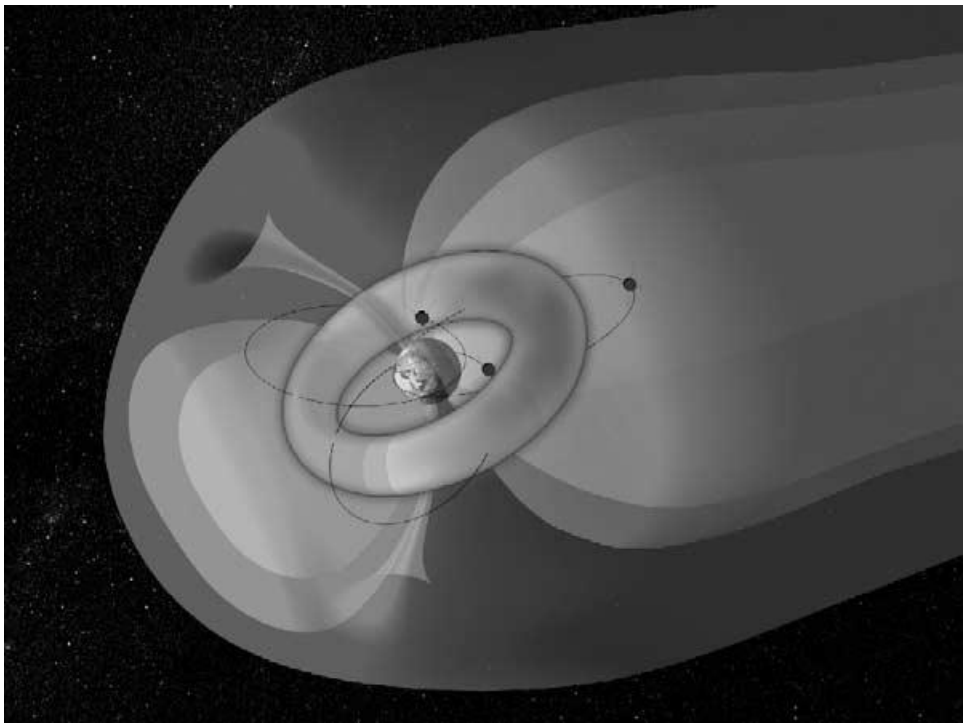

Figure 2.9: A schematic of Earth's ring current. From Daglis and Kozyra [2002].

2.3.1 Formation and Decay

The most popular mechanisms that contribute to the ring current generation include the earthward convection of plasma sheet particles due to enhanced E ×B drift, substorm injections, ionosphere outflows, and inward transport of previously trapped particles [e.g., Lyons and Williams, 1984; Daglis et al., 1999]. Sheldon and Hamilton [1993] studied the transport of ring current ions using the standard radial diffusion model and showed good agreement between model results and data from AMPTE/CCE for E>30 keV ions at L>4, indicating that for higher energy ring current ions radial diffusion is an important mechanism causing flux enhancements. Gerrard et al. [2014], using data from the Radiation Belt Storm Probes Ion Composition Experiment (RBSPICE) onboard the Van Allen Probes, showed observations of quiet time He ion which suggest inward radial diffusive motion of He ions that were previously injected into higher L shells. Gkioulidou et al. [2014, 2015], also using data from the RBSPICE instrument, investigated the ion injections during the ring current buildups and concluded that the small-scale ion injections could make a substantial contribution to the ring current buildups. On the other

hand, the decay of ring current ions are believed to be mainly caused by charge exchange processes [e.g., Smith and Bewtra, 1978; Jorgensen et al., 2001] and pitch angle scattering by plasma waves, e.g., EMIC waves and magnetosonic waves [e.g., Daglis et al., 1999], while the decay of ring current electrons is mainly caused by wave-particle interactions.

The direct sources of ring current particles are thought to be the plasma sheet and ionosphere. Since the particles in the plasma sheet are thought to have both ionospheric and solar wind origins, the ultimate sources of ring current particles are solar wind and ionosphere. However, the relative importance of these two sources is still under considerable debate. The composition information of the ring current, especially the relative abundance of O^+, is extremely important for the solution of this problem since the vast majority of O^+ in the inner magnetosphere comes from the ionosphere. The relative abundance of O^+ has been intensively studied [e.g., Gloeckler et al., 1985; Krimigis et al., 1985; Hamilton et al., 1988; Roeder et al., 1996; Greenspan and Hamilton, 2002; Zhao et al., 2015a]. It is widely believed that during geomagnetic quiet times, the ring current mainly consists of protons, while during storm times, O^+ ions account for a significant portion of the ring current energy and may even dominate during very intense storms [e.g., Gloeckler et al., 1985; Hamilton et al. 1988; Greenspan and Hamilton, 2002].

2.3.2 The Geomagnetic Storm and Dst Index

The enhancement of the ring current is responsible for worldwide depressions in the horizontal component of Earth's surface magnetic field, which are known as geomagnetic storms. Intense geomagnetic storms can cause severe disruption of electrical systems on the ground. The Dst index, which is derived based on the measurements from four magnetometers near the equator and shows the perturbation of the horizontal component of geomagnetic field at the center of the Earth, is generally used as an indicator of geomagnetic storms and a proxy of ring current [Sugiura and Kamei, 1991]. Usually, a geomagnetic storm is identified if the Dst index

reaches below -20 nT [Gonzalez et al., 1994]. The geomagnetic storms can be categorized using the minimum Dst index during the storms. Typically, a geomagnetic storm is categorized as a small storm with the minimum Dst index of -20 – -50 nT, as a moderate storm with the minimum Dst index of -50 – -100 nT, and as an intense storm with the minimum Dst index less than -100 nT. Figure 2.10 shows the Dst index during an intense storm of July 1984.

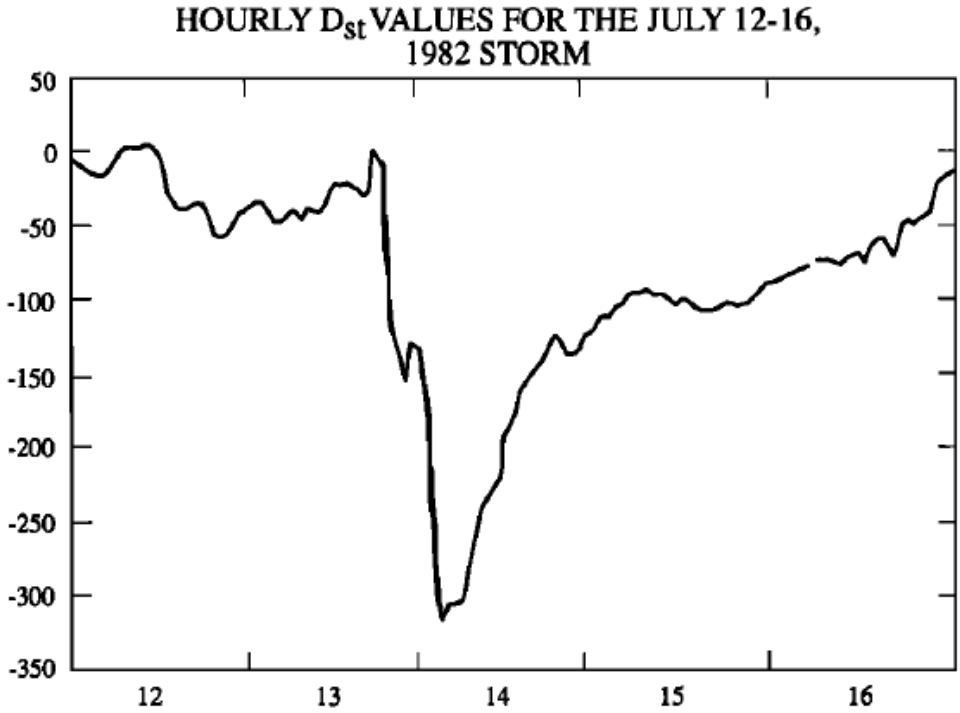

Figure 2.10: The Dst index during an intense geomagnetic storm of 12-16 July 1982. From Gonzalez et al. [1994].

The geomagnetic storm is typically composed of several phases: initial phase, main phase and recovery phase. Some geomagnetic storms begin with a sudden impulse in the Dst index caused by the interplanetary shock, which is known as the storm sudden commencement. Following the storm sudden commencement, the initial phase is a period of increased solar wind dynamic pressure, during which the Dst index tends to be positive due to the enhanced magnetopause currents. The main phase is a period during which the ring current builds up and decreases the magnetic field strength inside the current and thus the Dst index decreases. And

after the Dst index reaches its minimum value, it recovers gradually to the quiet time values as the ring current decays; this period is called the recovery phase.

Though designed to indicate the strength of the ring current, the Dst index is also influenced by multiple magnetospheric current systems. Ground-induced current may influence the magnetic field strength at the equator and thus the Dst index. Dessler and Parker [1959] showed that, theoretically, a perfectly diamagnetic Earth can increase the impressed magnetic field by ~50% at the equator. Langel and Estes [1985] also showed that the induced internal magnetic field magnitude is about 24%/29% of the near-Earth external field at the dusk/dawn sector respectively. The magnetotail current system could also contribute to the Dst index significantly. Turner et al. [2000] studied the contribution of the magnetotail currents to the Dst index using T89 and T96 dynamic geomagnetic field models and concluded that the contribution during moderate storms is about 25%. Ganushkina et al. [2004] showed the dominant role of near-Earth tail currents to the Dst index during moderate geomagnetic storms through modeling of storm-time magnetospheric magnetic field. Tsyganenko and Sitnov [2005] also showed that the major contributions to the Dst index are from the symmetric ring current and near-Earth tail currents, while the tail currents actually dominate at the storm main phase. Magnetopause currents would also contribute to the magnetic field perturbation at Earth's surface [e.g., Burton et al., 1975; O'Brien and McPherron, 2000; Zhao et al., 2011]. Burton et al. [1975] investigated the influence of magnetopause currents to the Dst index and suggested using equation $Dst^* = Dst - b\sqrt{P} + c$ to remove the contribution of magnetopause currents, where Dst^* is the pressure-corrected *Dst* index, P is the solar wind dynamic pressure, b and c are constants.

2.3.3 The Dessler-Parker-Sckopke (DPS) Relation

The magnetic field perturbation at the center of the Earth is shown to be correlated with the total kinetic energy of particles in the ring current, and this correlation can be expressed as a

simple equation, called Dessler-Parker-Sckopke (DPS) relation [Dessler and Parker, 1959; Sckopke, 1966]:

$$\frac{\Delta B}{B_S} = -\frac{2E}{3E_M}$$

where ΔB is the magnetic perturbation at the center of the Earth, B_S is Earth's magnetic field at Earth's surface, E_M is the total energy of Earth's dipole field above Earth's surface, and E is the total kinetic energy of particles drifting around Earth. This relation has been proved to be valid for any steady distributions of trapped particles in the Earth's magnetic field [Sckopke, 1966].

The DPS relation has been verified through some previous studies. For example, Frank [1967b], using data from OGO 3, investigated the temporal variations of the energy densities of 200 eV – 50 keV protons and electrons during two moderate geomagnetic storms and showed that the total kinetic energy of protons and electrons in the ring current is sufficient to account for the depression of Earth's surface near-equatorial magnetic field using the DPS relation. However, the DPS relation also has some limitations on predicting magnetic field depressions according to the ring current particle measurements. This is mainly because the magnetic field perturbation as well as the Dst index are influenced by ground induced current and other current systems, e.g., the magnetopause current, magnetotail current, and the partial ring current. Hamilton et al. [1988], in their study of the evolution of ring current ions during the intense storm of February 1986, found that the measured energy content of ring current ions was less than the value predicted by the DPS relation by a factor of ~2. Turner et al. [2001] investigated the energy content of the ring current during geomagnetic storms using data from the Charge and Mass Magnetospheric Ion Composition Experiment (CAMMICE) instrument on the Polar spacecraft and found that based on the DPS relation the ring current ions contribute about half of the depression of Earth's surface near-equatorial geomagnetic field on average.

Chapter 3

MeV Electrons in the Slot Region: Influence of the Solar Wind and Geomagnetic Storms on the Flux Enhancements

The following chapter is based on work that was published in Zhao and Li (2013a), Inward shift of outer radiation belt electrons as a function of Dst index and the influence of the solar wind on electron injections into the slot region, J. Geophys. Res. Space Physics, 118, 756–764, doi:10.1029/2012JA018179.

3.1 Introduction

Relativistic electrons in the inner magnetosphere are distributed into two regions: the inner radiation belt and the outer radiation belt. The inner radiation belt is relatively stable, while the outer radiation belt is highly dynamic and can exhibit great changes during geomagnetic storms. Geomagnetic storms can either increase or decrease relativistic electron fluxes in the outer radiation belt [Reeves et al., 2003]. Tverskaya et al. [2003] investigated storm-injected relativistic electrons during selected geomagnetic storms in 1993, 1997, 1998, and a great storm in April 2000 using SAMPEX, Polar, and the highly elliptical orbit (HEO) 1997-068 observations and found a strong correlation between the absolute value of the minimum Dst index (Dst_{min}) and the radial position of the intensity peak of electrons during the recovery phase of a storm. Iles et al. [2002] also confirmed that the L location of the peak electron count rate enhancement during geomagnetic storms from January 1995 to March 1998 has a dependence on Dst^* by using data from microsatellites the Space Technology Research Vehicle (STRV). More recently, Zheng et al. [2006], using SAMPEX 2-6 MeV electron data, showed that the penetration distance of 2-6 MeV electrons during geomagnetic storms with $Dst_{min} < -130$ nT from 1992 to 2004 has a good correlation with Dst_{min} delayed by 3 d.

Separating the inner and outer radiation belts is a region called the slot region, which is usually devoid of relativistic electrons. The formation of the slot region is believed to be due to

the balance between the inward transport of electrons and pitch angle diffusion [Lyons and Thorne, 1972]. During intense solar wind conditions, however, the slot region can be filled with relativistic electrons [e.g., Blake et al., 1992; Li et al., 1993; Baker et al., 2004a]. After filling, the electrons in the slot region subsequently decay. In the slot region, the lifetimes of electrons of different energies can be quite different [e.g., Fennell et al., 2005]. For 2-6 MeV electrons, it can vary from several days to a few weeks at different L [Baker et al., 2007]; in the center of the slot region (L=2.5), the lifetime of 2-6 MeV electrons is about 3.6 ±1.6 d [Meredith et al., 2009].

In this chapter, we examine the relationship between different definitions of L location of 2-6 MeV electron penetrations and minimum Dst index during all moderate and intense isolated storms from 1995 to 2004. We use daily averaged 2-6 MeV electron flux data from SAMPEX, which operates in a near-circular orbit with an altitude of 520 by 670 km and an 82 °inclination [Baker et al., 1993]. The electron flux data are sorted by L shell with $\Delta L = 0.1$. By using a wide intensity range of storms, with Dst_{min} from -50 nT to around -400 nT, and multiple L location definitions, we show the correlation between L location and Dst index in more depth than previous work. We also investigate electron flux during isolated storms at each L shell and the sum of electron fluxes throughout the slot region and outer belt, and find that almost all storms show flux enhancements at some L shell, but only about 40% of the storms cause increases of the total electron flux between L=2 and L=7, 20% cause decreases, and 40% produce no change. Additionally, using daily averaged 2-6 MeV electron flux data and 5 min solar wind data from OMNI Web, we perform a survey of the relationship between 2-6 MeV electron penetrations into the slot region and solar wind conditions, comparing the relative effectiveness of solar wind parameters and their combinations. In addition to solar wind conditions, we find another important factor, electron flux preconditioning, which greatly influences the likelihood of electron penetrations into the slot region.

3.2 Relativistic Electron Penetrations and Dst Index

To investigate the relationship between the L location of 2-6 MeV electron penetrations and the minimum Dst index during geomagnetic storms, we examine daily averaged data from SAMPEX of 2-6 MeV electrons from 1995 to 2004. We define L_{lowest} as the lowest L on which the flux changes by at least one order of magnitude, and L_{max}^{flux} as the L on which the flux at the end of penetration is the largest. Also, we define $L_{max}^{increase}$ (by percentage/value) as the L of the maximum flux enhancement, that is, the L shell on which the flux increases most by percentage/value from the beginning of the storm to the end of penetration; $L_{max}^{variation}$ (by percentage/value) is defined as the L of the maximum flux variation, that is, the L shell on which the flux increases most by percentage/value from the point of the lowest flux during the storm to the end of penetration.

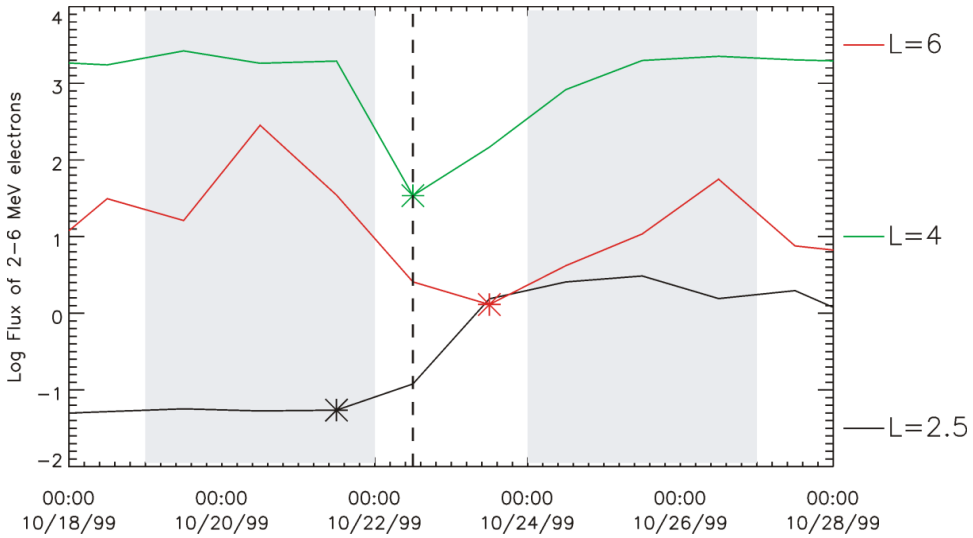

Figure 3.1: An illustration of the flux enhancement and flux variation during an isolated storm based on daily averaged 2-6 MeV electron flux data from SAMPEX. The dashed line marks the middle of the day of Dst_{min}. The fluxes averaged over the 3 d periods indicated by two gray blocks are defined to be the flux at the beginning of the storm (left) and the flux at the end of penetration (right), respectively. The asterisks represent the lowest fluxes during the storm at corresponding L shells.

Figure 3.1 shows an example of how to calculate the flux enhancement and variation. The dashed line marks the middle of the day of Dst_{min}. We define the flux at the end of a penetration

as the averaged flux 2-4 d after the day of Dst_{min}, and this time period is indicated by the gray block on the right of Figure 3.1; the flux at the beginning of the storm is defined as the averaged flux 1-3 d before the day of Dst_{min}, indicated by the gray block on the left of Figure 3.1. The colored asterisks represent the lowest fluxes during the storm at corresponding L shells. As Figure 3.1 shows, the lowest fluxes during the storm at different L shells can occur at different days; at L=2.5, the flux variation is similar in magnitude to the flux enhancement, but at L=4 or L=6, the flux variations are much larger than the flux enhancements.

In this study, we broaden the size of storms and enlarge the number of selected storms from previous studies [e.g., Tverskaya et al., 2003] by using all moderate and strong storms (with Dst_{min}<-50 nT) during 1995-2004. To avoid the influence of multiple storms, we use isolated storms only in this study. We set the criteria for isolated storms as the following: first, only those storms with no other storms occurring within 7 d before or 4 d after are included; for some strong storms, the electron flux is not likely to be significantly influenced by much smaller storms nearby, thus we also include those intense storms that are much larger than other storms (with ΔDst_{min}>100 nT) that happen within 7 d before and 4 d after. Figure 3.2 shows an example of the storm selection criteria. In April 2000, three storms meet our criteria, as marked with red asterisks. For storms on 16 April and 24 April, no other storms occurred within 7 d before or 4 d after, so these two storms are included; the storm on 5 April, marked with the green asterisk, is not counted as an isolated storm because 2 d later another large storm occurred. The storm on 7 April, however, is included despite being only 2 d after a storm because it is much larger than the nearby storm. From January 1995 to June 2004, a total of 124 storms met these requirements; 10 of them were large storms with much smaller storms nearby, and among these 10 storms the closest smaller storm occurred about 1 d before. Excluding storms during which the SAMPEX data are not available, a total of 119 storms are investigated; also excluding storms during which the electron fluxes did not increase at any L shell from L=2 to L=7, finally, a total of 117 storms are used in the following study.

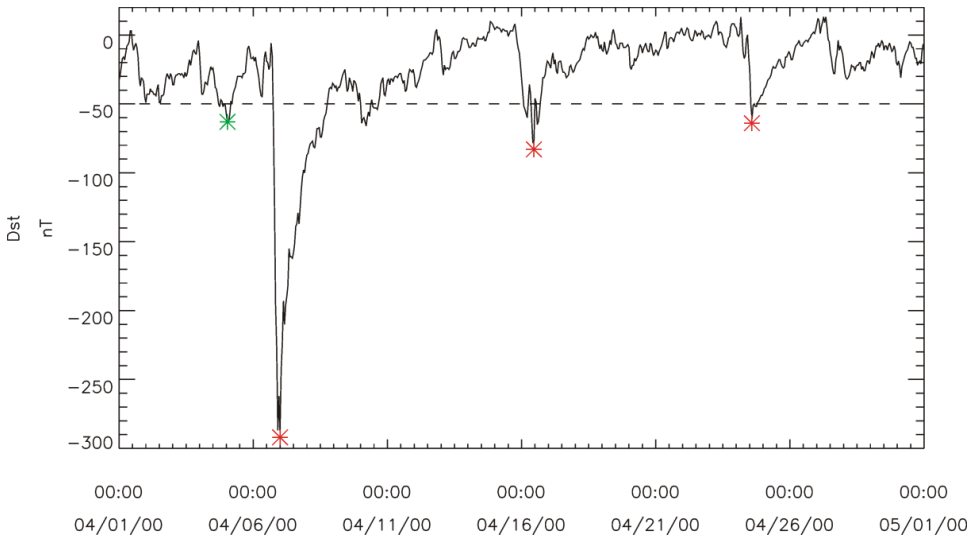

Figure 3.2: Selected isolated geomagnetic storms in April 2000. Three storms, marked with red asterisks, are selected according to our criteria, while the storm with the green asterisk is not included.

Figure 3.3 shows the six different L locations defined previously versus $|Dst_{min}|$ during 117 storms from 1995 to 2004. The magnitudes of the maximum flux, flux enhancement, and flux variation (by percentage/value) for each storm are also shown in Figure 3.3. L_{lowest}, L_{max}^{flux} and $L_{max}^{variation}$ (by value) have the highest correlations with $|Dst_{min}|$, with correlation coefficients of 0.78, 0.83, and 0.87, respectively. For intense storms (Dst_{min}<-100 nT), the magnitudes of the maximum flux enhancement and variation are generally higher than for moderate storms (-50 nT>Dst_{min}>-100 nT). The results indicate that the location of relativistic electron deepest penetration, location of the maximum flux at the end of penetration, and location of the highest flux variation by value during geomagnetic storms have strong correlations with Dst index and thus the intensity of the storm. The stronger the storm, the further inward electrons can penetrate. Compared to the deepest penetration and L location of the maximum flux and flux variation, the correlation coefficients between $L_{max}^{increase}$ by percentage/value and $|Dst_{min}|$ are not as high (0.48 and 0.53 respectively). Reeves et al. [2003] investigated relativistic electron fluxes in the outer radiation belt during geomagnetic storms and showed that during about half of geomagnetic storms the flux at a given L shell in the outer radiation belt increases, while for another half the electron flux either remains the same or decreases, and that this result is independent of the

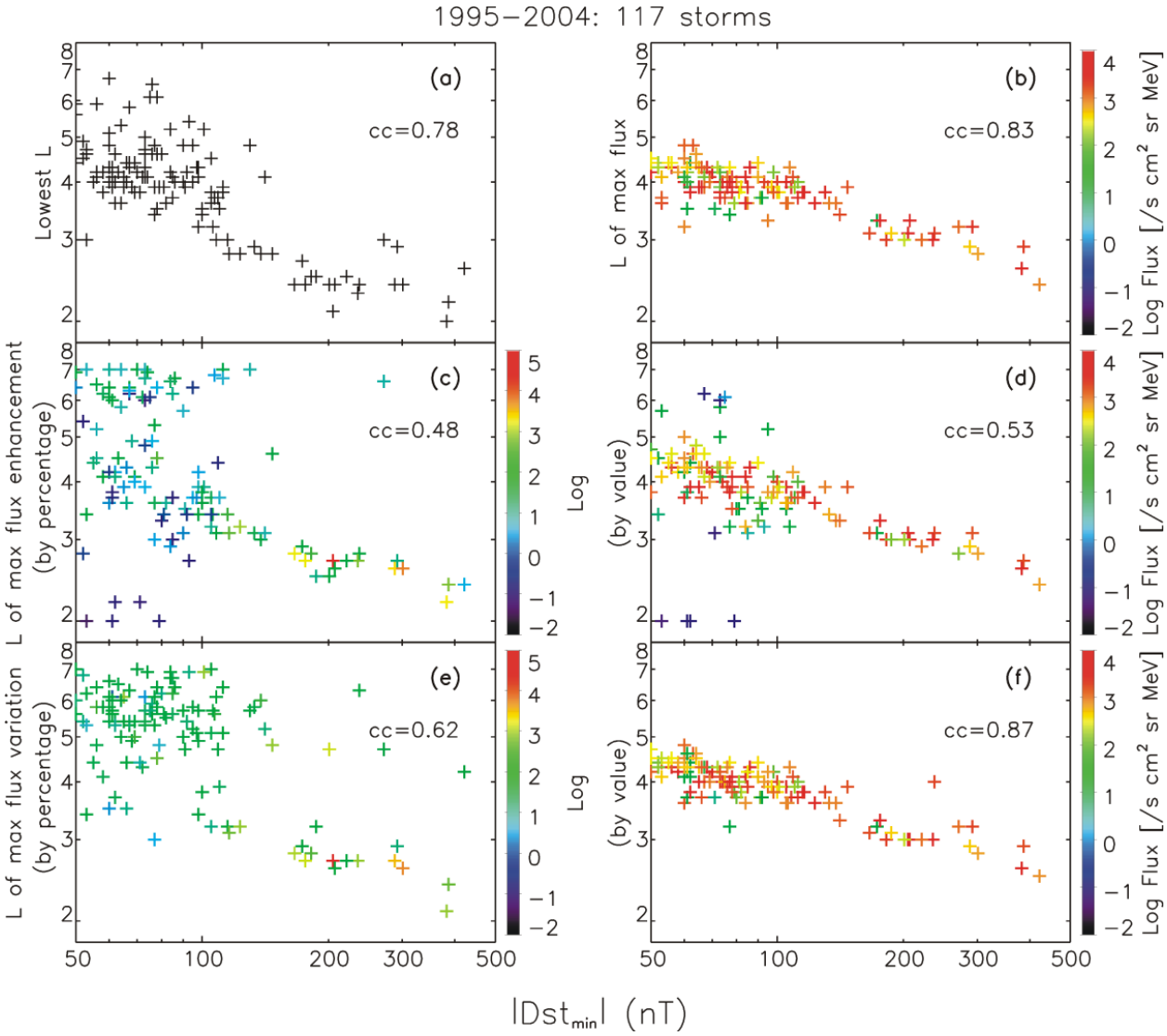

Figure 3.3: (a) Lowest L shell on which the flux changes by at least one order of magnitude, (b) L shell on which the flux at the end of penetration is the highest, (c and d) L shell on which the flux increases the most from the beginning of the storm to the end of penetration by percentage and by value, (e and f) L shell on which the flux increases the most from the lowest flux during the storm to the end of penetration by percentage and by value, versus $|Dst_{min}|$ during 117 isolated geomagnetic storms from 1995 to 2004. The correlation coefficient (cc) of each case is shown on each panel.

specific L shell investigated. This explains the weak correlation between $L_{max}^{increase}$ and Dst index. During some geomagnetic storms, especially some moderate storms, the flux at the outer radiation belt decreases, while at lower or even higher L the electron flux does not change or increases slightly, thus a lower or higher L shell would become the L shell on which the flux "increases" the most. As indicated in Figure 3.3(d), the magnitudes of the maximum flux

enhancement during some storms are quite low, and for these storms the L shell of the maximum flux enhancement is usually very low or very high. On the other hand, the L location of the maximum flux variation during the storm does have a strong correlation with storm intensity, as can be seen in the good correlation between $L_{max}^{variation}$ and Dst index. This indicates that the flux variations during the storm are also greatly affected by geomagnetic activity.

The results of this L-Dst study show that there is a strong correlation between relativistic electron penetrations and Dst index, not only confirming previous studies [e.g., Tverskaya et al., 2003] using a larger data set, but also adding more discussions on the same topic. In the next section, we focus on relativistic electron penetrations into the slot region and their relation with solar wind parameters.

3.3 Relativistic Electron Penetrations into the Slot Region and Correlation with Solar Wind Parameters

3.3.1 Penetration Events in the Slot Region

In the previous section, we showed that there is a strong correlation between electron penetrations and Dst index. In this section, we will show the relationship between electron penetrations into the slot region and solar wind parameters. To examine electron penetrations into the slot region, we define penetration events in the slot region (L=2-3), according to daily averaged SAMPEX 2-6 MeV electron flux data from 1995 to 2004, as follows: at L=2/2.1/…/3, if the daily averaged 2-6 MeV electron flux increases monotonically by one order or more within 3 days, we call it a penetration event at L=2/2.1/…/3. From 1995 to 2004, we find, for example, a total of 3 penetration events at L=2, 23 events at L=2.5, and 34 events at L=3. Figure 3.4 shows the number of penetration events at L=2-3.

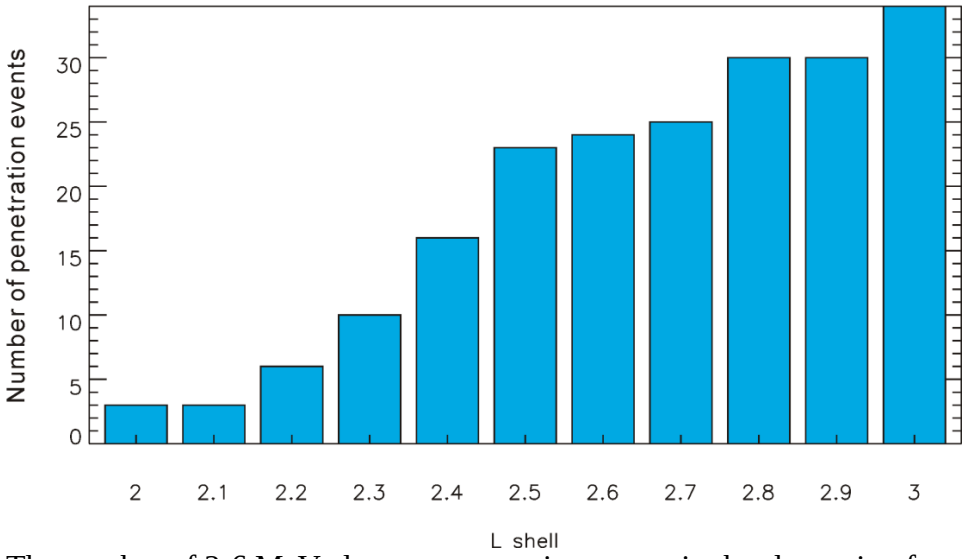

Figure 3.4: The number of 2-6 MeV electron penetration events in the slot region from January 1995 to June 2004.

3.3.2 Solar Wind Conditions for Electron Penetrations into the Slot Region

To show the correlation between solar wind parameters, including interplanetary magnetic field (IMF), and penetration events in the slot region, we choose to focus on the center of the slot region, L=2.5, because the electron flux at L=2.5 is usually the lowest within the slot region according to SAMPEX data. By examining data during 1995-2004, we find a total of 23 penetration events at L=2.5. The results show good correlation between IMF magnitude, IMF B_z in geocentric solar magnetospheric (GSM) coordinates, solar wind electric field E_y, and penetration events at L=2.5 using 5 min solar wind data from OMNI Web. During these penetration events, the maximum IMF magnitude (B_{max}) of each event is greater than 24 nT; IMF B_z remains less than -10 nT for more than 1 h; the maximum E_y ($E_{y\,max}$) is larger than 8 mV/m, while 21 of 23 events occurred with $E_{y\,max}$>9 mV/m. There is also some correlation between solar wind speed (V_{sw}) and penetration events. During most events (22 of 23) the maximum V_{sw} ($V_{sw\,max}$) is greater than 500 km/s. Solar wind density and dynamic pressure, however, show no obvious correlation with these penetration events.

We find that sufficient conditions for penetration events at L=2.5 are: B_{max}>24 nT, $E_{y\,max}$ > 9 mV/m, and E_y ×time (when E_y>0.5 mV/m) >7 mV/m·d. Here E_y ×time is calculated within 1.5 d before and after $E_{y\,max}$, and calculated only when E_y>0.5 mV/m, which means it only includes the positive part of E_y. For the period 1995-2004, there are a total of 10 intervals during which the solar wind conditions met these sufficient conditions, and a penetration event occurred for each of these intervals.

On the other hand, we wonder if there exist necessary solar wind conditions for the penetration events. The necessary conditions we find for penetration events at L=2.5 are IMF>24 nT, B_z<-10 nT for at least 3 h, $E_{y\,max}$>9 mV/m, and E_y ×time (when E_y>0.5 mV/m) >3.5 mV/m·d. For the period 1995-2004, there are a total of 30 intervals during which these criteria are fulfilled, and 21 of them caused penetration events at L=2.5. There are two exceptions during which the necessary conditions are not fulfilled. During one event, the solar wind parameters are not fully available; during the other event, the solar wind conditions are quite mild compared to other events, and this event (on 28 March 2001) will be discussed in the next subsection. The sufficient and necessary conditions for penetration events at L=2.5 are summarized in Table 3.1.

Table 3.1: The sufficient and necessary solar wind conditions for penetration events at L=2.5. The resolution of solar wind data is 5 min.

Sufficient Conditions	Necessary Conditions (except for two events)
IMF B_{max} > 24 nT	IMF B_{max} > 24 nT
$E_{y\,max}$ > 9 mV/m	IMF B_z < -10 nT lasting for > 3h
E_y ×time > 7 mV/m·d (when E_y > 0.5 mV/m)	$E_{y\,max}$ > 9 mV/m
	E_y ×time > 3.5 mV/m·d (when E_y > 0.5 mV/m)

There are some researches suggesting MeV electron penetrations into the slot region are caused by strong storms [e.g., Miyoshi and Kataoka, 2005]. Indeed, the results we found show that most penetration events at L=2.5 (22 of 23) occurred during intense geomagnetic storms

with Dst_{min}<-140 nT; however, there is still one event that happened under a moderate storm (Dst_{min}=-87 nT). Furthermore, intense storms do not always lead to penetration events in the slot region: there are 10 storms for the period 1995–2004 with Dst_{min}<-140 nT that did not cause penetration events at L=2.5.

We have examined the solar wind conditions associated with penetration events at L=2.5 and have shown that IMF and solar wind electric field have good correlations with penetration events. Here we also want to examine the correlation between the magnitude of flux enhancement at L=2.5 and solar wind parameters using a larger database of events. Because the Dst index can be predicted by solar wind parameters accurately [Temerin and Li, 2002, 2006], we use Dst index to identify those events for convenience. We choose to use storms with Dst_{min}<-50 nT during 1995-2004, and for multiple storms happening within 2 d, we choose the most intense one. There are a total of 209 events that meet these criteria.

We calculate the electron flux enhancement at L=2.5 as the ratio of the flux at the end of the event to the flux at the beginning of the event. Because now we focus only on flux enhancements at L=2.5, we use different definitions of the beginning and the end of the event from section 3.2. The beginning of the event here is defined to be 0 or 1 d before Dst reaches its minimum, depending on which day the electron flux at L=2.5 is lower, while the end of the event is defined to be 3 d after the beginning of the event. There is a time delay between solar wind impact and the electron flux enhancements in the slot region and we find it usually takes 2-3 d from the beginning of the event for electron flux to reach its peak value at L=2.5, which is also consistent with previously published results [e.g., Zheng et al., 2006]. Here we choose solar wind parameters during the time period of 2 d before Dst reaches its minimum and 1 d after that to investigate their correlations with the enhancement of the electron flux at L=2.5.

Figure 3.5 shows the relationship between solar wind parameters and electron flux enhancements at L=2.5 during the 209 events from 1995 to 2004. The results show good correlations between solar wind parameters E_y, IMF B_z, B, and the magnitude of flux enhancement. The correlation coefficients of $E_{y\,max}$, $B_{z\,min}$, and B_{max} with the logarithm of the

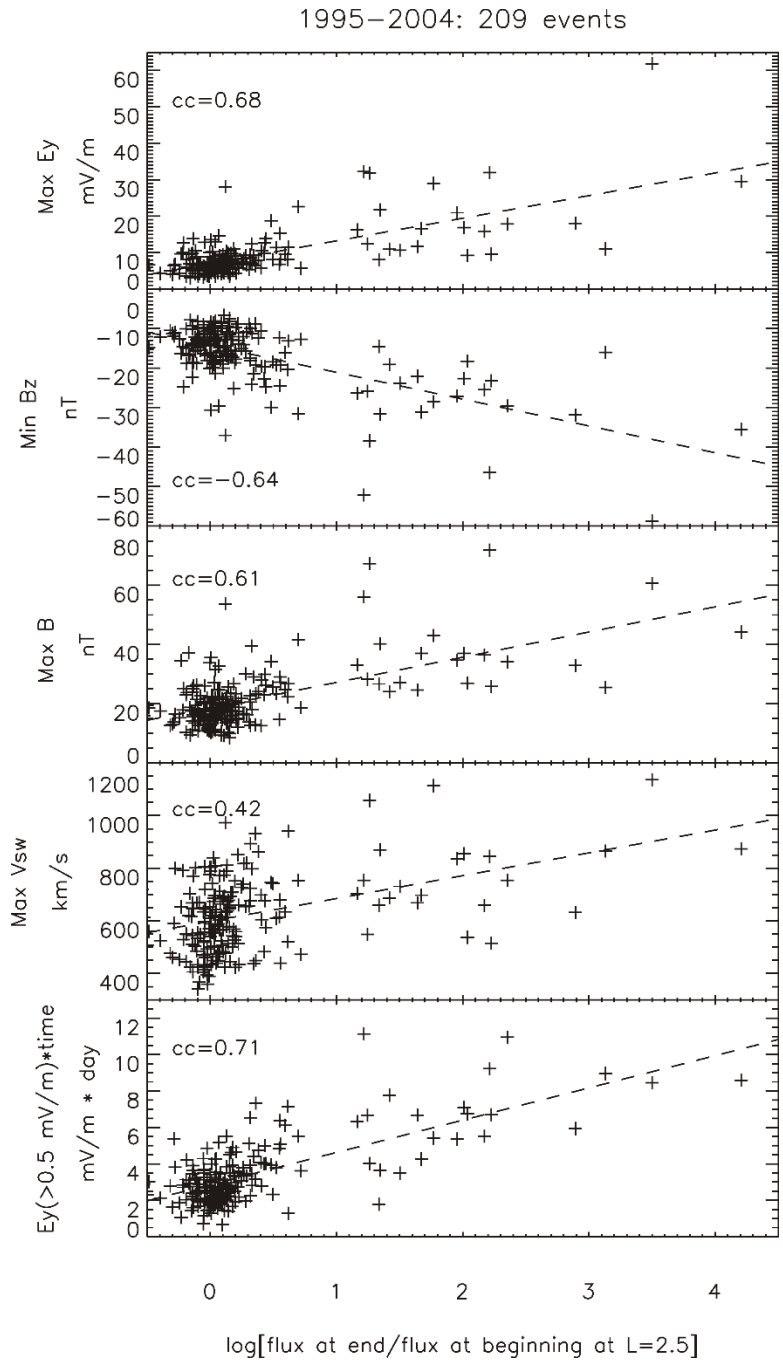

Figure 3.5: IMF and solar wind parameters versus logarithm of flux enhancement at L=2.5 during 209 events from 1995 to 2004. Dashed lines are linear fits to the points. The correlation coefficient (cc) is also shown in each panel.

magnitude of flux enhancement are 0.68, -0.64, and 0.61, respectively. $E_y \times$time (when E_y>0.5 mV/m) has the highest correlation coefficient with the logarithm of the flux enhancement (0.71). On the other hand, solar wind speed, which is widely believed to be the parameter most strongly

correlated with electron flux enhancements in the outer belt [e.g., Li et al., 2001, 2011], has a relatively weaker correlation with flux enhancements in the slot region (0.42). These results indicate that solar wind parameters have good correlations with electron flux enhancements in the slot region, and solar wind electric field is the most important parameter for controlling the magnitude of electron flux enhancements in the slot region.

3.3.3 Electron Flux Preconditioning for Relativistic Electron Penetrations into the Slot Region

In section 3.3.2, we discussed sufficient and necessary solar wind conditions for penetration events at L=2.5. We mentioned one event during which the solar wind conditions are quite mild compared to others. Figure 3.6 (left) shows this event on 28 March 2001. The red dashed line shows the beginning of this event. The most likely explanation for why this event caused MeV electron penetration into L=2.5 despite the mild solar wind conditions is that the electron flux at L greater than 2.5 is already high due to an intense storm on 19 March, while the flux at L=2.5 is still low. Thus, the steep electron flux radial gradient makes it easier for these electrons preexisting around L=3 to penetrate into L=2.5. According to this, we define a preconditioned event as when the 2-6 MeV electron flux at L=3 is at least two orders higher than the flux at L=2.5 prior to an event. Figure 3.6 (right) also shows a non-preconditioned event on 7 April 2000, which also caused a penetration event at L=2.5. Comparing these two events, we find that for the non-preconditioned event, much more intense solar wind conditions are required to cause a flux increase in the slot region. The minimum IMF B_z for the non-preconditioned event on 7 April 2000 is about -30 nT, and maximum E_y is about 17 mV/m; while for the preconditioned event on 28 March 2001, $B_{z\,min}$ and $E_{y\,max}$ are just roughly -13 nT and 8 mV/m, respectively. Thus, electron flux preconditioning is a very important factor for electron penetration into the slot region. It is worth mentioning that the electron fluxes after the event in March 2001 are relatively lower, with a post-event flux of less than 10 electrons/s/cm^2/sr/MeV. However, an electron flux enhancement of one order is quite significant at L=2.5 and among all

other 22 penetration events at L=2.5, 9 of them have similar post-event flux levels to this March 2001 event. Among these nine penetration events, some are caused by quite intense solar wind conditions and strong storms, with $|Dst_{min}|$ up to ~250 nT; but because the ratios of the electron flux at L=3 to L=2.5 before these penetration events are lower than that before the preconditioned event in March 2001, the post-event flux levels for these events are just similar to the March 2001 event, which also confirms the importance of electron flux preconditioning.

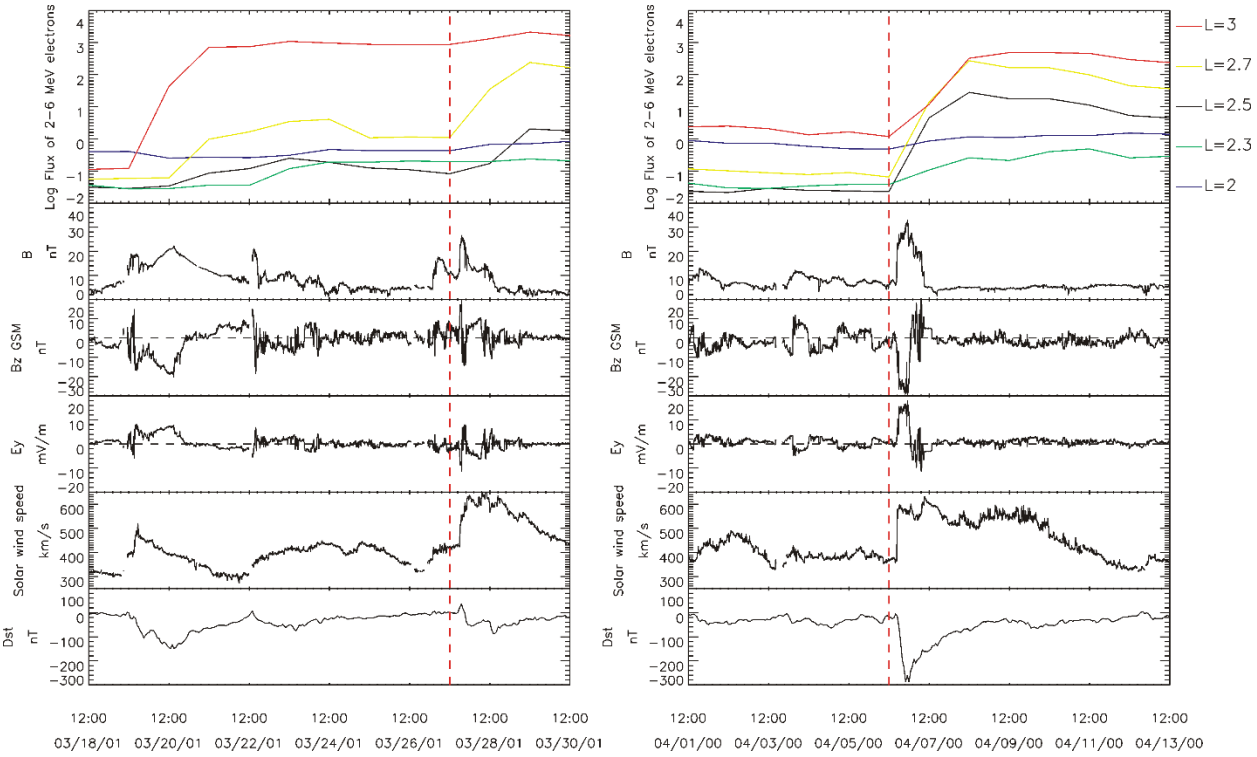

Figure 3.6: (From top to bottom) Daily averaged 2-6 MeV electron fluxes in the slot region, IMF magnitude, IMF B_z, solar wind electric field, solar wind speed, and Dst index on 18-30 March 2001 (left) and 1-13 April 2000 (right). Red dashed lines mark the beginning of these penetration events at L=2.5.

Additionally, to investigate the influence of electron flux preconditioning, we use all penetration events occurring in the slot region, from L=2 to L=3. Based on the definition of preconditioned events above, we divide penetration events into preconditioned events and non-preconditioned events according to the flux profile at the beginning of the event. The definition of the beginning of the event here is the same as the one in section 3.3.2. We then plot the lowest

L shell on which electron flux increased by at least one order (that is, the lowest L shell on which the penetration event occurred based on our definition) versus $|Dst_{min}|$ during the event (Figure 3.7). Figure 3.7 shows that for non-preconditioned events, the storm must be much stronger than preconditioned events to cause MeV electron penetrations into the slot region. This suggests that with proper preconditioning, such as defined above, relativistic electrons are more likely to penetrate into the center of the slot region, L=2.5, while without preconditioning, it is also possible for electrons to move inward but much larger storms and thus much more intense solar wind conditions are required.

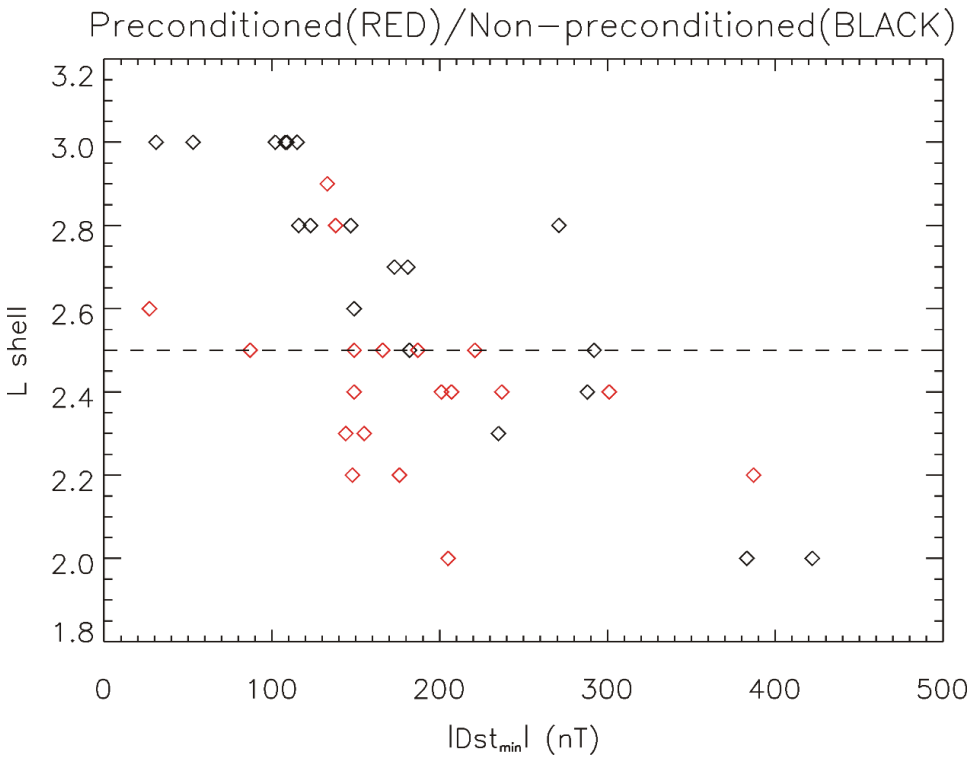

Figure 3.7: Lowest L shell on which 2-6 MeV electron flux increased by at least one order of magnitude versus $|Dst_{min}|$ during penetration events that occurred at L=2-3. Red points represent preconditioned events; black points represent non-preconditioned events. The dashed line shows L=2.5.

3.4 Discussion

Figure 3.3 shows the L-Dst dependence based on 117 geomagnetic storms during 1995-2004. It is worth noting that SAMPEX data may have saturation issues, and there may be some uncertainties in the L calculation. However, we demonstrate here that these uncertainties do not significantly affect the results in this L-Dst dependence study. For each storm, we examine the uncertainty in the L location of the maximum flux at the end of penetration. Figure 3.8 shows the uncertainties in the L location of the maximum flux previously examined in Figure 3.3(b). Red lines represent where the electron flux is greater than 90% of the maximum flux at the end of penetration. Figure 3.8 shows that even considering these uncertainties, the L shell of the maximum flux at the end of penetration still has a strong correlation with Dst index, and thus these uncertainties do not significantly affect the result of L-Dst dependence.

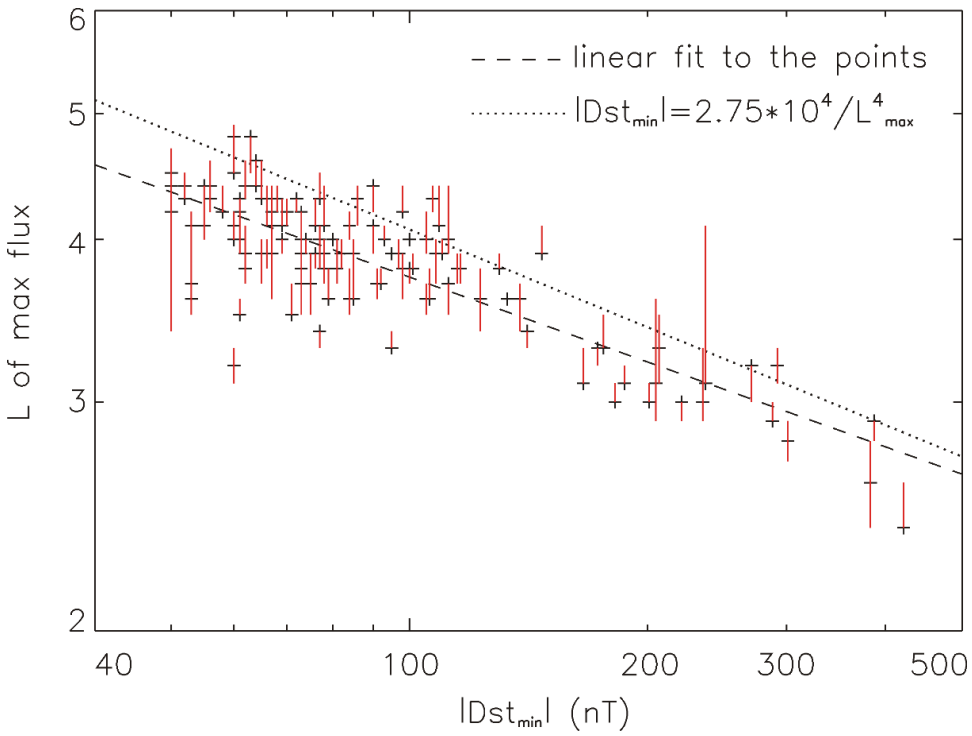

Figure 3.8: L shell of the maximum electron flux at the end of penetration versus $|Dst_{min}|$ for 117 storms during 1995-2004. Red lines represent where the flux is greater than 90% of the maximum flux. The dashed line is the linear fit to the points, and the dotted line shows the equation derived by Tverskaya [1986].

The result of Figure 3.3 indicates that the L location of relativistic electron penetration is greatly influenced by geomagnetic activity, confirming previous studies [e.g., Tverskaya, 1986, 2003]. Tverskaya [1986] investigated the relationship between the minimum Dst index and the L location of peak intensity of storm-injected relativistic electrons during storms and gave the following formula:

$$|Dst|_{max} = 2.75 \times 10^4 / L_{max}^4$$

The dotted line in Figure 3.8 shows the relationship between L_{max} and $|Dst|_{max}$ indicated by this equation. To compare with this equation, we also plot the dashed line, which is the linear fit to the points in Figure 3.8. It is apparent that although both the results from Tverskaya [1986] and our study show clear L-Dst dependence, our result shows deeper electron penetrations during storm times. Compared with previous studies [e.g., Tverskaya, 1986, 2003], our study gives clear criteria for storm selection and clear definition of L_{max}, which are much easier to follow and are reproducible by others. Furthermore, by using a larger database of storms and six different definitions of L_{max}, we examine the L-Dst dependence in more detail. The results show that besides the L location of the maximum flux, the L location of deepest penetration, maximum flux enhancement, and flux variation during isolated geomagnetic storms all correlate well with the minimum Dst index.

Additionally, as Figure 3.7 shows, the L value of the lowest penetration into the slot region for non-preconditioned events has a clear dependence on the minimum Dst index. This is because the L shell of the lowest penetration during a storm has a strong correlation with the storm intensity. For the preconditioned events, there is still a dependence of the L shell of lowest penetration on minimum Dst but it is not as clear. This may be because when the defined electron flux precondition is fulfilled, it is easier for energetic electrons to penetrate into L=2.5, and if the ratio of electron flux at L=3 to L=2.5 before the event is higher, the penetration into L=2.5 would be easier. Among the preconditioned events, some of them are better preconditioned than others with a higher ratio of flux at L=3 to L=2.5; thus, for these events, it is much easier to penetrate into the center of the slot region.

In addition, our choice to use 3 d averaged flux at the beginning of the storm and at the end of penetration may have some influence on the result of L-Dst dependence. To investigate in more detail, we try using different definitions for pre-storm flux and post-storm flux. For example, we use the flux of the day before Dst_{min} as the flux at the beginning of the storm, and use the flux of 3 d after Dst_{min} as the flux at the end of penetration; we also try using the maximum flux 1-3 d before Dst_{min} and the maximum flux 2-4 d after Dst_{min}. The results derived from these two different definitions are nearly identical with results showed in section 3.2.

It is worth mentioning that among all isolated storms with Dst_{min}<-50 nT from 1995 to 2004, there are only two storms during which the 2-6 MeV electron flux at the end of the penetration is lower than the flux at the beginning of the storm at every L shell from L=2 to L=7, and thus we did not include these two storms in our study. During all other storms, the electron fluxes at some L shells increased compared to pre-storm levels, although the increase may be very slight. The results of Reeves et al. [2003] showed that only about half of all storms produced an increase in relativistic electron fluxes, one quarter decreased the fluxes and one quarter produced little change. However, they focused only on one L shell at a time, between L=4 and L=7, while we investigate the flux enhancement at each L shell from L=2 to L=7 during the storm. Based on our study, besides those two storms during which the flux decreased at all L from L=2 to L=7, only 17 isolated storms (14%) produced little increase across all L shells, by a factor of less than 2. This indicates that most isolated geomagnetic storms (84%) do produce significant relativistic electron flux enhancements at some L, although the L location of peak enhancement may vary. Also, Reeves et al. [2003] suggested that the flux increase at a fixed L shell is independent of storm size. We find, however, that the magnitude of the maximum flux enhancement among all L shells from L=2 to L=7 does have a correlation with minimum Dst index. Figure 3.9 shows the magnitude of the maximum flux enhancement by percentage versus $|Dst_{min}|$ during the 117 storms investigated, and the correlation coefficient between them is 0.52. This indicates that although the position of peak enhancement may change, larger storms are more likely to produce greater flux enhancements at some L shell.

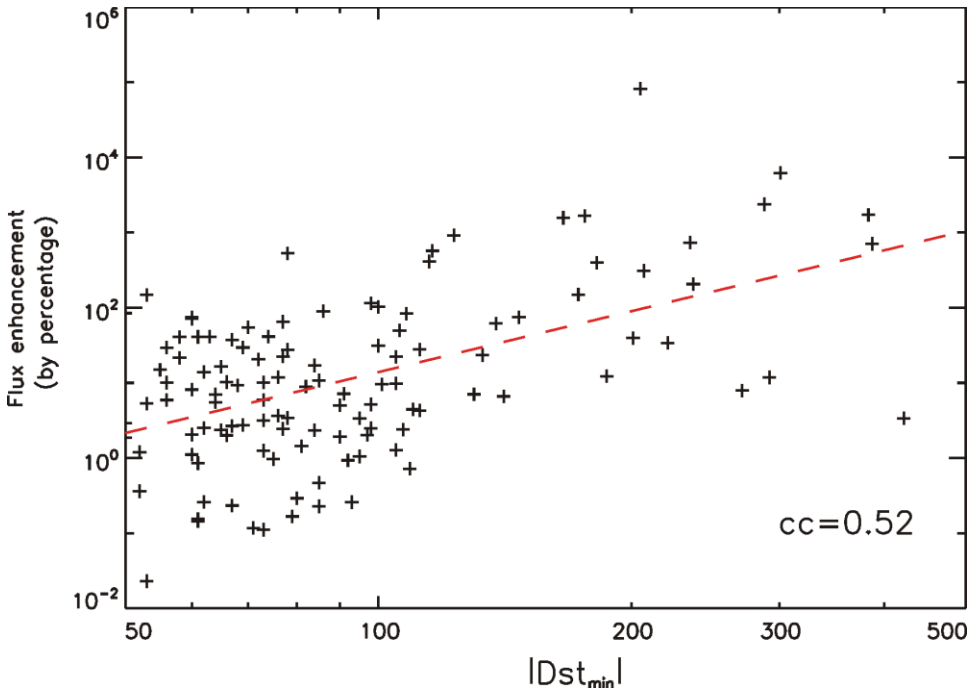

Figure 3.9: The magnitude of the maximum flux enhancement among L=2-7 (by percentage) versus $|Dst_{min}|$ during 117 isolated storms from 1995 to 2004.

On the other hand, 2-6 MeV electron fluxes between L=2 and L=7 are also integrated at the beginning of the storm and at the end of penetration, respectively, and these results are used as rough estimates of the total number of electrons throughout the slot region and the outer radiation belt, similar to Baker et al. [2004b]. We find, however, that among all 119 storms, 47 storms (~40%) caused increases in this total electron flux, 26 storms (~20%) caused decreases, 46 storms (~40%) produced little net change (within a factor of 2), and that the total flux enhancement has no correlation with storm intensity. This may be because larger storms are also more likely to produce greater losses.

Our results are not contradictory with Reeves et al. [2003], because they only focus on one L shell at a time, while we focus on all L shells from L=2 to L=7. It shows that although at a fixed L shell, about half of storms produce no change or decreases in the relativistic electron flux, throughout the slot region and the outer radiation belt, almost all storms will cause a flux enhancement at some L shell, and around 84% of them will produce significant increases at some L shell. However, only around 40% of storms will produce net increases in the total number of

electrons throughout the slot region and the outer belt, 40% will produce little net change, and around 20% will cause net decreases. It should also be noted that the relativistic electron flux data we use is only derived from the SAMPEX satellite, while the Reeves et al. [2003] study uses multiple satellites, including the Los Alamos National Laboratory (LANL) space environment monitors and Polar. Also, because we focus on multiple L shells at a time and the SAMPEX satellite has limited differential energy measurements, it is difficult to derive phase space density data for a large range of L, so we look only at fluxes rather than phase space densities.

We also check the difference between geomagnetic storms driven by coronal mass ejections (CMEs) and corotating interaction regions (CIRs) in the L-Dst dependence and the flux enhancement of energetic electrons. By using CME- and CIR-driven storms lists from Turner et al. [2009, and references therein], we find that among 119 isolated geomagnetic storms from January 1995 to June 2004, there are 54 CME-driven storms and 42 CIR-driven storms. Comparing the L-Dst dependence of CME- and CIR-driven storms, we find that there is no significant difference between them except that the CIR-driven storms are smaller relatively. For electron flux enhancements from L=2 to L=7, the difference between CME- and CIR-driven storms is still not significant. Among 54 CME-driven storms, only 6 storms (11%) produced little flux increase across all L shells by a factor of less than 2, all other storms (89%) produced significant increase at some L shell between L=2 and L=7; while among 42 CIR-driven storms, 2 storms (5%) decreased the fluxes at all L shells, 7 storms (17%) produced little increase across all L, and 33 storms (78%) increased the fluxes at some L shell significantly. The CIR-driven storms appear to produce less flux enhancement; however, this is mainly due to the fact that CIR-driven storms are relatively weaker than CME-driven storms in terms of minimum Dst, and as Figure 3.9 shows, the maximum flux enhancements among L=2-7 are correlated with the minimum Dst index. Also, comparing the total flux enhancement between L=2 and L=7, both CME- and CIR-driven storms produced net flux increases, decreases and little change, and there is no significant difference between them.

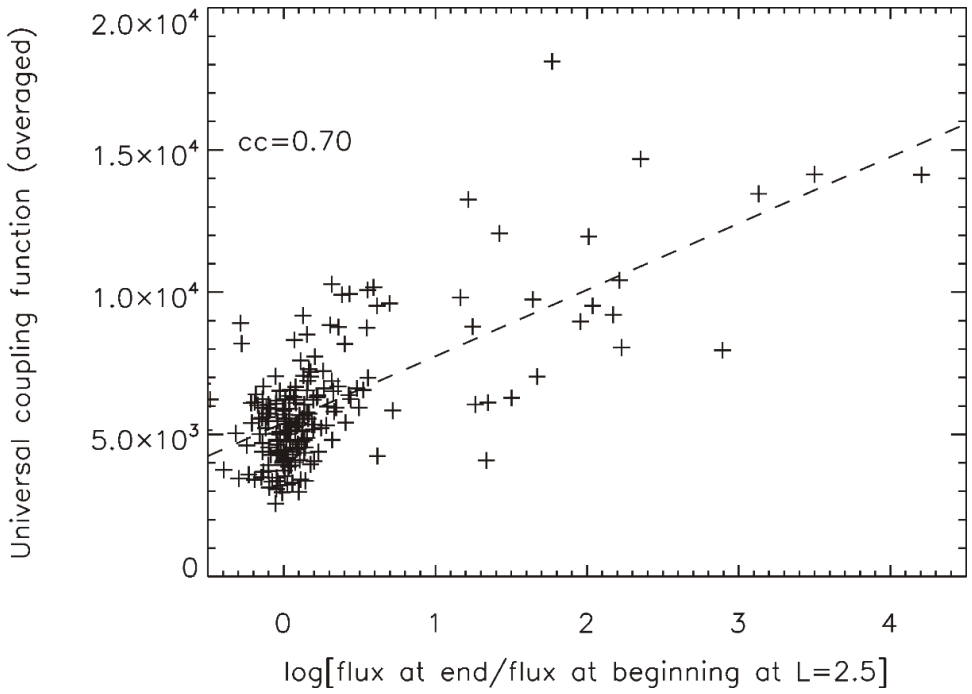

Figure 3.10: The universal solar wind-magnetosphere coupling function (averaged) versus logarithm of flux enhancement at L=2.5 during 209 events from 1995 to 2004. Dashed line is the linear fit to the points, and the linear correlation coefficient (cc) is also provided.

We also investigate the relationship between flux enhancements in the slot region and solar wind-magnetosphere coupling. Newell et al. [2007] examined the interaction between solar wind and the magnetosphere and found that the function that represents the rate of magnetic flux opened at the magnetopause correlates quite well with multiple geomagnetic indices and some variables characterizing magnetospheric activity. This function, which is called the universal solar wind-magnetosphere coupling function, can be expressed as

$$\frac{d\Phi_{MP}}{dt} = v^{4/3} B_T^{2/3} \sin^{8/3}(\theta_c/2)$$

where $\frac{d\Phi_{MP}}{dt}$ represents the rate of magnetic flux opened at the magnetopause, v represents the solar wind velocity, B_T represents the interplanetary magnetic field component perpendicular to the solar wind velocity, and θ_c represents the IMF clock angle, which is given by $\tan(\theta_c) = B_y/B_z$. Figure 3.10 shows the relationship between this universal coupling function and the logarithm of flux enhancement at L=2.5. We use the same event set and method as in section 3.3.2 to calculate the electron flux enhancement at L=2.5. The universal coupling function is

calculated by using 1 h solar wind data from OMNI Web, which is suggested by Newell et al. [2007], and averaged over 3 d (same time period used in section 3.3.2 for calculation of solar wind parameters). The linear trend in Figure 3.10 is quite clear, with a correlation coefficient of 0.70. It suggests that relativistic electron flux enhancements in the slot region are greatly influenced by solar wind-magnetosphere coupling and energy transfer.

3.5 Conclusion

In this chapter, we showed the relationship between Dst index and the L location of 2-6 MeV electron deepest penetration, maximum electron flux, maximum flux enhancement, and maximum flux variation during 119 moderate and strong isolated geomagnetic storms from 1995 to 2004 using daily averaged 2-6 MeV electron flux data from SAMPEX. Also, we defined penetration events in the slot region and investigated the correlation between electron penetrations at L=2.5 and solar wind parameters. Moreover, we found that electron flux preconditioning is also an important factor for penetrations in the slot region. The results are summarized as follows:

1. The L location of deepest penetration, the L location of the maximum flux at the end of penetration, and the L location of the maximum flux variation (by value) during the storm have strong correlations with minimum Dst index during isolated geomagnetic storms, with correlation coefficients of 0.78, 0.83, and 0.87, respectively.

2. From 1995 to 2004, only two isolated storms produced 2-6 MeV electron flux decreases at all L shells from L=2 to L=7, and 17 storms (14%) produced little increase in electron flux at any L shell. Most isolated storms (84%) produced significant increases in 2-6 MeV electron flux at some L shell, and the magnitude of the maximum flux enhancement during the storm is correlated with the storm size. However, the sum of fluxes throughout the slot region and the outer belt, a rough measurement of the total number of electrons, increased during

around 40% of storms, decreased during around 20% of storms, and did not change much during the other 40%. Moreover, the total flux enhancement has no correlation with storm size.

3. During 1995–2004, according to SAMPEX 2-6 MeV electron flux data, there are a total of 23 penetration events during which the electron flux at L=2.5 increases by at least one order of magnitude within 3 d. IMF magnitude, IMF Bz, solar wind electric field, and solar wind speed are correlated with penetration events. The solar wind electric field and E_y ×time (when E_y>0.5 mV/m) are the most effective parameters for MeV electron flux enhancements in the slot region.

4. By examining MeV electron penetration events at L=2.5, we find the sufficient and necessary solar wind conditions to cause these penetration events, as shown in Table 3.1. For the period 1995-2004, there are a total of 10 intervals during which the sufficient conditions are fulfilled and penetration events occurred for each interval; a total of 30 intervals exist during which the necessary conditions are met, and 21 of these caused penetration events at L=2.5.

5. Penetration events in the slot region are not only caused by extreme solar wind conditions; for events meeting defined electron flux preconditioning, it is much easier for electrons to penetrate into the center of the slot region (L=2.5). Under the defined preconditioning, MeV electron penetrations into the slot region can be caused by relatively mild solar wind conditions.

This chapter has focused on the MeV electron flux enhancements and the influence of solar wind parameters and geomagnetic storms on the MeV electron penetrations in the low L region. It has been shown that deep penetrations of MeV electrons into the low L region occurred infrequently and are usually associated with intense solar wind conditions or geomagnetic activities. In the following chapter, I will focus on the deep penetrations of hundreds of keV electrons into the slot region and inner radiation belt, which occurs much more often than that of MeV electrons and can happen under quite mild geomagnetic activities.

Chapter 4

Hundreds of keV Electrons in the Slot Region and Inner Radiation Belt I: Modeling the Deep Penetration into the Slot Region and Inner Radiation Belt

The following chapter is primarily based on work that was published in Zhao and Li (2013b), Modeling energetic electron penetration into the slot region and inner radiation belt, J. Geophys. Res. Space Physics, 118, 6936–6945, doi:10.1002/2013JA019240.

4.1 Introduction

Energetic electrons in the inner magnetosphere are distributed into two regions: the inner radiation belt and the outer radiation belt, while the region in between separated the two belts is called the slot region. The outer radiation belt is highly dynamic, while the inner radiation belt and slot region are relatively stable for MeV electrons as I showed in the previous chapter. But for hundreds of keV electrons, the situation is very different.

For the inner radiation belt particles, the most important source processes were recognized to be cosmic ray albedo neutron decay (CRAND) and radial diffusion [e.g., Walt and Farley, 1976]. Radial diffusion has long been considered one of the most important acceleration mechanisms for radiation belt electrons, energizing electrons by bringing them inward where magnetic fields are stronger while conserving the first adiabatic invariant [e.g., Schulz and Lanzerotti, 1974]. As for CRAND, many studies suggest that it is an important source for energetic protons in the inner belt, but not for electrons [e.g., Kellogg, 1960; Pizzella et al., 1962]. The loss processes for inner belt electrons include Coulomb collisions with atmospheric constituents and pitch angle scattering via wave-particle interactions with whistler mode waves. Atmospheric collisions dominate energetic electron loss only for $L<1.3$ [Walt, 1964]; while above $L=1.3$, wave-particle interaction play an important role in the loss of energetic electrons [Abel and Thorne, 1998]. The most important waves in the wave-particle interaction of the inner belt are plasmaspheric hiss, very low frequency (VLF) waves from high powered VLF

communication transmitters, and the lightning-induced whistlers. Together with Coulomb collisions, these waves account for energetic electron loss in the inner radiation belt.

The inner radiation belt is thought to be quite stable for MeV electrons and more energetic protons, but for 100s of keV electrons, large variations can occur. Pfitzer and Winckler [1968] first reported on an inner radiation belt 100s of keV electron flux enhancement during a strong geomagnetic storm in 1966 using OGO 1 and 3 satellite data. For long-term behavior, a positive correlation of the inner belt 100s of keV electron fluxes at L>1.4 with solar activity has been reported [Abel et al., 1994]; for short-term behavior, some studies have shown that only the most intense geomagnetic storms can influence the inner belt 100s of keV electron fluxes [e.g., Bostrom et al., 1970]; in both cases, the flux enhancements could be attributed to enhanced inward radial diffusion from the outer radiation zone. Selesnick [2012] simulated inner radiation belt electron transport and compared with observations from DEMETER and found that the observed decay rates below L=1.5 were much slower than predicted by scattering losses, which indicates the presence of continuous inward radial diffusion.

Separating the inner and outer belt is a region called the slot region. The slot region is usually devoid of energetic electrons, but during strong storms, the slot region can be filled with relativistic electrons [e.g., Blake et al., 1992; Li et al., 1993; Baker et al., 2004a; Zhao and Li, 2013a]. The slot region is believed to form as a balance between the inward transport of electrons and pitch angle diffusion [Lyons et al., 1972]. Kim et al. [2011] simulated the formation of the slot region using the time-dependent 3-D Versatile Electron Radiation Belt (VERB) code and indicated that the slot region forms as a balance between inward radial diffusion due to ultra-low frequency (ULF) electromagnetic fluctuations and pitch angle scattering due to plasmaspheric hiss and lightning-generated whistlers. The location of the slot region depends on electron energy. For higher-energy electrons, the slot region is closer to Earth [e.g., Lyons and Thorne, 1973].

In this chapter, we investigate 100s of keV electron flux enhancements in the slot region and inner belt using electron flux data from the Instrument for the Detection of Particle (IDP)

carried onboard the Detection of Electro-Magnetic Emissions Transmitted from Earthquake Regions (DEMETER) satellite, which is a microsatellite with a highly inclined low Earth orbit (710 km altitude, inclination of 98.3 degrees) [Sauvaud et al., 2006]. The IDP spectrometer with a maximum geometric factor of 1.2 cm^2sr is aimed to measure differential electron fluxes in the energy range from 70 keV to 2.5 MeV, with a time resolution of 4 s and an energy resolution of 17.8 keV in routine mode, while the measurement of higher-energy electrons (above 0.8 MeV) are not as accurate as the measurement of 70 keV-0.8 MeV electrons. Although many energetic electron flux measurements in the inner radiation belt suffer from energetic proton contamination, the energy spectrum in the inner belt from IDP data shows a series of peaks at discrete energies consistent with energetic electrons interacting with VLF waves and thus confirms the effectiveness of the IDP spectrometer in the inner radiation belt [Sauvaud et al., 2006, 2008; Selesnick et al., 2013].

By using the IDP data, we show that 100s of keV electron flux enhancements in the slot region and inner belt happen much more frequently than MeV electrons and can occur even during moderate storms. Also, using a radial diffusion model and solar wind-dependent diffusion coefficients, we model the flux enhancement event of April of 2010 for two different electron populations and compare the diffusion coefficients with the conventional Kp-dependent diffusion coefficients [Brautigam and Albert, 2000] and diffusion coefficients from more recent studies [Ozeke et al., 2012]. The results show that the radial diffusion coefficients in the inner belt and slot region disagree with those diffusion coefficients from previous studies, suggesting that one cannot simply extend the diffusion coefficients from previous studies to the lower L region.

4.2 Energetic Electron Flux Enhancements in the Slot Region and Inner Radiation Belt

Figure 4.1 shows the daily averaged trapped energetic electron fluxes measured by DEMETER, averaged in 0.1L bins, along with the Dst index from March to June of 2010. Four differential energy channels, 126.3 keV, 250.9 keV, 500.1 keV, and 802.7 keV, are shown (the

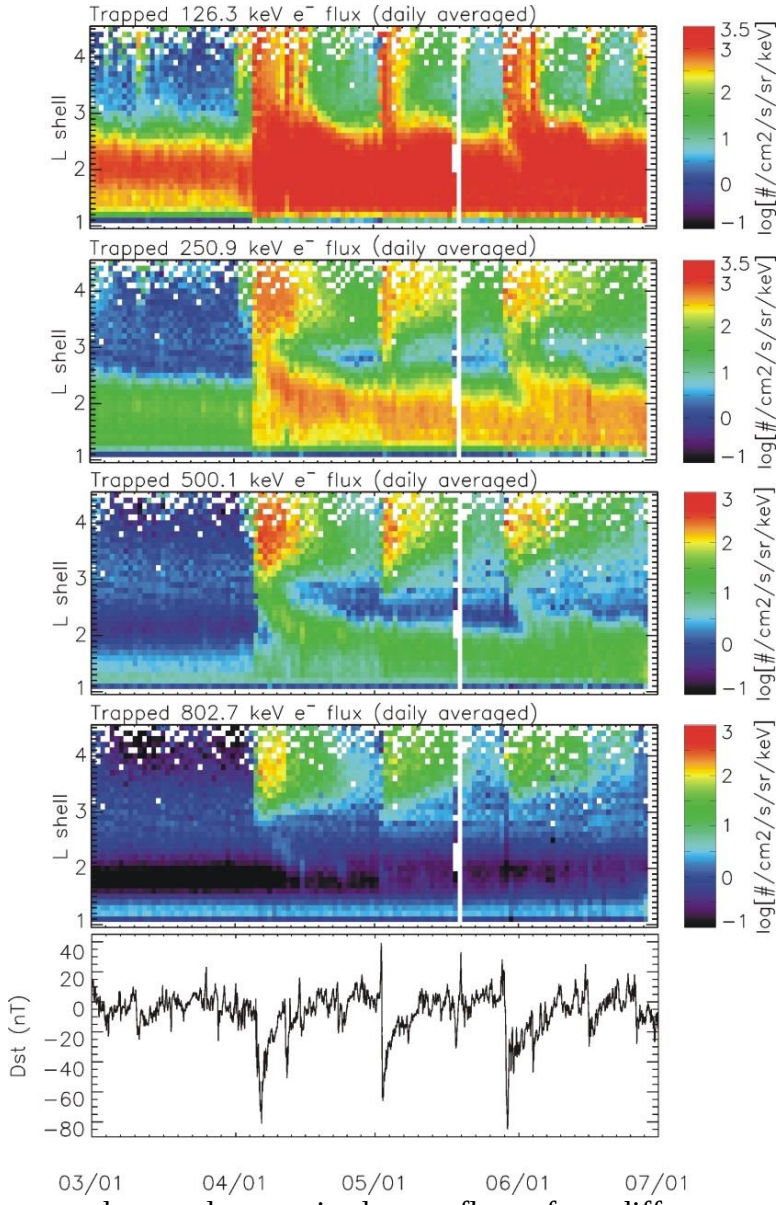

Figure 4.1: Daily averaged trapped energetic electron fluxes from different energy channels, measured by the DEMETER satellite, and the Dst index from 1 March to 1 July 2010.

color bars for the first two panels and the next two panels are different). It should be noted that only trapped energetic electron data are used in this study, which means these electrons are not going to be lost during a drift period assuming no external force. We separate the measured electrons into three populations: untrapped electrons, also known as electrons in the bounce loss cone (BLC), will be lost within a bounce period; quasi-trapped electrons, or electrons in the drift

loss cone (DLC), will be lost within a drift period; only the trapped electrons can survive a drift period if no scattering occurs.

The regions where trapped, quasi-trapped (in DLC), and untrapped (in BLC) electron populations were measured from 1 to 10 March 2010 by DEMETER are shown in Figure 4.2. The calculation for the different electron populations was based on the DEMETER orbital information, local pitch angle of the detector axis, and the IGRF model. We assume that the electron will be lost when it reaches 100 km altitude. In this study, we focus on the trapped electron population, which is mainly measured near the South Atlantic Anomaly (SAA) and is shown as the blue region in Figure 4.2.

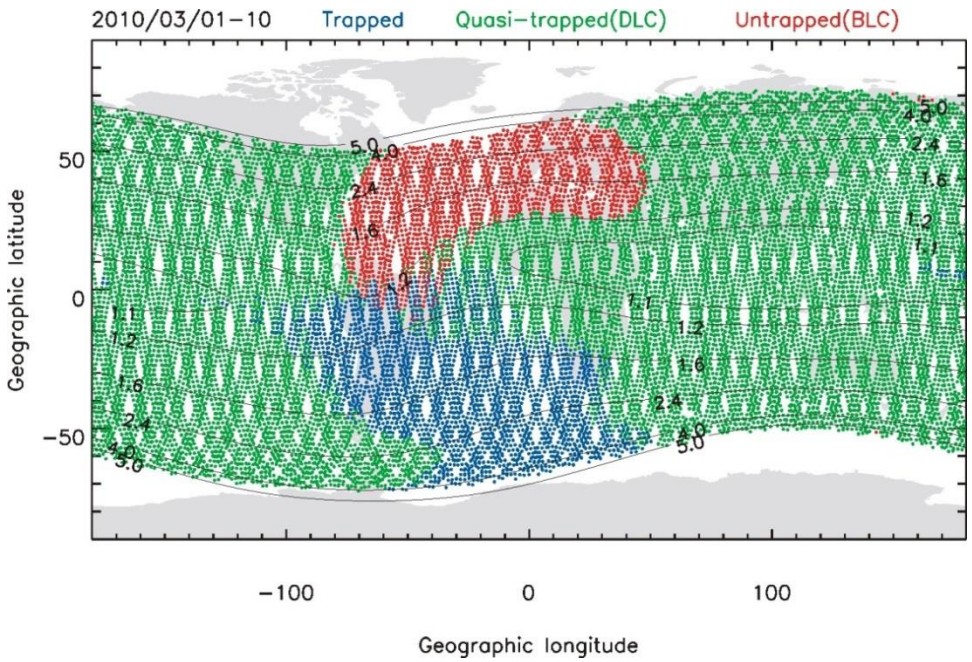

Figure 4.2: Trapped/quasi-trapped (DLC)/untrapped (BLC) electron populations measured by DEMETER IDP, shown in blue, green, and red, respectively, from 1 to 10 March 2010. The calculation was based on the DEMETER orbital information, local pitch angle of the detector axis, and the IGRF model. The electron is assumed to be lost when it reaches 100 km altitude.

It is evident in Figure 4.1 that from March to June 2010, there are several energetic electron penetrations into the slot region and inner belt. At the beginning of April, the strongest penetration during these 4 months occurred, which filled the whole slot region and strongly enhanced the energetic electron flux in the inner belt, particularly for the lower energy electrons.

The flux enhancement during this April event occurred as low as L~1.2. For 126.3 keV electrons, this penetration into the inner belt happened almost immediately (based on finer resolution data which are not shown here, the flux doubled at L=2 within half a day), while 250.9 keV and 500.1 keV electrons slowly diffused inward to the inner belt. Even for the highest energy channel of IDP used in this study, 802.7 keV electrons, we can also see the filling of the slot region after the April event. It is also evident that the deep penetrations happened during geomagnetic storms. However, these storms are just moderate, with -100 nT<Dst_{min}<-50 nT. This shows that although MeV electron penetrations into the slot region mostly occur during strong storms and intense solar wind conditions [e.g., Baker et al., 2007; Zhao and Li, 2013a], for 100s of keV electrons, flux enhancements in the slot region and inner belt occur much more often.

In the next section, we transform the flux into the phase space density (PSD), and then model the April flux enhancement event using a radial diffusion model.

4.3 Modeling Energetic Electron Penetration into the Slot Region and Inner Belt

4.3.1 Phase Space Density (PSD) Calculation

In order to model the flux enhancement event during April 2010 using a radial diffusion model, we need to transform the flux data into PSD. First, we need to determine the corresponding phase space coordinates, μ, K and L^*, based on the satellite position, electron energy, local pitch angle information, and geomagnetic field model. The first adiabatic invariant, μ, can be calculated using the following:

$$\mu = \frac{p_\perp^2}{2m_0 B}$$

where $p_\perp$ is the relativistic momentum component perpendicular to the local magnetic vector, m_0 is the rest mass of electron, and B is the local magnetic field magnitude. The second adiabatic invariant, K, can be calculated as follows:

$$K = \int_{S_m}^{S'_m} \sqrt{B_m - B(S)}\, ds$$

where S_m and S'_m are two mirror points, B_m and $B(S)$ are the magnetic field strength of mirror points and position S, respectively, and ds is the distance along the magnetic field line. The Roederer L, L^*, is defined as the radial distance in Earth radii to the equatorial point of the shell on which the electron would be found, if all non-dipolar perturbations of the magnetic field are adiabatically turned off [Roederer, 1970]. It can be calculated as follows:

$$L^* = \frac{2\pi M}{|\Phi| R_E}$$

where M is the Earth's dipole magnetic moment, R_E is the Earth's radius, and Φ is the third adiabatic invariant, which is the magnetic flux enclosed by the electron drift shell and can be calculated by

$$\Phi = \oint \vec{A} \cdot \overrightarrow{dx} = \int_S \vec{B} \cdot \overrightarrow{dS}$$

where $\vec{A}$ is the magnetic vector potential, $\vec{B}$ is the magnetic vector, $\overrightarrow{dx}$ is a vector along a curve that lies in the particle's drift shell, and S is the cross section of the drift shell.

Based on these equations, we can calculate μ, K, and L^* for each data point. In this chapter, we use the IRBEM library [Boscher et al., 2010] to do the magnetic field-related calculations and use LANL* [Yu et al., 2012] to calculate L^*. In our calculation, we use T89 as the external magnetic field model [Tsyganenko, 1989]. Based on the calculation, however, we found that according to DEMETER's measurements, we can only derive a very limited L^* range for the electrons with the same μ and K. This is mainly caused by the limited pitch angle coverage that DEMETER can provide due to its low Earth orbit.

In order to investigate the radial transport of the electrons, we need to examine a relatively large L^* range for electrons with the same first and second adiabatic invariants. Thus, we have to make some assumptions about the pitch angle distribution. Gannon et al. [2007] have investigated the pitch angle distribution of energetic electrons using data from the Combined Release and Radiation Effects Satellite (CRRES). They showed that 90 °peaked distributions dominate at 100s of keV of energies, especially at lower L shells near the equator. By fitting the

pitch angle distribution with a $\sin^n \alpha$ form, where α is the local pitch angle, they found that n mainly varies between 2 and 5 at L=3-8, and that 90 °peaked distributions are typically steeper at lower L. In this study, we assume a $\sin^3 \alpha$ pitch angle distribution. A discussion of the influence of the pitch angle distribution assumption on the model results will be presented in the next section.

With this pitch angle distribution assumption, we can focus on equatorially trapped electrons (K=0). First, for each data point, we trace the field line to the magnetic equator and calculate the equatorial pitch angle; then, based on the $\sin^3 \alpha$ pitch angle distribution assumption and the measured flux data, we calculate the flux and μ for 90 °equatorial pitch angle electrons. Then we can derive L^* for each data point using LANL*. Finally, we calculate the PSD according to the equation used in Chen et al. [2005]:

$$f = [\frac{j}{p^2 c^2} \times 1.66 \times 10^{-10}] \times 200.3$$

where j is the flux in units of $cm^{-2}\ s^{-1}\ sr^{-1}\ keV^{-1}$, p is the relativistic momentum, c is the speed of light, and f is the PSD. The multiplying factor here is used to transform the PSD to the GEM (Geospace Environment Modeling) units $(c/MeV/cm)^3$.

In this study, we model two different equatorially trapped electron populations: μ=28.5-31.5 MeV/G (denoted as μ=30 MeV/G) and μ=14.25-15.75 MeV/G (denoted as μ=15 MeV/G). Electrons with μ=30 MeV/G correspond to equatorially trapped electrons with an energy of 250 keV at L^*~3 or 500 keV at L^*~2.2, while the electrons with μ=15 MeV/G corresponds to equatorially trapped electrons with an energy of 250 keV at L^*~2.4 or 500 keV at L^*~1.8. Figure 4.3 (left) shows the PSD for electrons with μ=30 MeV/G, and Figure 4.3 (right) shows the daily averaged PSD radial profile during April 2010, while Figure 4.4 shows similar figures for μ=15 MeV/G electrons.

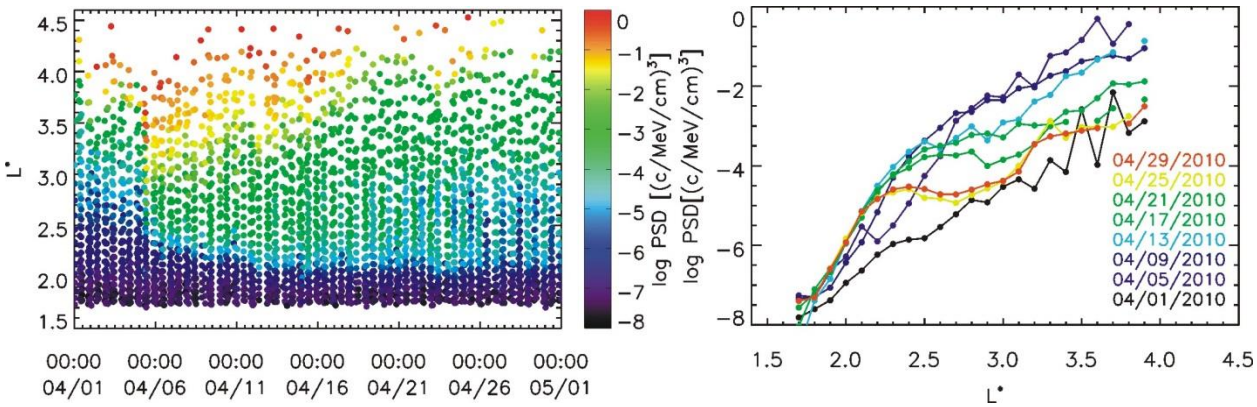

Figure 4.3: (left) PSD data for μ=30 MeV/G equatorially trapped electrons, assuming the pitch angle distribution at the equator has $\sin^3 \alpha$ form. (right) Daily averaged radial profile of PSD for μ=30 MeV/G equatorially trapped electrons during April 2010.

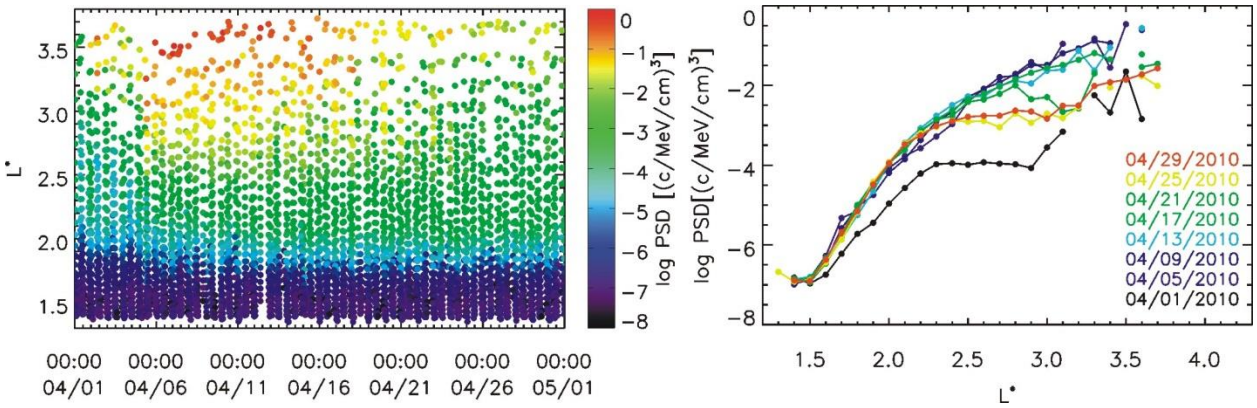

Figure 4.4: (left) PSD data for μ=15 MeV/G equatorially trapped electrons, assuming the pitch angle distribution at the equator has $\sin^3 \alpha$ form. (right) Daily averaged radial profile of PSD for μ=15 MeV/G equatorially trapped electrons during April 2010.

As Figure 4.3 shows, the PSD for μ=30 MeV/G equatorially trapped electrons were enhanced significantly throughout the slot region and the enhancement happened as low as L^*~2. For μ= 15 MeV/G equatorially trapped electrons, as Figure 4.4 shows, the PSD enhancement happened even lower, reaching L^*~1.8. From the radial profile, we find that for μ=30 MeV electrons, the enhancement happened in the outer region first and then slowly diffused inward to the slot region and inner belt. For μ=15 MeV electrons, however, the PSD enhancement in the inner belt occurred faster. After the deep penetration, μ=30 MeV electrons slowly decayed and formed a slot-like radial profile at the end of April, while for μ=15 MeV electrons this feature is not so clear.

4.3.2 Model Description

The radial diffusion model in this study uses the Fokker-Planck equation [Schulz and Lanzerotti, 1974]:

$$\frac{\partial f}{\partial t} = L^{*2}\frac{\partial}{\partial L^*}\left(\frac{D_{LL}}{L^{*2}}\frac{\partial f}{\partial L^*}\right) - \frac{f}{\tau}$$

where $f(L^*, t)$ is the drift period-averaged phase space density for fixed μ and K, D_{LL} is the radial diffusion coefficient, and τ is the electron lifetime. This equation can be solved numerically.

The radial diffusion coefficient, D_{LL}, is set as

$$D_{LL} = D_0\left(\frac{L^*}{L_{max}}\right)^4$$

where L_{max} is the L^* of the outer boundary used in our model. The temporal part of D_{LL} used in this study is similar to the one used in Li et al. [2009]:

$$D_0 = c\left(\frac{v}{v_0}\right)^{\gamma_1}\left(1 + \frac{v_x B_z + |v_x B_z|}{\alpha}\right)^{\gamma_2}$$

where c, α, γ_1 and γ_2 are constants, v is the solar wind speed, v_0 (=404 km/s) is the average solar wind speed in 2010, v_x and B_z are x component of solar wind speed and z component of interplanetary magnetic field (IMF), respectively. The γ parameters determine the relative contribution of the solar wind speed and the convection electric field. The solar wind speed term represents the energy transfer from dayside compression and through the Kelvin-Helmholtz instability; the convection electric field term represents the energy transfer from dayside reconnection. The solar wind speed, IMF B_z, and geomagnetic indices during April 2010 are shown in Figure 4.5. It can be seen that around 5 April, which corresponds to the time of deep electron penetration, there is an impulse in the solar wind speed and IMF B_z, with Kp of ~8 and elevated AE index. The minimum Dst index during the first several days in April is about -80 nT, indicating a moderate geomagnetic storm.

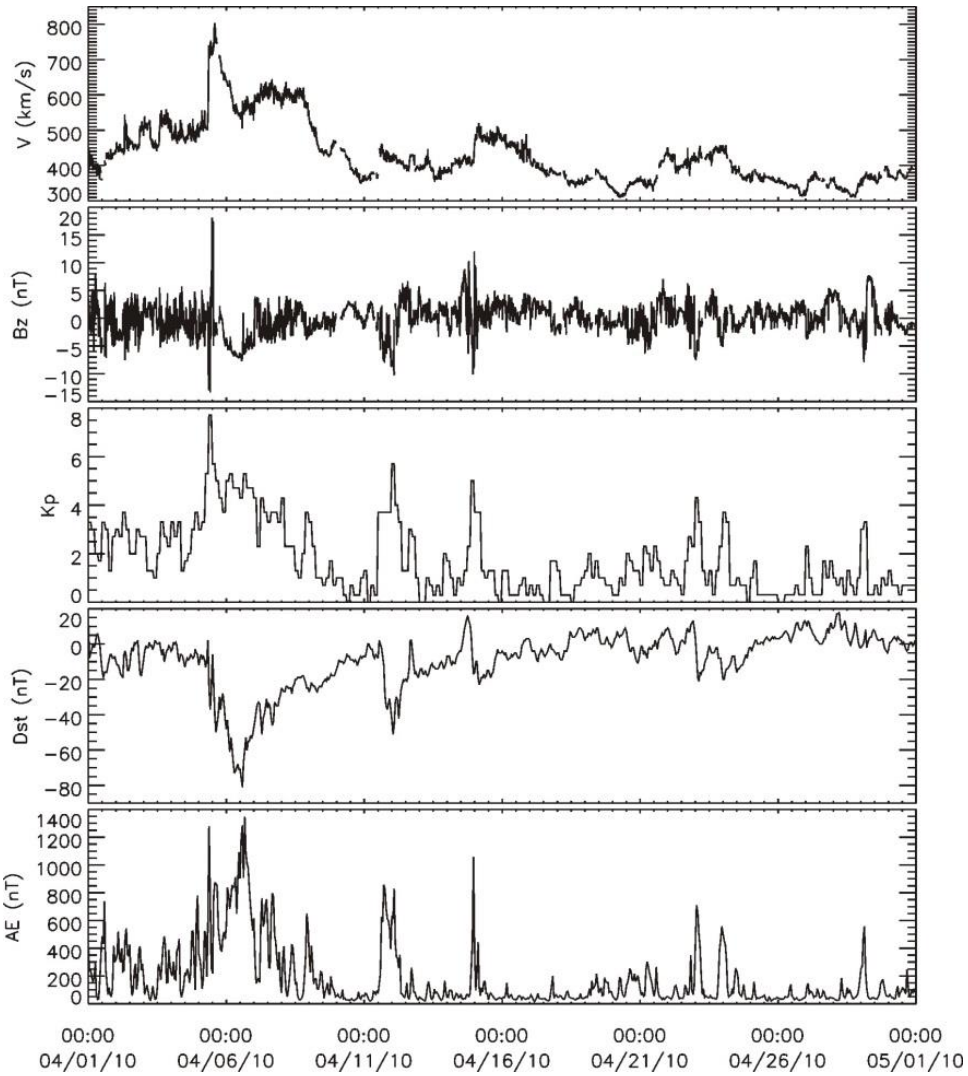

Figure 4.5: Solar wind speed, IMF B_z in GSM coordinates, Kp, Dst, and AE indices during April 2010.

The electron lifetime, τ, used in this study has no temporal variation, but has a spatial variation. Because of the presence of the slot region, we calculate the lifetime in two regions separately, divided by L_{cri} (to be discussed later). In each region, the lifetime is set as

$$\tau = \tau_0 \left(\frac{L_{max}}{L^*}\right)^p$$

where τ_0 and p are constants, and L_{max} is L^* of the outer boundary used in the model.

So far we have nine parameters in the radial diffusion model: c, α, γ_1, γ_2, τ_{01}, τ_{02}, p_1, p_2, and L_{cri}, which need to be optimized by fitting the PSD data. Here for τ_0 and p suffix 1 denotes the region outside L_{cri}, and suffix 2 refers to the region inside L_{cri}.

Based on the PSD data, we choose L^*=4 and L^*=1.8 as the outer and inner boundary for modeling μ=30 MeV electron PSD evolution, and L^*=3.5 and L^*=1.5 for μ=15 MeV electrons. The outer and inner boundary data are averaged over 0.2L with a time resolution of 10 min, and then interpolated across data gaps. The initial condition is set to be the PSD data averaged over 2 h and interpolated across L^*. To compare with the model results, the PSD data are also averaged in the model frame, which has a time resolution of 10 min and has been divided into 500 bins in L^* between outer and inner boundaries. In order to optimize the model results, we choose to minimize the root-mean-square deviation (RMSD), which is defined as

$$RMSD = \sqrt{\frac{\sum_1^n (\log\left(\frac{f}{\hat{f}}\right))^2}{n}}$$

where $\hat{f}$ is the PSD calculated by the radial diffusion model, f is the original PSD data, and n is the number of the data points. The optimized model results are shown in the next subsection.

4.3.3 Model Results

Since we focus on the slot region and inner belt, we optimize the model results for μ=30 MeV/G electrons by minimizing the RMSD between L^*=2.0 and L^*=3.0. The optimized parameters are c=0.0104, γ_1=2.8, γ_2=0.85, α=1652 km·nT/s, L_{cri}=3.27, τ_{01}=3.40, p_1=-2.91, τ_{02}=0.81, and p_2=4.21. Figure 4.6 shows the phase space density data and the optimized model results for μ=30 MeV/G electrons. Figure 4.7 shows the model results at various L^* compared with the original PSD data. We also calculated the prediction efficiency (PE) and linear correlation coefficient (LC) at different L^* inside the slot region and inner belt. The PE is defined as follows:

$$PE = 1 - \frac{\sum_i^n (\log f_i - \log \hat{f}_i)^2}{\sum_i^n (\log f_i - \overline{\log f})^2}$$

where f and $\hat{f}$ are the PSD data and the PSD calculated by the radial diffusion model respectively, $\overline{\log f}$ is the mean of the logarithm of the PSD data, which in this study is the

averaged $\log f$ at a specific L^* over a month, and n is the number of data points. The PE shows the agreement between the model results and the corresponding data: PE=0 indicates the model results are as good as the averaged data; PE>0 shows the model is better than taking the average and PE=1 means a perfect modeling.

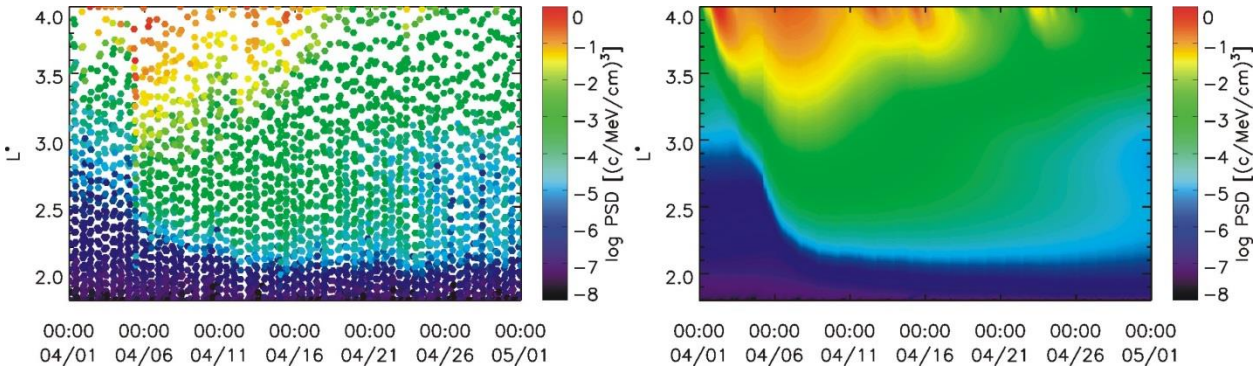

Figure 4.6: (left) Phase space density data and the (right) radial diffusion model results for μ=30 MeV/G equatorially trapped electrons.

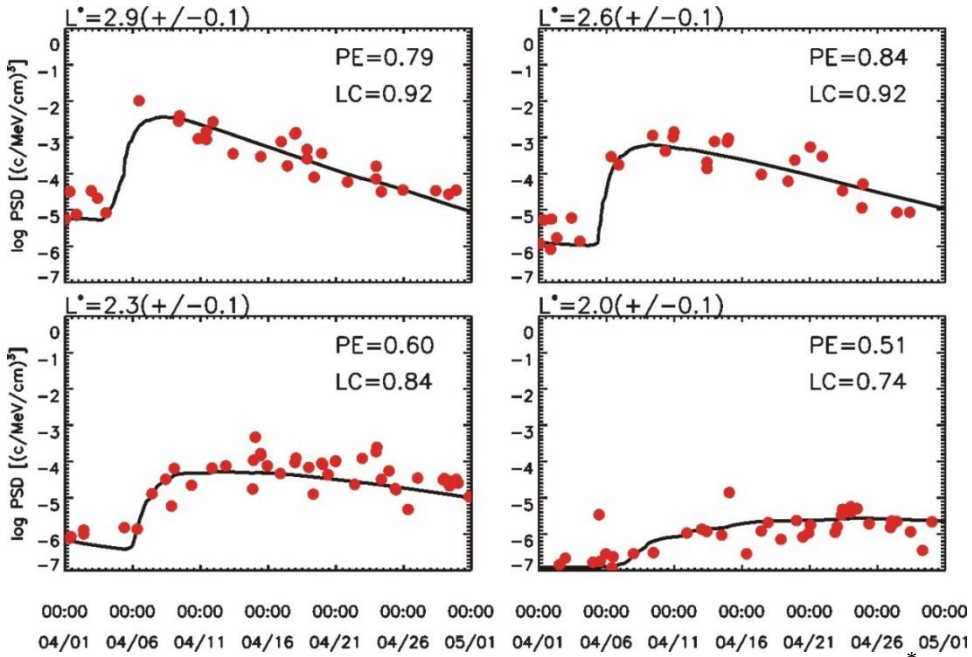

Figure 4.7: Comparison of model results and the original PSD data (at different L^*) for μ=30 MeV/G equatorially trapped electrons. The prediction efficiency (PE) and linear correlation coefficient (LC) for each panel are shown in the figure.

As can be seen in Figure 4.6, the model results reproduce well the main features in the PSD data, especially in the slot region and inner belt. The model results reproduce the deep penetration around 5 April; after that, the model results also show that electrons slowly diffuse inward; at the end of April, the model predicts the reappearance of the slot region, which agrees with the PSD data. Figure 4.7 shows that in the slot region (L^*=2-3), the model results fit the data quite well too. At L^*=2.9 ±0.1, 2.6 ±0.1, 2.3 ±0.1, and 2.0 ±0.1, the PEs are 0.79, 0.84, 0.60, and 0.51, respectively, and the LCs are 0.92, 0.92, 0.84, and 0.74, respectively, showing that the model results in the slot region reproduce the data with high accuracy. The PE at L^*=2.0 is relatively low, which is mainly caused by the low variation of the PSD data at L^*=2.0.

For μ=15 MeV/G electrons, we optimized the model results by minimizing the RMSD between L^*=1.8 and L^*=3.0, since for μ=15 MeV/G the deep penetration can reach as low as L^*=1.8. The parameters used in the model are c=0.000345, γ_1=5.1, γ_2=2.1, α=1208 km·nT/s, L_{cri}=2.67, τ_{01}=3.80, p_1=1.69, τ_{02}=0.60, and p_2=8.50. The optimized model results are shown in Figures 4.8 and 4.9. As shown in Figures 4.8 and 4.9, the model results reproduce the PSD data quite well throughout the slot region and inner belt. The penetration of μ=15 MeV/G electrons occurred much faster, which is reproduced by the model; while after the initial injection, model results show that the inward radial diffusion is not very efficient, and the electrons decay quite slowly below L^*~2.5, which is also consistent with the original PSD data. The PEs for different L^* in the slot region and inner belt are up to 0.82, and the LCs can be as high as 0.91.

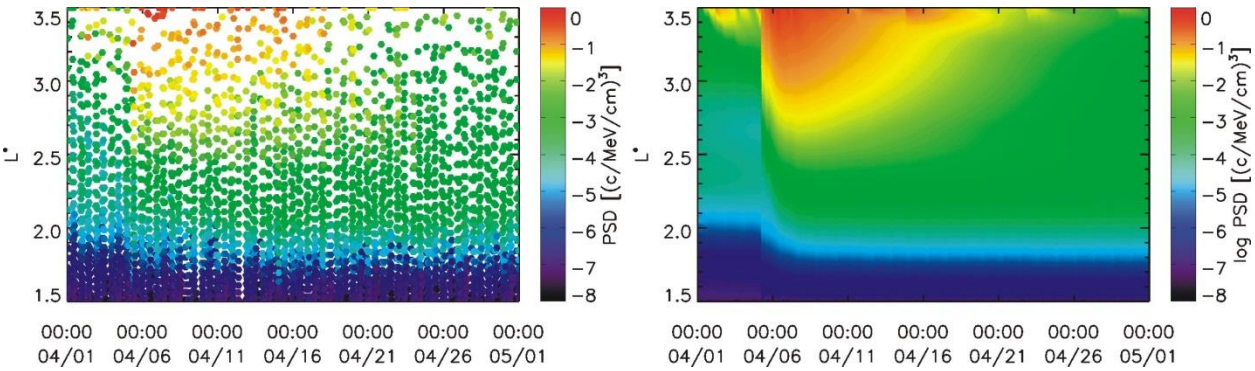

Figure 4.8: (left) Phase space density data and the (right) radial diffusion model results for μ=15 MeV/G equatorially trapped electrons.

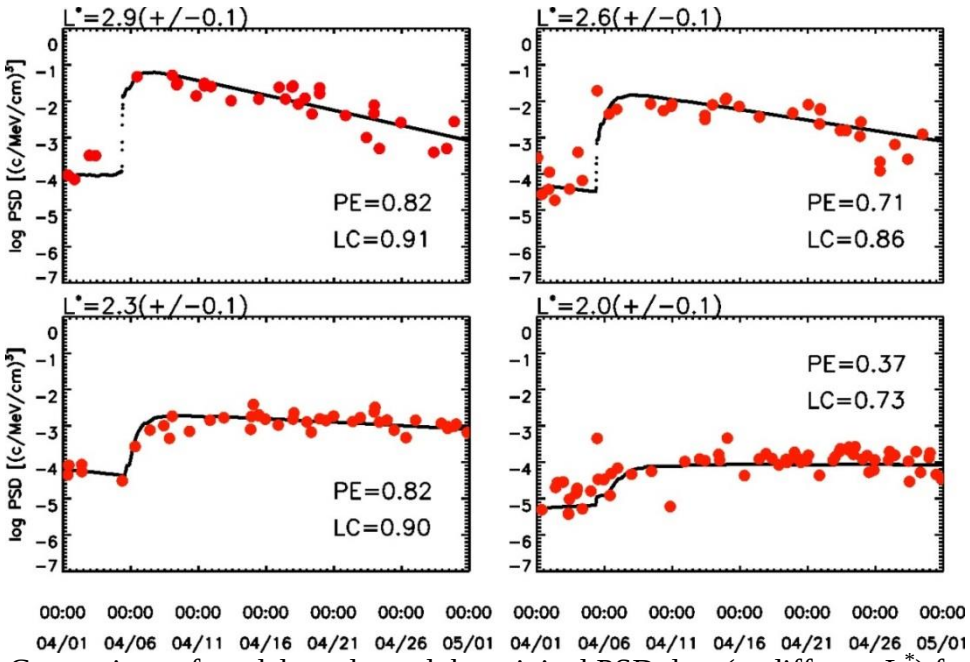

Figure 4.9: Comparison of model results and the original PSD data (at different L^*) for μ=15 MeV/G equatorially trapped electrons. The prediction efficiency (PE) and linear correlation coefficient (LC) for each panel are shown in the figure.

The optimized parameters used in our radial diffusion model are summarized in Table 4.1, and the PEs and LCs between data and model results for μ=15 MeV/G and 30 MeV/G equatorially trapped electrons at different L^* in the slot region are summarized in Table 4.2. It is also worth mentioning that we also tried to substitute the inner boundary condition here with commonly used condition PSD=0. Since the inner boundary PSDs are quite small, setting PSD=0 at the inner boundary almost does not influence the model results. For example, for μ=30 MeV/G electrons, by setting PSD=0 at L^*=1.8 and using the same parameters, PEs at L^* = 2.9±0.1, 2.6±0.1, 2.3±0.1 and 2.0±0.1 are 0.79, 0.84, 0.60 and 0.50, respectively, which are almost the same with the results using PSD data at the inner boundary.

Table 4.1: Optimized parameters used in the radial diffusion model for μ=30 MeV/G and 15 MeV/G equatorially trapped electrons.

	c	α (km·nT/s)	γ_1	γ_2	τ_{01} (days)	τ_{02} (days)	p_1	p_2	L_{cri}
μ=30 MeV/G e^-	0.0104	1652	2.8	0.85	3.40	0.81	-2.91	4.21	3.27
μ=15 MeV/G e^-	0.000345	1208	5.1	2.1	3.80	0.60	1.69	8.50	2.67

Table 4.2: Prediction efficiencies and linear correlation coefficients between data and model results for μ=30 MeV/G and 15 MeV/G equatorially trapped electrons at different L^* in the slot region.

		L^* = 2.9 ±0.1	L^* = 2.6 ±0.1	L^* = 2.3 ±0.1	L^* = 2.0 ±0.1
μ=30 MeV/G e^-	PE	0.79	0.84	0.60	0.51
	LC	0.92	0.92	0.84	0.74
μ=15 MeV/G e^-	PE	0.82	0.71	0.82	0.37
	LC	0.91	0.86	0.90	0.73

4.4 Discussion

4.4.1 The Radial Diffusion Coefficients

The diffusion coefficients D_{LL} used in the radial diffusion model for μ=30 MeV/G electrons and μ=15 MeV/G electrons at different L^* are shown in Figure 4.10, along with the widely-used Kp-dependent diffusion coefficients from Brautigam and Albert [2000]. The Kp-dependent D_{LL} includes electrostatic (D_{LL}^E) and electromagnetic (D_{LL}^B) contributions. The electrostatic radial diffusion coefficient used by Brautigam and Albert [2000] is given by

$$D_{LL}^E = \frac{1}{4}\left(\frac{cE_{rms}}{R_E B_0}\right)^2 \left[\frac{T}{1+(\omega_D T/2)^2}\right] L^6$$

$$\omega_D = \left(\frac{3\mu c}{eL^2 R_E^2}\right)\left(1+\frac{2\mu B}{E_0}\right)^{-1/2}$$

where ω_D is the electron drift frequency, E_{rms} is the root mean square of the electric field amplitude and is assumed as $E_{rms}(Kp) = 0.26(Kp-1)+0.1$ mV/m, Kp=1 to 6, T is the exponential decay time (0.75 hour), B_0 is the dipole moment, E_0 is the electron rest energy. It can be seen from the equation that D_{LL}^E is dependent of μ. The electromagnetic diffusion coefficient used by Brautigam and Albert [2000] is $D_{LL}^{Kp} = 10^{0.506Kp-9.325}L^{10}$, Kp=1 to 6, and has no dependence on μ. These equations were originally used for L=3-6.6. However, here we simply extend it to the slot region and inner belt. The D_{LL}s of our model showed in Figure 4.10 are averaged over 1 h.

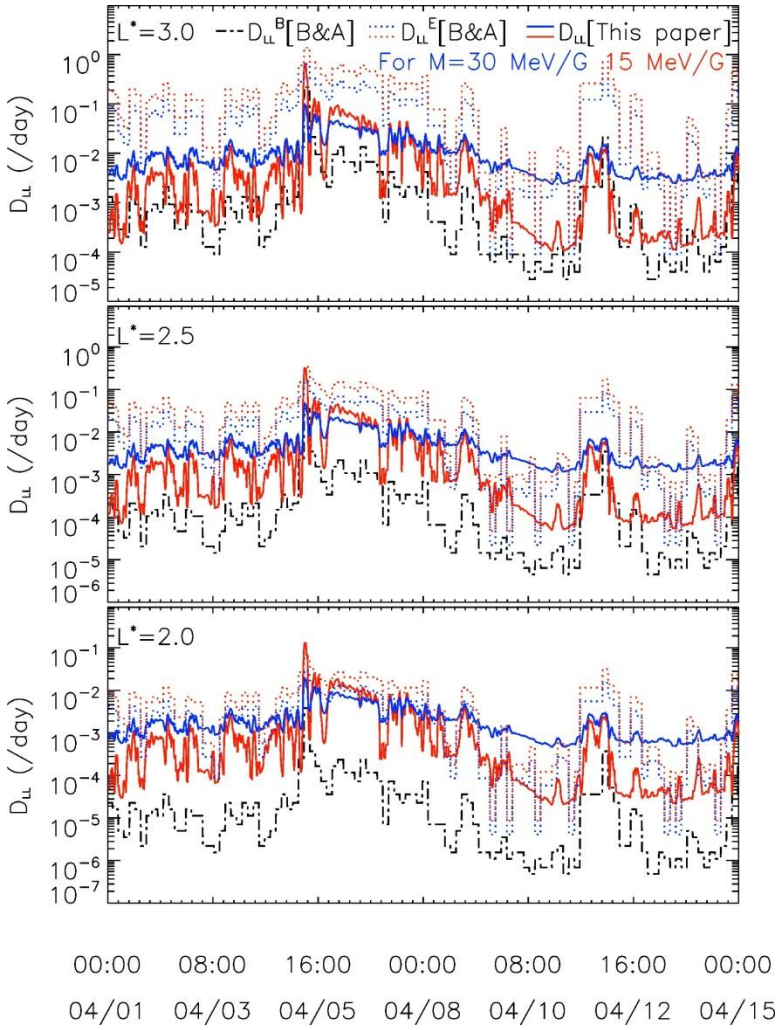

Figure 4.10: Diffusion coefficients D_{LL} for μ=30 MeV/G, K=0 electrons and μ=15 MeV/G, K=0 electrons at different L^*, along with the Kp-dependent diffusion coefficients from Brautigam and Albert [2000] during 1–15 April 2010.

Comparing the diffusion coefficient of the two different electron populations used in this paper, D_{LL} for μ=15 MeV/G electrons is larger than D_{LL} for μ=30 MeV/G electrons at the time of deep penetration, but is lower than that after the penetration, which is consistent with the fact that lower energy electrons are transported inward much faster, while higher energy electrons slowly diffuse inward. The radial diffusion coefficients depend on power spectrum of electric and magnetic field fluctuations, for which the information is not available for this study. However, there should not be such a large difference in radial diffusion coefficients in general between μ=15 MeV/G and μ=30 MeV/G electrons only at the time of deep penetration. So there can be

some other non-adiabatic processes involved at that time, the effects of which seem to be well represented by our empirical radial diffusion model, and thus the large diffusion coefficient of μ=15 MeV/G electrons at the time of penetration might not represent the real radial diffusion coefficient in a physical sense.

It is widely believed that the magnetic diffusion coefficient is substantially larger than the electric diffusion coefficient in the outer radiation belt. Recently, based on global MHD simulations and satellite measurements, Tu et al. [2012] have discussed the complexity of the radial diffusion coefficient and found that inside L = 4, the contribution to the diffusion coefficient mainly comes from electric field fluctuations rather than magnetic field perturbations; also, Ozeke et al. [2012] calculated the electric and magnetic diffusion coefficients using ground- and space-based observations of ULF wave power and found that electric field diffusion is much more important than magnetic field diffusion between L=3 and 7. By extending the Kp-dependent diffusion coefficients from Brautigam and Albert [2000] to the slot region and inner belt, as shown in Figure 4.10, it is apparent that at low L shells, their electrostatic diffusion coefficient is much larger than the electromagnetic one, indicating that radial diffusion is most likely caused by electric field perturbations rather than magnetic field perturbations. Comparing the diffusion coefficients used in this study with the Kp-dependent ones, we show that in the slot region and inner belt, the diffusion coefficients in our model are much higher than the widely used Kp-dependent electromagnetic diffusion coefficient D_{LL}^{B}, and the difference gets larger as L^{*} becomes smaller. However, the diffusion coefficients in our model are smaller than the Kp-dependent electrostatic diffusion coefficient D_{LL}^{E}, especially at larger L^{*}, and the difference gets smaller as L^{*} gets smaller. Also, comparing the diffusion coefficients for different μ, it is apparent that our results show more dynamic features than Kp-dependent ones, especially for lower μ electrons. Our results indicate that radial diffusion coefficients for different μ have different dependence on solar wind parameters, and rather than a constant scaling factor as used by Brautigam and Albert [2000], the difference between diffusion coefficients for different μ changes in time. This indicates that the widely-used Kp-dependent diffusion coefficients from

Brautigam and Albert [2000] cannot be simply extended into the lower L region and applied to different μ electrons.

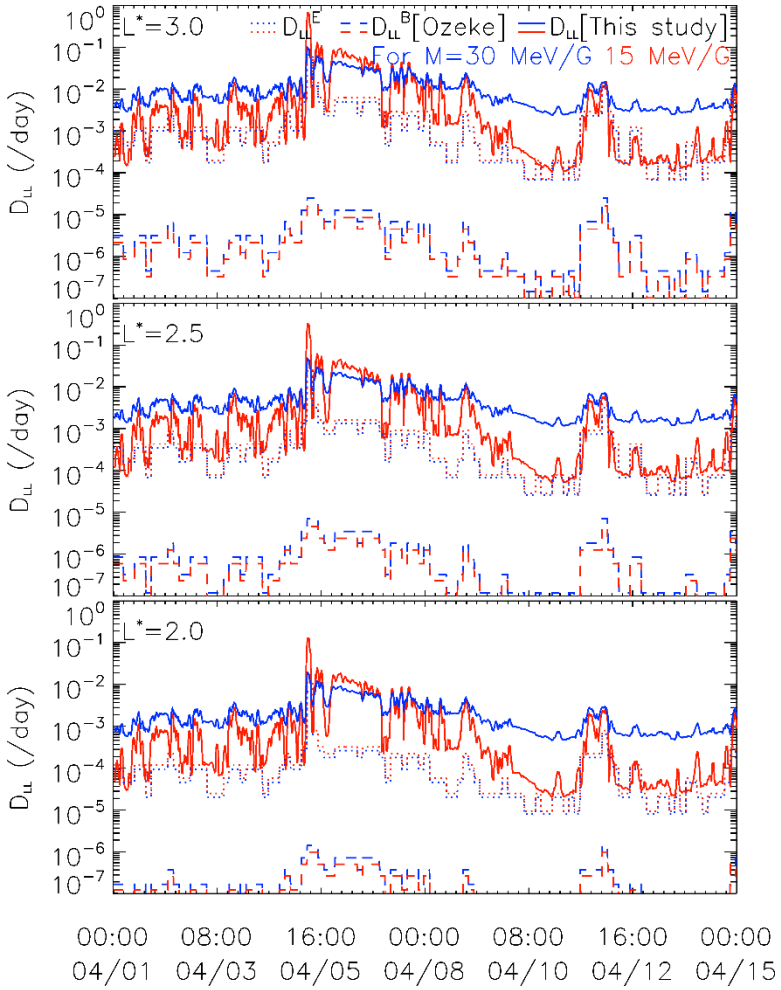

Figure 4.11: Comparison of diffusion coefficients for μ=30 MeV/G, K=0 electrons and μ=15 MeV/G, K=0 electrons in this study and electric (D_{LL}^E) and magnetic (D_{LL}^B) diffusion coefficients from Ozeke et al. [2012].

In addition, we also compared our diffusion coefficients with the radial diffusion coefficients shown in Ozeke et al. [2012], which utilizes ground- and space-based observations of ULF wave power to statistically characterize the electric and magnetic diffusion coefficients as a function of Kp index. Similarly, the diffusion coefficients from Ozeke et al. [2012] were extrapolated to lower μ electrons at lower L region. The comparison is shown in Figure 4.11. It is clear from Figure 4.11 that generally our diffusion coefficients are larger than D_{LL}^E from Ozeke

et al. [2012], with the differences get bigger at lower L shell; while our results are orders of magnitude larger than their magnetic diffusion coefficients D_{LL}^{B}. This again indicates the importance of electric diffusion coefficient in the low L region. On the other hand, our diffusion coefficients are also compared with the electric field radial diffusion coefficients from Brautigam et al. [2005] and the magnetic field diffusion coefficients from Ali et al. [2015], and the results are shown in Figure 4.12. The electric field radial diffusion coefficients from Brautigam et al. [2005] are derived using electric field data from CRRES, and the magnetic field diffusion coefficients from Ali et al. [2015] are derived using magnetic field data from the Van Allen Probes. It is still clear that the magnetic field radial diffusion coefficients are much smaller than the electric field diffusion coefficients at L^{*}=3, and are also much smaller than our diffusion coefficients. The electric field diffusion coefficients from Brautigam et al. [2005] fit our results for μ=30 MeV/G, K=0 electrons well, but are not so consistent with our results for μ=15 MeV/G, K=0 electrons. The differences between our diffusion coefficients and the diffusion coefficients from those previous studies could be due to that their diffusion coefficients are derived based on statistical study and thus are highly averaged and cannot be perfectly applied to a specific event, and could also be due to the extrapolation to the lower μ electrons and lower L shells. Again, this indicates that the diffusion coefficients from previous studies do not work perfectly just by simply extending into the low L region.

The disagreement between Kp-dependent D_{LL} and D_{LL} used in this study in the slot region and inner belt also suggests a different L dependence, rather than L^{10} or L^{6}, for the radial diffusion coefficient. To reproduce the data, we used a lower power in order to increase the diffusion coefficient at lower L shells and maintain a reasonable value of the diffusion coefficient in the outer belt. By trying with several different integers, the best result we found is a dependence of L^{4}. We also tried higher L powers, for example, a dependence of L^{6} for μ=30 MeV/G electrons, and tuned the parameters by optimizing the results in the slot region. The optimized results were similar to the one derived using a dependence of L^{4} in the lower L region, with the PEs at L^{*}=2.9 ±0.1, 2.6 ±0.1, 2.3 ±0.1, and 2.0 ±0.1 are 0.75, 0.75, 0.47, and 0.58,

respectively. However, once the parameters are tuned for optimizing the result between L^*=2 and 3, the results at L^*>3 do not fit the data as well as the results using L^4 dependence. For example, at L^*=3.4, using a dependence of L^6, the PE is negative; while a dependence of L^4 gives a PE of 0.44.

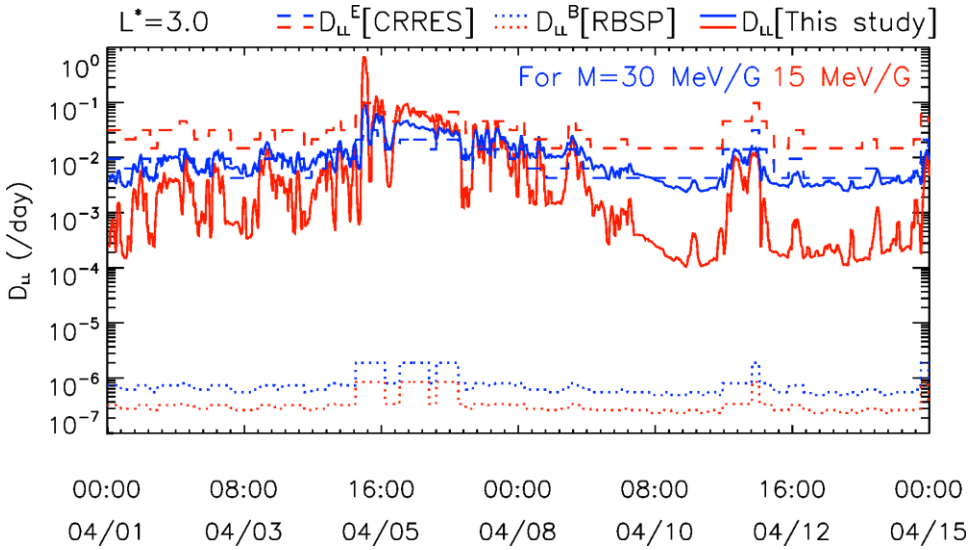

Figure 4.12: Comparison of diffusion coefficients for μ=30 MeV/G, K=0 electrons and μ=15 MeV/G, K=0 electrons in this study and electric (D_{LL}^E) diffusion coefficients from Brautigam et al. [2005] and magnetic (D_{LL}^B) diffusion coefficients from Ali et al. [2015] at L^*=3.

On the other hand, there is always some trade-off between the radial diffusion coefficient and electron lifetime. So we also examine the sensitivity of our model to D_{LL} and τ. In our model, by increasing D_{LL} and decreasing τ, we can get somewhat similar results within the slot region and inner belt; however, the results in the outer part (L^*>3) do not fit the data well. For example, for μ=30 MeV/G electrons, we increased D_{LL} by 50% and tuned the parameters τ_{01}, τ_{02}, p_1, p_2, and L_{cri} to minimize the RMSD between L^*=2.0 and L^*=3.0. As a result, PEs at L^*=2.9±0.1, 2.6±0.1, 2.3±0.1, and 2.0±0.1 are 0.79, 0.84, 0.56, and 0.26, respectively; while at L^*=3.4, PE is -1.68, showing bad agreement between the model and data. However, our model is based on the assumption that τ is constant in time. Considering the time-varying τ, we might get similar results by increasing D_{LL} and decreasing τ or opposite.

4.4.2 The Electron Lifetimes

Figure 4.13 shows the electron lifetimes used in the diffusion model for μ=30 MeV/G electrons (Figure 4.13, left) and μ=15 MeV/G electrons (Figure 4.13, right), versus L^* and the approximate corresponding electron energy. For μ=30 MeV/G electrons, the decay time is about 3 days at L^*=3 (corresponding to ~250 keV electrons) and about 10 days at L^*=2.2 (~500 keV electrons); for μ=15 MeV/G electrons, the decay time is about 10 days at L^*=2.4 (~250 keV electrons) and about 170 days at L^*=1.8 (~500 keV electrons). It is well accepted that in the outer radiation belt, 100s of keV and higher energy electron lifetime is expected to increase with increasing energy at a fixed L. However, since the electron lifetime depends on the loss processes, the situation is quite different for the slot region and inner belt. Comparing the electron lifetime for μ=30 MeV/G and μ=15 MeV/G in the lower L region, e.g., at L^*=2.0, the lifetime for higher energy electrons (625 keV for μ=30 MeV/G electrons) is much lower than lower energy electrons (358 keV for μ=15 MeV/G). The decreasing electron lifetimes with increasing electron energy in the slot region and inner belt is a result of wave-particle interaction. Although the relative importance of plasmaspheric hiss, VLF waves from transmitters, and lightning-induced whistlers is still debatable, this result shows that in the slot region and inner belt, for 100s of keV electrons, the resonant interaction with electromagnetic waves is more significant for higher energy electrons. Lyons et al. [1972] calculated the theoretical precipitation lifetimes for different energy electrons inside the plasmapause due to plasmaspheric whistler mode wave scattering, and showed that at lower L, the electron lifetime decreases with increasing energy, which is consistent with our results. This feature is also consistent with the fact that the slot region is closer to the Earth for higher energy electrons and the inner belt extends further for lower energy electrons.

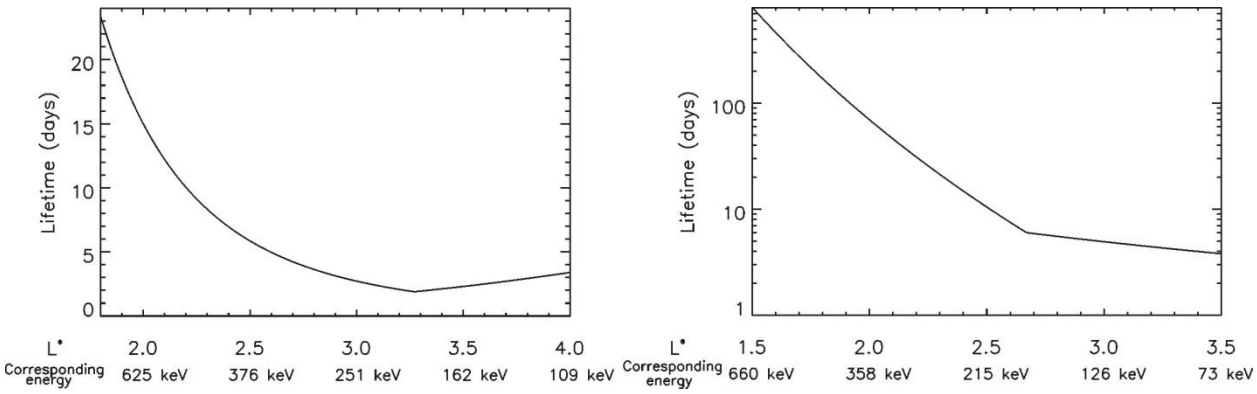

Figure 4.13: Electron lifetimes used in the model for (left) μ=30 MeV/G equatorially trapped electrons and (right) μ=15 MeV/G equatorially trapped electrons, versus L^* and corresponding electron energy.

In the model, we calculated τ in two regions, divided by L_{cri}. It is evident that the electron lifetime used in the model for μ=30 MeV/G electrons has a minimum at L_{cri}=3.27, which accounts for the reappearance of the slot region. The slot region forms as a balance between inward radial diffusion and scattering. Below L_{cri}=3.27, closer to Earth, the lifetime gets longer and the diffusion rate gets lower too, thus the balance between the two forms a slot region centered around L^*=2.9, as shown in Figure 4.6. For μ=15 MeV/G electrons, there is no clear feature of a slot region, and the two-region lifetime is used to give a better fit to the original PSD data.

4.4.3 The Pitch Angle Distribution Assumption

All PSD data we used are derived based on the assumption that the pitch angle distribution at the magnetic equator has the form of $\sin^3 \alpha$. To check the sensitivity of this assumption, we also tried to use $\sin^2 \alpha$ and $\sin^5 \alpha$ as the pitch angle distribution assumption. The results show that, although the magnitude of PSD data changes a lot, the shape of PSD profile does not change much, and thus the diffusion coefficients used in the model are very similar. The distribution of $\sin^2 \alpha$ gives a ~20% higher radial diffusion coefficient than $\sin^3 \alpha$, while the distribution of $\sin^5 \alpha$ gives a ~30% lower diffusion coefficient. Thus, the uncertainties in pitch angle distribution assumption do not significantly affect the result that the diffusion coefficients

needed in this April event disagree with the Kp-dependent diffusion coefficients from previous studies in the slot region and inner belt.

While uncertainties about diffusion coefficients and lifetimes used here exist, we demonstrate that fast enhancements of energetic electrons in the slot region and inner belt can be understood as the inward radial transport of lower energy electrons originally at larger L.

4.5 Conclusion

We investigated 100s of keV electron flux enhancements in the slot region and the inner belt using DEMETER IDP data, and modeled the flux enhancement event of April 2010 for μ=30 MeV/G and μ=15 MeV/G equatorially trapped electrons. The results are summarized as follows:

1. For 100s of keV electrons, the flux enhancements in the slot region and inner belt occur much more often than MeV electrons. Even moderate geomagnetic storms can cause 100s of keV electron flux enhancement in the lower L region.

2. By using a radial diffusion model, we modeled the radial diffusion of μ=30 MeV/G and μ=15 MeV/G equatorially trapped electrons in April 2010. The model results reproduce the PSD data calculated from the electron flux data quite well, indicating that the flux enhancement event can be well explained by inward radial transport.

3. Comparing the diffusion coefficients used in our model with the Kp-dependent diffusion coefficients from Brautigam and Albert [2000], we found that our diffusion coefficients are much larger than D_{LL}^{B} but smaller than D_{LL}^{E}. Comparison between our diffusion coefficients and those from Ozeke et al. [2012] also showed that our diffusion coefficients are generally larger than theirs. The results indicate that those diffusion coefficients from previous studies cannot be simply extended into the slot region and inner belt.

This chapter has mainly focused on the deep penetration of 100s of keV electrons into the slot region and inner radiation belt and the modeling results of radial diffusion model based on

the Fokker-Planck equation. It was showed that the inward radial diffusion is a very important physical process which is responsible for the deep penetrations of 100s of keV electrons. Besides the radial diffusion, many other physical processes exist in the slot region and inner belt and play important roles on the energetic electron dynamics. In the following chapter, continuing focusing on the dynamics of 100s of keV electrons in the slot region and inner belt, I will show the detailed pitch angle distribution analysis of 100s of keV electrons in the low L region, which can reveal physical processes that are taking effects in specific regions.

Chapter 5

Hundreds of keV Electrons in the Slot Region and Inner Belt II: Unveiled Pitch Angle Distributions Based on Van Allen Probes Measurements

The following chapter is primarily based on work that was published in Zhao et al. (2014a), Peculiar pitch angle distribution of relativistic electrons in the inner radiation belt and slot region, Geophys. Res. Lett., 41, 2250–2257, doi:10.1002/2014GL059725, and Zhao et al. (2014b), Characteristics of pitch angle distributions of hundreds of keV electrons in the slot region and inner radiation belt, J. Geophys. Res. Space Physics, 119, 9543–9557, doi:10.1002/2014JA020386.

5.1 Introduction

In the previous chapters, I have shown that in the inner radiation belt and slot region, though MeV electrons exhibit limited changes except during very active times, hundreds of keV electrons are subject to great variations, and various acceleration and loss processes are responsible for those variations [e.g., Li et al., 1993; Baker et al., 2004a, 2007; Baker and Blake, 2013; Zhao and Li, 2013a, 2013b]. In this chapter, I will continue focusing on the 100s of keV electrons in the low L region and explore the physical processes in this region by examining the pitch angle distributions (PAD) of 100s of keV electrons.

The electron PAD is an important characteristic of radiation belt electrons, since the evolution of PADs can give us important information on the source and loss processes in a specific region. Many previous studies have focused on the characteristics and evolution of electron PADs in the outer radiation belt [e.g., West et al., 1973; Gannon et al., 2007; Chen et al., 2014]. Generally, the electron PADs in the outer radiation belt can be categorized into three types: the normal distribution, butterfly distribution, and flat top distribution. The normal distribution is the most general type of PAD in the outer belt, for which the electron flux peaks at 90 °pitch angle (PA) and smoothly decreases at smaller PAs. It is thought to form as a result of

the loss to the atmosphere combining with the pitch angle diffusion. Inward radial diffusion can also cause the flux peak around 90 °. Due to the conservation of the first and second adiabatic invariants, when an electron moves inward, the perpendicular momentum increases more than the parallel component, which would increase the PA of electron and thus create a more 90 ° peaked PAD [e.g., Schulz and Lanzerotti, 1974]. The butterfly distribution has a minimum around 90 °, which looks like a butterfly in the polar plot (in which PA is the polar angle and flux is the radius). The butterfly distribution is thought to be caused by the drift-shell-splitting effect combining with magnetopause shadowing or strong negative radial flux gradient [e.g., Sibeck et al., 1987; Selesnick and Blake, 2002]. Horne et al. [2005] have also suggested that chorus wave heating could cause butterfly distribution by preferentially heating off-equator electrons. For the flat top distribution the electron flux is approximately equal at a wide PA range centered around 90 °. It can be a transition between the normal distribution and butterfly distribution or can be due to strong wave-particle interactions [Horne et al., 2003]. Besides these three types of PADs, another PAD type, "cap" PAD (also called "head-and-shoulder" PAD), has also been recognized [e.g., Lyons and Williams, 1975a; Sibeck et al., 1987]. This type of PAD looks like a bump around 90 °on top of a normal distribution. It is found to be present in the outer belt and slot region. As for the formation of cap distributions, Lyons and Williams [1975a] shows the comparison between the observation and modeling of wave-particle interaction, and the agreement between the two suggests that the cap distribution forms as a result of pitch angle scattering caused by the plasmaspheric whistler mode waves in the slot region. However, Sibeck et al. [1987] has also investigated the cap distribution in the outer belt and suggested that this type of PAD can be caused by a combination of the drift-shell-splitting effect and a substorm injection or a sudden magnetospheric compression. For tens to hundreds of keV electrons, "cigar" distribution with flux peaking along the direction of local magnetic field has also been found in the outer radiation belt, and it is thought to be related to the tail-like stretching of the nightside magnetic field prior to the substorms and thus could be used as an indicator of likely substorm onset [Baker et al., 1978].

However, comparing to the PADs in the outer belt, PADs in the inner radiation belt and slot region received limited attention during the past decades. Lyons et al. [1972] calculated the pitch angle diffusion rate in the slot region, and the results showed that the interaction between electrons and plasmaspheric hiss waves can cause cap PADs in the slot region, which is similar to observations at L=3-4 during the decay phase following an injection event. Also, Lyons and Williams [1975a, 1975b] examined the PADs of 35-560 keV electrons in the outer belt and slot region using data from Explorer 45. They found that during geomagnetic quiet times, the PADs in the slot region and outer regions of the plasmasphere near the magnetic equator observed by Explorer 45 can be primarily explained by resonance interactions with plasmaspheric hiss, while during active times, the PADs were greatly distorted because of injections, and during post-storm decay periods, 90 °minima in the PADs at L=2-4 were occasionally observed.

One reason for the lack of attention to the inner belt electrons during the past decades is the limited quality data available, which was then due to the unforgiving contamination from the very energetic inner belt protons [e.g., Selesnick et al., 2014] and also from sometimes newly formed very energetic electrons and protons in the slot region [Blake et al., 1992; Li et al., 1993; Hudson et al., 1995; Baker et al., 2004a]. Now the newly available Energetic Particle, Composition, and Thermal Plasma (ECT) [Spence et al., 2013] data from Magnetic Electron Ion Spectrometer (MagEIS) [Blake et al., 2013] onboard the Van Allen Probes spacecraft [Kessel et al., 2013] provide an unprecedented opportunity to study the detailed PADs for hundreds of keV electrons in the slot region and inner belt. The Van Allen Probes operate in an elliptical orbit, with the inclination of 10 °and altitude of ~600 km at perigee and geocentric distance of 5.8 R_E at apogee. With the spin axis approximately pointing to the Sun, the spacecraft is spinning with a period of ~12 s. The MagEIS instrument, as a part of the ECT suite, provides high-resolution energetic electron flux measurements with energy range of ~30-4000 keV. It contains four independent magnetic electron spectrometers on each spacecraft, one low-energy spectrometer (LOW), two medium-energy spectrometers (M75 and M35), and a high-energy spectrometer (HIGH). The low unit, high unit, and one of the medium units (M75) are mounted with the field

of view centered at 75 °to the spin axis, while the field of view of another medium unit (M35) is centered at 35 °to provide larger PA coverage. In this study, we mainly use the PA-resolved electron data from M75 of MagEIS, which provides ~200 keV-1 MeV electron flux measurements with good PA coverage. It is worth mentioning that the energy of each channel of MagEIS was changing during the mission, so for the statistical analysis presented in this study we use the electron data of energy channel closest to the specified energy channel.

In this study, we focus on hundreds of keV electron measurements from MagEIS and examine the pitch angle distributions of 100s of keV electrons in the slot region and inner belt. In section 5.2, I report the newly unveiled electron PADs with minima at 90 °in the inner radiation belt and slot region. Such kind of PADs, different from analytical results of wave-particle interaction [e.g., Lyons et al., 1972], remains almost continuously present in the inner belt while exhibits great variations during storm times in the slot region. In section 5.3, I further investigate and provide a comprehensive description of the PADs of hundreds of keV electrons below L=4 using over a year's data from MagEIS instrument, focusing on ~460 keV electron PADs as a function of L shell. In addition to the 90 °minimum PAD, normal and cap PADs in the low L region are also identified and the characteristics and distribution of these three types of PADs in the low L region are shown. Using the PADs observed in the slot region and inner belt, we can thus infer the source and loss processes in the low L region. In section 5.4 and 5.5, I focus on the 90 °peaked PADs and 90 °minimum PADs in the low L region, respectively. For the normal PADs, by fitting them into a $\sin^n \alpha$ form, the parameter n is calculated and results are discussed. For the 90 °minimum PAD, more detailed statistical analysis as well as the case study are performed and possible mechanisms responsible for the formation are proposed. The discussion and conclusion will be presented in section 5.6 and 5.7 respectively.

5.2 Peculiar Pitch Angle Distribution of Relativistic Electrons in the Inner Radiation Belt and Slot Region

5.2.1 Storm-time Observations

The PADs of 464 keV electrons at different L during 29-30 June 2013 are shown in Figure 5.1, in which all data are from outbound passes only from Van Allen Probe-A in order to avoid any local time dependence. Three rows correspond to PADs observed at L=3.0, 2.5, and 2.0, respectively. Here we use McIlwain L with TS04 magnetic field model [Tsyganenko and Sitnov, 2005]. Two parameters are calculated and shown in the top right corner of each panel: magnetic latitude (Mlat) and corresponding equatorial pitch angle of locally mirroring electrons (α_eq). This is a geomagnetic active time period, with a strong storm (minimum Dst~-100 nT and maximum AE~1200 nT) occurring on June 28. There is a significant electron flux increase at L=2.5 and above during this storm, while the flux level at L=2.0 almost does not change. One significant signature here is that during this time period, the minima at 90 °in PADs developed. At L=3.0 and 2.5, this 90 °minima appeared along with the flux enhancement on June 29 and persisted at least several orbits. At L=2.0, the 90 °minima was there earlier but became more significant as the flux enhancement occurred. It is worth mentioning that in the third column, no minimum at 90 °is observed because the magnetic latitude is too high (almost no minimum at 90 ° is observed in the inner belt and slot region when |Mlat|>~10 °). The structure of minima at 90 °is also present in lower energy channels (as low as 30 keV) but is less obvious. For the energy channels higher than 464 keV, the fluxes are too low and too close to the background to get clear PADs. Lyons and Williams [1975b] have reported this kind of structure that appeared around L=2-4 during some post-storm time periods using data from Explorer 45. However, they described this kind of structures as short lived (8-24 h) and only present during active period. The short-lived feature they described probably is because they did not take into consideration the magnetic latitude. As shown in Figure 5.1, when the corresponding equatorial pitch angle of locally mirroring particles is high enough, we can always see this kind of PAD. Though not

shown here, PADs with minima at 90 °can last for days at the outer edge of the slot region and for years in the heart of inner radiation belt according to Van Allen Probes observations. Another aspect in contrast to what Lyons and Williams [1975b] mentioned is that minima at 90 °in PADs do exist during the quiet times as well, as shown in the following subsection.

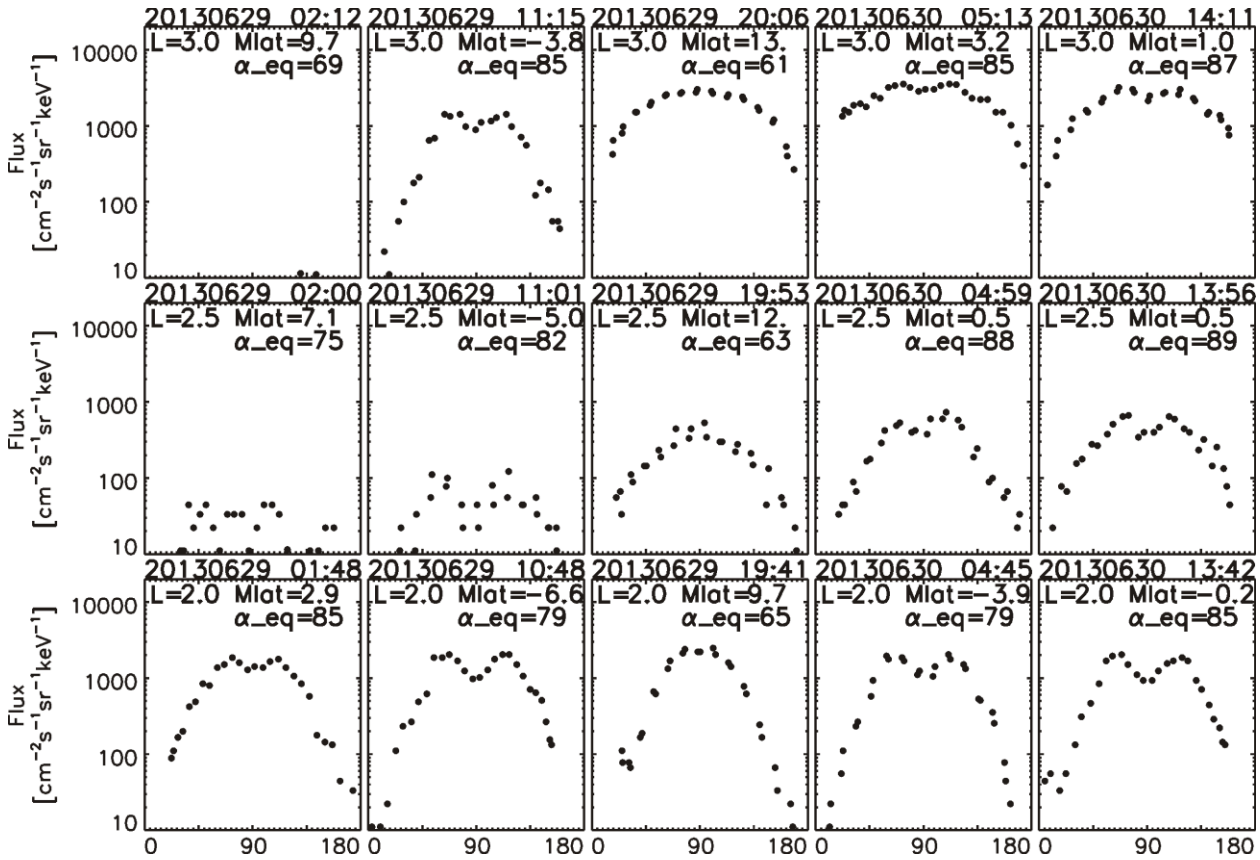

Figure 5.1: The pitch angle distributions of 464 keV electrons from Van Allen Probe-A during 29-30 June 2013, at (top) L=3.0, (middle) 2.5, and (bottom) 2.0, respectively. Two parameters shown in the top right corner of each panel are magnetic latitude (Mlat) and the corresponding equatorial pitch angle of locally mirroring electrons (α_eq). The data are from outbound passes only.

5.2.2 Quiet-time Observations

Figure 5.2 shows the PADs at L=1.5 during 4-5 January 2013, a geomagnetic quiet time period (Dst ~ 0 nT and AE < 200 nT), for three different energy channels (237 keV, 349 keV, and 456 keV from the top to bottom, respectively). The format of Figure 5.2 is similar to that of

Figure 5.1, but only the inbound passes from Van Allen Probe-A are plotted. It is clear that during this quiet time period, with passes close enough to the magnetic equator, PADs with minima at 90 °are always observed at L=1.5, and the situation is similar for all three energy channels. Figure 5.2 suggests that PADs with 90 °minima are generally present in the inner radiation belt, even during very quiet time period. In the slot region, however, this kind of PADs is not clearly observed at L=2.0-2.5 during this time period; at larger L the fluxes are low and close to background levels, and thus, no clear PAD patterns are measured. It is worth noting that in this study the uncorrected data from MagEIS instrument are used, and thus high fluxes inside the loss cone were observed in the inner radiation belt mainly because of the contamination from highly energetic protons. However, this would not affect our results about 90 °minima in the electron PADs since the fluxes around 90 °PA are usually much higher than background noises.

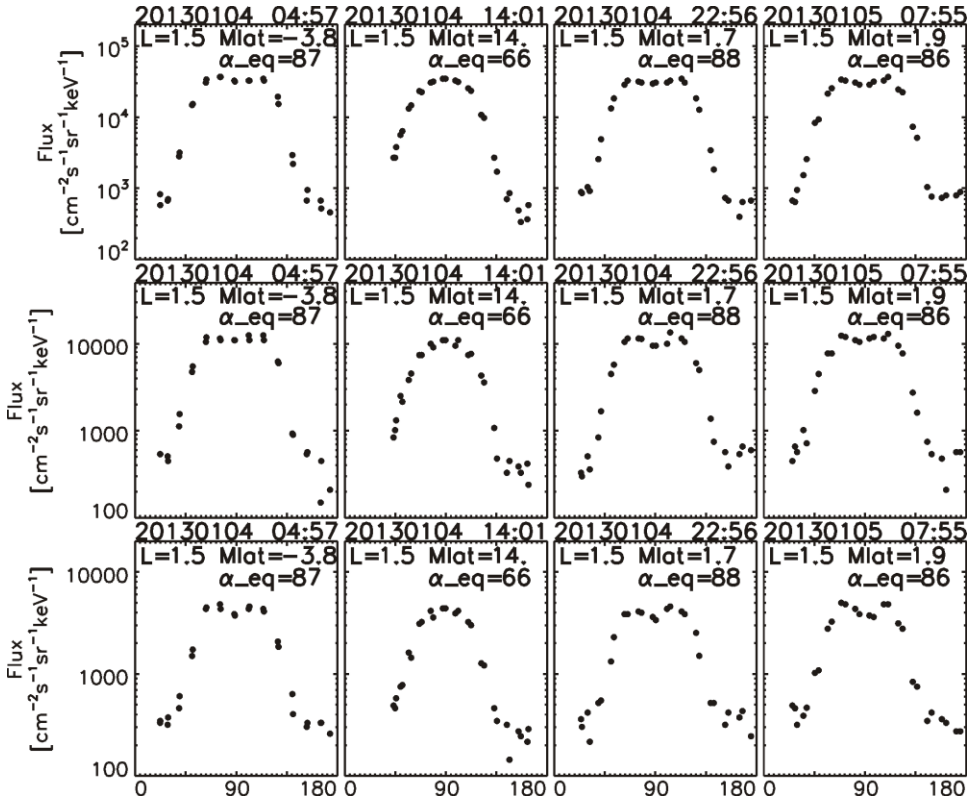

Figure 5.2: The PADs of (top) 237 keV, (middle) 349 keV, and (bottom) 456 keV electrons, respectively, at L=1.5 during 4-5 January 2013. The data are from inbound passes of Van Allen Probe-A only.

5.2.3 Statistics

In order to show the general features of PADs with minima at 90 °over time and L, we developed a program to automatically identify this kind of PAD inside the inner belt and slot region and then calculated the frequency of occurrence. The criteria we used include (1) $f_{avg}(85°:95°) < 0.95 \times f_{avg}(90° - \alpha: 90° + \alpha)$, where $f_{avg}(a:b)$ is the averaged flux of electrons with pitch angle between a and b and α is selected from 5 °to 45 °to maximize the value of $f_{avg}(90° - \alpha: 90° + \alpha)$, and (2) total square root of counts (summed over all pitch angles) is greater than 50. We only included those points when the satellite is close enough to the magnetic equator (the corresponding equatorial pitch angle of locally mirroring electrons is greater than 85 °) in the statistics. Using these criteria, we plotted the frequency of occurrence of PADs with 90 °minima of ~460 keV electrons over a year as a function of L and time in Figure 5.3 using data from both probes. Figure 5.3 also includes the daily averaged Dst and AE indices measured (real time) in black and predicted in red [Temerin and Li, 2002, 2006; Li et al., 2007; Luo et al., 2013]. The color bar in Figure 5.3 (top) indicates the frequency of occurrence of PADs with minima at 90 °, where red means this kind of PADs is always observed and black means no such kind of PADs. The white regions are where the second criterion cannot be met, or both satellites are away from the magnetic equator.

From Figure 5.3, it is clear that for ~460 keV electrons, at L=1.5, this kind of PAD is always observed and not correlated with geomagnetic activity; but at L=~1.8-3.0, the occurrence of PADs with 90 °minima is strongly correlated with both the AE and Dst indices. During quiet times, e.g., December 2012 to February 2013, PADs with minima at 90 °are rarely observed at and above L=1.8, while during active times, e.g., in July 2013, the frequency of occurrence of PADs with minima at 90 °between L=1.8-2.5 is very high. Also, after such PAD pattern is initially created, it lasts longer at lower L, and disappears faster at higher L.

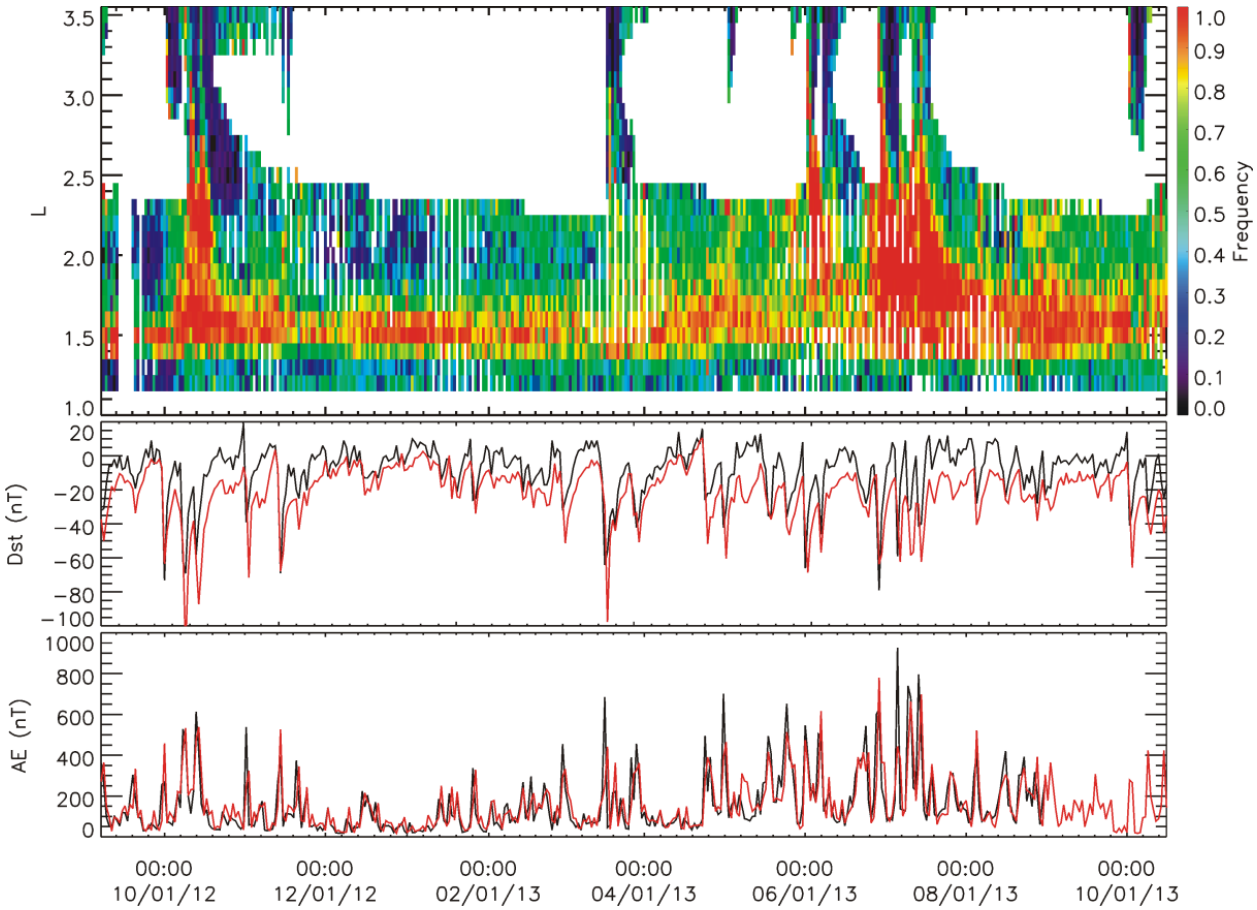

Figure 5.3: (top) The frequency of occurrence of PADs with minima at 90 °of ~460 keV electrons as a function of L and time from September 2012 to October 2013. (middle) The daily averaged real-time Dst index (black) and predicted Dst index (red). (bottom) The daily averaged real-time AE index (black) and predicted AE index (red).

5.2.4 Averaged Pitch Angle Distributions

It is also important to show the averaged PADs during quiet and active time and at different L. As an example, we calculate the averaged PADs of ~460 keV electrons during a geomagnetic quiet month (December 2012, Figure 5.4 (top)) and active month (July 2013, Figure 5.4 (bottom)), respectively, at L=1.5, 1.8, 2.0, and 2.3 (with ΔL=0.05) for comparison. The number of PADs being averaged is shown in the top right corner of each panel. Similarly, here we also use the PADs measured by both probes but only when the probe is close enough to the magnetic equator with α_eq > 85 °.

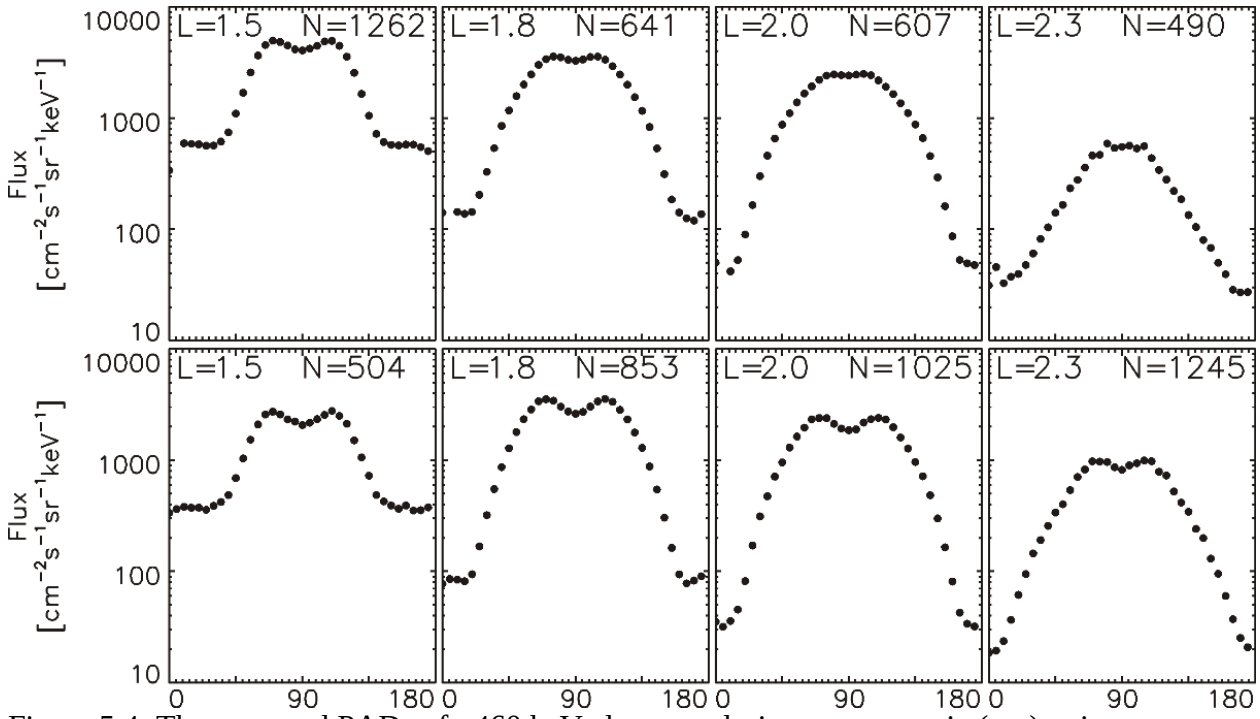

Figure 5.4: The averaged PADs of ~460 keV electrons during geomagnetic (top) quiet (December 2012) and (bottom) active times (July 2013), respectively, at L=1.5, 1.8, 2.0, and 2.3, using data from both probes. The L is shown in the top left corner for each panel, while the number of PADs being averaged is shown in the top right corner.

The results shown in Figure 5.4 are clear and significant: during active time, the PADs with minima at 90 °are present throughout the slot region and inner belt; during quiet time, such kind of PADs is still present in the inner belt but much less obvious in the slot region. Also, by comparing the averaged PADs at different L, we see that, at L=1.5, the structure almost does not change, while at L>1.8, the structure is less significant during quiet time and more notable during active time. As L increases, the minimum at 90 °disappears during quiet time. One thing notable is that we can clearly see from Figure 5.4 that the flux level inside the loss cone is high at L=1.5 and gradually decreases as L increases, which is likely due to the contamination of the inner belt protons. However, since the peak flux values are at least 1 order of magnitude higher than the background fluxes, such background should not affect the PADs near 90 °for ~460 keV electrons.

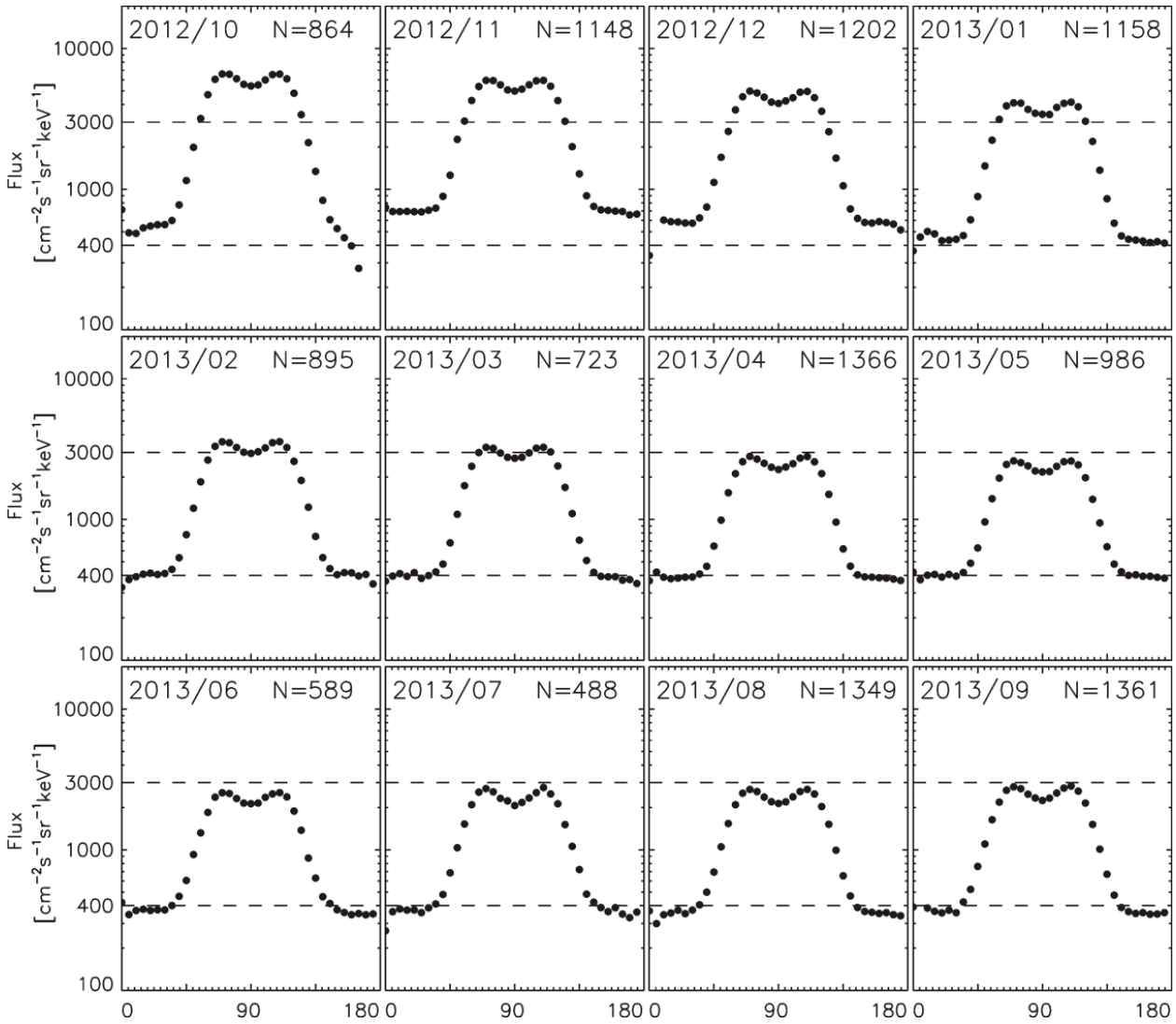

Figure 5.5: The monthly averaged PADs of ~460 keV electrons at L=1.5, from October 2012 to September 2013, using data from both probes. The number of PADs being averaged is shown in the top right corner of each panel. The two dashed lines in each panel are just for reference.

It should be interesting to look at the long-term behavior of PADs in the inner belt. Figure 5.5 shows the monthly averaged PADs of ~460 keV electrons at L=1.5, from October 2012 to September 2013 using the same criterion as in Figure 5.4. The situation is similar but confirming: the 90 °minima in the averaged PADs persist all the time, and the shapes of PADs did not change much over the whole year at L=1.5. It is worth noting that during the first 6 months of the mission, there are several gain changes and energy channels changes, which makes the backgrounds and the peak values of the measurements in the PADs change but not the PAD

shape itself. During the next 6 months, it is clear that the flux level and PADs at L=1.5 almost did not change, even during active time. This suggests that in the heart of inner belt, the flux of hundreds of keV electrons does not change much as expected from the low scattering rates by plasmaspheric hiss waves at low L region [e.g., Abel and Thorne, 1998] (unless there are much stronger magnetic storms, e.g., 24–25 March 1991 and 30–31 October 2003), and PADs with minima at 90 °are always expected. It is also worth mentioning that we have checked the monthly-averaged PADs of ~460 keV electrons over an even longer time period (from 2012 to 2015) using background-corrected data, and the results show that though during very active times the flux of ~460 keV electrons at L=1.5 does change, the 90 °minima are always observed in electron PADs.

To summarize, we found that the PADs inside the inner radiation belt and slot region are different from predictions of previous theories [e.g., Lyons et al., 1972]; actually, near the magnetic equator, the pitch angle distributions with minima at 90 °are always observed in the inner belt and are expected in the slot region during storm times. The PADs with minima at 90 ° have several features: (1) during the geomagnetic active times, this type of PADs is almost always present inside the inner belt and slot region; (2) during the geomagnetic quiet times, this type of PADs also exists in the inner belt but is much less significant in the slot region; and (3) the minima at 90 °in PADs can last for several days to months in the inner belt and slot region, depending on L, and this structure disappears faster with increasing L, possibly due to stronger pitch angle scattering by whistler mode hiss waves at higher L [e.g., Abel and Thorne, 1998; Artemyev et al., 2013].

5.3 Energetic Electron Equatorial Pitch Angle Distributions in the Slot Region and Inner Belt: Survey Plots

In the previous section, I introduced the newly unveiled 90 °minimum PAD of 100s of keV electrons in the slot region and inner belt. The presence of this peculiar type of PAD indicates the complexity in the inner belt dynamics and motivates us to further investigate the

physical processes existing in the low L region. In this section, I focus on the PADs of ~460 keV electrons in the low L region, show different types of PADs as a function of L and time for over a year, and discuss about the possible physical processes behind each of them.

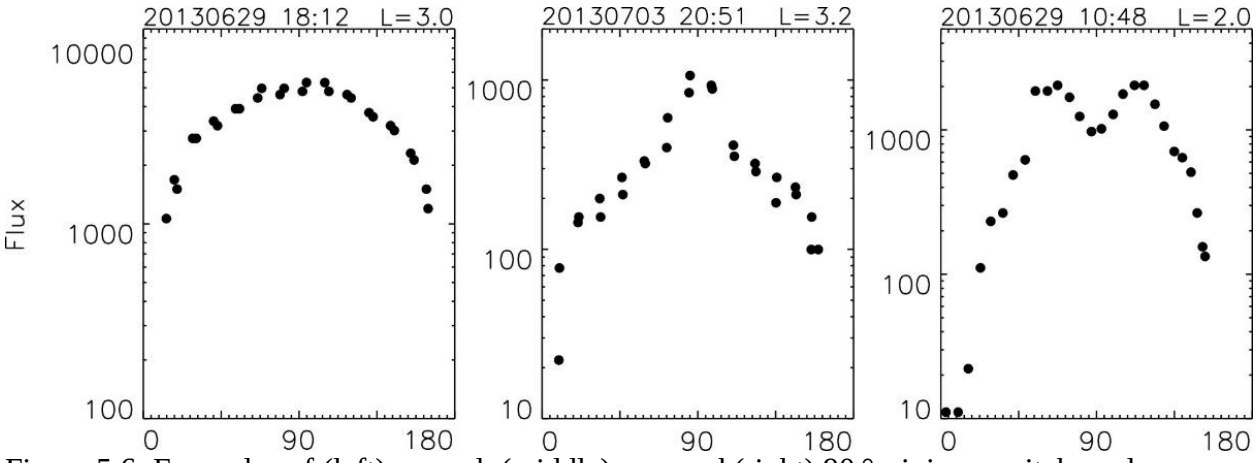

Figure 5.6: Examples of (left) normal, (middle) cap, and (right) 90 °minimum pitch angle distributions of ~460 keV electrons.

Based on MagEIS PA-resolved data, the PADs of hundreds of keV electrons in the slot region and inner radiation belt are most similar to Gaussian distributions combined with some modifications around 90 °PA. The PADs in the low L region can be roughly divided into two categories: 90 °peaked PADs and 90 °minimum PADs, while 90 °peaked PADs can again be categorized into the normal distribution and cap distribution. Figure 5.6 shows examples of normal PAD, cap PAD, and 90 °minimum PAD observed in the low L region using data from MagEIS onboard Van Allen Probe-A. For over a year, we found that most equatorial PADs in the slot region and inner belt can be described as one of these three categories, provided that the flux level is higher than the background noise. Thus, for the statistical analysis in this study, we exclude all PADs with the total square root of counts (summed over all pitch angles) less than 50. However, there is still a situation where the counts are high but the PAD is almost flat, indicating high background noises with small signal-to-noise ratio. This kind of situation occurs mostly at the inner edge of outer belt as well as the inner part of inner belt. As for the inner edge of outer belt, the high flux level of background is likely caused by the bremsstrahlung radiation produced

by very energetic electrons; while for the inner belt, it is more likely caused by the inner belt proton contamination. We call this type of PAD the "undefined" PAD since it cannot be categorized into any of the three well-defined PAD types and is likely formed due to contamination.

To show the categorization of PADs in the low L region, we use some criteria to identify different types of PADs. First, in order to identify those undefined PADs, we fit a PAD into a Gaussian function and calculate the correlation coefficient between the data and the Gaussian function. All PADs with correlation coefficients less than 0.8 are identified as undefined PADs. Using this criterion, we found between L=1.5 and 3 only ~2% PADs are undefined. Then, we identify the 90 °minimum PADs using the same criteria as used in section 5.2.3. If a PAD cannot meet the criteria of 90 °minimum PAD, we then separate data into two parts according to the PA (PA=[60 °, 120 °] and PA=[0 °, 60 °]∪[120 °, 180 °]) and fit them into two Gaussian functions respectively. If the full width at half maximum of the second Gaussian function (using data of PA= [0 °, 60 °]∪[120 °, 180 °]) is at least twice of the first Gaussian function (using data of PA=[60 °, 120 °]), we identify this PAD as a cap PAD. The rest of the PADs are characterized as normal PADs. However, at very low L (< 1.4), the loss cone is very large (up to ~ 40 °at L=1.4 and even higher at lower L), and the background noise from inner belt proton contamination is getting comparable with or higher than the electron flux with PA close to the loss cone, which makes some normal PADs at L~1.3 as cap PADs. Thus, we simply mark all cap PADs detected below L=1.4 as undefined PADs.

Figure 5.7 (top) shows the distribution of different PAD types of ~460 keV electrons between L=1 and 4 during 7 September 2012 to 24 March 2014 using the data from Van Allen Probe-A, with the corresponding equatorial pitch angle of locally mirroring electrons (α_eq) greater than 80 °. Different colors represent different types of PADs: blue represents 90 ° minimum PAD, green is the normal PAD, and red is the cap PAD. The undefined PADs are marked as grey. Note that the occasional white gaps between L~1.2 and 2.5 are where Van Allen Probe-A is away from the magnetic equator (α_eq < 80 °), while the gaps above L~2.5 are most

likely where the data were rejected because the counts are low (total square root of counts < 50). The spin-averaged flux of ~460 keV electrons during this time period is also provided for reference (Figure 5.7, bottom). The L parameter used in this study is the McIlwain L of locally mirroring particles with the T89 dynamic magnetic field model [Tsyganenko, 1989] using International Radiation Belt Environment Modeling (IRBEM) library [Boscher et al., 2010], while L^* parameter used in section 5.5, where the phase space density is calculated, is the Roederer L with the T89 model.

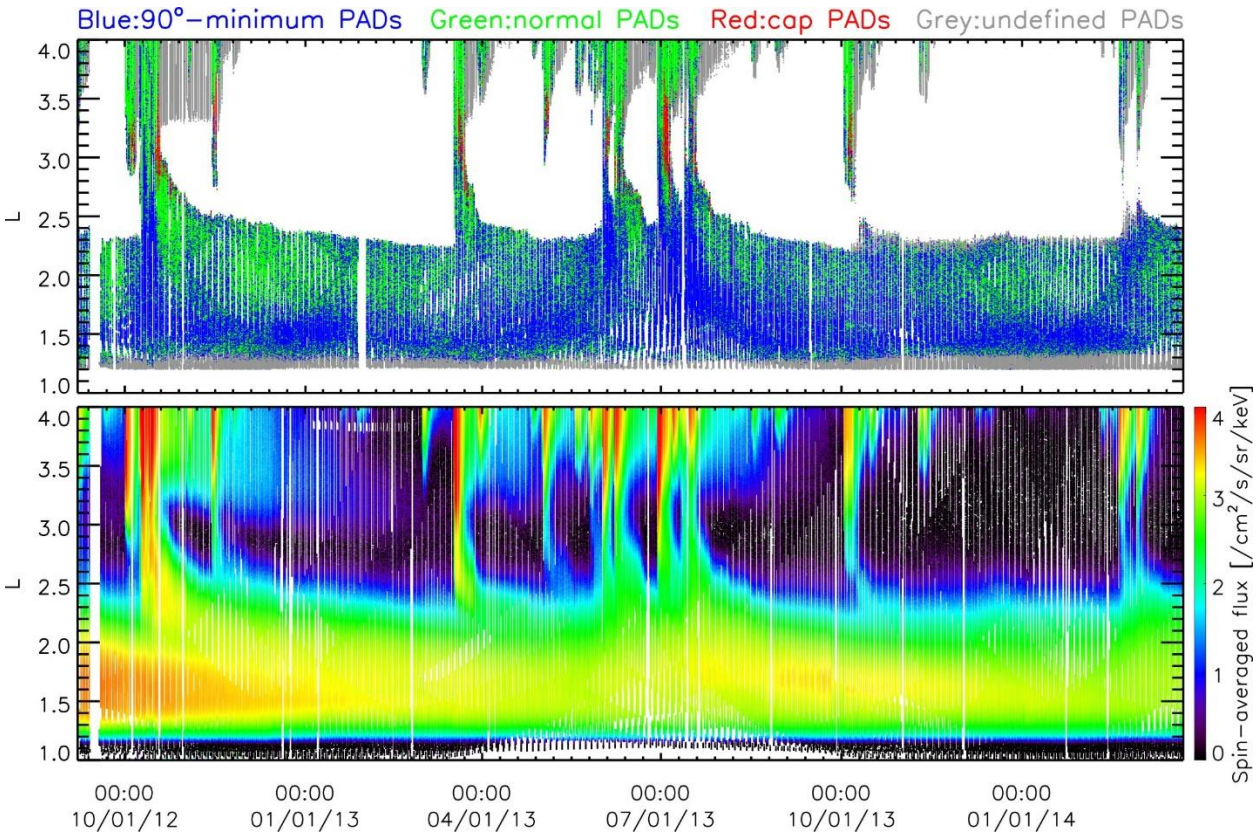

Figure 5.7: (top) Classification of pitch angle distributions of ~460 keV electrons during 7 September 2012 to 24 March 2014 using data from MagEIS onboard Van Allen Probe-A. Different colors represent different types of PADs: blue denotes the 90 °minimum PAD, green represents the normal PAD, and red represents the cap PAD, while grey indicates the undefined PAD. White regions are where the counts are too low to show clear PAD pattern or the satellite is away from the magnetic equator (with corresponding equatorial pitch angle of locally mirroring particle less than 80 °). (bottom) Spin-averaged flux of ~460 keV electrons during 7 September 2012 to 24 March 2014 using data from MagEIS onboard Van Allen Probe-A, when the equatorial pitch angle of locally mirroring particle is greater than 80 °.

As Figure 5.7 (top) shows, the 90 °minimum PADs dominate at L~1.4-1.8 almost all the time, while the normal PADs dominate at high L mostly (L>3.5). In the region between, the PADs are subject to the influence of storm time injections. During storm times, as the plasmasphere shrinks while the radial diffusion and wave heating increase, hundreds of keV electrons can penetrate into the slot region and sometimes even inner belt. Along with the injections, 90 °minimum PADs dominate in both the slot region and inner belt. After the formation, 90 °minimum PADs gradually disappear in the slot region, which is likely due to the pitch angle scattering caused by whistler mode waves, and the normal distribution becomes the dominant PAD type again between L=1.8 and 2.5. After the injections, as the electron flux decreases, the cap distributions gradually appear between L~2.5 and 3.5, until the flux is too low to show a clear PAD pattern. As the modeling results from Lyons et al. [1972] predict, the resonance interaction between electrons and plasmaspheric hiss waves can produce PAD with a bump near 90 °. Thus, the formation of the cap distribution in the slot region is likely due to the pitch angle scattering caused by plasmaspheric hiss waves. Grey regions, which represent the "undefined" PADs, are located near the inner edge of the outer belt after storms as well as L~1.2-1.3 and indicate the presence of high background noise from bremsstrahlung radiation or inner proton contamination.

To summarize, in this section we showed the equatorial PADs of ~460 keV electrons in the slot region and inner belt and identified three types of PADs: normal, cap, and 90 °minimum PAD. Below L~1.8, 90 °minimum PADs dominate, while between L~3.5 and 4 normal PADs dominate. In the region between, 90 °minimum PADs become dominant during storms and normal PADs dominate during quiet times. The cap distribution appears mostly during the decay periods in the slot region and thus is likely caused by the wave-particle interaction with plasmaspheric hiss waves. In the next two sections, we will discuss the 90 °peaked and 90 ° minimum PADs in detail and suggest the physical processes responsible for the formation of those PADs.

5.4 Ninety Degrees Peaked Pitch Angle Distributions and Corresponding Physical Processes in the Slot Region and Inner Belt

Ninety degrees peaked PADs can be categorized into two types: the normal PAD and cap PAD. The normal PAD can also be fitted into a $\sin^n \alpha$ form, where n represents the steepness of the normal PAD, with high n number indicating a highly 90 °peaked distribution. To show more detailed features of the normal PADs, we fit the normal PADs into $\sin^n \alpha$ according to the equation given by Vampola [1998]: $n = (\log(I_{90/45}) + 0.004105)/0.14303$, where $I_{90/45}$ is the ratio of the electron flux at 90 °to that at 45 °. In this study, we average the electron flux between PA = 85 °and 95 °and divide it by the averaged flux of electrons with PA of 40 °-50 ° and 130 °-140 °and use this result as $I_{90/45}$ in Vampola's equation. Figure 5.8 (top) shows the n values calculated by this method for normal PADs of ~460 keV electrons at L<4, with α_eq greater than 80 °and total square root of counts greater than 50. The grey region (L<1.8) represents where the n values cannot be accurately calculated by this method due to the inner belt proton contamination to the electron fluxes with PA of 40 °-50 °and 130 °-140 °. Similar to Figure 5.7, only data from Van Allen Probe-A are used. It is clear from Figure 5.8 that below L~ 3, the n values are much higher than that at the inner edge of the outer belt, which is consistent with previous studies [e.g., Gannon et al., 2007]. This could be caused by the wave-particle interaction between electrons and plasmaspheric hiss waves, which only exist inside the plasmasphere. The inward radial diffusion could also play a role. In the inner belt, the value of n is relatively uniform, while in the slot region the n parameter changes frequently during injections. If we focus on the electron injections into the low L region, e.g., during the 17 March 2013 storm, we can find that the n parameter in the slot region is very high at the beginning of the injection, indicating a steep normal distribution. Afterward n becomes a little smaller, while as the flux decays, n becomes larger again. We will discuss this phenomenon in the rest of this section by showing detailed PAD evolution. Note that at L<1.8, the background flux level is high due to the contamination from inner belt protons, which may elevate the flux at PA = 45 ° significantly; thus, in this region the parameter n cannot be accurately calculated using the

Vampola's equation. However, the peak flux of the electrons, around PA=90 °, is still significantly above the background at L>~1.3. Not shown here, we also examined the magnetic local time (MLT) and longitude dependence of the n parameter for L<4 and found no significant variations. Figure 5.8 (middle) is discussed in Section 5.5, and Figure 5.8 (bottom) shows the spin-averaged flux of ~460 keV electrons for reference.

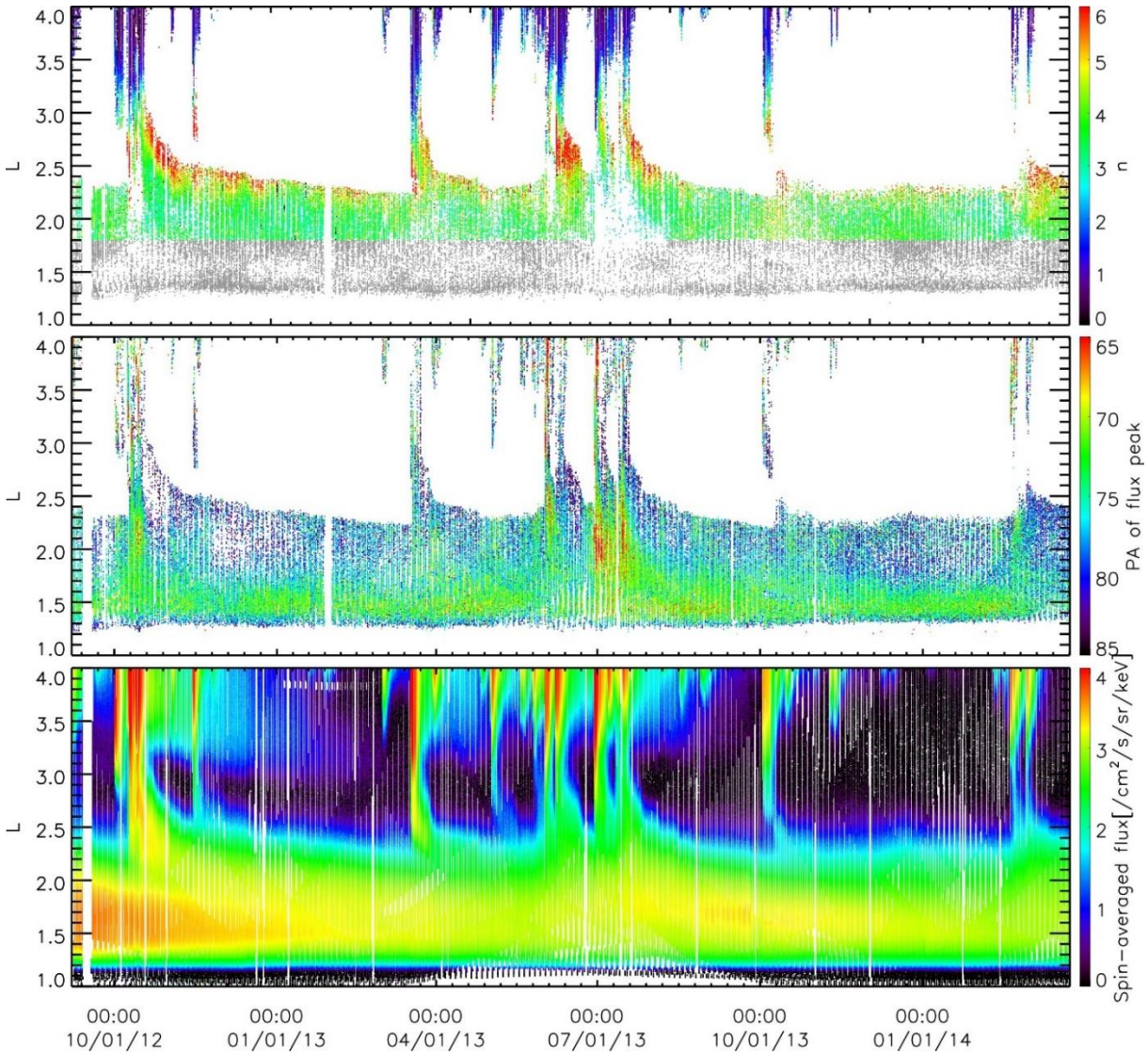

Figure 5.8: (top) The n values of normal PADs of ~460 keV electrons calculated from Vampola's equation as a function of L shell during 7 September 2012 to 24 March 2014. The grey region represents where the n value cannot be accurately calculated due to the contamination from inner belt protons. (middle) The corresponding equatorial pitch angle at the flux peak of 90 °minimum PADs of ~460 keV electrons during the same time period. (bottom) Spin-averaged flux of ~460 keV electrons, the same as in Figure 5.7.

To examine the evolution of 90 °peaked PADs in the slot region during the injection, we also plotted the detailed PADs of ~460 keV electrons at L=2.7 during 17-23 March 2013 (Figure 5.9). Here we use both inbound and outbound passes since there is no significant MLT dependence on n values, and only plot PADs with α_eq>80 °. The time of each plot is shown on the top and labeled as inbound or outbound pass in the top left corner.

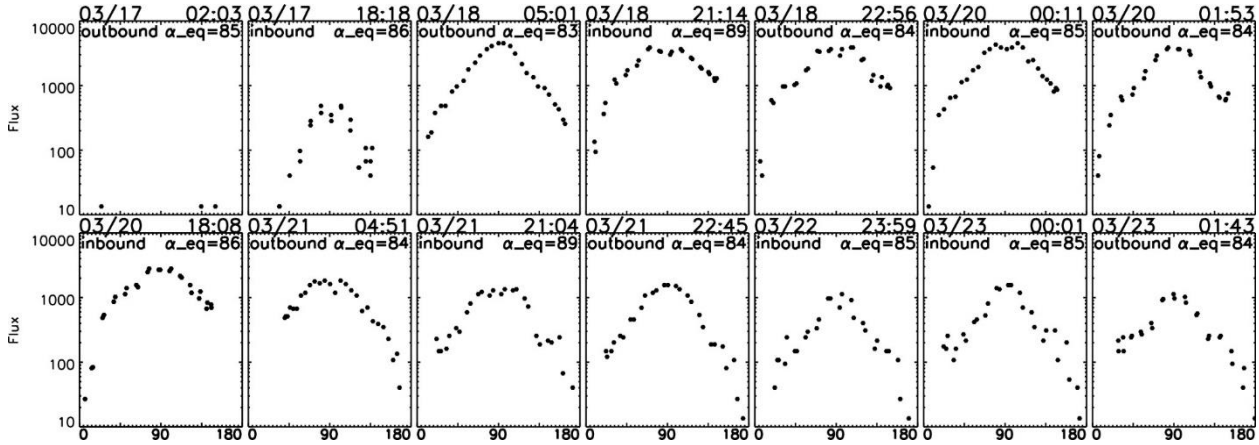

Figure 5.9: Pitch angle distributions of ~460 keV electrons at L=2.7 during 17–23 March 2013, with corresponding equatorial pitch angle of locally mirroring electrons (α_eq) greater than 80 °. Inbound/outbound pass is indicated in the top left corner of each panel. Only data from Van Allen Probe-A are used in this figure.

As Figure 5.9 shows, on 17 March, electron flux began to increase in the slot region, while the flux of electrons with PA~90 °increased first, forming a highly 90 °peaked PAD. This is a general feature in the slot region during injections. One possible reason that the flux of electrons with PA~90 °enhances first is the inward radial diffusion. As an electron diffuses inward, to conserve the first adiabatic invariant, the perpendicular momentum increases, and the PA of the electron becomes closer to 90 °; thus, a more 90 °peaked PAD forms. As the injection went on, the fluxes of electrons with lower PAs also increased and the n value became smaller. During the flux decay time, the fluxes of electrons with low PAs decreased faster than that of high PAs, which results in high n PADs again.

At the end of the time period shown here, the cap PAD appeared. Since it appeared along with the flux decaying, it was very likely caused by wave scattering. According to the modeling

results from Lyons et al. [1972], the edge of the "cap" in a PAD of 500 keV electrons caused by pitch angle scattering of plasmaspheric whistler mode waves should appear around 80 °at L=3. This is consistent with our observations.

On the other hand, the 90 °minima in PADs also appeared during the injection shown here and gradually disappeared afterward at this L shell. We will discuss the 90 °minimum PAD in detail in the next section.

In this section, we mainly examined the 90 °peaked PADs in the low L. By fitting the normal PADs into $\sin^n \alpha$, we found that n values in the inner belt and slot region are much higher than those in the outer belt, and the n parameter is almost constant in the inner belt, while it changes considerably in the slot region during injections. By investigating an event in detail, we found that the formation of the highly 90 °peaked PAD at the beginning of the injection is likely caused by inward radial diffusion, while during the decay time, due to the hiss wave scattering, low PA electrons are scattered into the loss cone more efficiently and steep normal PADs form again. Gradually, cap PADs occur due to the hiss wave scattering. Overall, plasmaspheric hiss wave scattering is an important mechanism which can lead to the steep normal PADs and cap PADs in the slot region and inner belt, while inward radial diffusion can also create highly 90 °peaked PADs at the beginning of injection.

5.5 Ninety Degrees Minimum Pitch Angle Distributions and Corresponding Physical Processes in the Slot Region and Inner Belt

5.5.1 Observations of Electrons with Different Energies at Different L Shells during an Injection Event

In this section, we mainly focus on the 90 °minimum PADs in the low L region. To investigate the possible mechanisms leading to the formation of 90 °minimum PADs, we will start with the observations of PADs of electrons with different energies and at different L shells during a specific injection event and then investigate the possible causes in detail.

Figure 5.10 shows the PADs of ~460 keV electrons at L=3.5, 3.0, 2.5, and 2.0, respectively, during 28 June to 2 July 2013, which is a geomagnetic active time period with minimum Dst index of ~-100 nT and maximum AE index of ~1200 nT. The magnetic latitude and the corresponding equatorial pitch angle of locally mirroring electrons are shown in the top right corner of each panel. Here we use outbound passes of Van Allen Probe-A to exclude any possible dependence on MLT. Note that only the passes close enough to the magnetic equator during this time period are shown here (with α_eq at all four L shells greater than 75 °).

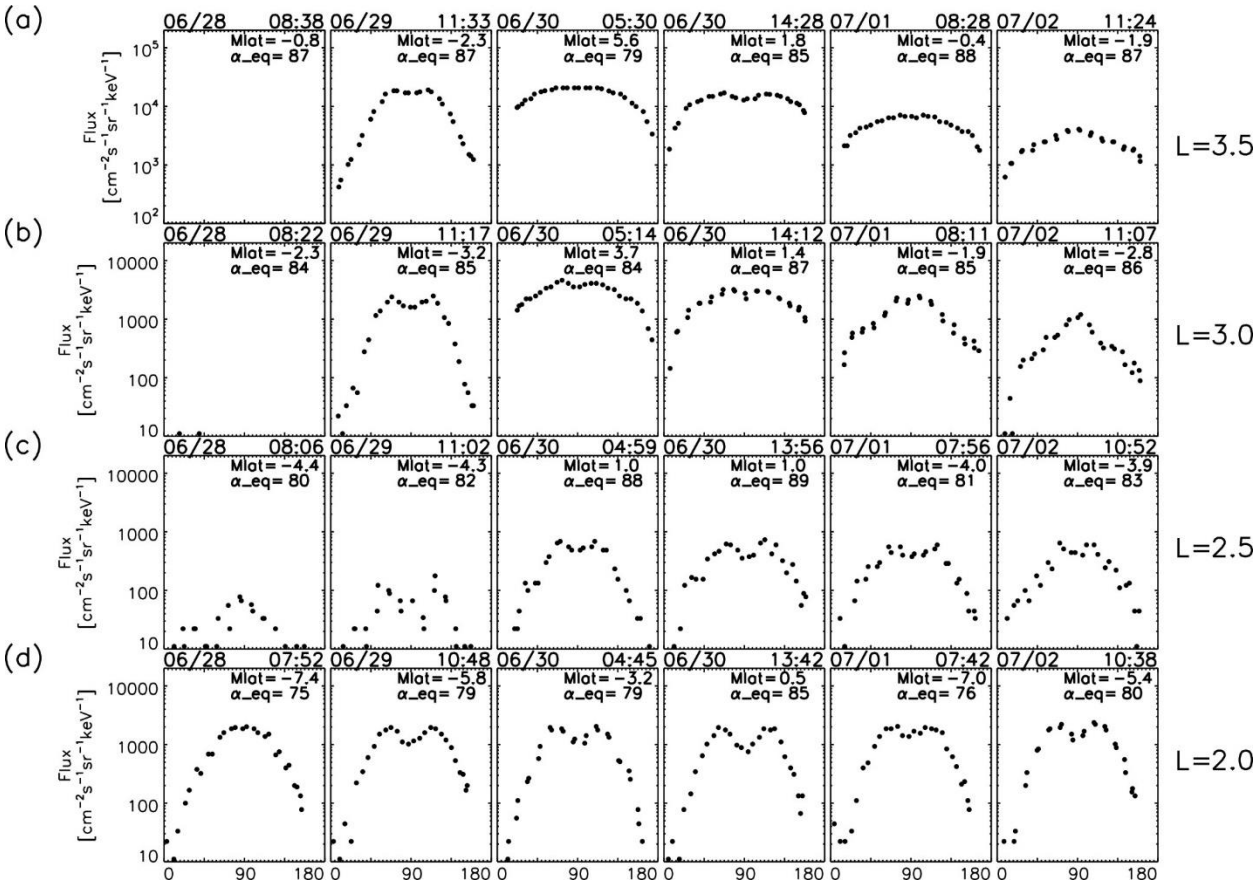

Figure 5.10: (a–d) Pitch angle distributions of 464 keV electrons at L = 3.5, 3.0, 2.5, and 2.0, respectively, during 28 June to 2 July 2013. The corresponding magnetic latitude (Mlat) and equatorial pitch angle of locally mirroring electrons (α_eq) are also shown in the top right corner of each panel. Only data from outbound passes of Van Allen Probe-A when it is close to the magnetic equator (with α_eq at four L shells greater than 75 °) are used in these plots.

It is clear from Figure 5.10 that on 29 June, electron fluxes were enhanced significantly at L=2.5 and above, while the flux at L=2 almost did not change. Along with the flux enhancement, the minima at 90 °PA appeared at all four L shells shown here. Afterward, the electron fluxes began to decay at L=3 and 3.5, while at L=2.0 and 2.5 the flux level did not change significantly during this time period. At L=3.5, the 90 °minimum PAD disappeared around 1 July 2013, while at L=3.0 we can still see a hint of 90 °minimum at this time and then the cap PAD appeared, indicating that the plasmaspheric hiss scattering was taking effect. At L=2.5 and 2.0, the 90 ° minimum PAD developed on 29 June persisted during this time period. The differences in the disappearance rates of minima at 90 °at different L shells indicate the presence of plasmaspheric hiss wave scattering, since according to the modeling results from Lyons et al. [1972], inside the plasmasphere the pitch angle diffusion coefficient of 500 keV electrons due to the hiss wave scattering is smaller at lower L shells. Also note that at the beginning of injection, the flux peaks at different L shells occurred at similar pitch angles. During the decay period, the flux peaks at L=3 and 3.5 moved to higher PAs gradually, which is also expected from the pitch angle scattering, while the flux peaks at L=2.5 and 2.0 almost did not change during this time period.

PADs of electrons with different energies are also investigated. PADs of 231 keV, 464 keV, and 593 keV electrons at L=3.0 are shown in Figure 5.11, and the time of each panel is the same with that of Figure 5.10 (b). It can be seen that the 90 °minimum PADs appeared at all three energy channels at the beginning of the injection, and the PA of the flux peak of each energy channel is about the same. As the electron fluxes decayed, the minima at 90 °gradually disappeared, while at higher-energy channels, minima at 90 °disappeared faster, indicating a more efficient pitch angle scattering. This is also consistent with the theoretical results from Lyons et al. [1972] that the pitch angle diffusion coefficient due to the hiss wave scattering of 500 keV electrons is higher than that of 200 keV electrons at L=3. Though we did not show here, this is true for L~2.5-3.5 also. Above L~3.5, the difference is too small, and between L~2 and 2.5, the flux of 593 keV electrons is too low to show valid PAD patterns.

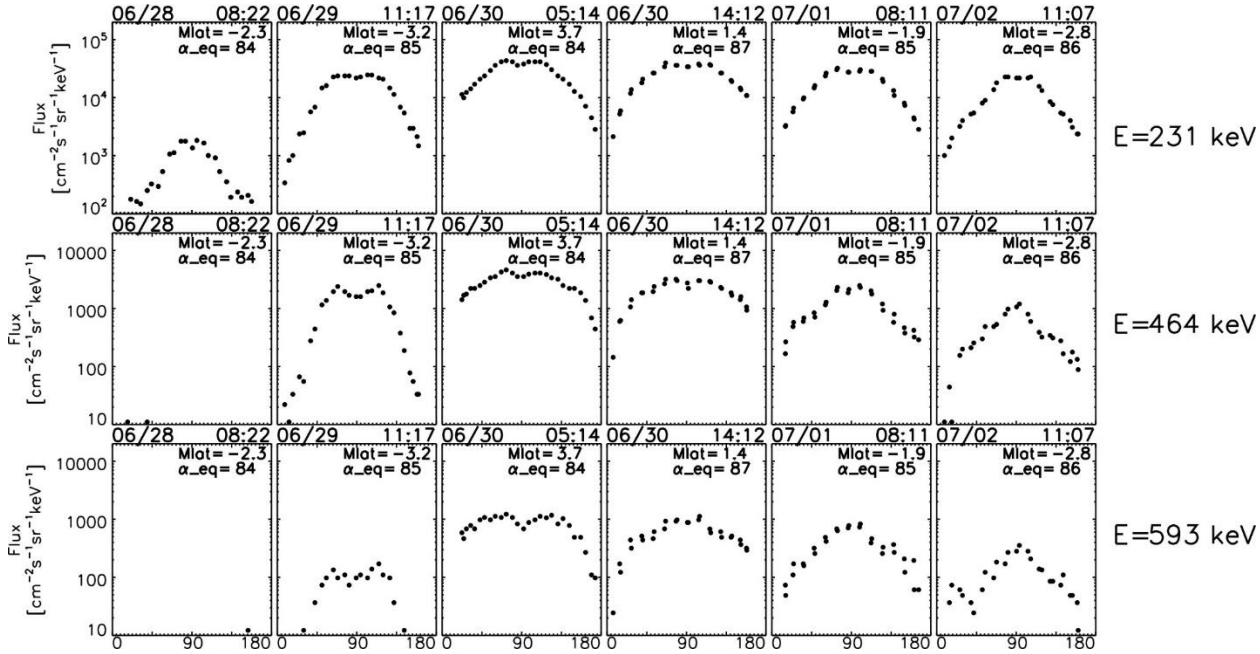

Figure 5.11: Pitch angle distributions of electrons of (top) 231 keV, (middle) 464 keV, and (bottom) 593 keV, respectively at L=3.0 during 28 June to 2 July 2013. The time of each panel is the same with Figure 5.10 (b).

From Figures 5.10 and 5.11 it is evident that the 90 °minimum PAD of hundreds of keV electrons exists in the inner belt and the slot region during the injection. Such kind of PAD appears at the beginning of the injection, while the flux peaks form at similar PAs at different L shells and for electrons with different energies. After the formation, this PAD pattern gradually disappears in the slot region and disappears faster at higher L and for higher-energy electrons. Thus, we conclude that the disappearance of 90 °minima in PADs is very likely due to the plasmaspheric hiss wave scattering inside the plasmasphere. In the next subsection, we will focus on the formation of the 90 °minimum PAD and discuss the possible mechanisms leading to it in the low L region.

5.5.2 Possible Mechanisms

Drift-shell-splitting/multipole-drift-shell-splitting. Figure 5.12 shows the occurrence rate of 90 °minimum PADs as a function of L shell and longitude (Figure 5.12, top) or MLT (Figure 5.12, bottom) for different levels of geomagnetic activity, represented by Dst index.

Figure 5.12 (left, middle, and right columns) shows the results during quiet (Dst > -20 nT), moderate (-50 nT < Dst < -20 nT), and intense (Dst < -50 nT) geomagnetic activity, respectively. The number of PADs, or sample size, in each bin is color coded and shown in the top right corner of each plot (the corresponding color bar is shown on the top right corner of each row). Comparing the situation under different levels of geomagnetic activity, it is clear that during quiet time, 90 °-minimum PADs exist in the inner radiation belt only; when the geomagnetic activity becomes moderate or intense, the occurrence rate of 90 °minimum PADs enhances significantly in the slot region. However, there is no significant longitudinal dependence or MLT dependence in the occurrence rate of 90 °minimum PAD. This indicates the formation of such kind of PAD is not due to the drift-shell-splitting or multipole-drift-shell-splitting effect. This is easy to understand since the drift-shell-splitting effect is expected to be very limited in the low L region, while the multipole-drift-shell-splitting effect is only significant at L close to 1 [e.g., Roederer et al., 1973].

Wave heating. Wave heating is believed to be one of the most important acceleration processes for radiation belt electrons. However, most previous studies focus on the wave heating in the outer radiation belt since most waves capable of accelerating electrons, such as chorus waves, were observed there. As for the inner belt and slot region, many studies suggest radial diffusion to be the main source for energetic electrons and very limited studies show the influence of wave heating. Here we examined detailed wave data to show the possibility of wave heating creating 90 °minimum PADs.

During active time, the plasmasphere shrinks and the plasmapause can reach very low L, sometimes as low as L=2 [e.g., Baker et al., 2004a] or even lower [e.g., O'Brien and Moldwin, 2003]. Existing outside the plasmasphere, chorus waves accelerate off-equator electrons more efficiently. Horne et al. [2005] calculated the bounce-averaged energy diffusion rate of chorus waves in different sectors and found that nightside chorus waves preferentially heat up hundreds of keV electrons with PA of 60 °-80 °. Fast magnetosonic waves could also be a potential mechanism causing 90 °minimum PAD. Magnetosonic waves exist both inside and outside the

plasmasphere, while outside the plasmasphere magnetosonic waves preferentially heat up hundreds of keV with PA of ~60 °, and inside the plasmasphere they are more efficient for electrons with even higher PAs (~80 °) [e.g., Horne et al., 2007; Ma et al., 2013; Mourenas et al., 2013].

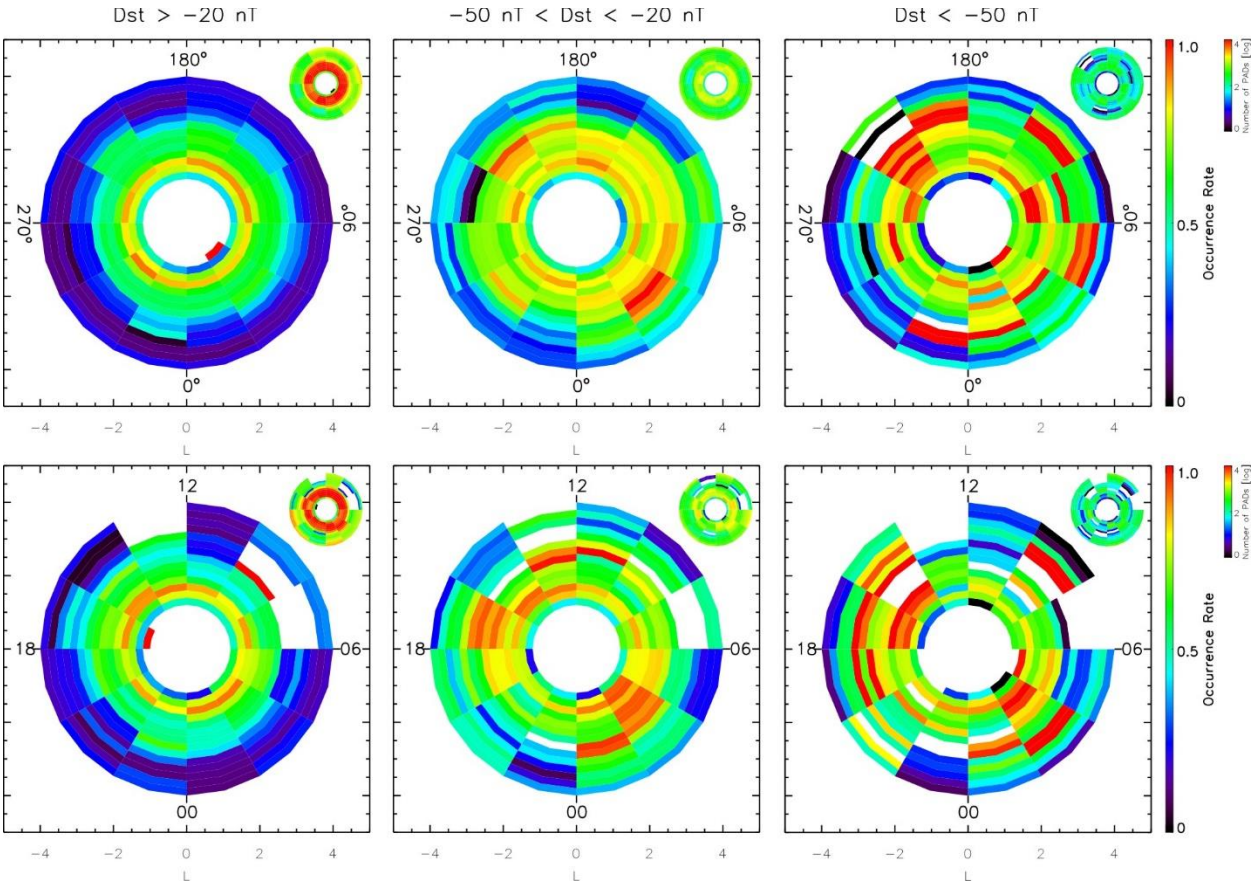

Figure 5.12: The occurrence rate of 90 °minimum PADs as a function of (top) L shell and longitude or (bottom) MLT. The number of PADs in each bin is color coded and shown on the top right corner of each plot, with the corresponding color bar showing on the top right corner of each row.

To investigate the possibility of wave heating, we examined the data from the Electric Field and Wave (EFW) instrument [Wygant et al., 2013] onboard Van Allen Probes during this injection event. During this event, chorus waves were observed by both probes. On 28 June 2013 and early 29 June 2013, which is just before the occurrence of 90 °minimum PAD, Van Allen Probe-A, locating at the midnight sector during that time, observed that chorus waves extended

to L~3. It is well known that chorus waves only exist outside the plasmasphere. During this event, the plasmapause location reached L~2.56 when judging from the sharp change in spacecraft potential along with the abrupt onset of hiss emission using data from EFW. Since mostly Van Allen Probes only crosses the plasmapause twice per 9 h, the plasmapause location could move even closer to the Earth between spacecraft passes. Thus, during this event chorus waves could have extended into even lower L region, so they are likely responsible for the formation of 90 ° minimum PADs in the slot region. Also, we calculated and plotted out the equatorial PA of the flux peak for 90 °minimum PADs of ~460 keV electrons from September 2012 to March 2014 (Figure 5.8, middle). It shows clearly that during this injection event the flux peaks in PADs formed at ~65 °-70 °. Thus, the observed PA of the flux peak is consistent with the theoretical results of nightside chorus wave heating derived by Horne et al. [2005].

However, chorus waves only exist outside the plasmasphere, and the plasmapause location can rarely reach L<2. It is still hard to explain the formation of PADs in even lower L by chorus wave heating. On the other hand, fast magnetosonic waves, which exist both inside and outside the plasmasphere, could create 90 °minimum PADs by preferentially heating up off-equator electrons in a wider L range. And after the publication of Zhao et al. [2014a, 2014b], many researchers started to explore the possibility of fast magnetosonic wave heating causing 90 ° minimum PADs in the low L region and some positive results were found. However, based on Figure 5.8 (middle), the PA of flux peak below L=2 is generally at ~70 °and sometimes even lower, which does not agree with the theoretical results derived by Horne et al. [2007] which predicts that the flux peak inside the plasmasphere caused by fast magnetosonic waves will appear at ~80 °.

Wave heating combining with inward radial diffusion. We have discussed the possibility of chorus waves creating 90 °minimum PADs and concluded that chorus waves can play an important role in the formation of such type of PADs outside the plasmapause. However, the 90 °minimum PAD generally exists in the center of the inner belt, where the plasmapause can rarely get to. Thus, we also considered the possibility of wave heating combining with inward

radial diffusion causing such type of PADs. It is possible that the 90 °minimum PADs are created by chorus waves outside the plasmapause, and then the electrons diffuse inward while the minima at 90 °in PADs is conserved.

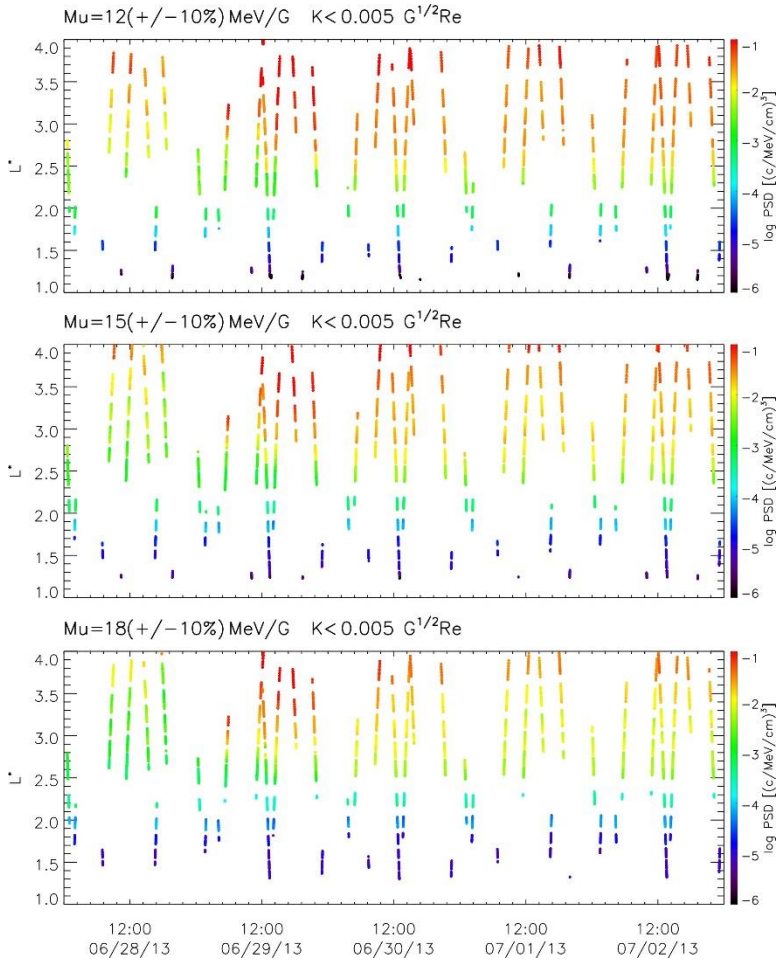

Figure 5.13: The phase space density data for electrons with μ=12, 15, and 18 ($\pm$10%) MeV/G, K<0.005 $G^{1/2}$ R_E, during 28 June to 2 July 2013, using data from MagEIS LOW and M75 units of both Van Allen Probes.

Figure 5.13 shows the phase space density data of μ=12, 15, and 18 ($\pm$10%) MeV/G, K<0.005 $G^{1/2}$ R_E equatorially trapped electrons, where electrons with μ=18 MeV/G, K<0.005 $G^{1/2}$ R_E approximately correspond to an energy of 460 keV at L^* = 2.0. The phase space densities are calculated using flux data from the LOW and M75 units of MagEIS on both Probes. Figure 5.13 shows that the radial gradient in phase space density is always positive during this injection

event, which indicates the presence of inward radial diffusion. It is well accepted that inward radial diffusion preferably energizes electrons with larger pitch angles. In this situation, if the 90 ° minimum PAD is created at larger L and then the electrons diffuse inward, we would expect the flux peak moves toward 90 °as the electrons move to lower L. However, as Figures 5.8 (middle) and 5.11 show, during the injection the flux peak appeared at similar PAs at different L and for electrons with different energies, almost occurring at the same time (within the time resolution of the spacecraft traversing the region). These facts indicate that inward diffusion is present during injections but does not play a significant role in causing 90 °minimum PADs in the inner belt.

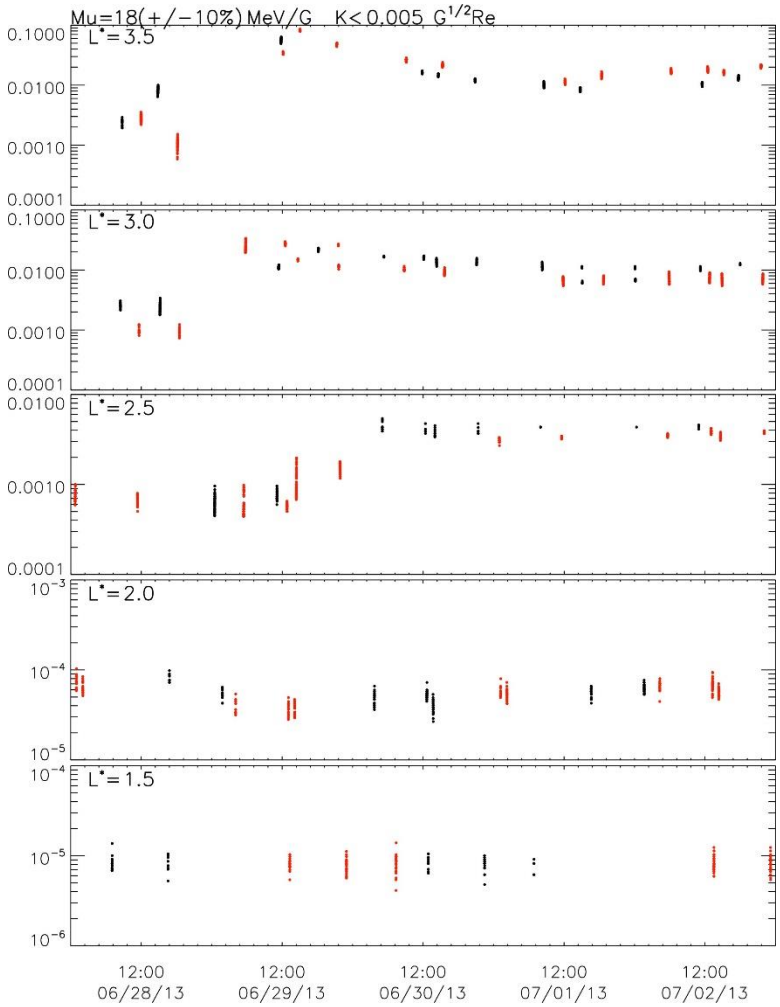

Figure 5.14: Phase space density data of electrons with μ=18 MeV/G and K<0.005 $G^{1/2}$ R_E at L^*=3.5, 3.0, 2.5, 2.0, and 1.5 (±0.05), respectively, during 28 June to 2 July 2013. Red dots are the data from Van Allen Probe-A, while black points are the data from Van Allen Probe-B.

Nonlinear bounce resonance with fast magnetosonic waves. Another mechanism that can effectively reduce the equatorially mirroring electrons is the nonlinear bounce resonances with fast magnetosonic waves. Chen et al. [2015], using a test particle simulation, showed that the nonlinear bounce resonances between equatorially mirroring electrons and fast magnetosonic waves can effectively reduce the equatorial pitch angles of electrons and thus reduce the fluxes of equatorially mirroring electrons. They suggested that this bounce resonant interaction might be the cause of 90 °minimum PADs we observed. Figure 5.14 shows the detailed phase space density data of electrons with μ=18 MeV/G and K<0.005 $G^{1/2}$ R_E at L^*=3.5, 3.0, 2.5, 2.0, and 1.5 (±0.05), respectively. It is clear that the phase space density increased at larger L shells first then gradually increased at lower L, which shows the presence of inward radial diffusion. However, note that the phase space density at L^*=2.0 decreased first as shown in Figure 5.14, and we can also find in Figure 5.10 (d) that the flux of locally mirroring electrons at L=2 decreased during this injection event, which is actually responsible for the formation of minimum at 90 °. This can hardly be explained by wave heating or radial diffusion. Though whistler mode wave scattering can scatter electrons close to 90 °at this L shell, it can only smooth the PAD without creating a minimum at 90 °[e.g., Abel and Thorne, 1998]. The nonlinear bounce resonance suggested by Chen et al. [2015] may be able to explain the decrease of flux and phase space density of near-equatorially mirroring electrons. However, according to the results presented by Chen et al. [2015], the nonlinear bounce resonance can only alter the equatorially mirroring electrons' pitch angles by up to ~10 °, and the original simulation they performed only focused on L>5 so the effect of this nonlinear bounce resonance on the inner belt electrons is still not clear. Thus, the formation of 90 °minimum PAD in the inner belt still can hardly be explained by the mechanisms discussed here.

To summarize so far, in this section we showed the 90 °minimum PADs of electrons with different energies and at different L shells during an injection event, and then we discussed about the possible mechanisms which could be responsible causing such type of PADs. From Figure 5.12, we know that there is no longitude or MLT dependence of occurrence rate of 90 °minimum

PADs; thus, we can rule out the possibility of drift-shell-splitting or multipole-drift-shell-splitting effect. Wave heating by chorus waves or fast magnetosonic waves is still the most likely explanation for the formation of 90 °minimum PADs, while the nonlinear bounce resonance with fast magnetosonic waves is also possibly able to create 90 °minimum PADs. The inward radial diffusion is present during the injection but does not play an important role in the formation of such type of PADs in the inner belt. Though chorus wave heating works well for the formation of 90 °minimum PADs in the slot region, the formation of 90 °minimum PADs at L^*~2 and lower is still a mystery and cannot be well explained by any known mechanisms examined here.

5.6 Discussion

In this chapter, we examined the PADs in the slot region and inner belt using data from MagEIS onboard Van Allen Probes. The high-quality data from Van Allen Probes give us an unprecedented opportunity to investigate the detailed PADs in the low L region. Using these data, we reported the existence of 90 °minimum PADs in the slot region and inner belt which is contradictory with predictions from existing theories. Further, we categorized the PADs below L=4 into three types: normal, cap, and 90 °minimum. Based on our categorization, during September 2012 to March 2014, about 98% of equatorial PADs (α_eq > 80 °) of ~460 keV electrons between L=1.5 and 3 can be classified into one of these three types, provided the total square root of counts (summed over all pitch angles) is greater than 50. We also found, between L=1.5 and 3, 61% of equatorial PADs are categorized as 90 °minimum PADs, 36% of them are normal PADs, and 1% of them are cap PADs. While in the whole region below L=4, about 32% of equatorial PADs are categorized into the normal PAD, 2% of them are cap PADs, 49% of them are 90 °minimum PADs, and 17% of them are undefined. These values show that the 90 ° minimum PAD is the most prevalent PAD type which is generally present in the low L region.

Previously, a few studies also investigated the PADs in the low L region. Lyons and Williams [1975b] studied 35-560 keV electron PADs throughout the slot region and outer belt

during some storm and post-storm time and found that the PADs are subject to the influence from storm injections. For 240-560 keV electrons, they found that normal PADs form during injections, while the PADs with the bumps surrounding 90 °(cap PADs) gradually appear during the post-storm time. This is consistent with our observations between L~2.5 and 3.5, though we also identified the appearance of highly 90 °peaked PADs at the beginning of injections, which are likely caused by enhanced inward radial diffusion. Lyons and Williams [1975b] also observed that 90 °minimum PADs occasionally occur and disappear in the slot region with time scales from 8 to 24 h. However, we found this could be because they did not take magnetic latitude into consideration. Figure 5.7 (top) shows in the equatorial region the 90 °minimum PADs almost always form during injections and afterward gradually disappear due to pitch angle scattering, while Figure 5.10 shows for ~460 keV electrons, minima at 90 °disappear in about 2 days at L=3 and 3.5 and persist even longer at lower L shells.

Also, Horne et al. [2003] and Gannon et al. [2007] reported on the hundreds of keV electron PADs in the slot region. Using CRRES data, Gannon et al. [2007] found that between L=2 and 3, the PADs of 510 keV electrons are mostly 90 °peaked. However, this could be because they identified the 90 °peaked PADs as distributions where the flux of 90 °PA electrons is higher than that of 45 °PA. Based on this criterion, 90 °minimum PADs we observed in the slot region and inner belt cannot be identified because the bite out around 90 °is small in pitch angle extent. Also, by using CRRES data, Horne et al. [2003] found the distributions at L~2 are rounded and dominated by Coulomb collisions. This could also be due to high magnetic latitudes since CRRES was operating in an orbit with inclination of 18 °and was away from the magnetic equator more often than Van Allen Probes.

Some previous studies also identified butterfly PADs in the outer radiation belt or the slot region, which have minima at 90 °PA, but the flux peaks in the PADs are at much lower PA (~45 ° or even lower). Several possible mechanisms were also suggested in those studies. Adiabatic effect (or ring current effect) is one of the suggested mechanism which can cause the development of minima at 90 °PA in electron PADs in the outer radiation belt [Lyons, 1977;

Ebihara et al., 2008]. As a geomagnetic storm develops, the ring current builds up and decreases the geomagnetic field magnitude significantly near the equator in the outer belt. As a result of conservation of the first two adiabatic invariants of electrons and the decrease in the electron flux with increasing energy, minima at 90 °PA in electron PADs develop in the outer radiation belt near the equator. However, the ring current effect is not significant enough in the slot region and inner radiation belt to cause 90 °minimum PAD, since the magnetic field strength in the low L region does not change much during geomagnetic storms. For example, comparing the magnitude of magnetic field at the time of first two columns in Figure 5.10, using T89 model, we found that the magnetic field strength changed only 3% at L=2, 1% at L=2.5, and <1% at L=3 near the magnetic equator. Such a subtle difference in magnetic field magnitude is not able to produce minima at 90 °PA through adiabatic effect. Another proposed mechanism is the recirculation process, which was initially identified as a possible mechanism for the energetic particles in the Jovian outer magnetosphere [Nishida, 1976] and then was used to explain the butterfly pitch angle distributions in the Earth's outer radiation belt [Baker et al., 1989; Fujimoto and Nishida, 1990]. The recirculation process assumes that there exists an energy-conserving cross-L outward transport of energetic electrons at low L region near the mirror point combining with the conventional inward radial diffusion and pitch angle diffusion, and thus, the energetic electrons can get energized by going through this process repeatedly. The cross-L transport near the mirror point results in butterfly distributions. However, since the cross-L transport occurs at low altitude near the mirror point, the resulting PAD should have peaks at very small PAs. For example, Fujimoto and Nishida [1990] simulated the recirculation process and found it can cause the butterfly distributions which have flux peaks at ~10 °-20 °PA at L=6.6. But the 90 °minimum PADs found in the slot region and inner belt show flux peaks at ~70 °or even higher. Also, it is hard to explain the 90 °minimum PAD formation in the very low L by the recirculation process. Thus, the recirculation process is not likely to be associated with the 90 °minimum PAD in the slot region and inner belt. On the other hand, Morioka et al. [2001] reported butterfly pitch angle distribution of MeV electrons in the inner belt and slot region using observations of Akebono

and proposed a possible mechanism of UHR mode waves. However, their observation showed there is no significant 90 °minimum in the PAD of 0.3-0.95 MeV electrons. This could be due to the limitation of the instrument, or the high magnetic latitude since Akebono was operating in a high-inclination orbit and was mostly away from the magnetic equator.

5.7 Conclusion

In this chapter, using data from MagEIS onboard Van Allen Probes, we reported a peculiar type of electron PADs, the 90 °minimum PADs, in the low L region, which is a persistent feature in the inner belt and appears in the slot region during geomagnetic active times. Further, we investigated the PADs of hundreds of keV electrons in the region of L<4, categorized them into different types, and examined the possible physical processes responsible for the formation of different types of PADs. The main conclusions are as follows:

1. Equatorial electron PADs in the slot region and inner belt can be divided into three types: normal, cap, and 90 °minimum PAD. For ~460 keV electrons, 90 °minimum PADs dominate at L~1.4-1.8, while normal PADs dominate at L~3.5-4; in between, 90 °minimum PADs dominate during injections, while afterward minima at 90 °in PADs gradually disappear and normal PADs become dominant. Cap PADs generally appear at L=2.5-3.5 during the flux decay period following an injection.

2. Based on the equatorial PADs of ~460 keV electrons during September 2012 to March 2014, between L=1.5 and 3, 98% of PADs can be categorized as one of these three PAD types. While 61% of PADs are categorized as 90 °minimum PADs, 36% of them are normal PADs and 1% of them are cap PADs, which shows the 90 °minimum PAD is the most prevalent PAD type in the low L region.

3. Fitting the normal PADs into $\sin^n \alpha$ form based on Vampola's equation, we found that below L=3 the n parameter is much higher than that of the outer belt. The n parameter is almost constant in the inner belt; but in the slot region, it is generally higher at the beginning of

injections and during the decay period, which is likely due to inward radial diffusion and plasmaspheric hiss wave scattering, respectively.

4. The 90 °minima in PADs of hundreds of keV electrons are a persistent feature in the inner radiation belt and appear in the slot region during geomagnetic disturbed times. By performing a detailed case study, we showed that 90 °minimum PADs of hundreds of keV electrons occur in the slot region during injections and gradually disappear afterward, while the flux peak forms at similar PAs for electrons with different energies. While the disappearance of 90 °minimum PADs can be attributed to pitch angle scattering caused by hiss waves, the formation of this type of PAD in the slot region is likely caused by the chorus/fast magnetosonic wave heating. However, the mechanisms examined in this study can hardly explain the formation of 90 °minimum PADs in the center of inner belt.

Once again, the clean measurements of hundreds of keV electrons from MagEIS onboard Van Allen Probes enabled us for a detailed characterization of the PADs of hundreds of keV in the inner part of the outer belt, the slot region, and the inner belt, which is new and compelling. In addition, clean and comprehensive measurements from Van Allen Probes also provide us an unprecedented opportunity to study the energetic electrons and ions in the ring current, which is also essential to understand the inner magnetosphere dynamics. In the following chapters, some new understandings of ring current ions and electrons based on Van Allen Probes measurements will be shown and discussed.

Chapter 6

Energetic Ions in the Ring Current: The Evolution of Energy Density and Content during Geomagnetic Storms Based on Van Allen Probes Measurements

The following chapter is based on work that was published in Zhao et al. (2015a), The evolution of ring current ion energy density and energy content during geomagnetic storms based on Van Allen Probes measurements, J. Geophys. Res. Space Physics, 120, doi:10.1002/2015JA021533.

6.1 Introduction

In previous chapters, I mainly focused on the relativistic electrons in the slot region and inner radiation belt; in the following chapters, based on the comprehensive measurements from Van Allen Probes, the dynamics of energetic ions and electrons in the ring current is studied. The clean and comprehensive measurements from Van Allen Probes provide new understandings of evolution of ring current particles and shed light on the inner magnetosphere dynamics.

The ring current is a near equatorial electric current flowing toroidally around the Earth, formed by charged particle pressure gradients and drift motion. It is present during geomagnetic quiet times, and greatly enhances during geomagnetic storms, depressing the equatorial horizontal magnetic field strength at the Earth's surface. The Dst index, derived based on measurements from four magnetometers azimuthally spaced near the equator around the Earth, shows the perturbation of the horizontal component of the geomagnetic field. This index is generally used as a proxy of the ring current and an indicator of geomagnetic storms [Sugiura and Kamei, 1991].

The main carriers of the ring current are thought to be ions with energies of a few keV – 100s of keV [e.g., Frank, 1967a; Smith and Hoffman, 1973; Berko et al., 1975; Williams, 1981; Krimigis et al., 1985; Daglis et al., 1993]. During quiet times, the ring current mainly consists of protons, while during storm times, O^+ ions account for a significant portion of the ring current

and may even dominate during very intense storms [e.g., Gloeckler et al., 1985; Hamilton et al. 1988; Greenspan and Hamilton, 2002]. A number of previous studies focused on the energy spectra of the ring current during storm times. Krimigis et al. [1985] studied an intense geomagnetic storm of 4 Sep 1984 using ion data in the energy range of ~ keV to a few MeV from the Active Magnetospheric Particle Tracer Explorers Charge Composition Explorer (AMPTE/CCE) and found that the energy density of the ring current is dominated by protons with energies > ~50 keV, with a peak at ~100-300 keV for both quiet time and storm time. Williams [1980, 1981], using data from particle detectors on the Explorer 45 spacecraft and assuming that the measurements were for protons only, showed that at L~4, over ~80% of the ring current energy density is contained in protons with energies of ~20 – 300 keV during both quiet times and storm times. William's work also showed that at this L shell (L~4) the medium point of the accumulated energy density is much higher in energy (~210 keV) at quiet times than at storm times (~85 keV). Korth et al. [2000] investigated several moderate and intense geomagnetic storms using data from the CRRES satellite. In contrast to previous studies, they found that ions with lower energies (~5-28 keV) contributed significantly to the ring current energy densities during the main phases of storms.

The most invoked mechanisms that contribute to ring current enhancements include the earthward convection of plasma sheet particles due to enhanced E ×B drift, substorm injections, ionosphere outflows, and the inward motion of previously trapped particles [e.g., Lyons and Williams, 1984; Daglis et al., 1999]. Sheldon and Hamilton [1993] studied the transport of ring current ions using the standard radial diffusion model combined with charge exchange and Coulomb collision losses. Their results showed good agreement with data from AMPTE/CCE for E>30 keV ions at L>4, indicating that for ring current ions with higher energies the radial diffusion is an important mechanism causing flux enhancements. Gerrard et al. [2014] showed quiet time He ion fluxes using data from the Radiation Belt Storm Probes Ion Composition Experiment (RBSPICE) onboard the Van Allen Probes and the observations suggest inward radial diffusive motion of He ions which were previously injected into higher L shells.

Gkioulidou et al. [2014, 2015], also using data from the RBSPICE instrument, investigated the ion injections during the ring current build-ups and concluded that the small-scale ion injections could make a substantial contribution to the augmentation of the ring current.

The magnetotail plasma sheet and Earth's ionosphere are thought to be the direct sources of the ring current particles. Since the particles in the plasma sheet are thought to have both ionospheric and solar wind origins, the ultimate sources of ring current particles are therefore the solar wind and the ionosphere. However, the relative importance of these two sources is still under considerable debate. The composition information of the ring current, especially the relative abundance of O^+, is extremely important for the solution of this problem since the vast majority of O^+ in the inner magnetosphere comes from the ionosphere. Krimigis et al. [1985], using data from AMPTE/CCE, showed that during an intense geomagnetic storm the oxygen ions contribute about 27% of the ring current energy density at L~4 during the main phase of the storm. Hamilton et al. [1988] investigated a "super storm" of February 1986 with minimum Dst of ~-310 nT using 1-310 keV/e ion data from AMPTE/CCE and found that O^+ dominated (~47% of the energy density comparing to H^+ of ~36%) during the main phase of the storm while protons carried most of the ring current energy during the rest of the storm. Roeder et al. [1996] used 1-426 keV/e ion measurements from the CRRES satellite during an intense geomagnetic storm and found that ~29% of total ring current energy density at L=3-5 came from oxygen ions.

The total kinetic energy of ring current particles has been shown to be correlated with magnetic field perturbation at Earth's surface near the equator. The correlation was first expressed as a simple equation, called the Dessler-Parker-Sckopke (DPS) relation [Dessler and Parker, 1959; Sckopke, 1966]:

$$\frac{\Delta B}{B_S} = -\frac{2E}{3E_M}$$

where ΔB and B_s are the magnetic field variation near the equator and the magnetic field magnitude at Earth's surface, respectively, E_M is the total energy of Earth's dipole field outside the Earth's surface, and E is the total kinetic energy of the particles azimuthally drifting around

the Earth. This relation was proved to be valid for any steady distribution of trapped particles in Earth's magnetic field [Sckopke, 1966].

A number of prior studies have focused on the energy content of the ring current and the validation of the DPS relation. Frank [1967b], using data from OGO-3, investigated the temporal variations of the energy densities of protons and electrons with energies of 200 eV – 50 keV during two moderate geomagnetic storms. The results indicated that the total kinetic energy of protons and electrons in the ring current is sufficient to account for the depression of Earth's surface, near-equatorial, magnetic field using the DPS relation. Hamilton et al. [1988], in their study of the evolution of ring current ions during the "super storm", found that the measured energy content of ring current ions was less than the value predicted by the DPS relation by a factor of ~2. Statistical studies have also been carried out to examine the DPS relation. Greenspan and Hamilton [2000] tested the DPS relation using a set of geomagnetic storms with minimum Dst index values less than -50 nT. Strong correlation was found between the ring current energy content estimated from nightside measurements and the Dst index, while for dayside measurements the correlation was found to be relatively weak. Turner et al. [2001] investigated the energy content of the ring current during geomagnetic storms using data from the Charge and Mass Magnetospheric Ion Composition Experiment (CAMMICE) on the POLAR spacecraft and found that the ring current ions on average contribute about half of the depression of Earth's surface, near-equatorial, geomagnetic field. Also, Jorgensen et al. [1997] used the energetic neutral atom (ENA) measurements from the POLAR satellite and the DPS relation to estimate the ring current energy content, and good correlation between their results and Dst index validated the DPS relation and also suggested that the Dst index is dominated by the ring current contribution.

Previous studies on the ring current energy spectra, density and content do not agree very well, which could be due to the differences in different geomagnetic storms and could also be related to differences in measurements from different instruments. Now the comprehensive ion measurements from the Van Allen Probes spacecraft enable the study of ring current ions over a

wide energy range with high energy resolution. With two spacecraft and shorter orbital period, the Van Allen Probes provide measurements with better temporal and spatial resolution than previous missions, e.g., AMPTE/CCE. Further, while many previous studies have focused on the ring current development during intense and super geomagnetic storms [e.g., Krimigis et al., 1985; Hamilton et al., 1988; Roeder et al., 1996], fewer studies have examined the ring current evolution during small and moderate storms [e.g., Daglis, 1997]. In this study, using data from Van Allen Probes, we report the evolution of ring current ions during geomagnetic storms and specifically focus on a moderate geomagnetic storm. Ring current energy density and contributions from ions with different energies and species are investigated in detail. The contribution of ring current ions to the Dst index is also calculated using the DPS relation.

Ion data from the Helium Oxygen Proton Electron mass spectrometer (HOPE), MagEIS, and RBSPICE instruments on the Van Allen Probes spacecraft are used for this study. Both Van Allen Probes operate in elliptical orbits with inclinations of ~10 °, perigees of ~ 600 km altitude and apogees of ~5.8 R_E. The orbital period is ~ 9 h. The spacecraft spin period is ~12 s, with the spin axis pointing approximately in the solar direction [Mauk et al., 2012]. As components of the RBSP-ECT suite [Spence et al., 2013], the HOPE instrument [Funsten et al., 2013] provides measurements of fluxes of ions (H^+, O^+, and He^+) with energies of ~ 1 eV-50 keV, while MagEIS [Blake et al., 2013] provides total ion measurement (no ion composition discrimination) in the energy range of ~ 60 keV – 1 MeV. Based on previous studies, during quiet times and small geomagnetic storms, protons contribute the majority of ring current energy density [e.g., Krimigis et al., 1985; Daglis et al., 1993]. Thus in this study, we assume that MagEIS provides measurements for protons only. The error introduced by this assumption is small and will be discussed in Section 6.3.1 using ~50-300 keV proton and O^+ flux data from the RBSPICE instrument [Mitchell et al., 2013]. The spin-averaged fluxes measured by HOPE and MagEIS are used in the Section 6.2 of this study, while pitch-angle-resolved data from MagEIS are used in Section 6.3.2 to compare with the results derived using the spin-averaged data. MAGPD data

[Hanser, 2011] from the GOES-13 and -15 spacecraft are also used to investigate the contribution of ring current protons at geosynchronous orbit (Section 6.3.2).

6.2 Observations and Analysis

6.2.1 Long-term Variations of Ring Current Proton Fluxes

Figure 6.1 shows the daily averaged proton fluxes with energies of 10, 50, 100, 190 and 300 keV as a function of dipole L and time, measured by HOPE and MagEIS on the Van Allen Probe-A during Nov 2012 – Sep 2013, along with the provisional Dst and AE indices. In most sections of this chapter, the L parameter is for a dipole field, except in Section 6.3.2 where the McIlwain L is used to show the differences in results derived using different L and geomagnetic field models. All HOPE data used in this chapter have been multiplied by 3 to match the measurements from MagEIS and RBSPICE instruments. This factor of 3 is just used to match the measurements and is somewhat arbitrary since no cross-calibration has been done for these instruments.

It is clear from Figure 6.1 that during geomagnetic storms and substorms, proton fluxes exhibit great changes. Comparing fluxes of protons with different energies, the enhancement of fluxes of protons with lower energies occurred more frequently than those with higher energies: 10-50 keV proton fluxes are much more dynamic, are enhanced rapidly, and also decay rapidly, closely associated with geomagnetic activity indicated by the Dst and AE indices. The 300 keV proton fluxes only exhibit large enhancements during intense geomagnetic storms, and decay slowly afterwards. Protons with lower energies can penetrate deeper inside the magnetosphere than those with higher energies. The 10 keV protons penetrate into L<3 frequently, while the fluxes of 300 keV protons at L<3 change little. This is consistent with the results from Smith and Hoffman [1974], which showed the observations of storm time ring current protons at the dusk sector using data from Explorer 45, and the feature that lower energy protons penetrate deeper in the dusk sector is shown to be well explained by a combination of convection, gradient drift and

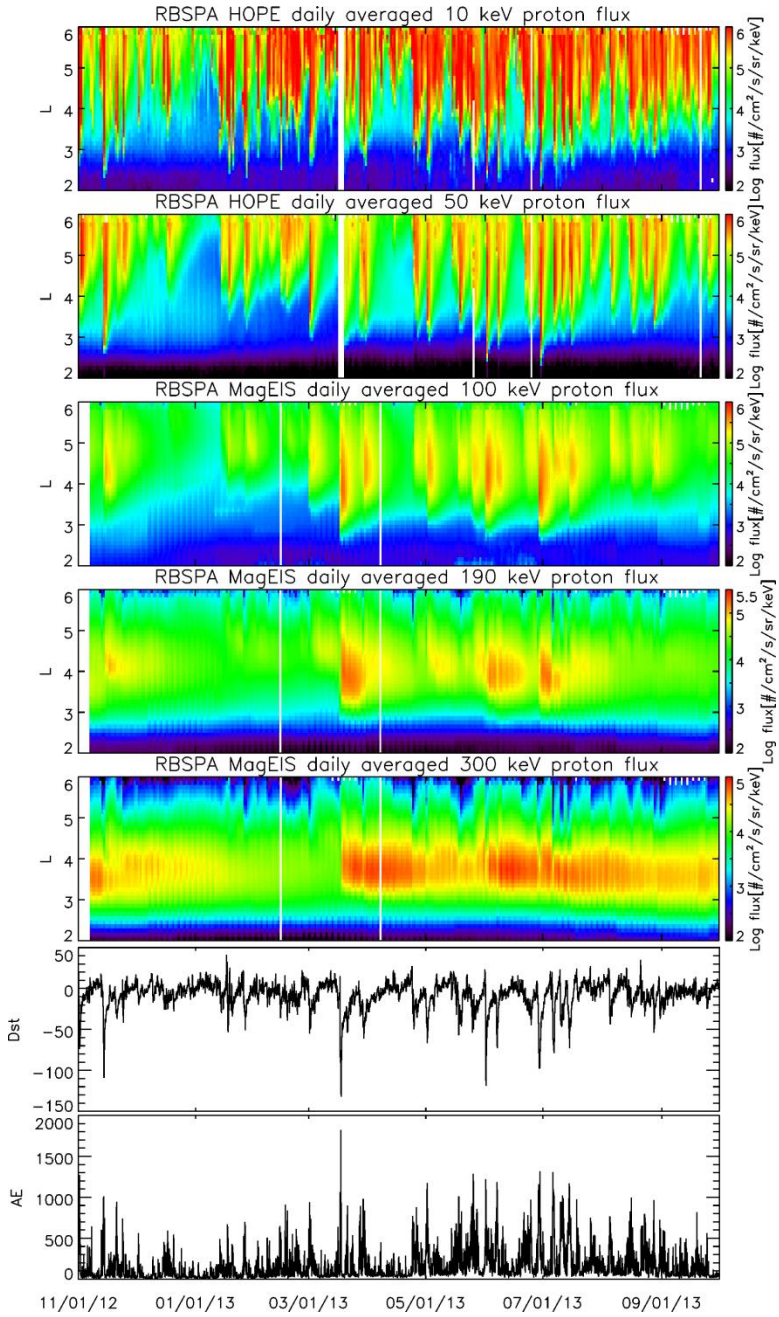

Figure 6.1: Daily averaged spin-averaged fluxes of protons with energies of 10 keV, 50 keV, 100 keV, 190 keV and 300 keV during Nov 2012 – Sep 2013, measured by HOPE and MagEIS instruments onboard Van Allen Probe – A, along with the provisional Dst and AE indices.

corotation. Also, some simulation results of previous studies on flow patterns of ring current particles showed the energy dependence of the ring current particles injection, which can well explain our observations of deeper penetrations of lower energy protons [e.g., Ejiri, 1978; Korth et al., 1999]. Some other numerical simulations using largescale convection electric field models

also showed consistent results and the important role of lower energy ions in the ring current build-up [e.g., Kozyra et al., 1998; Ebihara and Ejiri, 2000; Liemohn et al., 2001b; Jordanova et al., 2001]. On the other hand, the lower energy protons also decay much faster than those of higher energies. This is consistent with previous studies on the charge exchange lifetimes of ions with different energies [Smith and Bewtra, 1978; Smith et al., 1981], which showed that the charge exchange lifetime of protons increases with protons' energy for >~10 keV protons, though the original studies only focused on energies up to ~100 keV.

6.2.2 Evolution of Ring Current Energy Density and Energy Content during the 2013/03/29 Geomagnetic Storm

In this subsection we focus on the evolution of ring current ions during a geomagnetic storm from 26 March to 10 April 2013. During the moderate geomagnetic storm of 26 March to 10 April 2013, Dst reached its minimum value of -61 nT and AE increased to ~1000 nT (Figure 6.2). Also shown in Figure 6.2 are the spin-averaged fluxes of protons with different energies measured by HOPE and MagEIS during this time period, along with the provisional Dst and AE indices. The apogee of the Van Allen Probe-A spacecraft was near local midnight when the moderate storm with double minima in Dst occurred. Fluxes of protons with energies of 10, 50, and 100 keV were enhanced significantly during the storm. The fluxes of 300 keV protons changed little before and after the storm, while at the time of the minimum Dst the 300 keV proton fluxes decreased slightly at L~3.5-4 and significantly at higher L. To investigate the cause of the flux decrease, the proton phase space densities are calculated using T89D geomagnetic field model [Tsyganenko, 1989]. Using adiabatic coordinates, at lower L^* (~3-4) the phase space densities stayed unchanged during this time period, which indicates that flux decrease at lower L was caused by the adiabatic effect (the Dst effect) [Li et al., 1997]. This is similar with the results from Lyons and Williams [1976]. While at higher L^* (~4.5-5), the phase space densities decreased at the main phase of the storm, which indicates the presence of some real loss of protons at higher L during the main phase, though there could also be some contribution from

adiabatic effect. The real loss of protons could be due to the loss to the magnetopause or precipitation to the atmosphere. The enhancement of 10 keV proton fluxes occurred almost simultaneously with the increase in the AE index, while there is some time delay for the enhancement of proton fluxes with higher energies. A time delay of high energy proton flux enhancements is often observed during storms investigated.

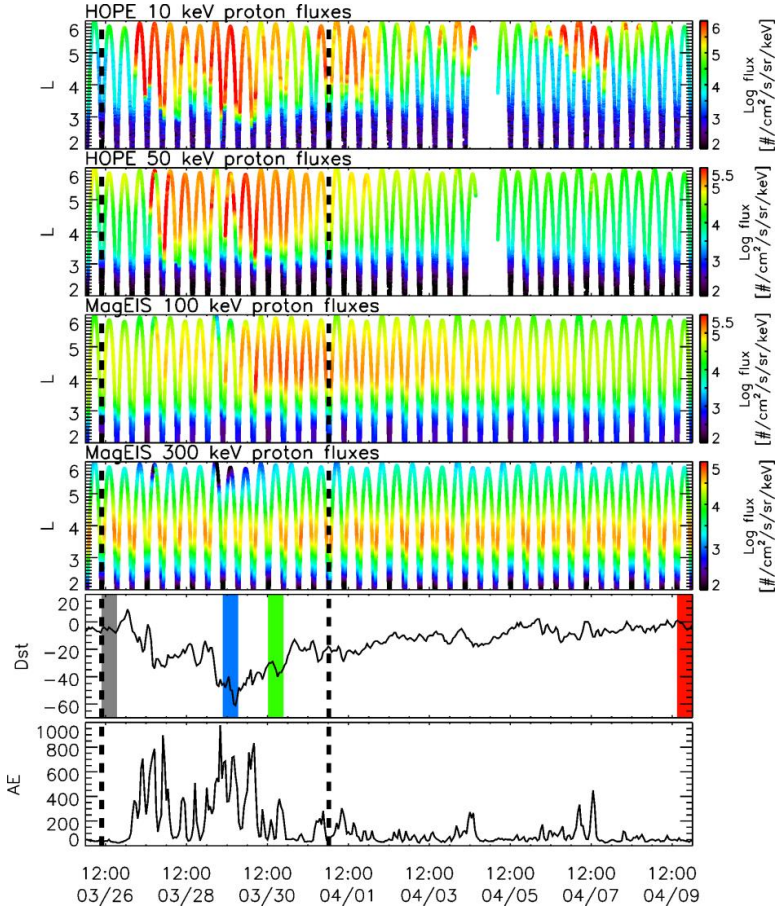

Figure 6.2: Spin-averaged fluxes of 10 keV, 50 keV, 100 keV and 300 keV protons during 26 March – 10 April 2013, measured by HOPE and MagEIS instruments onboard Van Allen Probe – A, along with the provisional Dst and AE indices. For orbits between two dashed lines, orbit-averaged energy densities are shown in Figure 6.3. Four bars shown along with the Dst index indicate four different phases of the storm: pre-storm (grey), main phase (blue), recovery phase (green) and post-storm (red), for which the ring current energy density and energy content are further investigated and shown in Figure 6.4, 6.5, and 6.6.

Using data from HOPE and MagEIS, the energy densities of H^+ with energies from ~0.2 – 1000 keV and O^+ with energies of ~0.2-50 keV are calculated. The ring current energy density

and energy content are calculated during the storm using spin-averaged flux data from HOPE and MagEIS. The total energy density ε can be determined as:

$$\varepsilon = \int Efdv^3 = 2\pi \int_0^\infty v^2 E \left(\int_0^\pi f sin\alpha d\alpha \right) dv = \pi \int_0^\infty \sqrt{2mE} \left(\int_0^\pi j(\alpha, E) sin\alpha d\alpha \right) dE$$

where m and E are the non-relativistic mass and kinetic energy of the ring current particles, f is the distribution function and $f = \frac{dN}{dx^3 dv^3} = \frac{m}{v^2} j$, where $j(\alpha, E)$ is the differential flux of particles with pitch angle α and energy E.

To simplify the calculation, we assume that the pitch angle distributions are isotropic and use spin-averaged differential fluxes $j(E)$ instead. Then

$$\varepsilon \approx 2\pi \int_{E_{min}}^{E_{max}} \sqrt{2mE} j(E) dE$$

Ideally, E_{min} and E_{max} should be 0 and infinity, respectively. However, the majority of the ring current energy density comes from ~0.2-1000 keV ions; thus we set E_{min}=0.2 keV and E_{max}=1000 keV. Since MagEIS does not provide measurements of O^+, in this section we only include O^+ with energies of ~0.2-50 keV using data from HOPE. (In Section 6.3.1 we discuss the contribution from oxygen ions and helium ions over a wider energy range using data from the HOPE and RBSPICE instruments.) The energy densities of ~0.2 – 50 keV protons and O^+ are calculated using data from HOPE, and those of ~60 – 1000 keV protons are from MagEIS. Fluxes of protons with energies between ~50 – 60 keV are extrapolated using MagEIS data and then used to calculate the energy density. The error introduced by using spin-averaged fluxes instead of pitch-angle-resolved fluxes is fairly small during the time period we focus on (see Section 6.3.2 and Appendix B).

With the energy densities, we can calculate the total ring current energy content based on the equation:

$$E_{rc} = \int \varepsilon dx^3$$

Here E_{rc} is the total energy content of the ring current. However, due to the limited MLT coverage Van Allen Probes can provide during the storm, we have to make the assumption that the energy density is constant at a fixed L shell to do the integration, which assumes that the ring current is MLT symmetric and the pitch angle distributions are isotropic. Based on these assumptions, we can calculate energy content as:

$$E = \int \varepsilon dx^3 = \sum_{L=L_{min}}^{L_{max}} \varepsilon(L)\Delta V(L)$$

and

$$V(L) = V_E[L^3\left(1-\frac{1}{L}\right)^{\frac{1}{2}}\left(\frac{1}{7L^3}+\frac{6}{35L^2}+\frac{8}{35L}+\frac{16}{35}\right)-\left(1-\frac{1}{L}\right)^{\frac{1}{2}}]$$

where $V(L)$ is the volume contained between the Earth's surface and the dipole L shell, and $\Delta V(L) = V(L+0.05) - V(L-0.05)$. Here we choose to use L_{min}=2 and L_{max}=6.

Figure 6.3 shows the detailed evolution of orbit-averaged energy densities of ring current ions for every other orbit during March 26 – April 1, the time period shown in Figure 6.2 between the two vertical black dashed lines. The energy content of the ring current ions is shown at the bottom of each panel. The orbits corresponding to the two Dst minima during the March 29 storm are identified in the figure. Before the storm, it is clear that protons with energies greater than 50 keV measured by MagEIS dominated the ring current energy densities, while the contributions of lower energy protons and O^+ measured by HOPE were orders of magnitude lower than the high energy protons. As the storm occurred, the energy densities of low energy ions were significantly enhanced, and near the two minima of Dst, ions with energies of ~0.2-50 keV dominated at L>~5. Afterwards, the energy densities of the lower energy ions decayed rapidly, and protons with energies greater than 50 keV became dominant again. The total energy content of the ring current during this moderate storm increased by a factor of ~2, and it reached its maximum around the second Dst minimum.

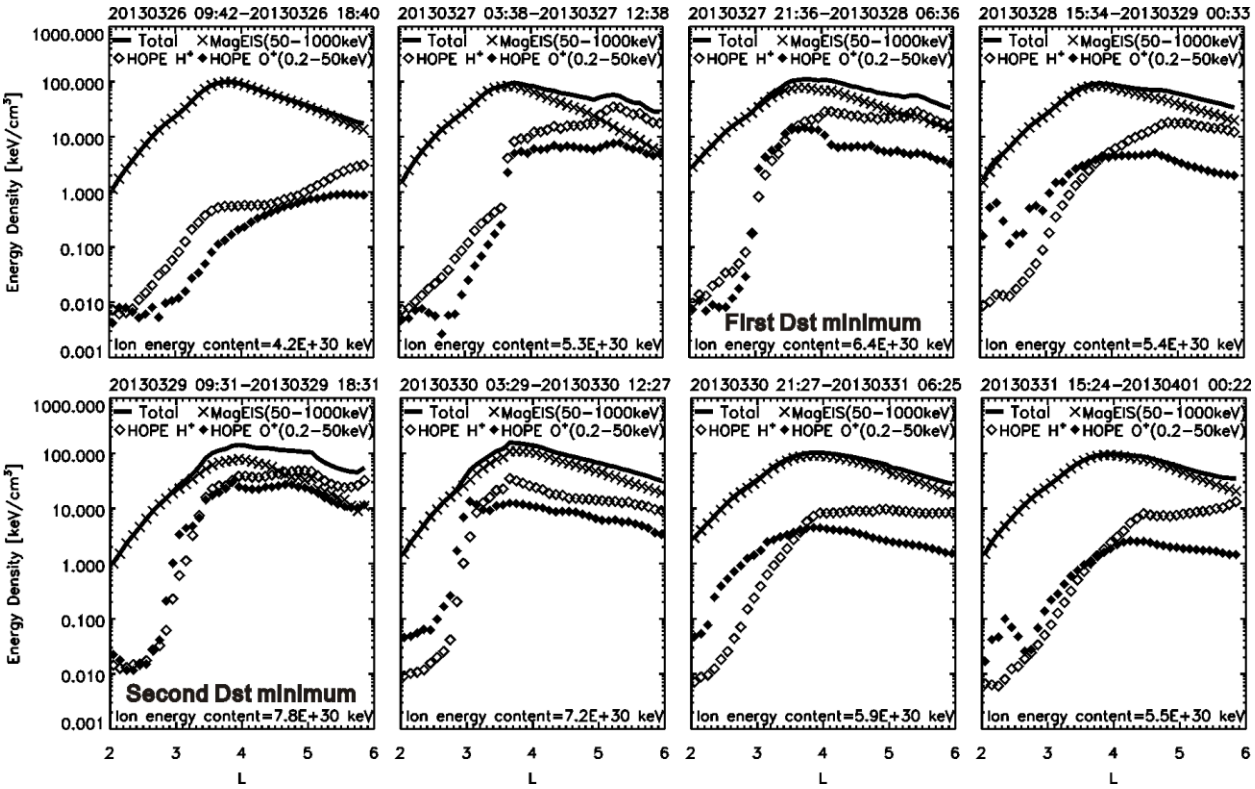

Figure 6.3: Orbit-averaged energy densities for every other orbit during 26 March – 1 April 2013. X signs show energy densities calculated using MagEIS ~50-1000 keV proton data, white diamonds show those calculated using HOPE ~0.2-50 keV proton data, black diamonds are results using HOPE ~0.2-50 keV O^+ data, and solid lines shows the total energy densities including data from both MagEIS and HOPE instruments. The ring current ion energy content is shown on the bottom of each panel. The orbits corresponding to the two Dst minima during the March 29 storm are identified in the figure.

The energy densities of ~0.2-50 keV O^+ measured by HOPE are in general much smaller than the proton energy densities. But near the second Dst minimum, the O^+ fluxes became significantly enhanced, with energy densities of O^+ at high L about a factor of 2-3 lower than the energy densities of ~0.2-50 keV protons, comparable to the energy densities of the higher energy protons measured by MagEIS. O^+ of ~0.2-50 keV contributed ~ 20% of the total ring current energy content during the orbit near the second Dst minimum. This indicates that even during this moderate storm, O+ can be an important constituent of the ring current, and therefore the ionosphere is a significant contributor of ring current particles. The results also indicate the importance of low energy O^+ (< 50 keV) to the total ring current energy density and content. Some previous studies have shown the significant contribution of O^+ to the low-energy ring

current ion energy density. Lundin et al. [1980], using data from the PROGNOZ-7 satellite, showed that for the ring current ions with E<17 keV, O^+ and He^+ dominated over H^+ during quiet times and storm recovery phases at L<4. And Krimigis et al. [1985], using data from AMPTE/CCE, showed that during an intense geomagnetic storm O^+ dominates <10 keV ring current ion energy density. While our results show that ~0.2-50 keV O^+ contribute significantly not only to the low energy portion of ring current, but also to the total ring current energy.

Since MagEIS only provides ion fluxes with no composition information, we are not able to calculate the contribution from higher energy O^+ using MagEIS data only. However, using data from RBSPICE, we found that the contribution from O^+ with energies greater than ~50 keV was only up to ~5% during the main phase of this storm (see Section 6.3.1). Daglis [1997], using measurements from CRRES satellite, showed that 50-430 keV O^+ contributed ~20% of the total energy density in the L range of 5-7 R_E during a moderate storm with a minimum Dst of -80 nT. Though the total contribution of O^+ is similar with the results in this study, we showed that the majority of O^+ contribution to the ring current energy content comes from < 50 keV O^+ while the contribution from > 50 keV O^+ is very small during the March 29 storm. The discrepancy between our study and Daglis [1997] on the contribution of > 50 keV O^+ could be due to different L range used in the calculation or different solar activities during studied storms. The moderate storm Daglis [1997] studied occurred in 1991 around the solar maximum, during which the solar activity is more intense thus the fluxes of ring current O^+ are expected to be higher than those during the March 29 storm [e.g., Yau et al., 1988].

To show the differences in ring current ion distributions during different phases of the storm, we compared the ring current energy densities and energy contents during four different phases. Data during four orbits (as shown in Figure 6.2 by the vertical bars with different colors) during this moderate storm are used to represent four different phases of the storm: pre-storm (March 26 09:42-18:40; gray), main phase (March 29 09:31-18:31; blue), recovery phase (March 30 12:27-21:27; green) and post-storm (April 9 14:53-23:51; red). Figure 6.4 shows the ring current energy content contained in a thin L shell with $\Delta L=0.1$ as a function of L at the four

storm phases, along with the plasmapause locations of inbound passes (dashed lines) and outbound passes (dotted lines). The plasmapause crossings were identified based on the Electric Field and Wave instrument data [Wygant et al., 2013] as sharp changes in the spacecraft potential. At the orbits of pre-storm and post-storm time, the plasmapause locations cannot be clearly identified and are likely to be at L shells higher than the Van Allen Probe's apogee. During quiet times, the ring current energy content is dominated by high energy protons measured by MagEIS, and the peak location of ring current energy content is generally located in the range L=3-4. During storm times, the energy content contributed by low energy protons and O^+ was significantly enhanced and became dominant during the main phase at high L shells. The peak location of the ring current energy content also moved to higher L (L=~4-5). Also, the plasmapause locations were correlated with the lower energy ion injections: as the plasmasphere shrank, the lower energy ions penetrated deeper.

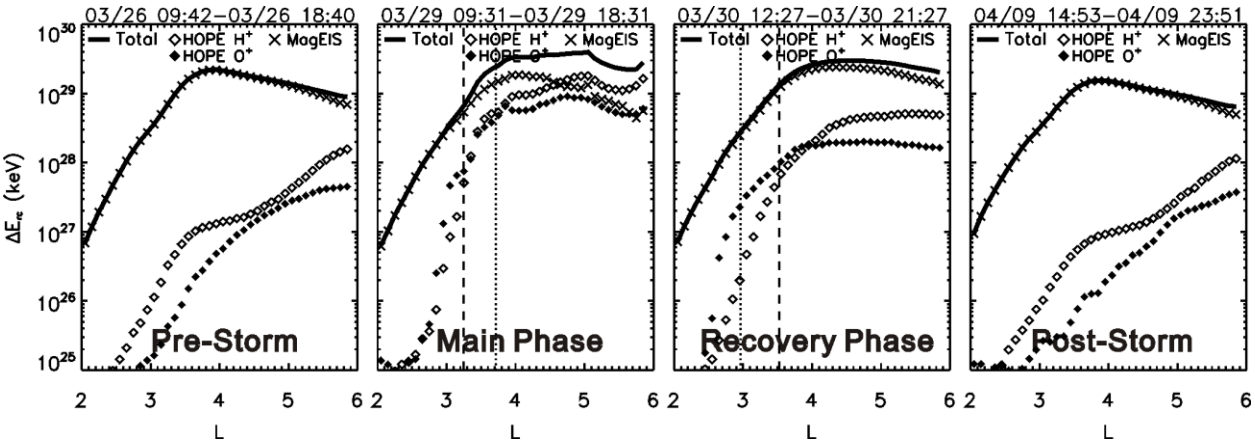

Figure 6.4: Energy content contained in a thin L shell with ΔL=0.1 as a function of L at different phases of the storm. Four different phases are indicated by the vertical bars of different colors in Figure 6.2. The dashed lines indicate the plasmapause crossings of inbound passes, and the dotted lines indicate those of outbound passes. During pre-storm and post-storm time, the plasmapause cannot be clearly identified.

Some previous studies have shown that the location of the peak of the ring current energy density is correlated with the intensity of the Dst index. During storm times the ring current energy density peak has been reported to shift earthward [e.g., Hamilton et al., 1988; Roeder et

al., 1996]. However, during the March 29 storm studied here, and focusing on the ring current energy density (Figure 6.3), it is clear that the peak location (at L~3.8) did not change substantially during the storm. The significant energy density enhancement at higher L broadened the peak and extended it to higher L during the main phase. The discrepancy between this study and previous studies could be due to the storm selection: previous studies mostly focused on very intense and super storms, while the storm in this study is a moderate one, which may not be sufficient to cause a significant increase in the ring current in the low L region. It could also be due to different energy ranges used in this study and previous studies. Many previous studies, e.g., Hamilton et al. [1988] and Roeder et al. [1996], used the measurements of ring current ions with energies generally below ~300-400 keV. However, as can be seen later from Figure 6.5 and 6.6, the protons with energies greater than a few hundred keV still contribute significantly especially at L<4. These high energy ions could be critical in determining the location of the ring current energy density peak especially during the small and moderate storms.

Since protons are the major contributor to the ring current energy density and content during the March 29 storm, we focus on the distribution of ring current protons during this time period. Figure 6.5 shows the accumulated percentage of the proton ring current energy content as a function of energy during four different phases of the storm, in which the y axis shows the ratio of energy content below energy E to the total energy content. The orbits selected to represent each phase of the storm is the same as those in Figure 6.4. At quiet times (pre-storm and post-storm phases), high energy protons dominated the ring current energy content and about 90% of the proton ring current energy content came from protons with energies greater than 100 keV. This is consistent with previous studies [e.g., Williams, 1981] and is due to the long lifetimes of high energy protons. During the main phase of the storm, the fluxes and energy densities of lower energy protons were significantly enhanced; the majority of the proton ring current came from protons with energies 10-300 keV (accounting for ~ 80% of proton ring current energy content), and protons with energies less than 50 keV accounted for ~50% of the proton ring

current energy content. Though the contribution from O^+ is not shown in Figure 6.5, including O^+ will further increase the relative contribution from ions with energies less than 50 keV (as inferred from Section 6.3.1). At the recovery phase, the contribution from lower energy protons decreased faster, and gradually the high energy protons became dominant again.

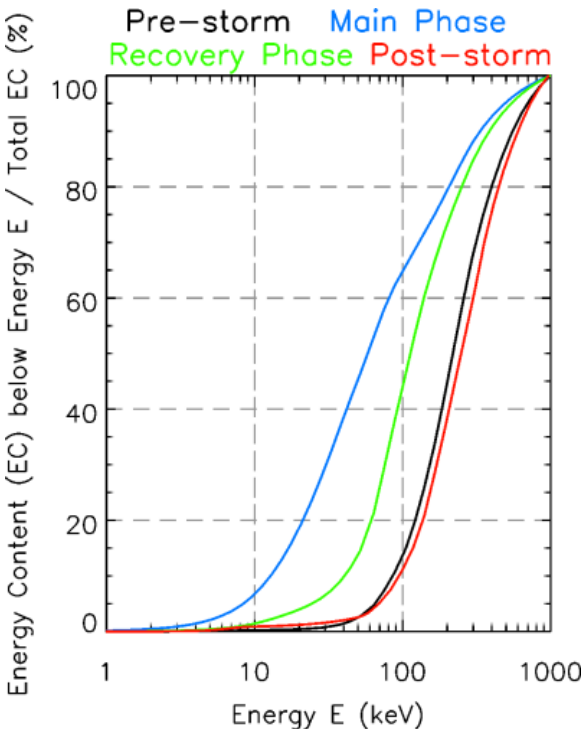

Figure 6.5: Accumulated percentage of the proton energy content versus energies during different phases of the storm. Four different phases are indicated by the vertical bars of different colors in Figure 6.2.

Though many previous studies considered protons with energies above ~50 keV as carrying most of the ring current energy [e.g., Williams, 1981; Krimigis et al., 1985], our results indicate that protons with E<~50 keV contribute significantly during the storm main phase, consistent with the results of Korth et al. [2000]. Also, if we include the contribution from O^+, <50 keV ions will actually dominate the ring current energy content at the storm main phase (as can be inferred from Figure 6.7 and Section 6.3.1). In addition, we show that the contribution from protons with energies greater than 300 keV to the ring current energy content exist all the time, with ~40% during quiet times and ~10% during storm times, which is similar with the

results from Williams [1981], though he only focused on the contribution of high energy protons to the ring current energy density at L~4.

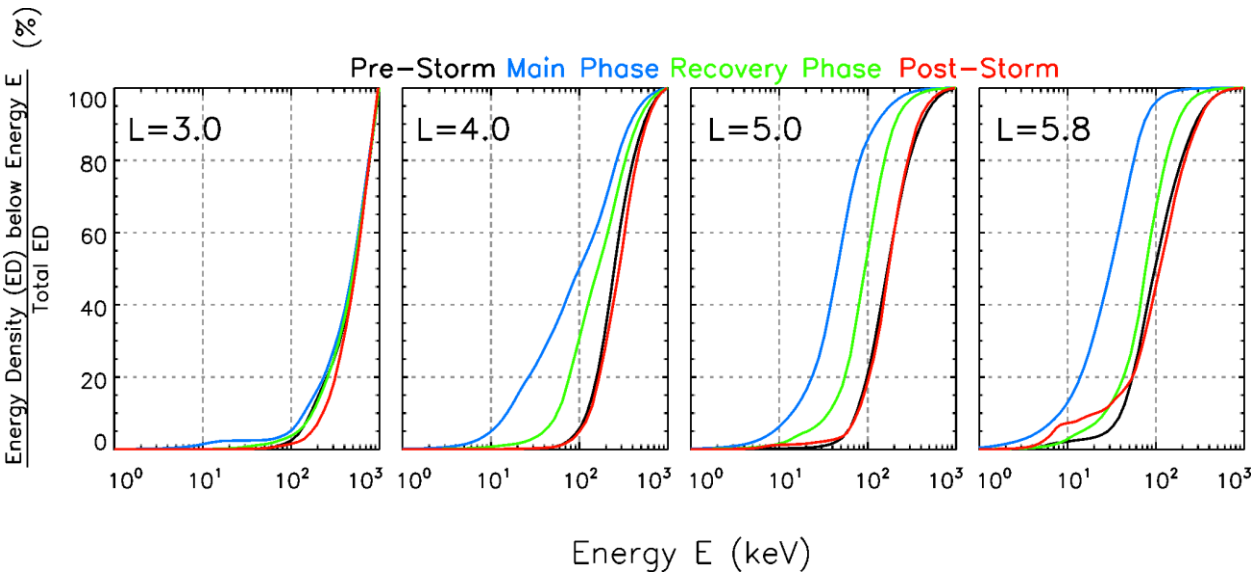

Figure 6.6: Accumulated percentage of the proton energy density as a function of energy at different L shells at different phases of the storm.

Figure 6.6 shows the accumulated percentage of proton energy density as a function of energy at L=3.0, 4.0, 5.0 and 5.8 at four different phases of the storm using proton data from HOPE and MagEIS. The Figure shows that higher energy protons generally contribute more to the energy density at lower L, while the lower energy protons account for a larger portion of the energy density at higher L, especially during storm times. At L=3.0, protons with energies greater than 100 keV almost always account for >~95% of the ring current energy density; at L=5.8, protons with energies of ~50-300 keV account for ~80% of ring current energy density during quiet times and protons with energies of ~10-50 keV dominate during storm main phase. Also, the storm has different influences on the ring current energy spectra at different L. At L=3.0, the distribution curves are similar during the different phases of the storm, except during the main phase the contribution of the ~10 keV flux is slightly enhanced compared to the quiet times. This indicates the penetration of ~10 keV protons to low L values during the storm main phase. At higher L, the distribution curves differ significantly during the different phases of the

storm. During quiet times at L=4.0, 5.0 and 5.8, protons with relatively higher energies contribute the majority of the energy densities; during the main phase, the contribution of the lower energy protons is enhanced significantly, and the ring current is dominated by protons with lower energies. After Dst reached its maximum, the contribution from lower energy protons decayed rapidly, and the portion of the contribution from higher energy protons increased and gradually returned to the pre-storm level.

6.2.3 The Relation between Ring Current Ion Energy Content and the Depression of Earth's Surface Magnetic Field (the DPS Relation)

Using the DPS relation, we calculated the depression of Earth's surface magnetic field according to the ring current total energy content measured by the Van Allen Probe – A instruments and compared it with the Dst index. Figure 6.7 shows that the calculated ΔB follows the profile of the Dst index very well. The background in ΔB caused by high energy protons measured by MagEIS is clearly shown in Figure 6.7, which is about -10 nT during this entire time period. As discussed earlier (see Figure 6.1), the fluxes of high-energy protons (>300 keV) did not change much between quiet times and moderate storms and these protons contribute to a steady ring current. The contribution of the steady ring current has been subtracted when deriving the Dst index [Temerin and Li, 2015]. So in order to directly compare to the Dst index, we need to use the depression of ΔB during this storm.

Comparing the values at the minimum Dst, the depression of ΔB predicted by the DPS relation is about -20 nT, while for the Dst index the value is about -45 nT (averaged over 9 hrs to match the Van Allen Probe's measurements). Thus the DPS relation shows that the ring current ions can account for ~45% of the Dst index. This is consistent with some previous studies [e.g., Hamilton et al., 1988; Greenspan and Hamilton, 2000; Turner et al., 2001] and is also expected since induced ground currents and other magnetospheric currents can also contribute to the Dst index.

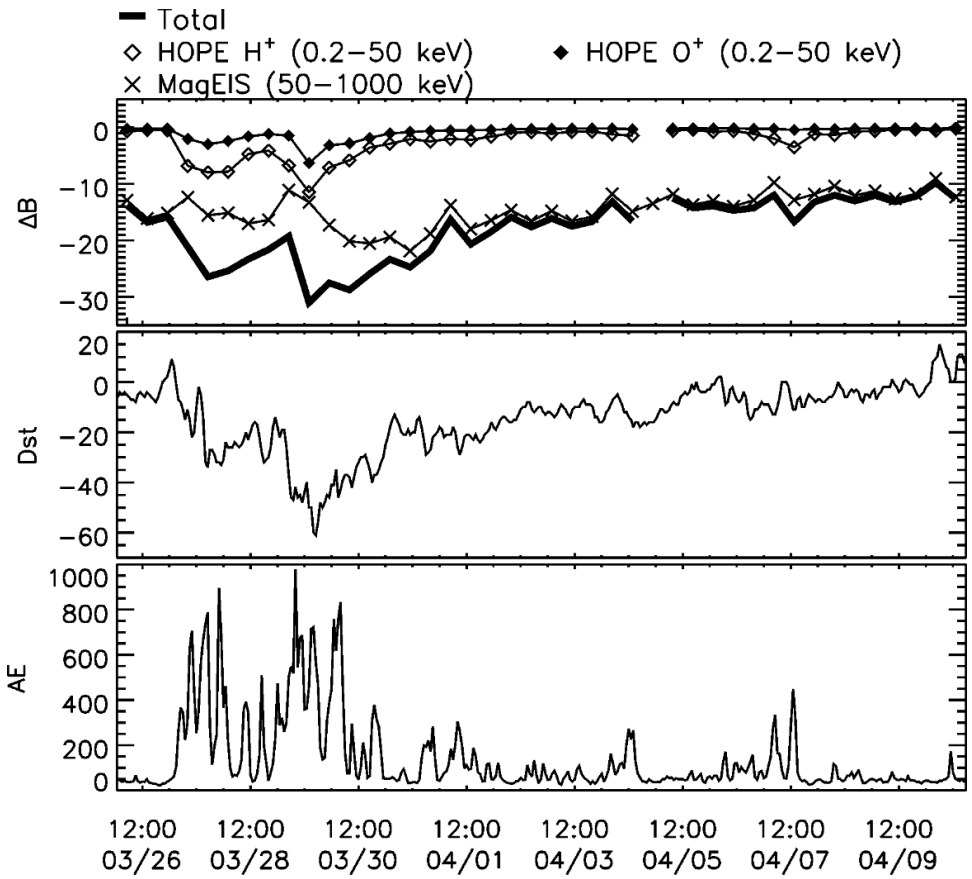

Figure 6.7: (Top) The calculated ΔB based on the DPS relation; (middle) provisional Dst index; and (bottom) provisional AE index during 29 March 2013 storm.

Dessler and Parker [1959] showed that, theoretically, a perfectly diamagnetic Earth can increase the impressed magnetic field by ~50% at the equator. Langel and Estes [1985] also showed that the induced internal magnetic field magnitude is about 24%/29% of the near-Earth external field at the dusk/dawn sector respectively. Thus to include the effect of a diamagnetic Earth, ΔB calculated using the DPS relation should be multiplied by 1.3-1.5 to compare to the measured Dst index.

The magnetotail current system could also contribute to the Dst index significantly. Turner et al. [2000] studied the contribution of the magnetotail current to the Dst index using the T89 and T96 dynamic geomagnetic field models and concluded that the contribution during moderate storms is about 25%. Tsyganenko and Sitnov [2005] also showed that the major

contributions to the Dst index are from the symmetric ring current and the near-Earth tail current, while the tail current actually dominates at the storm main phase.

Magnetopause currents would also contribute to the magnetic field perturbation at Earth's surface. Burton et al. [1975] suggested using equation $Dst^* = Dst - b\sqrt{P} + c$ to remove the contribution of magnetopause currents to the Dst index, where Dst^* is the pressure-corrected Dst index, P is the solar wind dynamic pressure, b and c are constant. During the March 29 storm the solar wind dynamic pressure was quite small and the pressure-corrected Dst index calculated using Burton et al. [1975]'s equation is very close to the Dst index, which indicates that the Dst index was not significantly influenced by magnetopause currents.

On the other hand, Liemohn [2003] showed that when using the DPS relation an implicit assumption is actually used, which assumes that all of the plasma pressure is contained within a finite region. And when this assumption is not valid, the DPS relation will overestimate the depression in the geomagnetic field due to the current introduced by the pressure truncation at the outer boundary of the integration region.

All of these factors contribute to the differences between the calculated ΔB and the Dst index. It is also worth mentioning that to match the observations from HOPE, MagEIS and RBSPICE, we multiplied all HOPE ion data by a factor of 3. This factor is suggested by Dr. Lynn Kistler based on comparative studies of HOPE, Cluster and THEMIS data (private communication with Dr. Kistler). However, if we choose to use original data from all instruments, or to divide MagEIS and RBSPICE data by a factor of 3, the calculated total energy content of ring current would be smaller.

Comparing the contributions of different energy ions, including both H^+ and O^+, to ΔB (or equivalently, the ring current energy content), the high energy ions dominated during the quiet times and storm recovery phase (the contribution from high energy O^+ is relatively small as shown in Section 6.3.1), while the low energy ions dominated at the time of minimum Dst. Also, as for the low energy protons and O^+, the contributions to ΔB grew faster and followed the elevated AE index well; however, for high energy protons measured by MagEIS, the

contribution reached its maximum at the recovery phase rather than the time of minimum Dst. This also can be seen in Figure 6.2 as the fluxes of lower energy protons increased first and those of higher energy protons enhanced later. We have examined several other moderate and intense storms (with minimum Dst of ~ -50 to -120 nT while Van Allen Probe – A was located at different MLTs) and the results are similar, indicating that this is a common feature and is independent of MLT (see Section 6.3.2 and Appendix B for more detailed discussion about the MLT dependence). Similar results have been shown in Temporin and Ebihara [2011], though they focused on the proton fluxes at specific L shells near the equator and showed that high-energy proton fluxes tend to increase on the dayside during recovery phases; and Lyons and Williams [1976] also showed similar trends of proton fluxes at several different radial distances at dusk sector. One possible explanation for the delayed enhancement of higher energy protons is inward diffusive transport by violation of the third adiabatic invariant [e.g., Schulz and Lanzerotti, 1974]. Lyons and Williams [1980] proposed that inward radial transport of the pre-existing trapped particles at higher L can produce significant flux enhancement at L<4 during storm times. Sheldon and Hamilton [1993] studied the ring current ion transport using a radial diffusion model and good agreement between model results and data from the AMPTE/CCE for E>30 keV ions at L>4 indicates that the radial diffusion is an important mechanism causing flux enhancements of ring current ions with higher energies. Chen et al. [1994] showed that diffusive transport of high-energy protons during storms with main phase longer than ~6 hrs contributes to the augmentation of the ring current. Also, Jordanova and Miyoshi [2005] simulated one geomagnetic storm and investigated the effect of convection and radial diffusion. Their results showed that the transport of ring current ions with energies of ~30 keV is dominated by convection, while for high energy ions (~80 keV) radial diffusion enhances their fluxes significantly near the minimum Dst and during the storm recovery phase. These studies showed that the inward radial diffusion can cause the enhancement of high energy proton fluxes during the recovery phases of the storms.

6.3 Discussion

6.3.1 The Contribution of Ring Current Heavy Ions

In Section 6.2.2 and 6.2.3, we examined the contribution of protons with E=~0.2-1000 keV and O^+ with E=~0.2-50 keV to the storm-time ring current using data from MagEIS and HOPE instruments, with specific emphasis on protons. In this subsection we will discuss the contributions of ring current heavy ions using data from HOPE and RBSPICE.

Since MagEIS provides ion measurements without composition information, we use spin-averaged flux data from RBSPICE for protons and O^+ with energies greater than 50 keV in this subsection. RBSPICE provides measurements of oxygen ions without differentiating different charge states, but O^+ should dominate. Figure 6.8 shows the daily averaged fluxes of protons and O^+ with energies of ~10 keV, 50 keV, 100 keV and 300 keV measured by HOPE and RBSPICE onboard Van Allen Probe-B from 15 March to 1 Oct 2013. The data show that generally the fluxes of O^+ are much lower than the proton fluxes, while the differences between the two become even larger during quiet times. For O^+ > ~50 keV this is mainly due to the much shorter charge exchange lifetimes than those for similar energy protons [e.g., Smith and Bewtra, 1978; Ebihara and Ejiri, 2003]. For tens of keV O^+, the quiet time difference could also be due to O^+ loss caused by drift-bounce resonant interaction with Pc 5 waves [Li et al., 1993]. It is also worth mentioning that the decay of ~300 keV O^+ is much faster than that of ~300 keV protons. Gerrard et al. [2014], using O^+ measurements from the RBSPICE instrument, also showed that O^+ decay very rapidly at all L shells with high-energy O^+ (>500 keV) decaying much faster than expectation, though the reason is still unclear.

The top 4 panels of Figure 6.8 show that during storm times the daily averaged fluxes of O^+ of energies of ~10 keV and ~50 keV are about 1 order less than protons with the same energies, and their differences get larger during quiet times. This is consistent with the results reported by Denton et al. [2005], which show that the ratio of ~1 eV – 45 keV O^+ to H^+ density increases as the convection enhances. In Section 6.2.2 and 6.2.3, we showed that the 0.2-50 keV

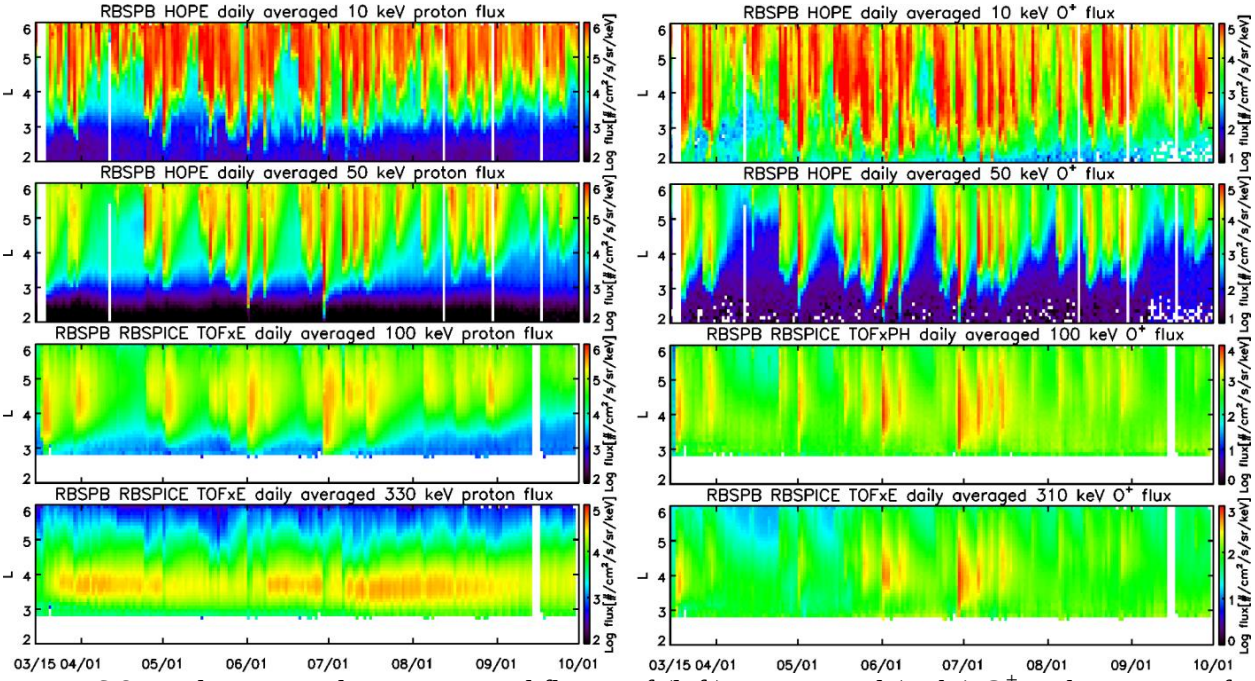

Figure 6.8: Daily averaged spin-averaged fluxes of (left) protons and (right) O^+ with energies of ~10 keV, 50 keV, 100 keV and 300 keV measured by HOPE and RBSPICE onboard Van Allen Probe-B during 15 March – 1 Oct 2013.

O^+ accounted for up to ~20% of the total ring current energy content during the March 29 storm. The bottom 4 panels of Figure 6.8 show that for ~100 keV and ~300 keV O^+, however, the daily averaged fluxes during storm times are much smaller than the proton fluxes (~ 2 orders lower) during quiet times as well as small and moderate storms. Thus O^+ with energies of ~100 keV and above would not contribute significantly to the ring current during small and moderate storms. And this is confirmed by the calculation – using data from RBSPICE, the energy content of ~100-1000 keV O^+ only account for ~1% of the total ring current energy content at the main phase of the March 29 storm. Also, using data from RBSPICE, the energy content contributed by O^+ with energies between ~50 and 100 keV is found to account for up to ~5% of the total ring current energy around the second Dst minimum of the March 29 storm. During quiet times, the contribution from O^+ with energies of ~50-100 keV is ~1%. Since RBSPICE TOFxPH data may have background issues, the contribution from 50-100 keV O^+ calculated here should be an upper limit and the actual contribution should be even smaller. Thus we conclude that the total

contribution from O^+ to the ring current is ~25% during the main phase of the March 29 storm, and the contribution of O^+ principally comes from those ions with energies < ~50 keV.

For oxygen ions with other charge states (e.g., O^{++}), though no data is available, the contribution should also be small. Fennell et al. [1996], using data from MICS on the CRRES satellite, studied the oxygen charge state abundance in the inner magnetosphere. They concluded that O^+ is the dominant oxygen ion for energy > 60 keV/Q at all times, while the fluxes of O^{++} were ~1/5 of O^+ fluxes during average conditions and were ~4/5 of O^+ fluxes during quiet times; while the fluxes of oxygen with charge > +3 were even smaller. Ebihara et al. [2009], using data from POLAR satellite, also showed that during storm times, the fluxes of $O^{>3+}$ increased at L<5 but the abundance is still much smaller than O^+ and O^{++}. Thus the contribution from oxygen ions other than O^+ is negligible.

We also determined the contribution from He^+ to the ring current energy density and content. Overall the contribution from He^+ is found to be very small. He^+ with energies of ~0.2 – 50 keV contribute ~3% of the ring current energy content during the main phase of the March 29 storm and ~1% during quiet times using HOPE data. He^+ with higher energies also contribute little to the total ring current energy, since their fluxes are much lower than protons with similar energies during storm times according to RBSPICE data.

In summary, since the contributions from He^+ and high energy O^+ are fairly small during this storm, the results derived in Section 6.2.2 and 6.2.3 are not affected by the exclusion of the heavy ion components of the ring current.

6.3.2 The Uncertainties in the Ring Current Energy Content Calculation

The ring current MLT asymmetry. In Section 6.2.2, the ring current energy content is calculated based on the assumption that the ring current energy density is constant at all MLTs. However, it is well known that the ring current is MLT asymmetric especially at the storm main phases, and the peak of ring current energy density is generally located in the dusk to pre-

midnight sector. Li et al. [2011], using data from 25 geomagnetic stations, showed that the depression of horizontal component of magnetic field is asymmetric during the storm main phases and early recovery phases. Ebihara et al. [2002], using 1-200 keV proton data from POLAR/MICS instrument, studied the statistical distribution of the storm-time proton ring current energy density as a function of L, MLT and storm phases. They showed that during storm main phases, the MLT asymmetry of the ring current energy density is strong and the energy density is significantly higher on the nightside than that on the dayside. While Lui [2003], using ~1 keV – 4 MeV ion data from AMPTE/CCE, showed that during active times ($Kp > 3^{+}$), proton pressure at L~4.5-6 is higher at dusk-midnight sector, but the asymmetry of the proton pressure is much weaker than the results from Ebihara et al. [2002]. The difference could be due to different energy ranges included in these studies, since higher energy protons are expected to be more symmetrically distributed; it could also be due to the storm phase selection: Ebihara et al. [2002] showed the significant MLT asymmetry at storm main phases and much weaker dependence at recovery phases, while the study of Lui [2003] did not specify the storm phase.

Thus the energy content in Section 6.2.2 and ΔB in Section 6.2.3 could be overestimated especially during the storm main phase. Perez et al. [2012], using TWINS ENA images, derived the global image of equatorial ion intensities for a moderate storm on July 2009. They showed that the ring current ion intensities were more asymmetric at the main phase while less asymmetric at the recovery phase, and at the main phase the peak of ion intensities located at ~23 MLT for <30 keV ions and gradually moved to ~21 MLT for >50 keV ions. If we simply use the ring current energy density distribution pattern similar to 22.5-67.5 keV ion intensity distribution shown in Perez et al. [2012] at the main phase of July 2009 storm, the ring current energy content decreases by ~30% compared to the energy content calculated using MLT symmetry assumption. Detailed results are shown in Appendix B.1. However, it is worth mentioning that for higher energy ions the energy density distribution should be more MLT symmetric, and those higher energy ions still account for a large portion of the ring current energy content, thus the influence of MLT asymmetry to the ring current energy content should be smaller.

Even if the ring current energy content were overestimated due to the assumption of ring current MLT symmetry, the conclusions would still hold that <50 keV ions dominate the ring current energy content at the storm main phase and the fluxes and energy content of higher energy ions reach their maximum at the recovery phase rather than the main phase. We examined 15 moderate to intense storms (with minimum Dst=~50 nT - ~120 nT) from Nov 2012 to Oct 2013 with the assumption that the ring current is MLT symmetric while Van Allen Probe – A was located at different MLTs during these storms. For all 15 storms, <50 keV ions dominate the ring current energy density at the storm main phases; while for 14 of 15 storms, the energy densities of >50 keV protons reach their maximum at the recovery phases. Thus these two conclusions are not affected by the assumption of the ring current symmetry.

Spin-averaged fluxes vs. pitch-angle-resolved fluxes. The assumption that the energy densities are constant at a fixed L shell also includes the assumption that the energy densities are constant along a fixed field line, which assumes the pitch angle distributions of the ring current ions are isotropic and thus spin-averaged fluxes are used in our previous calculations instead of pitch-angle-resolved fluxes. Here we investigate the uncertainties introduced by this assumption.

To simplify the calculation, we use the dipole field only and assume all pitch angle distributions can be fitted by the $\sin^n\alpha$ form. The equations used to calculate the ring current energy densities based on pitch-angle resolved data are shown in the Appendix B.2.1. As an example, pitch-angle-resolved fluxes for protons with energies of ~60-1000 keV from the MagEIS instrument are used in the calculation to compare with results derived with spin-averaged fluxes of protons with the same energy range. We derived the *n* value of each pitch angle distribution by converting it to the equatorial pitch angle distribution and then fitting it to $\sin^n \alpha$. If the pitch angle distribution is isotopic (n=0), then the results calculated using pitch-angle-resolved data should be the same with those derived using spin-averaged data.

Detailed calculations and figures are shown in Appendix B.2. The results indicate that using pitch-angle-resolved data does not change the results significantly. At the main phase of the March 29 storm, for over 90% of time the energy densities calculated using pitch-angle-

resolved data is similar to those calculated using spin-averaged data (with differences less than 20%). During the time period we focused on, the PADs tend to be more isotropic for protons with lower energies and at higher L shells. The ring current energy densities calculated using pitch-angle-resolved data at L>~5.0 are very close to those calculated using spin-averaged data, while at lower L the difference can be up to ~30%. The ring current energy content calculated using pitch-angle-resolved data are only ~10% lower than those using spin-averaged fluxes at the storm main phase. Though this result is for protons with E=~60-1000 keV only, it is expected to be valid for lower energy protons also, since their PADs are more isotropic.

The calculation discussed in this subsection has some limitations. For simplicity, we assumed that all PADs can be fitted into a $\sin^n \alpha$ form; however, at higher L shells, butterfly pitch angle distributions are occasionally observed. But as for the energy densities and energy content calculation, the existence of butterfly pitch angle distributions can somewhat compensate for pancake PADs, making the differences between the results calculated using two different sets of data even closer. Thus we conclude that the assumption that the PADs of ring current ions are isotropic would not significantly influence the ring current energy density and content calculation.

The influence of external magnetic field. In Section 6.2.2, the ring current energy content is obtained based on the calculated energy densities using a dipole field. Applying an external magnetic field may influence the results by changing the L values and the volume of L shells used in the calculation. Thus we investigated the influence of an external magnetic field using the T89 dynamic magnetic field model [Tsyganenko, 1989]. We use the McIlwain L in the T89 model in this subsection, and the volume contained within thin L shells with $\Delta L=0.1$ are calculated using the T89 model also. As noted above, during the March 29 storm, the Van Allen Probes were located in the midnight sector; the McIlwain L calculated using the T89 model in the midnight sector is generally higher than those calculated using the dipole field only (as would be expected, especially during storm times). Though Van Allen Probes can only reach a dipole L up to ~5.8, during the March 29 storm the spacecraft actually can get to McIlwain L~7 or even

higher under the T89 model. Thus we calculated the ring current energy content using T89D with an L range of 2-7 instead of 2-6 in the dipole field only case. Since the volume of L shells included in the calculation gets larger, an increase in the ring current energy content is expected. The ring current energy content calculated using T89D is ~20% higher than that calculated using the dipole field only during the main phase of the storm. Thus the difference is not large enough to change the results significantly.

The contribution of ring current ions at higher L shells. Due to the apogees of the Van Allen Probes, no data coverage on dipole L shells higher than 6 are possible. However, as Figure 6.3 shows, at the main phase of the storm it is likely that some ring current ions existed at higher physical L shells. Ignoring the contribution from those ions would make the calculated ring current energy content lower than the actual value. Thus we also checked proton measurements from the MAGPD instruments on GOES satellites [Hanser, 2011]. GOES-13 and -15 were operating in geosynchronous orbit near the geomagnetic equator (with geomagnetic latitudes of ~10 °for GOES-13 and ~5 °for GOES-15) during the March 29 storm. Fluxes of protons with energies of ~80-800 keV are provided in 5 energy channels. Comparing proton fluxes measured by MagEIS and GOES MAGPD when they located at similar MLTs (near midnight) during the March 29 storm, the fluxes measured by MAGPD are ~1-2 orders lower than the fluxes measured by MagEIS given that the difference in radial distances is ~0.8 R_E. This indicates that there is a steep radial gradient of ~80-800 keV proton fluxes existing between L=~5.8 and L=~6.6 around local midnight. Overall, therefore, the contribution from protons with energies greater than ~80 keV at higher L shells to the total ring current energy content is very small. However, protons with lower energies at higher L could still contribute to the total ring current energy content; this is an uncertainty (likely small as well) in the interpretation of the results derived in section 6.2.

6.4 Conclusion

Comprehensive ion measurements from Van Allen Probes enable us to analyze the detailed energy density and content evolution for ring current ions with different energies and species with wide energy coverage and fine energy resolution. Having examined several moderate and intense magnetic storms using data from Van Allen Probes, we present the detailed evolution of ring current energy density and energy content during a moderate geomagnetic storm. The results are similar for other storms we investigated. The major conclusions are summarized as follows:

1. During active times, the enhancement of fluxes of protons with lower energies (<50 keV) occurred much more often than those with higher energies, and protons with lower energies penetrate deeper than higher energy protons, but they also decay much faster than higher energy protons.

2. During quiet times, the ring current is dominated by protons with energies greater than 100 keV. During storm times, ions with energies less than 50 keV dominate the ring current energy content at the storm main phase, while the higher energy protons dominate during the recovery phase.

3. The enhancement of fluxes as well as energy content of higher energy protons generally occurs later than those of lower energy protons. This could be due to the fact that the high energy proton flux enhancement is more likely through inward radial diffusion, while for lower energy protons convection is more important.

4. The oxygen ions contributed up to ~25% of the total ring current energy content during the March 29 storm, indicating that the ionosphere is a significant contributor to the ring current ions even during moderate storms; the majority of O^+ contribution comes from O^+ with energies below 50 keV, suggesting the important role of low energy O^+ to the ring current.

5. Based on the DPS relation, the calculated magnetic field perturbation caused by ring current ions accounts for ~45% of the Dst index depression during the main phase of the storm.

This is consistent with previous studies [e.g., Turner et al., 2001] and is expected since the induced ground currents and other magnetospheric currents can also contribute to the surface equatorial magnetic field depression.

In this chapter, I mainly focused on the evolution of ring current ions during geomagnetic storms. In the following chapter, the role of energetic electrons in the ring current will be examined using Van Allen Probes measurements.

Chapter 7

Energetic Electrons in the Ring Current: The Evolution of Energy Density and Content during Geomagnetic Storms Based on Van Allen Probes Measurements

The following chapter is based on the paper Zhao et al. (2015b), Ring current electron dynamics during geomagnetic storms based on the Van Allen Probes measurements, to be submitted to J. Geophys. Res. Space Physics.

7.1 Introduction

The geomagnetic storm is featured as the enhancement of the ring current, a near-equatorial electric current flowing toroidally around the Earth. The enhancement of this current is responsible for worldwide depressions in the horizontal component of Earth's surface magnetic field near the magnetic equator. Such a depression in the magnetic field is indicated by the Dst index [Sugiura and Kamei, 1991], which is derived based on the measurements from four magnetometers near the equator around the Earth, and is shown to be correlated with the total kinetic energy of charged particles azimuthally drifting around the Earth.

The storm time ring current mainly consists of ions with energies of a few keV to hundreds of keV, while electrons with similar energies flowing around the Earth also contribute to the ring current and are responsible for the generation of whistler mode chorus waves, which are very important to the acceleration and loss of radiation belt electrons (~MeV). A number of previous studies have focused on the dynamics of ring current ions and their contribution to the magnetic field perturbation near the equator at the surface of the Earth [e.g., Krimigis et al., 1985; Hamilton et al., 1988]. However, limited studies have focused on the dynamics of the ring current electrons during geomagnetic storms using either satellites' observations [e.g., Frank, 1967; DeForest and McIlwain, 1971; Liu et al., 2005] or simulations [e.g., Jordanova and Miyoshi, 2005; Liu et al., 2005].

Frank [1967] investigated the temporal variations of energy densities of protons and electrons with energies of 200 eV – 50 keV during two moderate geomagnetic storms using data from OGO 3. The results indicated that the total energy of ring current protons and electrons is sufficient to account for the depression of Earth's surface magnetic field according to the DPS relation, while the contribution of electrons to the storm-time ring current energy was ~25%. DeForest and McIlwain [1971], using ~50 eV – 50 keV proton and electron measurements from the geostationary satellite ATS 5, found that during an injection of plasma the particle pressure at geosynchronous orbit was usually dominated by protons, while the contribution from electrons was also important and occasionally was even dominant (twice as the proton pressure). Liu et al. [2005] evaluated the importance of electrons in the ring current during storm times using both observations from Explorer 45 (digitalized from Lyons and Williams [1975, 1976, and 1980]) and simulation. The observations showed that at L=2.5-5, electrons with energies of ~1-50 keV contribute the most to the electron ring current energy content, and during an intense storm (minimum Dst=-171 nT) on 17 December 1971 the ring current electrons contributed ~8% of the ring current energy at this L range. However, their simulation results showed the contribution from ring current electrons can reach ~19% of the total ring current energy content during storm time. Jordanova and Miyoshi [2005] also investigated the role of ring current electrons during an intense geomagnetic storm using their global drift-loss model. They found that the electrons' contribution to the ring current energy varies from ~2% during quiet times to ~10% near the main phase of the storm. Significant discrepancy exists among those previous studies regarding the role of ring current electrons and their contribution to the total ring current buildup.

Due to the limitations of previous measurements, electron data with limited energy ranges and limited L shells have been used in previous studies of ring current electrons' energy content calculation, which could lead to significant errors. With the launch of Van Allen Probes, the study of the role of ring current electrons is enabled by the comprehensive measurements of both electrons and ions (including composition). Launched on 30 Aug 2012, the Van Allen Probes operate in elliptical orbits with an inclination of ~10 °, perigees of ~ 600 km altitude and

apogees of ~5.8 R_E, providing comprehensive particle and field measurements in the inner magnetosphere [Mauk et al., 2012]. HOPE, MagEIS and Relativistic Electron-Proton Telescope (REPT) instruments of ECT suite provide electron flux data with energy range of ~eV – tens of MeV [Baker et al., 2013; Blake et al., 2013; Funsten et al., 2013; Spence et al., 2013]; HOPE and RBSPICE instruments [Mitchell et al., 2013] on the Van Allen Probes provide data of H^+, O^+ and He^+ with energy range of ~eV – MeV, while MagEIS provides ion flux measurements with energies of ~60 keV – MeV with no composition discrimination (and in this study we assume MagEIS measures protons only). In this study, electron data from HOPE, MagEIS and REPT and ion data from HOPE, MagEIS and RBSPICE are used to investigate the role of electrons in ring current dynamics.

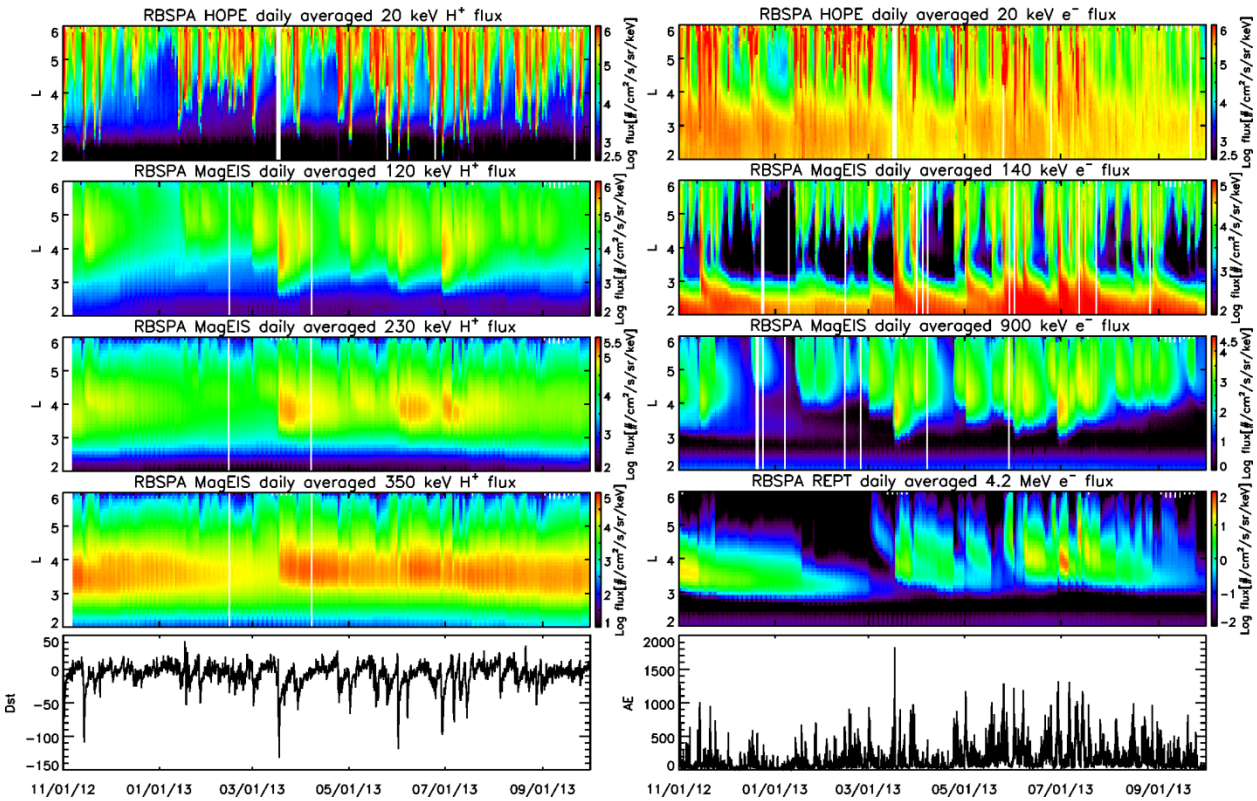

Figure 7.1: Daily averaged fluxes of (left) protons with energies of ~20, 120, 230 and 350 keV, and (right) electrons with energies of ~20, 140, 900 keV and 4.2 MeV during Nov 2012 – Oct 2013, measured by HOPE, MagEIS and REPT instruments on the Van Allen Probe – A. Provisional Dst and AE indices are also shown for this time period.

Figure 7.1 shows the daily spin-averaged fluxes of protons (left panels) and electrons (right panels) with different energies during Nov 2012 - Oct 2013, measured by HOPE, MagEIS and REPT on the Van Allen Probe – A, along with the provisional Dst and AE indices. The L shell used in this chapter is for the dipole field only. The HOPE ion data used in this study have been multiplied by a factor of 3 to match the measurements from MagEIS and RBSPICE, and the influence of this factor will be discussed in section 7.3. As for the electrons, since the background-corrected electron data from MagEIS are not always available, the data used here may contain some background contamination at low L (<2.5), which will not affect the results discussed below.

The similarities of long-term behaviors of protons and electrons are clearly shown in Figure 7.1. As the geomagnetic storms occurred, both electron and proton fluxes exhibited great changes. For both electrons and protons, the flux enhancements of lower energy particles occurred much more often than those of higher energy ones and the lower energy particles also penetrated deeper than the higher energy particles. This is consistent with some previous observations and can be explained by the drift pattern of different energy electrons and protons resulting from a combination of convection, gradient and curvature drift, and corotation [e.g., Smith and Hoffman, 1974; Ejiri, 1978; Korth et al., 1999]. In the outer radiation belt region, after the initial enhancements the lower energy particles also decayed much faster than those higher energy ones.

However, the differences in the protons' and electrons' long-term behaviors are more prominent. Tens to hundreds of keV electrons penetrated deep into the low L region frequently, and once present in the inner zone, those electrons decayed slowly, persisting for a long time. However, hundreds of keV protons rarely penetrated into the low L region. Though tens of keV protons also penetrated into L<3 frequently, they decayed comparatively fast and only existed for a short time period in the low L region. As the top four plots of Figure 7.1 show, abundant ~20 and 140 keV electrons commonly exist in the low L region, while ~20 and 120 keV proton fluxes at L<3 are low. The short lifetime of protons in the low L region could be due to the proton

charge exchange loss [e.g., Smith et al., 1981]; while for the electrons, the wave scattering due to plasmaspheric hiss waves, lightning-generated VLF waves and VLF waves from transmitters are not efficient enough to rapidly reduce the tens to hundreds of keV electron fluxes in the inner belt [e.g., Abel and Thorne, 1998]. Another major difference between proton and electron long-term behaviors is that the lifetimes of hundreds of keV protons are much longer than those with similar or even higher energy electrons in the outer belt region (L>~4). It is obvious that ~230 and ~350 keV protons only exhibited significant enhancements during intense geomagnetic storms and decayed slowly afterward; while hundreds of keV electrons decayed much faster than protons with similar energies. This could be due to the limited charge exchange loss for the high energy protons in the outer belt and efficient loss of these electrons by wave-particle interactions.

On the other hand, the intriguing similar behaviors between protons and electrons with different energies can also be seen in Figure 7.1. For example, ~900 keV electrons behaved similarly to ~120 keV protons, though the lifetime of electrons is a little bit shorter; while from Nov 2012 to March 2013, ~4.2 MeV electrons and ~350 keV protons also behaved similarly as their fluxes both decayed slowly, though their total flux levels are very different. Protons and electrons are subject to different physical processes in the inner magnetosphere, and it is still not clear what kind of underlying physical reasons are responsible for the exhibited similarities.

In this study, we will focus on the role of electrons in the ring current dynamics during geomagnetic storms based on the observations from Van Allen Probes. Two storms – one moderate storm and one intense storm – will be examined in the following section to show the dynamics of ring current electrons. Detailed calculations on the ring current electron and ion energy content and energy densities will be shown and the contribution of electrons to the ring current energy will be investigated. The magnetic local time (MLT) dependence of ring current electron distribution will also be examined through a statistical study. The discussion will be provided in section 7.3, and section 7.4 will be the conclusion.

7.2 Observations and Analysis

7.2.1 The Ring Current Evolution during the 29 March 2013 Moderate Geomagnetic Storm

The 29 March 2013 storm is a moderate storm with minimum Dst of -61 nT and AE up to ~1200 nT. During this storm, the Van Allen Probes apogee was located around local midnight. The evolution of the ring current ions during this storm has been investigated in detail in the previous chapter. Here I mainly focus on the dynamics of the ring current electrons during this moderate storm and show the contribution of electrons to the ring current energy based on the measurements from the Van Allen Probes.

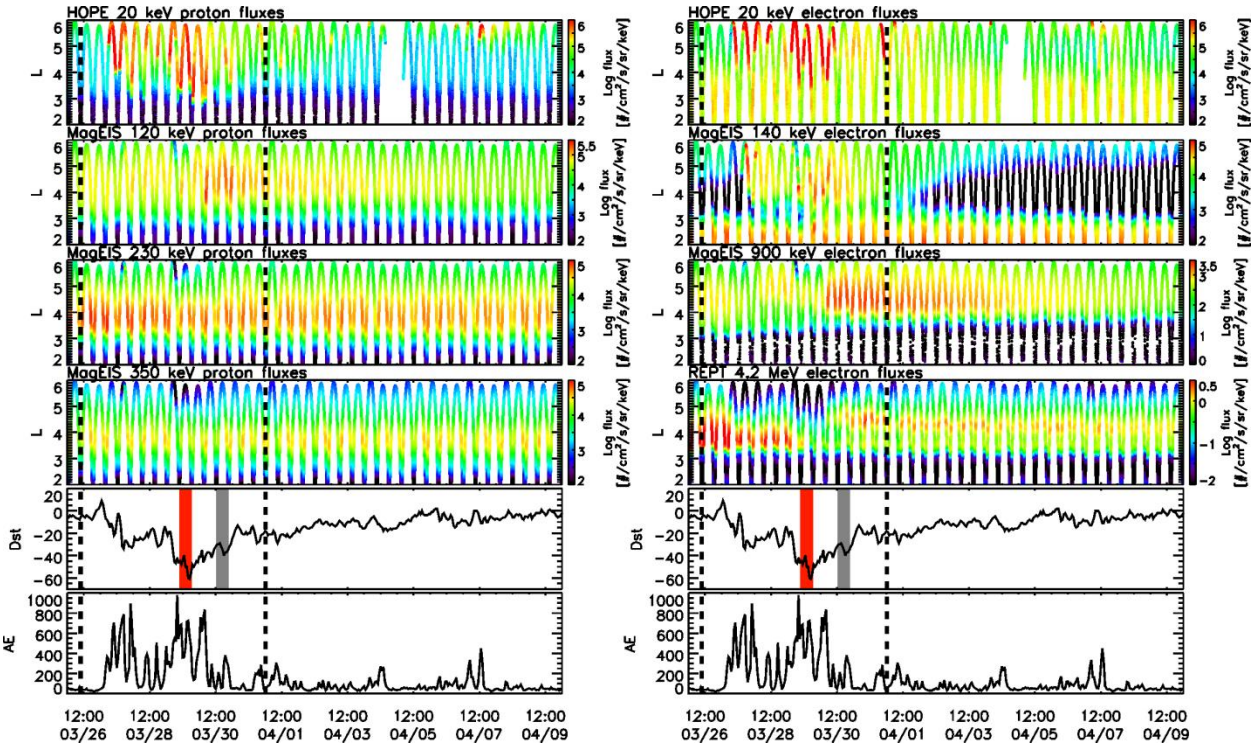

Figure 7.2: The spin-averaged fluxes of (left) protons and (right) electrons with various energies during 26 March – 10 April 2013 as a function of L and time. The energies of protons and electrons are the same as those in Figure 7.1. Provisional Dst and AE indices are also shown in the bottom panels. The detailed ring current energy densities and content are calculated and shown in Figure 7.3 for the time period between two vertical dashed lines. The red bar indicates the main phase of the storm and the grey bar indicates the recovery phase of the storm, during which the detailed energy density and content distribution of electrons are calculated and shown (Figure 7.4).

Figure 7.2 shows the spin-averaged fluxes of (left) protons and (right) electrons of different energies during 26 March - 10 April 2013 based on the measurements from HOPE, MagEIS and REPT on the Van Allen Probe – A, along with provisional Dst and AE indices. For this time period, the background-corrected electron flux data from MagEIS are available and thus are used. One clear difference here comparing with the 900 keV electron fluxes shown in Figure 7.1 is that no measurable 900 keV electrons exist in the inner belt [Li et al., 2015; Fennell et al., 2015]. During this moderate storm, ~20 and 120 keV proton fluxes enhanced significantly, while higher energy proton fluxes did not change much; however, for electrons of all energies shown here, the flux enhancements can be clearly seen during this storm, though MeV electron fluxes enhanced during the late recovery phase, later than the enhancements of tens to hundreds of keV electrons.

The energy density for a single species of ions at a specific location can be calculated as:

$$\varepsilon = \int Efdv^3 = 2\pi \int_0^{\infty} v^2 E \left(\int_0^{\pi} f sin\alpha d\alpha \right) dv = \pi \int_0^{\infty} \sqrt{2mE} \left(\int_0^{\pi} j(\alpha, E) sin\alpha d\alpha \right) dE$$
$$\approx 2\pi \int_{E_{min}}^{E_{max}} \sqrt{2mE} j(E) dE$$

where m and E are the non-relativistic mass and kinetic energy of the ring current ions, f is the distribution function and $f = \frac{dN}{dx^3 dv^3} = \frac{m}{v^2} j$, and $j(\alpha, E)$ is the differential flux of particles with pitch angle α and energy E. To simplify the calculation, we assume that the pitch angle distributions are isotropic and use spin-averaged differential fluxes $j(E)$ instead.

For electrons, the relativistic equation is needed:

$$\varepsilon \approx 4\pi \int_{E_{min}}^{E_{max}} \frac{E_k(E_k + m_0 c^2)}{\sqrt{E_k^2 c^2 + 2m_0 c^4 E_k}} j(E_k) dE_k$$

where m_0 and E_k are the rest mass and kinetic energy of the electrons, and c is the speed of light. Since the contribution from electrons with energies greater than MeV to the total electron ring current energy content is negligible during storm times according to our calculation, E_{min}=0.2

keV and E_{max}=1000 keV are used in this study unless otherwise noted. Similarly, the isotropic pitch angle distributions are assumed for electrons also.

Assuming the ring current energy densities as a function of L are constant at all MLT, the ring current energy content can be calculated based on the energy densities:

$$E = \int \varepsilon dx^3 \approx \sum_{L=L_{min}}^{L_{max}} \varepsilon(L)\Delta V(L)$$

and

$$V(L) = V_E[L^3\left(1-\frac{1}{L}\right)^{\frac{1}{2}}\left(\frac{1}{7L^3}+\frac{6}{35L^2}+\frac{8}{35L}+\frac{16}{35}\right)-\left(1-\frac{1}{L}\right)^{\frac{1}{2}}]$$

where $V(L)$ is the volume contained between the Earth's surface and the dipole L shell, and $\Delta V(L) = V(L+0.05) - V(L-0.05)$. L_{min}=2 and L_{max}=6 are used based on the Van Allen Probes' orbits.

In this study, to show the dynamics of ring current electrons during geomagnetic storms and compare them with the ring current ions, the energy densities of electrons, protons, O^+ and He^+ are calculated based on the HOPE, MagEIS and RBSPICE measurements. The energy densities of ~0.2-35 keV electrons and ~0.2-50 keV protons, O^+ and He^+ are calculated using spin-averaged flux data from HOPE instrument on the Van Allen Probe – A; those of ~35-1000 keV electrons and ~50-1000 keV protons are calculated using data from MagEIS on the Van Allen Probe – A. For ~50-1000 keV O^+ and He^+, RBSPICE data are used. However, the measurements from RBSPICE on the Van Allen Probe – A are relatively sparse compared to those from RBSPICE on the Van Allen Probe – B. Since the Van Allen Probes were very close to each other during the time period of interest, the O^+ and He^+ spin-averaged fluxes from RBSPICE on the Van Allen Probe – B are used in the calculation. Also, during this 29 March 2013 storm, He^+ measurements from RBSPICE only covered energies up to ~520 keV, thus for this moderate storm only ~0.2-500 keV He^+ are included in the calculation. It is worth mentioning that the L range of RBSPICE measurements is limited to above ~2.5-3. It has been demonstrated in the previous chapter that the error introduced by using the spin-averaged fluxes

instead of pitch angle-resolved fluxes is fairly small, especially for low-energy particles whose pitch angle distributions are close to isotropic, and the error introduced by using the dipole field instead of dynamic magnetic field models is also likely to be small. The MLT dependence of the ring current particles has potential impact on the calculation shown here, and the influence will be discussed later in this section.

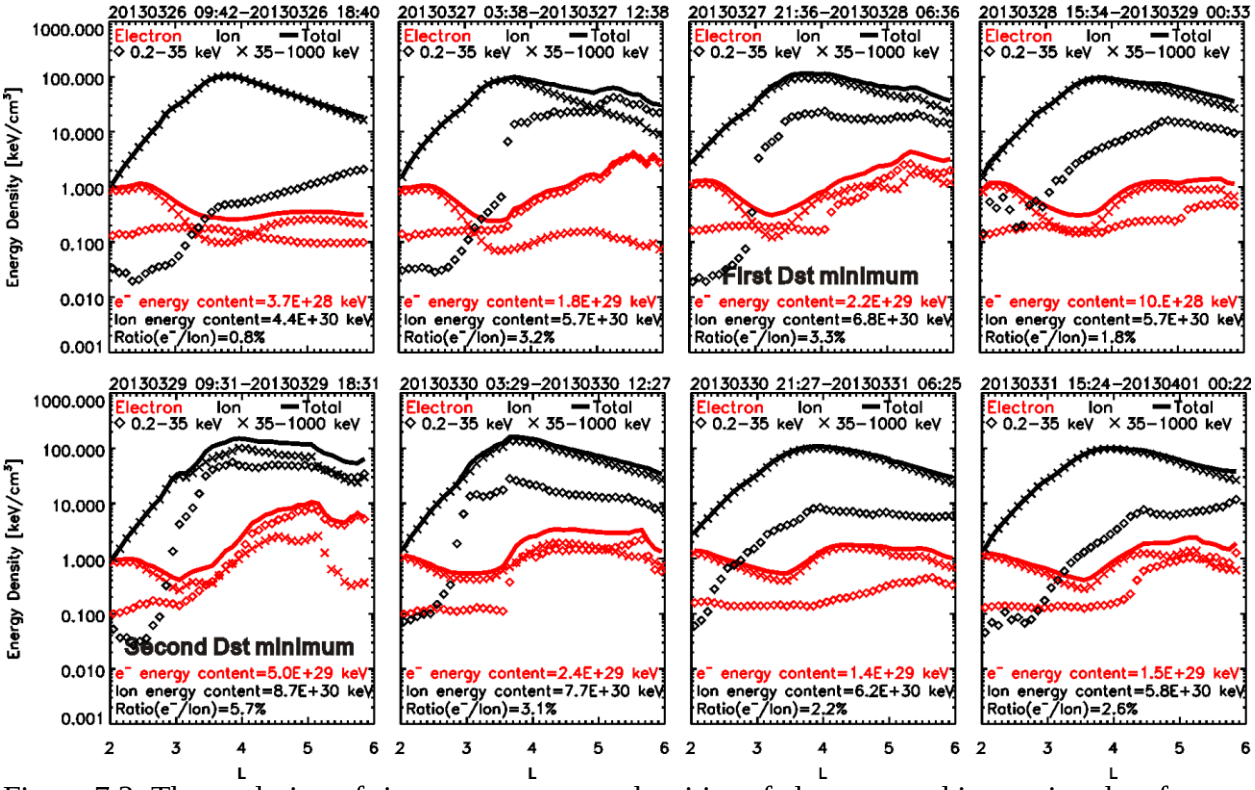

Figure 7.3: The evolution of ring current energy densities of electrons and ions using data from HOPE and MagEIS on the Van Allen Probe - A and RBSPICE on the Van Allen Probe - B for every other orbit of Van Allen Probe - A during 26 March – 1 April 2013. The energy densities of electrons are shown as red lines and symbols, while those of ions are shown as black ones. The solid lines show the energy densities of particles with energies of ~0.2 – 1000 keV, the diamonds are for particles of E~0.2 – 35 keV, and the cross signs are for particles with energies of ~35 – 1000 keV. The energy content of electrons and ions and the ratio of the two are shown in the text at the bottom of each panel. Two Dst minima during the 29 March 2013 storm are identified in the figure.

Figure 7.3 shows the evolution of the ring current energy densities of both electrons and ions using data from HOPE, MagEIS and RBSPICE instruments on the Van Allen Probes. Every other orbit of Van Allen Probe –A during 26 March – 1 April 2013 is shown. Different colors

imply different species: red is for electrons and black is for ions. The solid lines show the energy densities of ~0.2-1000 keV particles, the diamonds show the energy densities of lower energy particles (~0.2-35 keV), and the cross signs show those of higher energy particles (~35-1000 keV). The energy content of electrons and ions and the ratio of them are shown in the bottom of each panel. Two Dst minima during this moderate storm are also identified in Figure 7.3.

Overall the energy densities of electrons were much smaller than those of ions during this moderate storm. During quiet times, the energy content of electrons was just ~1% of that of ions, and the ring current energy was greatly dominated by the higher energy ions. As the geomagnetic storm occurred, the energy densities of both electrons and ions greatly enhanced, but the enhancement of electrons energy densities was more significant (percentage wise). Comparing the energy densities and energy content before the storm and at the time of minimum Dst, the energy densities of ions at L>4 increased by a factor of ~2-3, while those of electrons enhanced by more than 1 order of magnitude; the total energy content of ions increased by a factor of ~2, while that of electrons increased by more than 1 order of magnitude. The contribution of electrons to the ring current energy content increased from ~1% of ion contribution during quiet times to ~6% of ion contribution at the time of minimum Dst. And if we only focus on the enhancement of the energy content of electrons and ions comparing to the quiet time values, the energy content enhancement of electrons is ~10% of ion energy content enhancement at the storm main phase. This indicates that during quiet times, the electrons are not an important carrier of ring current energy; while during the main phase of the storm, electrons contribute a small but potentially important amount to the overall enhancement of the ring current.

It is obvious that as the storm occurred, the lower energy electrons enhanced first and dominated the electrons energy densities at the storm main phase. Afterward, the decay of these lower energy electrons was fast and gradually the high-energy electrons began to enhance. Since the decay of those high-energy electrons was relatively slow compared to that of low-energy electrons, during the recovery phase the high-energy electrons became dominant. This behavior is consistent with ring current ions as I showed in the previous chapter.

The behaviors of different energy electrons during different phases of the storm can also be clearly seen from Figure 7.4. Figure 7.4 shows the cumulative distribution function of ring current electron energy content and energy densities at different L, for the main phase and recovery phase of 29 March 2013 storm respectively. As shown in left panel of Figure 7.4, during the main phase the ring current electron energy content was greatly dominated by lower energy electrons: the electrons with energies < ~35 keV accounted for ~75% of the total ring current electron energy content. These lower energy electrons decayed fast and the higher energy ones enhanced during the recovery phase of the storm, so that the high-energy electrons dominated the electron energy content during the recovery phase (>100 keV electrons accounted for ~70% of the total electron energy content). Though the ring current protons also have similar behaviors as shown in the previous chapter, the differences here between lower and higher energy electrons are more prominent.

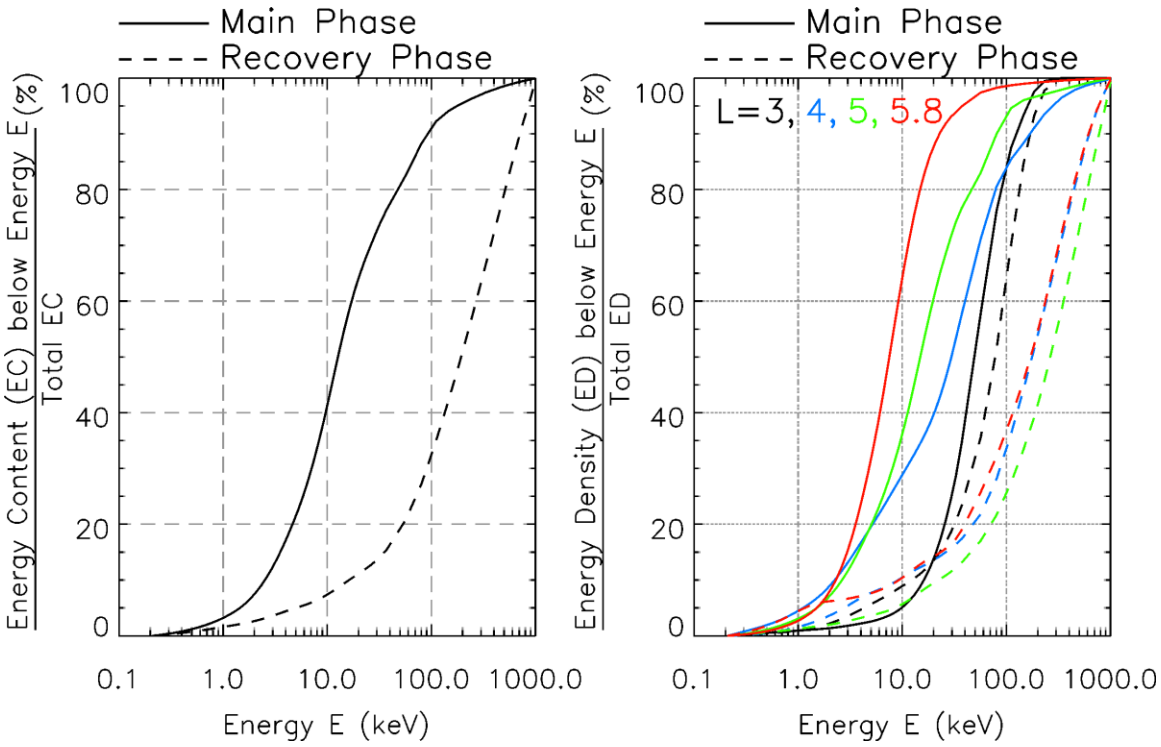

Figure 7.4: The cumulative distribution function of (left) ring current electron energy content and (right) energy densities at different L shells for the main phase and recovery phase of 29 March 2013 storm respectively. The orbits of main phase and recovery phase are identified in Figure 7.2.

Comparing the electron energy densities at different L shells (right panel of Figure 7.4), at lower L the higher energy electrons accounted for a large portion of the electron energy densities, while at higher L the energy densities were dominated by those lower energy electrons. At L=5.8, <~100 keV electrons accounted for all most all of the ring current electron energy density.

Based on the DPS relation, the depression of near-equator geomagnetic field at Earth's surface caused by the ring current particles is calculated. Figure 7.5 (a) and (b) show the calculated ΔB based on the DPS relation using ring current ion and electron energy content respectively. The ratio of the electron energy content to ion energy content is also shown in panel (c). Overall the calculated ΔB using ring current ion energy content followed the Dst index profile very well, while the enhancement of calculated ΔB using ring current electron energy content is also similar to that of the Dst index but the recovery is faster than the Dst. The contribution of electrons to the ring current energy is small during this storm. It is clear from Figure 7.5 that the ratio of electron's contribution to ion's contribution to the ring current energy reached its maximum value (~7%) at the storm main phase just before Dst reached its minimum. And compared to the Dst index, the calculated ΔB using ring current electron energy content accounted for ~4% of the Dst depression at the time of minimum Dst (the Dst index is averaged over 9 hours to match the Van Allen Probes' measurements).

Also, similar to the ring current ions, the lower energy electrons enhanced faster than higher energy electrons during the main phase, and also decayed faster during the recovery phase of the storm. At the main phase of the storm, those lower energy electrons dominated the electron ring current. The higher energy electron energy content reached its maximum at early recovery phase of the storm and decayed slowly afterward, thus the higher energy electrons dominated the ring current electron energy content during the recovery phase. Compared to the ring current ions, the lower energy electron energy content enhanced more significant but also decreased faster.

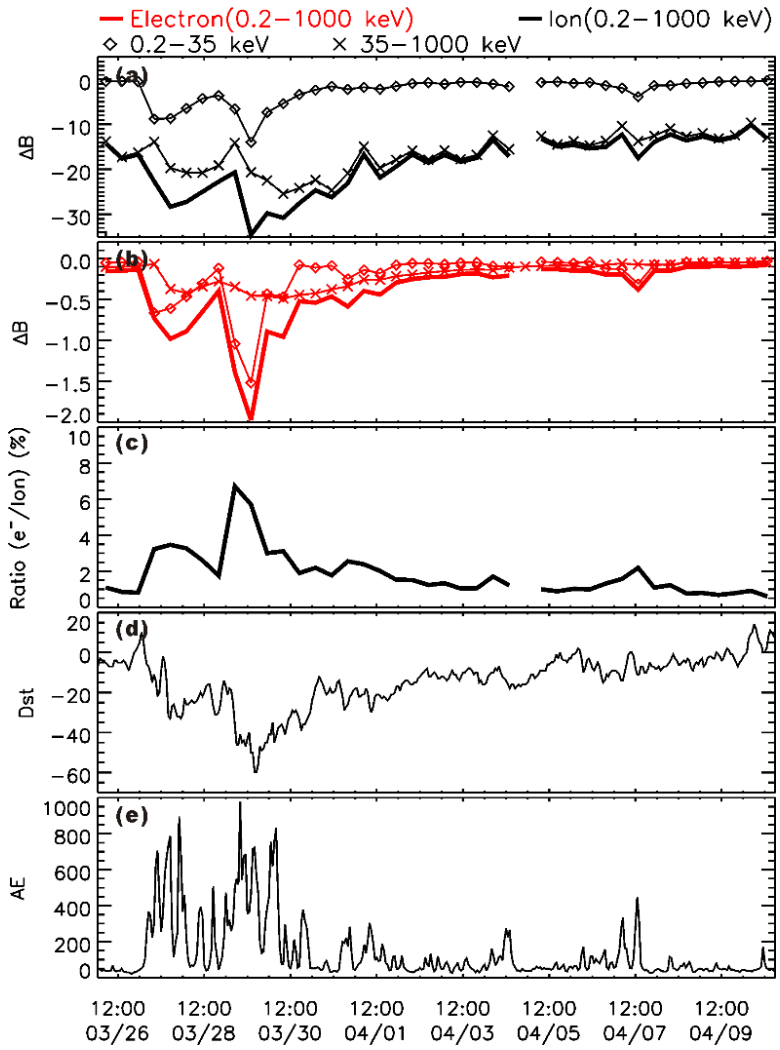

Figure 7.5: (a) The calculated ΔB using ring current ion energy content based on the DPS relation; (b) the calculated ΔB using ring current electron energy content based on the DPS relation; (c) the ratio of electron energy content to ion energy content; (d) and (e) provisional Dst and AE indices during the 29 March 2013 storm.

7.2.2 The Ring Current Evolution during the 17 March 2015 Very Intense Geomagnetic Storm

In the previous subsection, we focused on the ring current electron dynamics during a moderate storm. In this subsection, we will show the evolution of the ring current energy content during an intense storm of 17 March 2015. The 17 March 2015 storm has a minimum Dst index of -223 nT. This is the most intense storm since the launch of the Van Allen Probes, while during

this storm the Van Allen Probes' apogees were also located close to local midnight. During this storm, because of the degradation of MagEIS proton telescope which influenced the lower energy proton measurements the most, data from RBSPICE are used for ~50-330 keV protons and MagEIS data are used for protons with higher energies. Again, data from HOPE and MagEIS on the Van Allen Probe – A and RBSPICE on the Van Allen Probe – B are used in the calculation.

Figure 7.6 shows the calculated ΔB using ring current ion and electron energy content during the 17 March 2015 storm, which has the similar format with Figure 7.5. In contrast to the moderate storms, during this intense storm the contribution from higher energy ions significantly enhanced and greatly dominated the ring current energy content, while lower energy ions contributed little throughout the storm. Comparing ions of different species, the contribution from O^+ greatly enhanced during the main phase of the storm and dominated the ring current energy content around the time of minimum Dst, which is expected for intense storms [e.g., Greenspan and Hamilton, 2002], while He^+ also contributed to the ring current energy. At the time of minimum Dst, H^+, O^+, and He^+ accounted for ~ 37%, ~53% and ~10% of the ring current ion energy content respectively. At the recovery phase, the O^+ energy content decreased much faster than that of protons, thus protons gradually dominated again as the ring current decayed. This is most likely to be caused by different charge exchange lifetimes of O^+ and protons [e.g., Smith and Bewtra, 1978; Ebihara and Ejiri, 2003] and also drift-bounce resonance interaction of O^+ with ULF waves [Li et al., 1993]. It is worth mentioning that ~50-140 keV O^+ measurements from RBSPICE during this intense storm may be contaminated and should be treated as an upper limit. But even if we exclude data of ~50-140 keV O^+, O^+ still contribute significantly at the time of minimum Dst (~ 44% of the ring current ion energy content, comparable to protons). At the time of minimum Dst, for this intense storm, the calculated ΔB based on both ring current ions and electrons only accounts for ~25% of the Dst index, while for the 29 March 2013 moderate storm the value is about 45%. This may indicate that during intense geomagnetic storms, the

contributions to the Dst index from other current systems, such as the partial ring current and magnetotail current, can be more significant.

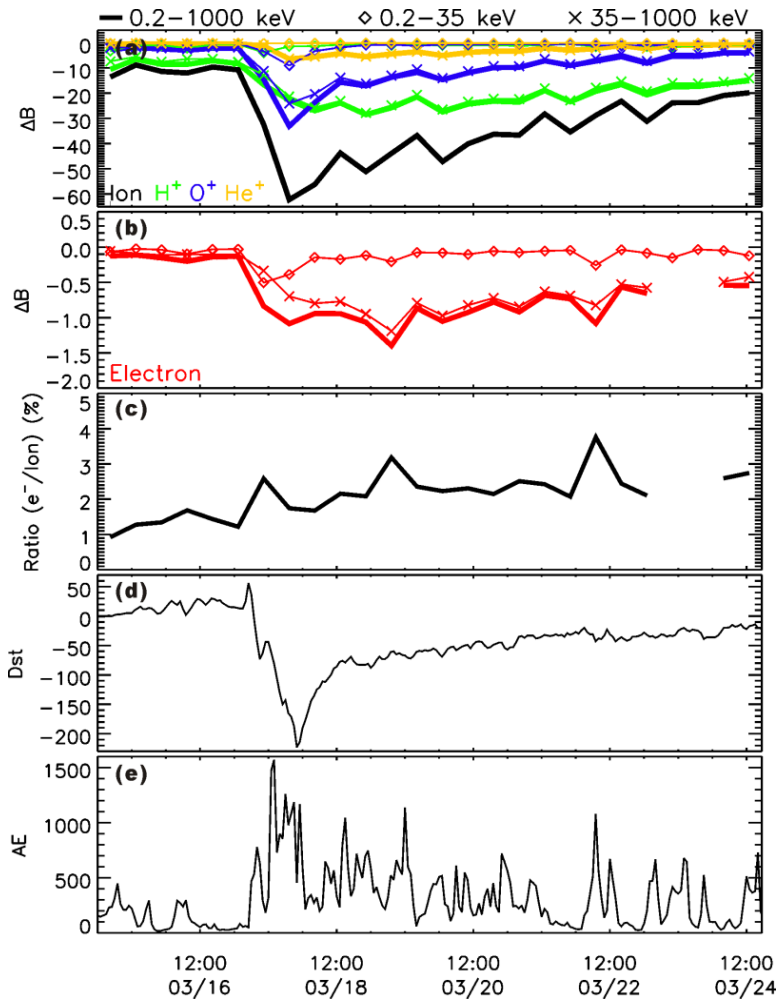

Figure 7.6: Similar format as Figure 7.5 but for the 17 March 2015 intense geomagnetic storm.

The electron relative contribution to the ring current energy content during this intense storm is much smaller than those during moderate storms. The ratio of electron energy content to ion energy content was only about 2-3% during this storm, and the contribution of ring current electrons to the depression of Dst index was less than 1% at the main phase. Also, the contribution from lower energy electrons was smaller than that from higher energy electrons almost all the time. It may suggest that as the storm gets more intense, the contribution from electrons, especially those lower energy electrons, becomes more negligible. However, it may be

also related to the uncertainties in measurements, which will be discussed in section 7.3. The relative contributions from H^+, O^+, He^+, and e^- at the time of minimum Dst during the 29 March 2013 moderate storm and the 17 March 2015 intense geomagnetic storm are compared in Table 7.1.

Table 7.1: The relative contributions from H^+, O^+, He^+, and e^- to the total ring current energy content at the time of minimum Dst during the 29 March 2013 moderate storm and the 17 March 2015 intense storm.

	H^+	O^+	He^+	e^-
29 March 2013	67%	25%	2%	6%
17 March 2015	36%	52%	10%	2%

7.2.3 The Contribution of Ring Current Electrons to the Dst Index: the Statistics and MLT Dependence

In section 7.2.1 and 7.2.2, the electron energy contents were calculated during two geomagnetic storms, one moderate and one intense storm. For the 29 March 2013 moderate storm, the contribution of electrons to the Dst index was ~4% at the time of minimum Dst; while for the 17 March 2015 storm, the contribution of electrons was less than 1%. In this subsection, we examine the ring current electron energy content during 42 moderate storms with minimum Dst of -50 – -100 nT using data from Van Allen Probes from Nov 2012 to May 2015. The ring current electron energy contents are calculated based on the assumption that the ring current electron distribution is MLT symmetric. The ratios of ΔB calculated using electron energy content to the Dst index at the time of minimum Dst during these moderate storms are shown in Figure 7.7, and their dependence on the MLT at which Van Allen Probes were located is investigated.

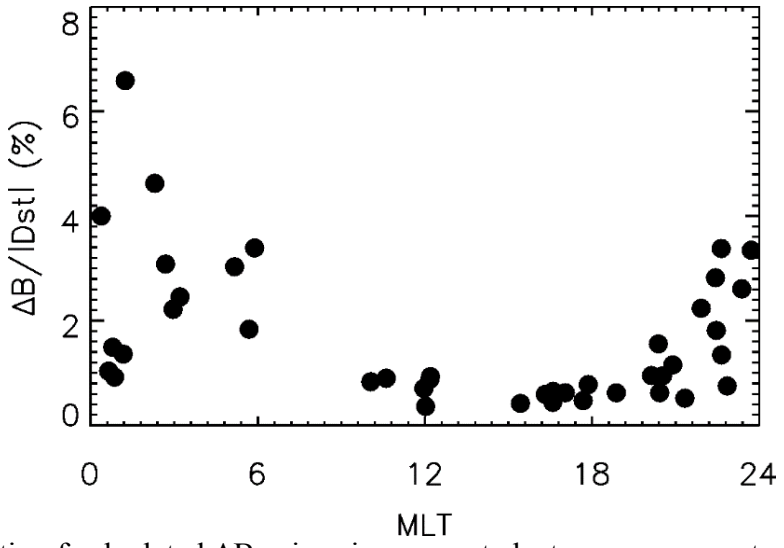

Figure 7.7: The ratio of calculated ΔB using ring current electron energy content to the Dst index at the time of minimum Dst during 42 moderate geomagnetic storms with minimum Dst of ~ -50 – -100 nT, as a function of MLT of Van Allen Probe's apogee.

Figure 7.7 shows the ratio of calculated ΔB using electron energy content to the Dst index at the time of minimum Dst during 42 moderate storms (with minimum Dst of -50 – -100 nT) as a function of MLT of Van Allen Probe's apogee. The Dst index used here is averaged over the corresponding Van Allen Probe's orbit period. As for these 42 moderate storms, the ring current electrons accounted for up to ~7% of the Dst index at the time of minimum Dst, while for the majority of these storms, the ring current electrons only accounted for ~1 – 4% of the Dst index at the time of minimum Dst. Since the Dst index is also influenced by other current systems, e.g., ground induced currents and magnetotail currents, the contribution of electrons to the ring current energy should be a little higher (percentage wise). But still the contribution of electrons to the depression of Earth's surface magnetic field should be small.

On the other hand, the calculation of ring current energy content we did is based on the assumption that ring current is MLT symmetric, while this assumption may not be valid especially during the main phase of the storm. It is clear from Figure 7.7 that the distribution of ring current electrons is MLT asymmetric: the calculated electrons' energy content is generally higher when Van Allen Probe's apogee was located at dawn and midnight sectors, while much lower when the apogee was at noon and dusk sectors. Since the intensities of these storms are

similar, the result indicates that the ring current electron energy densities are generally higher at dawn and midnight sectors while lower at noon and dusk sectors, which is consistent with the drift patterns of the energetic electrons after being injected from the plasmasheet on the nightside. For both storms shown in previous subsections, since the Van Allen Probes were located at the midnight sector, the electron energy contents derived for those two storms are likely to be overestimated; but the ratios of electron and ion energy content should be close to the actual values since the apogees of Van Allen Probes during both storms were located around local midnight.

7.3 Discussion

Over the past decades, many studies have focused on the dynamics of ring current ions during geomagnetic storms; however, only few studies showed the contribution of electrons to the ring current based on the observations. Frank [1967], using data of protons and electrons with energies of ~200 eV – 50 keV from OGO 3, investigated the evolution of ring current particles during two moderate geomagnetic storms. The results showed that the contribution of electrons to the storm-time ring current energy is significant (~25%). But the electrons' contribution in this study could have been overestimated because of the limited energy range: the protons with energies greater than 50 keV is believed to be a very important carrier of storm time ring current [e.g., Daglis et al., 1999], which were not included in the study. The study of Liu et al. [2005] covered a wider range of energy (~1 keV – 400 keV) using data from Explorer 45. The results showed that during an intense storm with minimum Dst of ~-171 nT, the contribution of ring current electrons to the ring current energy content is ~7.5% of the contribution of ring current protons. However, their results may contain significant uncertainties since all the data they used were digitalized from Lyons and Williams [1975, 1976, and 1980] as well as interpolated and extrapolated across the L shells and energies. Furthermore, their data only cover L shells from ~2.5 to 5, which are not sufficient for ring current study since the contribution of ring current

particles at L>5 can be significant. Using Van Allen Probes' data, we investigated the role of ring current electrons with more comprehensive measurements. All major ring current particle species, e^-, H^+, O^+ and He^+, are included in our study to improve the accuracy of the calculation. Wider energy range of ~0.2-1000 keV and L shell range of 2-6 are also used.

Comparing to the ring current ion energy content, the ring current electron energy content is very small even during storm times. During the 29 March 2013 moderate storm, the ring current electrons contribute only ~6% as the ring current protons to the ring current energy content at the time of minimum Dst; while during the 17 March 2015 intense storm, this value is even smaller (~2%). The statistical results from Figure 7.7 also showed that the overall contribution from electrons to the Dst index is also very small. Comparing to the previous observations as well as simulations, the contributions from electrons to the ring current energy we derived during these storms are overall smaller. But the enhancement of ring current electron energy content during the 29 March 2013 storm is ~10% of that of ring current ions, indicating a more dynamic feature of the ring current electrons.

However, it is worth mentioning that the results we derived here may be influenced by the uncertainties in the measurements as well, especially for the storms in 2014 and 2015. In 2014 and 2015, measurements from HOPE instruments suffered from gain changes and the differences between HOPE data and data from other instruments became larger. And the factor of 3 we used for HOPE ion data in this study may not be enough, while the electron data may also need to be multiplied by a factor to match the measurements from MagEIS. With higher factors for both lower energy ions and electrons, the contributions from lower energy particles to the ring current energy will be enhanced. For the 17 March 2015 storm, using a factor of 5 instead of 3 for ions and a factor of 3 for electrons for HOPE measurements, the ring current energy will still be dominated by the higher energy ions, but the lower energy electrons will then dominate the ring current electron energy during the main phase. The contribution of ring current electrons to that of ions will be ~4.5% at the time of minimum Dst, which is still much smaller than all of the previous studies showed.

7.4 Conclusion

In this study, using comprehensive measurements from Van Allen Probes, the dynamics of ring current electrons during storm times is examined with comparison to ions. The evolution of ring current electrons is shown in details during two storms with different intensities, while the MLT dependence of ring current electrons is also investigated. The main conclusions are as follows:

1. Obvious differences exist in the long-term behaviors of ring current protons and electrons. Tens to hundreds of keV electrons penetrate deep into the inner magnetosphere frequently and stay in the low L region for a long time, while the deep penetration of hundreds of keV protons is rare. Though tens of keV protons also penetrate deep into the inner magnetosphere, after injections the loss of these protons in the low L region is much faster. Intriguing similarities also exit between lower-energy protons and higher-energy electrons, though the underlying physical mechanism is still not clear.

2. The ring current electron energy content is much smaller than the ring current ion energy content. At the time of minimum Dst of the 29 March 2013 moderate storm, the ratio of ring current electron energy content to that of proton is ~6%; while for the 17 March 2015 intense storm the value is only ~2%. These values are much smaller than those from previous studies. But the enhancement of ring current electron energy content during the 29 March 2013 storm is ~10% of that of ring current protons, indicating a more dynamic feature of the electrons.

3. During moderate geomagnetic storms, the lower energy electrons (< 35 keV) dominate the ring current electron energy content. But during the 17 March 2015 intense storm, the contribution from lower energy electrons was small comparing to that of higher energy electrons. This is also similar for ring current ions, which could indicate that as the storm becomes more intense, the higher energy charged particles play more dominant role in the ring current buildup.

4. By examining 42 moderate storms with minimum Dst of -50 ~ -100 nT, the contributions of ring current electrons to the Dst index were generally ~1-4 %, with the

maximum of ~7%. It was shown that the distribution of ring current electron energy density is highly asymmetric, with higher energy densities at midnight and dawn sectors while lower energy densities at noon and dusk sectors, which is consistent with the drift pattern of the electrons after injected from plasmasheet from nightside.

Chapter 8

Conclusion

8.1 Summary and Conclusions

The primary goal of this work is to study the characteristics of energetic electrons and ions in the inner radiation belt, slot region and ring current, which play important roles in understanding the radiation belt and ring current dynamics but have received limited attention in the past. To achieve this goal, observations from multiple satellites as well as simulations have been used in this study and intriguing features of energetic electrons and ions have been unveiled.

The dynamics of MeV electrons in the outer radiation belt has been intensively and extensively studied. However, limited attention has been paid to MeV electron characteristics in the slot region and inner belt. In Chapter 3, using data from the SAMPEX satellite, the flux enhancement of MeV electrons in the slot region and its correlation with geomagnetic storms as well as solar wind conditions have been investigated. It was showed that the penetration of MeV electrons into the low L region is well correlated with the geomagnetic storm intensity represented by the Dst index and the MeV electron flux enhancement in the slot region is significantly influenced by the solar wind conditions and electron flux preconditioning.

Though MeV electrons rarely penetrate into the slot region and inner belt, the penetration of 100s of keV electrons into the low L region occur much more often and abundant 100s of keV electrons exist in the inner belt. In Chapter 4 and 5, I mainly focused on the dynamics of 100s of keV electrons in the slot region and inner belt. Using data from the DEMETER satellite, the penetration of 100s of keV electrons is identified and modeled with a radial diffusion model in Chapter 4. The simulation results indicate the penetration can be well explained by the inward radial transport, but the radial diffusion coefficients derived from the model are very different from those of previous studies. Besides the radial diffusion, other physical mechanisms also exist in the low L region and may have significant effect on the energetic electrons. In Chapter 5, using newly available data from Van Allen Probes, 100s of keV electron pitch angle distributions

are investigated in detail and three main types of pitch angle distributions in the low L region are identified. While the normal and cap pitch angle distributions can be well explained by inward radial diffusion and wave scattering respectively, the newly discovered peculiar type of pitch angle distributions with minima at 90 °pitch angle is contradictory with the theoretical predictions from known physical processes and indicates the complexity in the inner belt dynamics. Chorus/fast magnetosonic wave heating is suggested to explain the formation of this peculiar type of PADs, but to fully understand the underlying physical processes future work is still needed.

Similar to the relativistic electrons in the low L region, very limited studies have focused on the energetic electrons in the ring current, though they contribute to the ring current energy and are responsible for the generation of whistler mode chorus waves, thus are very important to the ring current and radiation belt dynamics. In Chapter 6 and 7, the evolutions of ring current ions and electrons during geomagnetic storms are studied using data from Van Allen Probes. Detailed analyses of ring current ion energy densities and content during a moderate geomagnetic storm in Chapter 6 not only provide a solid background for the study of the role of ring current electrons shown in Chapter 7, but also reveal the important role of <50 keV protons and O^+ in the ring current buildups. With the new understandings of ring current ions, the dynamics of ring current electrons during geomagnetic storms is investigated in Chapter 7. Using comprehensive data from Van Allen Probes, the energy densities and content of ring current electrons are calculated during a moderate and an intense storm. The contributions of electrons to the ring current energy content during these storms are shown to be about a few percent of those of ions, smaller than the values from previous studies. But the enhancement of electrons during the moderate storm is ~10% of that of ring current protons, indicating a more dynamic feature of the ring current electrons.

Individually, these studies reveal important characteristics of energetic electrons and ions and achieve significant results. Altogether, they combine to form a more cohesive picture of the dynamics of energetic electrons and ions in the inner belt, slot region, and ring current, which

has not been adequately studied and thus has not gained enough insights. These unveiled features of energetic particles in the inner magnetosphere shed light on the physical processes in the corresponding regions and introduce the complexities in the inner magnetospheric dynamics. Our findings regarding different populations in the inner magnetosphere contribute to a more comprehensive understanding of radiation belt and ring current dynamics.

8.2 Future Work

Some possible extensions and future work along the line of this thesis include a statistical study of ring current ion and electron energy density, content, and MLT distribution during geomagnetic storms using Van Allen Probes data (with HOPE data incorporated gain changes) and investigating the deep penetration of electrons versus ions into the low L region.

In Chapter 6 and 7, detailed energy density and content evolutions of ring current ions and electrons are studied during specific geomagnetic storms and intriguing results are found. A statistical study of ring current configuration and contributions from various species and energies of ring current particles will be an interesting extension to our work presented here. Though some statistical studies have been conducted on the distribution of proton ring current during storm times [e.g., De Michelis et al., 1997; Ebihara et al., 2002], contribution of ring current ions to the Dst index [e.g., Greenspan and Hamilton, 2000; Turner et al., 2001], and the relative abundance of ring current O^+ to protons [e.g., Greenspan and Hamilton, 2002], the statistical study using clean and comprehensive data from Van Allen Probes with better spatial and temporal coverage will still contribute to a better understanding of statistical behaviors of ring current. Especially, with clean measurements on energetic electrons with a wide energy range, it will be interesting to statistically study the contribution of ring current electrons versus ions to the ring current energy and the MLT distributions of ring current electrons during various storm phases. In Chapter 7, a preliminary statistical study on ring current electron MLT distribution is conducted. However, using uncorrected HOPE data, the results could have been influenced by

the changing gains of HOPE instruments. Once the HOPE data with gain changes incorporated become available, a more in depth statistical study can be performed and statistical properties of ring current can be well revealed.

Another interesting study along the line of this thesis is to investigate the deep penetrations of electrons and ions into the low L region. In Chapter 3 and 4, I showed that though the deep penetrations of >MeV electrons occur rarely, the deep penetrations of 100s of keV electrons happen frequently. Also, in Chapter 6 and 7, the comparison between electron and ion daily-averaged fluxes showed intriguing differences in penetration depth. Understanding the underlying mechanisms responsible for these deep penetrations is very important to the understanding of overall physical picture of inner magnetosphere. With data from Van Allen Probes, both statistical study and case study can be conducted to investigate the penetration timescale and depth of electrons and ions with different energies. The energy spectra and pitch angle distributions of electrons and ions during penetrations will also be examined, and the results will be compared to speculate the physical mechanisms acting on them.

Bibliography

Abel, B., R. M. Thorne, and A. L. Vampola (1994), Solar cyclic behavior of trapped energetic electrons in Earth's inner radiation belt, J. Geophys. Res., 99(A10), 19,427–19,431.

Abel, B., and R. M. Thorne (1998), Electron scattering loss in Earth's inner magnetosphere: 1. Dominant physical processes, J. Geophys. Res., 103(A2), 2385–2396.

Ali, A. F., S. R. Elkington, D. M. Malaspina, J. Wygant, S. Thaller, and C. A. Kletzing (2015), Electric and Magnetic Radial Diffusion Coefficients Using the Van Allen Probes Data, Manuscript in Preparation.

Artemyev, A., D. Mourenas, O. Agapitov, and V. Krasnoselskikh (2013), Parametric validations of analytical lifetime estimates for radiation belt electron diffusion by whistler waves, Ann. Geophys., 31, 599–624.

Baker, D. N., P. R. Higbie, E. W. Hones Jr., and R. D. Belian (1978), High-resolution energetic particle measurements at 6.6 Re 3. Low-energy electron anisotropies and short-term substorm predictions, J. Geophys. Res., 83(A10), 4863–4868, doi:10.1029/JA083iA10p04863.

Baker, D. N., J. B. Blake, L. B. Callis, R. D. Belian, and T. E. Cayton (1989), Relativistic electrons near geostationary orbit: Evidence for internal magnetospheric acceleration, Geophys. Res. Lett., 16(6), 559–562.

Baker, D. N., et al. (1993), An overview of the SAMPEX mission, IEEE Trans. Geosci. Electr., 31, 531.

Baker, D.N., et al. (1998a), A strong CME-related magnetic cloud interaction with the Earth's magnetosphere: ISTP observations of rapid relativistic electron acceleration on May 15, 1997, Geophys. Res. Lett., 25, 2975.

Baker, D.N., et al. (1998b), Coronal mass ejections, magnetic clouds, and relativistic magnetospheric electron events: ISTP, J. Geophys. Res., 103, 17,279-17,291.

Baker, D. N., S. G. Kanekal, X. Li, S. P. Monk, J. Goldstein, and J. L. Burch (2004a), An extreme distortion of the Van Allen belt arising from the 'Hallowe'en' solar storm in 2003, Nature, 432, 878–881.

Baker, D. N., S. G. Kanekal, and J. B. Blake (2004b), Characterizing the Earth's outer Van Allen zone using a radiation belt content index, Space Weather, 2, S02003, doi:10.1029/2003SW000026.

Baker, D. N., S. G. Kanekal, R. B. Home, N. P. Meredith, and S. A. Glauert (2007), Low-altitude measurements of 2-6 MeV electron trapping lifetimes at $1.5 \leq L \leq 2.5$, Geophys. Res. Lett., 34, L20110, doi:10.1029/2007GL031007.

Baker, D. N., and J. B. Blake (2013), SAMPEX: A long-serving radiation belt sentinel, in Dynamics of the Earth's Radiation Belts and Inner Magnetosphere, edited by D. Summers et al., AGU, Washington, D. C., doi:10.1029/2012GM001368.

Baker, D. N., et al. (2014), An impenetrable barrier to ultra-relativistic electrons in the Van Allen radiation belt, Nature, 515, 531–534, doi:10.1038/nature13956.

Berko, F. W., L. J. Cahill Jr., and T. A. Fritz (1975), Protons as the prime contributors to storm time ring current, J. Geophys. Res., 80(25), 3549–3552, doi:10.1029/JA080i025p03549.

Blake, J. B., W. A. Kolasinski, R. W. Fillius, and E. G. Mullen (1992), Injection of electrons and protons of tens of MeV into L<3 on 24 March 1991, Geophys. Res. Lett., 19, 821.

Blake, J. B., U. S. Inan, M. Walt, T. F. Bell, J. Bortnik, D. L. Chenette, and H. J. Christian (2001), Lightning-induced energetic electron flux enhancements in the drift loss cone, J. Geophys. Res., 106(A12), 29,733–29,744.

Blake, J. B., et al. (2013), The magnetic electron ion spectrometer (MagEIS) instruments aboard the radiation belt storm probes (RBSP) spacecraft, Space Sci. Rev., doi:10.1007/s11214-013-9991-8.

Blum, L. W., Q. Schiller, X. Li, R. Millan, A. Halford, and L. Woodger (2013), New conjunctive CubeSat and balloon measurements to quantify rapid energetic electron precipitation, Geophys. Res. Lett., 40, 5833–5837, doi:10.1002/2013GL058546.

Blum, L. W., A. Halford, R. Millan, J. W. Bonnell, J. Goldstein, M. Usanova, M. Engebretson, M. Ohnsted, G. Reeves, H. Singer, et al. (2015), Observations of coincident EMIC wave activity and duskside energetic electron precipitation on 18–19 January 2013, Geophys. Res. Lett., 42, 5727–5735, doi:10.1002/2015GL065245.

Boscher, D., S. Bourdarie, P. O'Brien, and T. Guild (2010), IRBEM library V4.3, 2004–2008, ONERA-DESP, Toulouse France, Aerospace Corporation, Washington, D. C.

Bostrom, C. O., D. S. Beall, and J. C. Armstrong (1970), Time history of the inner radiation zone, October 1963 to December 1968, J. Geophys. Res., 75(7), 1246–1256.

Brautigam, D. H., and J.M. Albert (2000), Radial diffusion analysis of outer radiation belt electrons during the October 9, 1990, magnetic storm, J. Geophys. Res., 105(A1), 291–309, doi:10.1029/1999JA900344.

Brautigam, D. H., G. P. Ginet, J. M. Albert, J. R. Wygant, D. E. Rowland, A. Ling, and J. Bass (2005), CRRES electric field power spectra and radial diffusion coefficients, J. Geophys. Res., 110, A02214, doi:10.1029/2004JA010612.

Burton, R. K., R. L. McPherron, and C. T. Russell (1975), An empirical relationship between interplanetary conditions and Dst, J. Geophys. Res., 80(31), 4204–4214, doi:10.1029/JA080i031p04204.

Chen, L., A. Maldonado, J. Bortnik, R. M. Thorne, J. Li, L. Dai, and X. Zhan (2015), Nonlinear bounce resonances between magnetosonic waves and equatorially mirroring electrons, J. Geophys. Res. Space Physics, 120, 6514–6527, doi:10.1002/2015JA021174.

Chen, M. W., L. R. Lyons, and M. Schulz (1994), Simulations of phase space distributions of storm time proton ring current, J. Geophys. Res., 99(A4), 5745–5759, doi:10.1029/93JA02771.

Chen, Y., R. H. W. Friedel, G. D. Reeves, T. G. Onsager, and M. F. Thomsen (2005), Multisatellite determination of the relativistic electron phase space density at geosynchronous orbit: Methodology and results during geomagnetically quiet times, J. Geophys. Res., 110, A10210, doi:10.1029/2004JA010895.

Chen, Y., G. D. Reeves and R. H. W. Friedel (2007), The energization of relativistic electrons in the outer Van Allen radiation belt, Nature Physics, 3(9), 614-617.

Chen, Y., R. H. W. Friedel, M. G. Henderson, S. G. Claudepierre, S. K. Morley, and H. Spence (2014), REPAD: An empirical model of pitch angle distributions for energetic electrons in the Earth's outer radiation belt, J. Geophys. Res. Space Physics, 119, 1693–1708, doi:10.1002/2013JA019431.

Daglis, I. A., E. T. Sarris, and B. Wilken (1993), AMPTE/CCE observations of the ion population at geosynchronous altitudes, Ann. Geophys., 11, 685.

Daglis, I. A. (1997), The role of magnetosphere-ionosphere coupling in magnetic storm dynamics, Magnetic Storms, 107-116.

Daglis, I. A., R. M. Thorne, W. Baumjohann, and S. Orsini (1999), The terrestrial ring current: Origin, formation, and decay, Rev. Geophys., 37(4), 407–438, doi:10.1029/1999RG900009.

Daglis, I. A., and J. U. Kozyra (2002), Outstanding issues of ring current dynamics, J. Atmos. Sol. Terr. Phys., 64, 253–264.

De Michelis, P., I. A. Daglis, and G. Consolini (1997), Average terrestrial ring current derived from AMPTE/CCE-CHEM measurements, J. Geophys. Res., 102(A7), 14103–14111, doi:10.1029/96JA03743.

DeForest, S. E., and C. E. McIlwain (1971), Plasma clouds in the magnetosphere, J. Geophys. Res., 76(16), 3587–3611, doi:10.1029/JA076i016p03587.

Denton, M. H., M. F. Thomsen, H. Korth, S. Lynch, J. C. Zhang, and M. W. Liemohn (2005), Bulk plasma properties at geosynchronous orbit, J. Geophys. Res., 110, A07223, doi:10.1029/2004JA010861.

Dessler, A. J., and E. N. Parker (1959), Hydromagnetic theory of geomagnetic storms, J. Geophys. Res., 64(12), 2239–2252, doi:10.1029/JZ064i012p02239.

Ebihara, Y., and M. Ejiri (2000), Simulation study on fundamental properties of the storm-time ring current, J. Geophys. Res., 105(A7), 15843–15859, doi:10.1029/1999JA900493.

Ebihara, Y., M. Ejiri, H. Nilsson, I. Sandahl, A. Milillo, M. Grande, J. F. Fennell, and J. L. Roeder (2002), Statistical distribution of the storm-time proton ring current: POLAR measurements, Geophys. Res. Lett., 29(20), 1969, doi:10.1029/2002GL015430.

Ebihara, Y. and M. Ejiri (2003), Numerical simulation of the ring current: Review, Space Sci. Rev., 105, 377-452.

Ebihara, Y., M.-C. Fok, J. B. Blake, and J. F. Fennell (2008), Magnetic coupling of the ring current and the radiation belt, J. Geophys. Res., 113, A07221, doi:10.1029/2008JA013267.

Ebihara, Y., S. Kasahara, K. Seki, Y. Miyoshi, T. A. Fritz, J. Chen, M. Grande, and T. H. Zurbuchen (2009), Simultaneous entry of oxygen ions originating from the Sun and Earth into the inner magnetosphere during magnetic storms, J. Geophys. Res., 114, A05219, doi:10.1029/2009JA014120.

Ejiri, M. (1978), Trajectory traces of charged particles in the magnetosphere, J. Geophys. Res., 83(A10), 4798–4810, doi:10.1029/JA083iA10p04798.

Elkington, S. R., M. K. Hudson, and A. A. Chan (1999), Acceleration of relativistic electrons via drift-resonant interaction with toroidal-mode Pc-5 ULF oscillations, Geophys. Res. Lett., 26 (21), 3273.

Elkington, S. R., M. K. Hudson, and A. A. Chan (2003), Resonant acceleration and diffusion of outer zone electrons in an asymmetric geomagnetic field, J. Geophys. Res., 108 (A3), 1116, doi:10.1029/2001JA009202.

Fälthammar, C.-G. (1965), Effects of time-dependent electric fields on geomagnetically trapped radiation, J. Geophys. Res., 70(11), 2503–2516, doi:10.1029/JZ070i011p02503.

Fennell, J. F., J. L. Roeder, M. Grande, and B. Wilken (1996), Oxygen charge state abundance in the inner magnetosphere, AIP Conference Proceedings 383, 145, doi:10.1063/1.51527.

Fennell, J. F., J. B. Blake, R. Friedel, and S. Kanekal (2005), The energetic electron response to magnetic storms: HEO satellite observations. in Physics and Modeling of the Inner Magnetosphere, AGU monograph 115, 87.

Fennell, J. F., Claudepierre, S. G., Blake, J. B., O'Brien, T. P., Clemmons, J. H., Baker, D. N., Spence, H. E. and Reeves, G. D. (2015), Van Allen Probes show that the inner radiation zone contains no MeV electrons: ECT/MagEIS data. Geophys. Res. Lett., 42: 1283–1289. doi:10.1002/2014GL062874.

Frank, L. A. (1967a), Initial observations of low-energy electrons in the Earth's magnetosphere with OGO 3, J. Geophys. Res., 72(1), 185–195, doi:10.1029/JZ072i001p00185.

Frank, L. A. (1967b), On the extraterrestrial ring current during geomagnetic storms, J. Geophys. Res., 72(15), 3753–3767, doi:10.1029/JZ072i015p03753.

Fujimoto, M., and A. Nishida (1990), Energization and anisotropization of energetic electrons in the Earth's radiation belt by the recirculation process, J. Geophys. Res., 95(A4), 4265–4270.

Funsten, H. O., et al. (2013), Helium, Oxygen, Proton, and Electron (HOPE) Mass Spectrometer for the Radiation Belt Storm Probes Mission, Space Sci. Rev., doi:10.1007/s11214-013-9968-7.

Gannon, J. L., X. Li, and D. Heynderickx (2007), Pitch angle distribution analysis of radiation belt electrons based on Combined Release and Radiation Effects Satellite Medium Electrons A data, J. Geophys. Res., 112, A05212, doi:10.1029/2005JA011565.

Ganushkina, N. Yu., T. I. Pulkkinen, M. V. Kubyshkina, H. J. Singer, and C. T. Russell (2004), Long-term evolution of magnetospheric current systems during storms. Ann. Geophys., 22 (4), 1317-1334.

Gerrard, A., L. Lanzerotti, M. Gkioulidou, D. Mitchell, J. Manweiler, and J. Bortnik (2014), Quiet time observations of He ions in the inner magnetosphere as observed from the RBSPICE instrument aboard the Van Allen Probes mission, Geophys. Res. Lett., 41, 1100–1105, doi:10.1002/2013GL059175.

Gerrard, A., L. Lanzerotti, M. Gkioulidou, D. Mitchell, J. Manweiler, J. Bortnik, and K. Keika (2014), Initial measurements of O-ion and He-ion decay rates observed from the Van Allen Probes RBSPICE instrument, J. Geophys. Res. Space Physics, 119, 8813–8819, doi:10.1002/2014JA020374.

Gkioulidou, M., A. Y. Ukhorskiy, D. G. Mitchell, T. Sotirelis, B. H. Mauk, and L. J. Lanzerotti (2014), The role of small-scale ion injections in the buildup of Earth's ring current pressure: Van Allen Probes observations of the 17 March 2013 storm, J. Geophys. Res. Space Physics, 119, 7327–7342, doi:10.1002/2014JA020096.

Gkioulidou, M., S. Ohtani, D. G. Mitchell, A. Y. Ukhorskiy, G. D. Reeves, D. L. Turner, J. W. Gjerloev, M. Nosé, K. Koga, J. V. Rodriguez, and L. J. Lanzerotti (2015), Spatial structure and temporal evolution of energetic particle injections in the inner magnetosphere during the 14 July 2013 substorm event. J. Geophys. Res. Space Physics, 120, 1924–1938. doi:10.1002/2014JA020872.

Gloeckler, G., F. M. Ipavich, B. Wilken, W. Stuedemann, and D. Hovestadt (1985), First composition measurement of the bulk of the storm-time ring current (1 to 300 keV/e) with AMPTE-CCE, Geophys. Res. Lett., 12, 325–328, doi:10.1029/GL012i005p00325.

Greenspan, M. E., and D. C. Hamilton (2000), A test of the Dessler-Parker-Sckopke relation during magnetic storms, J. Geophys. Res., 105(A3), 5419–5430, doi:10.1029/1999JA000284.

Greenspan, M. E., and D. C. Hamilton (2002), Relative contributions of H^+ and O^+ to the ring current energy near magnetic storm maximum, J. Geophys. Res., 107(A4), doi:10.1029/2001JA000155.

Hamilton, D. C., G. Gloeckler, F. M. Ipavich, B. Wilken, and W. Stuedemann (1988), Ring current development during the great geomagnetic storm of February 1986, J. Geophys. Res., 93, 14,343–14,355, doi:10.1029/JA093iA12p14343.

Hanser, F. A. (2011), EPS/HEPAD calibration and data handbook, Tech. Rep. GOESN-ENG-048D, Assurance Technology Corporation, Carlisle, Mass.

Horne, R. B., and R. M. Thorne (1998), Potential waves for relativistic electron scattering and stochastic acceleration during magnetic storms, Geophys. Res. Lett., 25, 3011, 1998.

Horne, R. B., N. P. Meredith, R. M. Thorne, D. Heynderickx, R. H. A. Iles, and R. R. Anderson (2003), Evolution of energetic electron pitch angle distributions during storm time electron acceleration to megaelectronvolt energies, J. Geophys. Res., 108(A1), 1016, doi:10.1029/2001JA009165.

Horne, R. B., R. M. Thorne, S. A. Glauert, J. M. Albert, N. P. Meredith, and R. R. Anderson (2005), Timescale for radiation belt electron acceleration by whistler mode chorus waves, J. Geophys. Res., 110, A03225, doi:10.1029/2004JA010811.

Horne, R. B., R. M. Thorne, S. A. Glauert, N. P. Meredith, D. Pokhotelov, and O. Santolik (2007), Electron acceleration in the Van Allen radiation belts by fast magnetosonic waves, Geophys. Res. Lett., 34, L17107, doi:10.1029/2007GL030267.

Hudson, M. K., A. D. Kotelnikov, X. Li, I. Roth, M. Temerin, J. Wygant, J. B. Blake, and M. S. Gussenhoven (1995), Simulation of proton radiation belt formation during the March 24, 1991 SSC, Geophys. Res. Lett., 22, 291–294, doi:10.1029/95GL00009.

Hudson, M.K., S.R. Elkington, J.G. Lyon, and C.C. Goodrich (2000), Increase in relativistic electron flux in the inner magnetosphere: ULF wave mode structure, Adv. Space Res., 25 (12), 2327.

Iles, R. H. A., A. N. Fazakerley, A. D. Johnstone, N. P. Meredith, and P. Bühler (2002), The relativistic electron response in the outer radiation belt during magnetic storms, Ann. Geophysicae, 20, 957–965.

Jaynes, A. N., et al. (2015), Source and seed populations for relativistic electrons: Their roles in radiation belt changes, J. Geophys. Res. Space Physics, 120, 7240–7254, doi:10.1002/2015JA021234.

Jordanova, V. K., C. J. Farrugia, R. M. Thorne, G. V. Khazanov, G. D. Reeves, and M. F. Thomsen (2001), Modeling ring current proton precipitation by electromagnetic ion cyclotron waves during the May 14–16, 1997, storm, J. Geophys. Res., 106(A1), 7–22, doi:10.1029/2000JA002008.

Jordanova, V. K., and Y. S. Miyoshi (2005), Relativistic model of ring current and radiation belt ions and electrons: Initial results, Geophys. Res. Lett., 32, L14104, doi:10.1029/2005GL023020.

Jorgensen, A., H. Spence, M. Henderson, G. Reeves, M. Sugiura, and T. Kamei (1997), Global Energetic Neutral Atom (ENA) measurements and their association with the Dst index, Geophys. Res. Lett., 24, 3173– 3176, doi:10.1029/97GL03095.

Jorgensen, A. M., M. G. Henderson, E. C. Roelof, G. D. Reeves, and H. E. Spence (2001), Charge exchange contribution to the decay of the ring current, measured by energetic neutral atoms (ENAs), J. Geophys. Res., 106(A2), 1931–1937, doi:10.1029/2000JA000124.

Jorgensen, A. M., H. E. Spence, W. J. Hughes, and H. J. Singer (2004), A statistical study of the global structure of the ring current, J. Geophys. Res., 109, A12204, doi:10.1029/2003JA010090.

Kellogg, P. J. (1960), Electrons of the Van Allen radiation, J. Geophys. Res., 65(9), 2705–2713.

Kessel, R. L., N. J. Fox, and M. Weiss (2013), The Radiation Belt Storm Probes (RBSP) and space weather, Space Sci. Rev., 179(1-4), 531–543, doi:10.1007/s11214-012-9953-6.

Kim, H.-J., and A. A. Chan (1997), Fully adiabatic changes in storm time relativistic electron fluxes, J. Geophys. Res., 102, 22,107-22,116, doi:10.1029/97JA01814.

Kim, K.-C., Y. Shprits, D. Subbotin, and B. Ni (2011), Understanding the dynamic evolution of the relativistic electron slot region including radial and pitch angle diffusion, J. Geophys. Res., 116, A10214, doi:10.1029/2011JA016684.

Kivelson, M. G., and C. T. Russell (1995), Introduction to Space Physics, Cambridge Univ. Press, Cambridge, U. K. Korth, H., M. F. Thomsen, J. E. Borovsky, and D. J. McComas (1999), Plasma sheet access to geosynchronous orbit, J. Geophys. Res., 104(A11), 25047–25061, doi:10.1029/1999JA900292.

Korth, H., M. F. Thomsen, J. E. Borovsky, and D. J. McComas (1999), Plasma sheet access to geosynchronous orbit, J. Geophys. Res., 104(A11), 25047–25061, doi:10.1029/1999JA900292.

Korth, A., R. H. W. Friedel, C. G. Mouikis, J. F. Fennell, J. R. Wygant, and H. Korth (2000), Comprehensive particle and field observations of magnetic storms at different local times from the CRRES spacecraft, J. Geophys. Res., 105(A8), 18729–18740, doi:10.1029/1999JA000430.

Kozyra, J. U., V. K. Jordanova, J. E. Borovsky, M. F. Thomsen, D. J. Knipp, D. S. Evans, D. J. McComas, and T. E. Cayton (1998), Effects of a high-density plasma sheet on ring current development during the November 2–6, 1993, magnetic storm, J. Geophys. Res., 103(A11), 26285–26305, doi:10.1029/98JA01964.

Krimigis, S. M., G. Gloeclker, R. W. McEntire, T. A. Potemra, F. L. Scarf, and E. G. Shelley (1985), The magnetic storm of September 4, 1984, a synthesis of ring current spectra and energy densities measured with AMPTE/CCE, Geophys. Res. Lett., 12(5), 329–332, doi:10.1029/GL012i005p00329.

Langel, R. A., and R. H. Estes (1985), Large-scale, near-field magnetic fields from external sources and the corresponding induced internal field, J. Geophys. Res., 90(B3), 2487–2494, doi:10.1029/JB090iB03p02487.

Li, H., C. Wang, and J. R. Kan (2011), Contribution of the partial ring current to the SYMH index during magnetic storms, J. Geophys. Res., 116, A11222, doi:10.1029/2011JA016886.

Li, W., Y. Y. Shprits, and R. M. Thorne (2007), Dynamic evolution of energetic outer zone electrons due to wave-particle interactions during storms, J. Geophys. Res., 112, A10220, doi:10.1029/2007JA012368.

Li, X., I. Roth, M. Temerin, J. Wygant, M. K. Hudson, and J. B. Blake (1993), Simulation of the prompt energization and transport of radiation belt particles during the March 24, 1991 SSC, Geophys. Res. Lett., 20, 2423-2426.

Li, X., M. Hudson, A. Chan, and I. Roth (1993), Loss of ring current O^+ ions due to interaction with Pc 5 waves, J. Geophys. Res., 98(A1), 215–231, doi:10.1029/92JA01540.

Li, X., D. N. Baker, M. Temerin, T. E. Cayton, E. G. D. Reeves, R. A. Christensen, J. B. Blake, M. D. Looper, R. Nakamura, and S. G. Kanekal (1997), Multisatellite observations of the outer zone electron variation during the November 3–4, 1993, magnetic storm, J. Geophys. Res., 102(A7), 14123–14140, doi:10.1029/97JA01101.

Li, X., M. Temerin, D. N. Baker, G. D. Reeves, and D. Larson (2001), Quantitative prediction of radiation belt electrons at geostationary orbit based on solar wind measurements, Geophys. Res. Lett., 28(9), 1887–1890.

Li, X., K. S. Oh, and M. Temerin (2007), Prediction of the AL index using solar wind parameters, J. Geophys. Res., 112, A06224, doi:10.1029/2006JA011918.

Li, X., A. B. Barker, D. N. Baker, W. C. Tu, T. E. Sarris, R. S. Selesnick, R. Friedel, and C. Shen (2009), Modeling the deep penetration of outer belt electrons during the “Halloween” magnetic storm in 2003, Space Weather, 7, S02004, doi:10.1029/2008SW000418.

Li, X., M. Temerin, D. N. Baker, and G. D. Reeves (2011), Behavior of MeV electrons at geosynchronous orbit during last two solar cycles, J. Geophys. Res., 116, A11207, doi:10.1029/2011JA016934.

Li, X., Selesnick, R. S., Baker, D. N., Jaynes, A. N., Kanekal, S. G., Schiller, Q., Blum, L., Fennell, J. and Blake, J. B. (2015), Upper limit on the inner radiation belt MeV electron intensity. J. Geophys. Res. Space Physics, 120: 1215–1228. doi:10.1002/2014JA020777.

Liemohn, M. W., J. U. Kozyra, M. F. Thomsen, J. L. Roeder, G. Lu, J. E. Borovsky, and T. E. Cayton (2001a), Dominant role of the asymmetric ring current in producing the stormtime Dst*, J. Geophys. Res., 106(A6), 10883–10904, doi:10.1029/2000JA000326.

Liemohn, M. W., J. U. Kozyra, C. R. Clauer, and A. J. Ridley (2001b), Computational analysis of the near-Earth magnetospheric current system during two-phase decay storms, J. Geophys. Res., 106(A12), 29531–29542, doi:10.1029/2001JA000045.

Liemohn, M. W. (2003), Yet another caveat to using the Dessler-Parker-Sckopke relation, J. Geophys. Res., 108(A6), 1251, doi:10.1029/2003JA009839.

Liu, S., M. W. Chen, J. L. Roeder, L. R. Lyons, and M. Schulz (2005), Relative contribution of electrons to the stormtime total ring current energy content, Geophys. Res. Lett., 32, L03110, doi:10.1029/2004GL021672.

Lorentzen, K. R., J. B. Blake, U. S. Inan, and J. Bortnik (2001), Observations of relativistic electron microbursts in association with VLF chorus, J. Geophys. Res., 106, 6017.

Lui, A. T. Y. (2003), Inner magnetospheric plasma pressure distribution and its local time asymmetry, Geophys. Res. Lett., 30(16), 1846, doi:10.1029/2003GL017596.

Lundin, R., Lyons, L. R. and Pissarenko, N. (1980), Observations of the ring current composition at L < 4. Geophys. Res. Lett., 7: 425–428. doi:10.1029/GL007i006p00425.

Luo, B., X. Li, M. Temerin, and S. Liu (2013), Prediction of the AU, AL, and AE indices using solar wind parameters, J. Geophys. Res. Space Physics, 118, 7683–7694, doi:10.1002/2013JA019188.

Lyons, L. R., R. M. Thorne, and C. F. Kennel (1972), Pitch-angle diffusion of radiation belt electrons within the plasmasphere, J. Geophys. Res., 77(19), 3455–3474, doi:10.1029/JA077i019p03455.

Lyons, L. R., and R. M. Thorne (1973), Equilibrium structure of radiation belt electrons, J. Geophys. Res., 78(13), 2142–2149, doi:10.1029/JA078i013p02142.

Lyons, L. R., and D. J. Williams (1975a), The quiet time structure of energetic (35-560 keV) radiation belt electrons, J. Geophys. Res., 80(7), 943–950.

Lyons, L. R., and D. J. Williams (1975b), The storm and poststorm evolution of energetic (35-560 keV) radiation belt electron distributions, J. Geophys. Res., 80(28), 3985–3994.

Lyons, L. R., and D. J. Williams (1976), Storm-associated variations of equatorially mirroring ring current protons, 1–800 keV, at constant first adiabatic invariant, J. Geophys. Res., 81(1), 216–220, doi:10.1029/JA081i001p00216.

Lyons, L. R. (1977), Adiabatic evolution of trapped particle pitch angle distributions during a storm main phase, J. Geophys. Res., 82(16), 2428–2432.

Lyons, L. R., and D. J. Williams (1980), A source for the geomagnetic storm main phase ring current, J. Geophys. Res., 85(A2), 523–530, doi:10.1029/JA085iA02p00523.

Lyons, L. R., and D. J. Williams (1984), Quantitative aspects of magnetospheric physics, Springer, New York.

Ma, Q., W. Li, R. M. Thorne, and V. Angelopoulos (2013), Global distribution of equatorial magnetosonic waves observed by THEMIS, Geophys. Res. Lett., 40, 1895–1901, doi:10.1002/grl.50434.

Mauk, B. H., N. J. Fox, S. G. Kanekal, R. L. Kessel, D. G. Sibeck, and A. Ukhorskiy (2012), Science objectives and rationale for the radiation belt storm probes mission, Space Sci. Rev., 1–15, doi:10.1007/s11214-012-9908-y.

McIlwain, C. E. (1961), Coordinates for mapping the distribution of magnetically trapped particles, J. Geophys. Res., 66(11), 3681–3691, doi:10.1029/JZ066i011p03681.

Meredith, N. P., R. B. Horne, R. M. Thorne, D. Summers, and R. R. Anderson (2004), Substorm dependence of plasmaspheric hiss, J. Geophys. Res., 109, A06209, doi:10.1029/2004JA010387.

Meredith, N. P., R. B. Horne, S. A. Glauert, R. M. Thorne, D. Summers, J. M. Albert, and R. R. Anderson (2006), Energetic outer zone electron loss timescales during low geomagnetic activity, J. Geophys. Res., 111, A05212, doi:10.1029/2005JA011516.

Meredith, N. P., R. B. Horne, S. A. Glauert, and R. R. Anderson (2007), Slot region electron loss timescales due to plasmaspheric hiss and lightning-generated whistlers, J. Geophys. Res., 112, A08214, doi:10.1029/2007JA012413.

Meredith, N. P., R. B. Home, S. A. Glauert, D. N. Baker, S. G. Kanekal, and J. M. Albert (2009), Relativistic electron loss timescales in the slot region, J. Geophys. Res., 114, A03222, doi:10.1029/2008JA013889.

Mitchell, D., et al. (2013), Radiation Belt Storm Probes Ion Composition Experiment (RBSPICE), Space Sci. Rev., 179, 263–308, doi:10.1007/s11214-013-9965-x.

Miyoshi, Y., and R. Kataoka (2005), Ring current ions and radiation belt electrons during geomagnetic storms driven by coronal mass ejections and co-rotating interaction regions, Geophys. Res. Lett., 32, L21105, doi:10.1029/2005GL024590.

Morioka, A., H. Misawa, Y. Miyoshi, H. Oya, M. Iizima, and T. Nagai (2001), Pitch angle distribution of relativistic electrons in the inner radiation belt and its relation to equatorial plasma wave turbulence phenomena, Geophys. Res. Lett., 28(5), 931–934.

Mourenas, D., A. V. Artemyev, O. V. Agapitov, and V. Krasnoselskikh (2013), Analytical estimates of electron quasilinear diffusion by fast magnetosonic waves, J. Geophys. Res. Space Physics, 118, 3096–3112, doi:10.1002/jgra.50349.

R. Nakamura, J. B. Blake, S. R. Elkington, D. N. Baker, W. Baumjohann, and B. Klecker (2002), Relationship between ULF waves and radiation belt electrons during the March 10, 1998, storm, Adv. Space Res., 30 (10), 2163-2168.

Newell, P. T., T. Sotirelis, K. Liou, C.-I. Meng, and F. J. Rich (2007), A nearly universal solar wind-magnetosphere coupling function inferred from 10 magnetospheric state variables, J. Geophys. Res., 112, A01206, doi:10.1029/2006JA012015.

Nishida, A. (1976), Outward diffusion of energetic particles from the Jovian radiation belt, J. Geophys. Res., 81(10), 1771–1773.

O'Brien, T. P., and M. B. Moldwin (2003), Empirical plasmapause models from magnetic indices, Geophys. Res. Lett., 30(4), 1152, doi:10.1029/2002GL016007.

O'Brien, T. P., and R. L. McPherron (2000), An empirical phase space analysis of ring current dynamics: Solar wind control of injection and decay, J. Geophys. Res., 105(A4), 7707–7719, doi:10.1029/1998JA000437.

O'Brien, T. P., M. D. Looper, and J. B. Blake (2004), Quantification of relativistic electron microbursts losses during the GEM storms, Geophys. Res. Lett., 31, L04802, doi:10.1029/2003GL018621.

Ozeke, L. G., I. R. Mann, K. R. Murphy, I. J. Rae, D. K. Milling, S. R. Elkington, A. A. Chan, and H. J. Singer (2012), ULF wave derived radiation belt radial diffusion coefficients, J. Geophys. Res., 117, A04222, doi:10.1029/2011JA017463.

Pfitzer, K. A., and J. R. Winckler (1968), Experimental observation of a large addition to the electron inner radiation belt after a solar flare event, J. Geophys. Res., 73(17), 5792–5797.

Pizzella, G., C. D. Laughlin, and B. J. O'Brien (1962), Note on the electron energy spectrum in the inner Van Allen belt, J. Geophys. Res., 67(9), 3281–3287.

Reeves, G. D., K. L. McAdams, R. H. W. Friedel, and T. P. O'Brien (2003), Acceleration and loss of relativistic electrons during geomagnetic storms, Geophys. Res. Lett., 30(10), 1529, doi:10.1029/2002GL016513.

Roeder, J. L., J. F. Fennell, M. W. Chen, M. Schulz, M. Grande, and S. Livi (1996), CRRES observations of the composition of the ring-current ion populations, Adv. Space Res., 17(10), 17–24, doi:10.1016/0273-1177(95)00689-C.

Roederer, J. G. (1970), Dynamics of Geomagnetically Trapped Radiation, Springer, New York.

Roederer, J. G., H. H. Hilton, and M. Schulz (1973), Drift shell splitting by internal geomagnetic multipoles, J. Geophys. Res., 78(1), 133–144, doi:10.1029/JA078i001p00133.

Sauvaud, J. A., T. Moreau, R. Maggiolo, J.-P. Treilhou, C. Jacquey, A. Cros, J. Coutelier, J. Rouzaud, E. Penou, and M. Gangloff (2006), Highenergy electron detection onboard

DEMETER: The IDP spectrometer, description and first results on the inner belt, Planet. Space Sci., 54, 502–511.

Sauvaud, J.-A., R. Maggiolo, C. Jacquey, M. Parrot, J.-J. Berthelier, R. J. Gamble, and C. J. Rodger (2008), Radiation belt electron precipitation due to VLF transmitters: Satellite observations, Geophys. Res. Lett., 35, L09101, doi:10.1029/2008GL033194.

Schulz, M., and L. Lanzerotti (1974), Particle Diffusion in the Radiation Belts, Springer, New York.

Sckopke, N. (1966), A general relation between the energy of trapped particles and the disturbance field near the Earth, J. Geophys. Res., 71(13), 3125–3130, doi:10.1029/JZ071i013p03125.

Selesnick, R. S., and J. B. Blake (2002), Relativistic electron drift shell splitting, J. Geophys. Res., 107(A9), 1265, doi:10.1029/2001JA009179.

Selesnick, R. S. (2012), Atmospheric scattering and decay of inner radiation belt electrons, J. Geophys. Res., 117, A08218, doi:10.1029/2012JA017793.

Selesnick, R. S., J. M. Albert, and M. J. Starks (2013), Influence of a ground-based VLF radio transmitter on the inner electron radiation belt, J. Geophys. Res. Space Physics, 118, 628–635, doi:10.1002/jgra.50095.

Selesnick, R. S., D. N. Baker, A. N. Jaynes, X. Li, S. G. Kanekal, M. K. Hudson, and B. T. Kress (2014), Observations of the inner radiation belt: CRAND and trapped solar protons, J. Geophys. Res. Space Physics, 119, 6541–6552, doi:10.1002/2014JA020188.

Sheldon, R. B., and D. C. Hamilton (1993), Ion transport and loss in the Earth's quiet ring current: 1. Data and standard model, J. Geophys. Res., 98(A8), 13491–13508, doi:10.1029/92JA0286.

Shprits, Y. Y., R. M. Thorne, R. Friedel, G. D. Reeves, J. Fennell, D. N. Baker, and S. G. Kanekal (2006), Outward radial diffusion driven by losses at magnetopause, J. Geophys. Res., 111, A11214, doi:10.1029/2006JA011657.

Shprits, Y. Y., D. A. Subbotin, N. P. Meredith, and S. R. Elkington (2008), Review of modeling of losses and sources of relativistic electrons in the outer radiation belt II: Local acceleration and loss, J. Atmos. Sol. Terr. Phys., 70(14), 1694–1713, doi:10.1016/j.jastp.2008.06.014.

Shprits, Y. Y. (2009), Potential waves for pitch-angle scattering of near-equatorially mirroring energetic electrons due to the violation of the second adiabatic invariant, Geophys. Res. Lett., 36, L12106, doi:10.1029/2009GL038322.

Sibeck, D. G., R. W. McEntire, A. T. Y. Lui, R. E. Lopez, and S. M. Krimigis (1987), Magnetic field drift shell splitting: Cause of unusual dayside particle pitch angle distributions

during storms and substorms, J. Geophys. Res., 92(A12), 13,485–13,497, doi:10.1029/JA092iA12p13485.

Smith, P. H., and R. A. Hoffman (1973), Ring current particle distributions during the magnetic storms of December 16-18, 1971, J. Geophys. Res., 78(22), 4731-4737.

Smith, P. H., and R. A. Hoffman (1974), Direct observations in the dusk hours of the characteristics of the storm time ring current particles during the beginning of magnetic storms, J. Geophys. Res., 79(7), 966–971, doi:10.1029/JA079i007p00966.

Smith, P. H., and N. K. Bewtra (1978), Charge exchange lifetimes for ring current ions, Space Sci. Rev., 22, 301.

Smith, P. H., N. K. Bewtra, and R. A. Hoffman (1981), Inference of the ring current ion composition by means of charge exchange decay, J. Geophys. Res., 86(A5), 3470–3480, doi:10.1029/JA086iA05p03470.

Spence, H. E., et al. (2013), Science goals and overview of the energetic particle, composition, and thermal plasma (ECT) suite on NASA's radiation belt storm probes (RBSP) mission, Space Sci. Rev., doi:10.1007/s11214-013-0007-5.

Sugiura, M., and T. Kamei (1991), Equatorial Dst Index 1957–1986, IAGA Bull., 40, ISGI, Saint-Maur-des-Fosses, France.

Temerin, M., and X. Li (2002), A new model for the prediction of Dst on the basis of the solar wind, J. Geophys. Res., 107(A12), 1472, doi:10.1029/2001JA007532.

Temerin, M., and X. Li (2006), Dst model for 1995–2002, J. Geophys. Res., 111, A04221, doi:10.1029/2005JA011257.

Temerin M. and X. Li (2015), The Dst index underestimates the solar cycle variation of geomagnetic activity, J. Geophys. Res. Space Physics, 120, doi:10.1002/2015JA021467.

Temporin, A., and Y. Ebihara (2011), Energy-dependent evolution of ring current protons during magnetic storms, J. Geophys. Res., 116, A10201, doi:10.1029/2011JA016692.

Thorne, R. M., T. P. O'Brien, Y. Y. Shprits, D. Summers, and R. B. Horne (2005), Timescale for MeV electron microburst loss during geomagnetic storms, J. Geophys. Res., 110, A09202, doi:10.1029/2004JA010882

Thorne, R. M. (2010), Radiation belt dynamics: The importance of wave-particle interactions, Geophys. Res. Lett., 37, L22107, doi:10.1029/2010GL044990.

Thorne, R. M., et al. (2013), Rapid acceleration of relativistic radiation belt electrons by magnetospheric chorus, Nature, 504, 411–414, doi:10.1038/nature12889.

Tsyganenko, N. A. (1989), A magnetospheric magnetic field model with a warped tail current sheet, Planet. Space Sci., 37, 5-20.

Tsyganenko, N. A., and M. I. Sitnov (2005), Modeling the dynamics of the inner magnetosphere during strong geomagnetic storms, J. Geophys. Res., 110, A03208, doi:10.1029/2004JA010798.

Tu, W., S. R. Elkington, X. Li, W. Liu, and J. Bonnell (2012), Quantifying radial diffusion coefficients of radiation belt electrons based on global MHD simulation and spacecraft measurements, J. Geophys. Res., 117, A10210, doi:10.1029/2012JA017901.

Turner, N. E., D. N. Baker, T. I. Pulkkinen, and R. L. McPherron (2000), Evaluation of the tail current contribution to Dst, J. Geophys. Res., 105(A3), 5431–5439, doi:10.1029/1999JA000248.

Turner, N. E., D. N. Baker, T. I. Pulkkinen, J. L. Roeder, J. F. Fennell, and V. K. Jordanova (2001), Energy content in the storm time ring current, J. Geophys. Res., 106(A9), 19149–19156, doi:10.1029/2000JA003025.

Turner, N. E., W. D. Cramer, S. K. Earles, and B. A. Emery (2009), Geoefficiency and energy partitioning in CIR-driven and CME-driven storms, J. Atmos. Solar-Terr. Phys., 71, 1023–1031.

Turner, D. L., Y. Shprits, M. Hartinger, and V. Angelopoulos (2012), Explaining sudden losses of outer radiation belt electrons during geomagnetic storms, Nat. Phys., 8, 208–212, doi:10.1038/nphys2185.

Tverskaya, L. V. (1986), On the boundary of electron injection into the magnetosphere. Geomagn. Aeron., 26(5), 864–865.

Tverskaya, L. V., N. N. Pavlov, J. B. Blake, R. S. Selesnick, and J. F. Fennell (2003), Predicting the L-position of the storm-injected relativistic electron belt, Adv. Space Res., 31(4), 1039–1044.

Ukhorskiy, A. Y., B. J. Anderson, P. C. Brandt, and N. A. Tsyganenko (2006), Storm time evolution of the outer radiation belt: Transport and losses, J. Geophys. Res., 111, A11S03, doi:10.1029/2006JA011690.

Usanova, M. E., et al. (2014), Effect of EMIC waves on relativistic and ultrarelativistic electron populations: Groundbased and Van Allen Probes observations, Geophys. Res. Lett., 41, 1375–1381, doi:10.1002/2013GL059024.

Vampola, A. L. (1998), Outer zone energetic electron environment update, in Proceedings of the Conference on the High Energy Radiation Background in Space, pp. 128–136, Inst. of Electr. and Electr. Eng., New York.

Walt, M. (1964), The effects of atmospheric collisions on geomagnetically trapped electrons, J. Geophys. Res., 69(19), 3947–3958.

Walt, M., and T. A. Farley (1976), The physical mechanisms of the inner Van Allen belt, Fundam. Cosmic Phys., 2, 1–110.

West, H. I., Jr., R. M. Buck, and J. R. Walton (1972), Observation of the shadowing of electron azimuthal-drift motions near the noon magnetopause, Nature, 240, 6.

West, H. I., Jr., R. M. Buck, and J. R. Walton (1973), Electron pitch angle distributions through the magnetosphere as observed on Ogo 5, J. Geophys. Res., 78, 1064–1081.

Williams, D. J. (1980), Ring current composition and sources, in Dynamics of the Magnetosphere, edited by S.-I. Akasofu, p. 407, D. Reidel Pub. Co., Dordrecht, 1980.

Williams D. J. (1981), Ring current composition and sources: an update, Planet. Space Sci., 29, 1195, 1981.

Wygant et al. (2013), The Electric Field and Waves (EFW) instruments on the Radiation Belt Storm Probes Mission, Space Sci. Rev., 179,183–220, doi:10.1007/s11214-013-0013-7.

Yau, A. W., Peterson, W. K. and Shelley, E. G. (1988), Quantitative Parametrization of Energetic Ionospheric Ion Outflow, in Modeling Magnetospheric Plasma (eds T. E. Moore, J. H. Waite, T. W. Moorehead and W. B. Hanson), American Geophysical Union, Washington, D. C.. doi:10.1029/GM044p0211.

Yu, Y., J. Koller, S. Zaharia, and V. Jordanova (2012), L* neural networks from different magnetic field models and their applicability, Space Weather, 10, S02014, doi:10.1029/2011SW000743.

Zhao, H., Q. G. Zong, Y. Wei, and Y. Wang (2011), Influence of solar wind dynamic pressure on geomagnetic Dst index during various magnetic storms, Sci. China Tech. Sci., 54, 1445-1454, doi:10.1007/s11431-011-4319-y.

Zhao, H., and X. Li (2013a), Inward shift of outer radiation belt electrons as a function of Dst index and the influence of the solar wind on electron injections into the slot region, J. Geophys. Res. Space Physics, 118, 756–764, doi:10.1029/2012JA018179.

Zhao, H., and X. Li (2013b), Modeling energetic electron penetration into the slot region and inner radiation belt, J. Geophys. Res. Space Physics, 118, 6936–6945, doi:10.1002/2013JA019240.

Zhao, H., X. Li, J. B. Blake, J. F. Fennell, S. G. Claudepierre, D. N. Baker, A. N. Jaynes, D. M. Malaspina, and S. G. Kanekal (2014a), Peculiar pitch angle distribution of relativistic electrons in the inner radiation belt and slot region, Geophys. Res. Lett., 41, 2250–2257, doi:10.1002/2014GL059725.

Zhao, H., X. Li, J. B. Blake, J. F. Fennell, S. G. Claudepierre, D. N. Baker, A. N. Jaynes, and D. M. Malaspina (2014b), Characteristics of pitch angle distributions of hundreds of keV electrons in the slot region and inner radiation belt, J. Geophys. Res. Space Physics, 119, 9543–9557, doi:10.1002/2014JA020386.

Zhao, H., X. Li, D. N. Baker, J. F. Fennell, J. B. Blake, B. A. Larsen, R. Skoug, H. Funsten, R. H. Friedel, G. D. Reeves, H. Spence, D. Mitchell, L. J. Lanzerotti, and J. Rodriguez (2015a),

The evolution of ring current ion energy density and energy content during geomagnetic storms based on Van Allen Probes measurements, J. Geophys. Res. Space Physics, 120, doi:10.1002/2015JA021533.

Zhao, H., X. Li, D. N. Baker, S. G. Claudepierre, J. F. Fennell, J. B. Blake, B. A. Larsen, R. Skoug, H. Funsten, R. H. Friedel, G. D. Reeves, H. Spence, D. Mitchell, and L. J. Lanzerotti (2015b), Ring current electron dynamics during geomagnetic storms based on the Van Allen Probes measurements, to be submitted to J. Geophys. Res. Space Physics.

Zheng, Y., A. T. Y. Lui, X. Li, and M.-C. Fok (2006), Characteristics of 2–6 MeV electrons in the slot region and inner radiation belt, J. Geophys. Res., 111, A10204, doi:10.1029/2006JA011748

Appendix A

An Empirical Model of 100s of KeV Electron Pitch Angle Distributions in the Inner Radiation Belt and Slot Region

A.1 Introduction

The electron pitch angle distribution reflects the effects of different physical processes and the competition between them in a specific region. Understanding the evolution of pitch angle distributions can contribute to the identifying and understanding of those processes and thus the understanding of the inner magnetospheric dynamics. In Chapter 5, detailed analyses on 100s of keV electron pitch angle distributions in the low L region are performed. In this appendix, using data from MagEIS instruments on the Van Allen Probes, an empirical model of 100s of keV electron equatorial PADs as a function of electron energy, L shell, MLT, and geomagnetic activity is constructed. Following the method used by Chen et al. [2014], we use Legendre polynomials to fit directional fluxes observed near the magnetic equator, and calculate the median and standard deviation of the coefficients. The averaged PADs at different L, MLT, and geomagnetic activity of different energy electrons can be reconstructed using medians of coefficients. This empirical model provides statistical pictures of 100s of keV electron pitch angle distributions at the magnetic equator, sheds light on the physical processes in the low L region, and is very useful in predicting fluxes along a given magnetic field line based on single point measurement.

A.2 Data

In this study, pitch-angle-resolved electron flux data from MagEIS instruments on the Van Allen Probes are used. MagEIS provides high-resolution energetic electron flux measurement with energy range of ~35 – 4000 keV. It contains four independent magnetic electron spectrometers on each spacecraft, one low energy spectrometer (LOW), two medium energy spectrometers (M75 and M35) and a high energy spectrometer (HIGH). The low unit,

high unit, and one of the medium units (M75) are mounted with the field of view centered at 75 ° to the spin axis, while the field of view of another medium unit (M35) is centered at 35 °to provide larger PA coverage. Since our goal is to investigate the equatorial PADs, we only use data when Van Allen Probes are near the magnetic equator with magnetic latitude < 10 °, and propagate the electron PADs to the magnetic equator using T89 magnetic field model [Tsyganenko, 1989]. Then data are averaged into time bins of 1 min and PA bins of 10 °and are forced to be symmetric.

A.3 Methodology

To construct a statistical model for relativistic electron PADs, the PADs need to be quantified. One way to quantify the PADs is fitting PADs to Legendre polynomials. The electron PADs can be expressed as

$$j(\alpha) = \sum_{n=0}^{\infty} C_n P_n[\cos(\alpha)]$$

where $j(\alpha)$ is the flux of electrons with pitch angle α, $P_n[\cos(\alpha)]$ is the nth-degree Legendre polynomial, and C_n is the corresponding coefficient. The coefficient of each Legendre polynomial can be calculated using the orthogonal property:

$$C_n = \frac{2n+1}{2}\int_0^{\pi} j(\alpha) P_n[\cos(\alpha)]\sin(\alpha)d\alpha$$

The coefficients derived using this equation are then normalized as

$$c_n = \frac{C_n}{C_0}$$

Here C_0 is the actual directionally averaged flux.

Any PAD can be fully represented by a whole set of Legendre polynomials. However, in a statistical model we can only keep finite number of coefficients and the number of coefficients should be kept as small as possible. Based on the previous study [Chen et al., 2014], C_n decreases quickly with increasing n, and including the Legendre polynomials up to 6th degree is enough to reproduce most observed PADs in the outer radiation belt. Some example fits of three

major PAD types in the outer radiation belt are shown in Figure A.1, along with the coefficients c_0 - c_6 and root-mean-square deviation (RMSD) of each fit. The RMSD is calculated as

$$RMSD = \sqrt{\frac{\sum_n (log(\hat{j}) - log(j))^2}{n}}$$

where j is the measured flux and $\hat{j}$ is the fitting result. The RMSD overall is very small, showing good fitting results. As shown in Figure A.1, normal PADs usually have large negative c_2 with near zero c_4, and butterfly PADs have large negative c_4 with negligible c_2, while flattop PADs are combinations of these two types, for which c_2 and c_4 are both negative. All coefficients with odd n are 0, which is expected as we impose symmetry of PADs, and this also validates our fitting method.

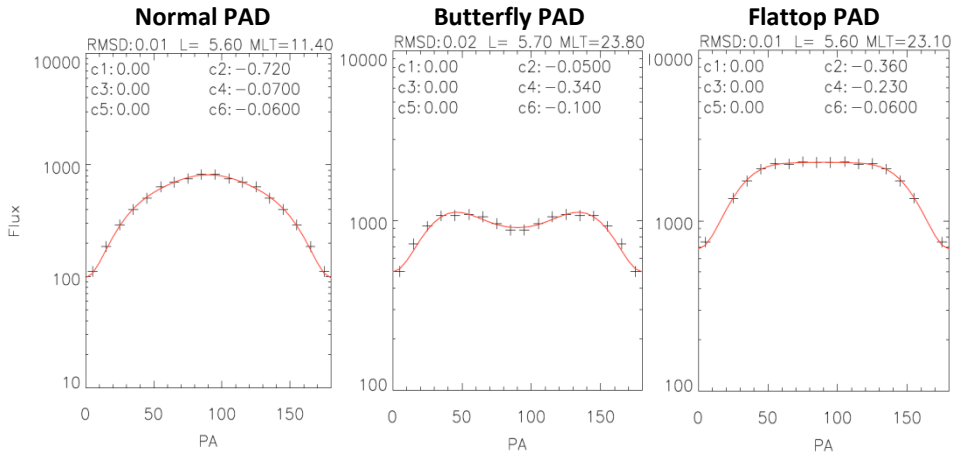

Figure A.1 Example fits of normal, butterfly, and flattop PADs observed in the outer radiation belt. Black dots are data and red curves are fitting results using Legendre polynomials. The RMSD for each fit is shown on the top of each panel, and the coefficients of Legendre polynomials are shown in each panel as well.

However, the situation in the inner belt and slot region is very different. The electron PADs in the inner belt and slot region usually have some detailed features, e.g., 90 °minimum PAD and cap PAD, which cannot be well represented by Legendre polynomials up to 6th degree. Thus for PADs in the low L region (L<3.5) we need to use higher-degree Legendre polynomials. Also, in the low L region the loss cone is very large, within which the fluxes are expected to be close to zero. But the existence of those zeros in the electron PAD will require the PAD to be

fitted to very high-degree Legendre polynomials, which is not realistic when constructing a model. Thus, we simply exclude data within loss cone to do the fitting. Two examples of comparison of different fitting methods in the inner belt and slot region are shown in Figure A.2 and Figure A.3 respectively. It is clear that the fitting results using Legendre polynomials up to 8^{th} degree and data points outside the loss cone fit data much better than the results using 0^{th} to 6^{th} degree Legendre polynomials or using all data points. To give the best fitting results in the low L region, we choose to fit measured PADs to a summation of 0^{th} to 10^{th} degree Legendre polynomials when constructing the model.

In addition, the electron PADs in the radiation belt are expected to be symmetric with respect to 90 °pitch angle. In this study, to give a full coverage on all pitch angles, we average PADs in bins of 10 °PA and force them to be symmetric. Since only even-th degree Legendre polynomials are symmetric, we expect $c_n$with odd n to be 0. Thus in our statistical model, only the statistics of c_n with even n are considered.

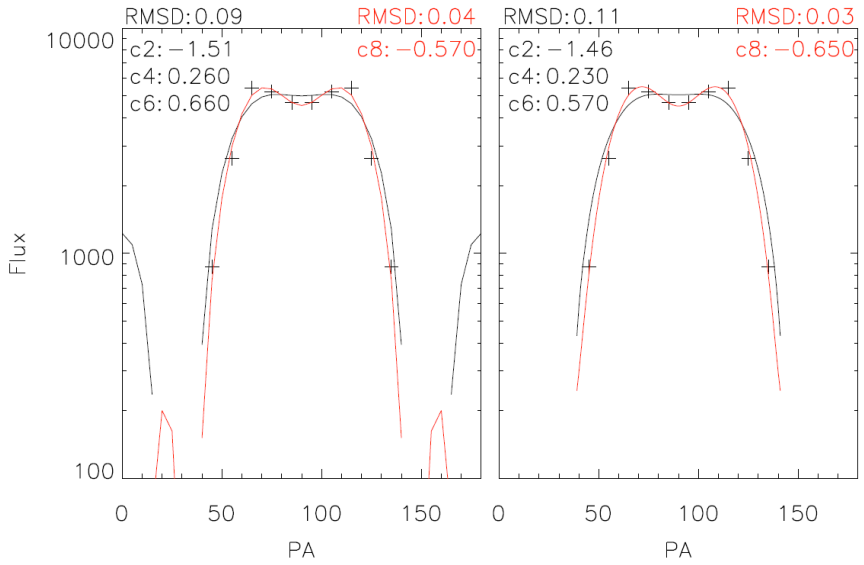

Figure A.2: An example fit of ~460 keV electron PAD at L=1.5. Black dots are data and black (red) curves are fitting results using Legendre polynomials with up to 6^{th} (8^{th}) degree. The left panel shows the fitting results using all data points, while the right panel shows the fitting results using data points outside the loss cone. The RMSD for each fit is shown on the top of each panel, and the coefficients of Legendre polynomials are shown in each panel as well.

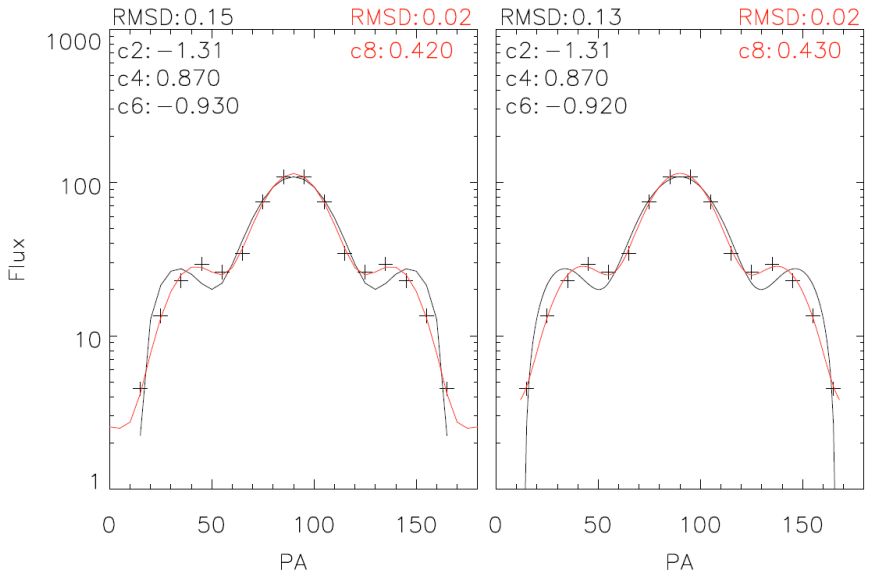

Figure A.3: An example fit of ~460 keV electron PAD at L=3.0. The format is the same as Figure A.2.

The accuracy of our model strongly depends on the accuracy of the fitting results, so we use the PADs that can be well represented by the Legendre polynomials to construct the statistical model. Only good fits with RMSD<0.05 are included in the statistics. According to our results, most fits are valid in the outer belt and inner belt. For example, for MagEIS ~460 keV electrons, less than 10% of fits are rejected due to poor fitting in the outer belt and inner belt. In the slot region, due to the scattered PADs caused by wave-particle interaction, about 30% of fits are rejected due to poor fitting. On the other hand, it is essential to make sure that the fitting results represent the real PADs, so only PADs with full PA coverage are included. PADs with no data points within high PA range [80 °, 100 °] or low PA range [0 °, 20 °]/[160 °, 180 °] are excluded from the statistics.

Based on this fitting method, a statistical relativistic electron equatorial PAD model is constructed as a function of L, MLT, geomagnetic activity and electron energy. The model includes 26 L bins from L=1 to L=6 with ΔL=0.2 and 12 MLT bins with ΔMLT=2. The geomagnetic activity, represented by the geomagnetic index Dst, is divided into three levels. The data of ~ 35 keV – 1 MeV electrons from MagEIS are used to construct the model. The medians

and standard deviations of Legendre polynomial coefficients are derived and recorded in each L and MLT bin for electrons with a specific energy under a specific geomagnetic condition.

A.4 Results

Using the method described in Section A.3, we construct a statistical model for electron PADs as a function of L, MLT, geomagnetic activity, and electron energy using data from Van Allen Probes. Some interesting results are shown and discussed as follows.

Figure A.4 shows the medians of model coefficients c_2 and c_8 as a function of L and MLT for ~460 keV electrons during geomagnetic quiet times (Dst > -20 nT, top panels) and disturbed times (-20 nT > Dst > -50 nT, bottom panels). As can be indicated from Figure A.1, a more negative c_2 generally indicates a more peaked PAD; while a negative c8 suggests the existence of a small bite-out at 90 °PA as shown in Figure A.2. As can be seen in Figure A.4, medians of c_2 are much more negative in the low L region than in the high L region, suggesting more peaked PADs in the low L region which is consistent with our results shown in Chapter 5, and medians of c_8 are negative in the inner belt but almost zero in the outer belt, indicating the existence of 90 ° minimum PADs in the inner belt. Comparing results during quiet times and disturbed times, it is clear that as the geomagnetic activity gets more intense, the region where c_2 is highly negative shrinks to lower L shells. The highly anisotropic PADs at lower L shells are likely to be caused by the plasmaspheric hiss waves which are generally present inside the plasmasphere. The plasmaspheric hiss waves are very effective for electrons with relatively lower energies [e.g., Abel and Thorne, 1998]. As the geomagnetic activity gets more intense, the enhanced convection electric field brings charged particles to dayside through E ×B drift and shrinks the plasmasphere, thus the region with highly 90 °peaked PADs are also confined to lower L regions. Also, during geomagnetic quiet times, the region with negative c_8 is confined in the inner belt; while during disturbed times, the region with negative c_8 expands to the slot region, which is also consistent with our observations shown in Chapter 5.

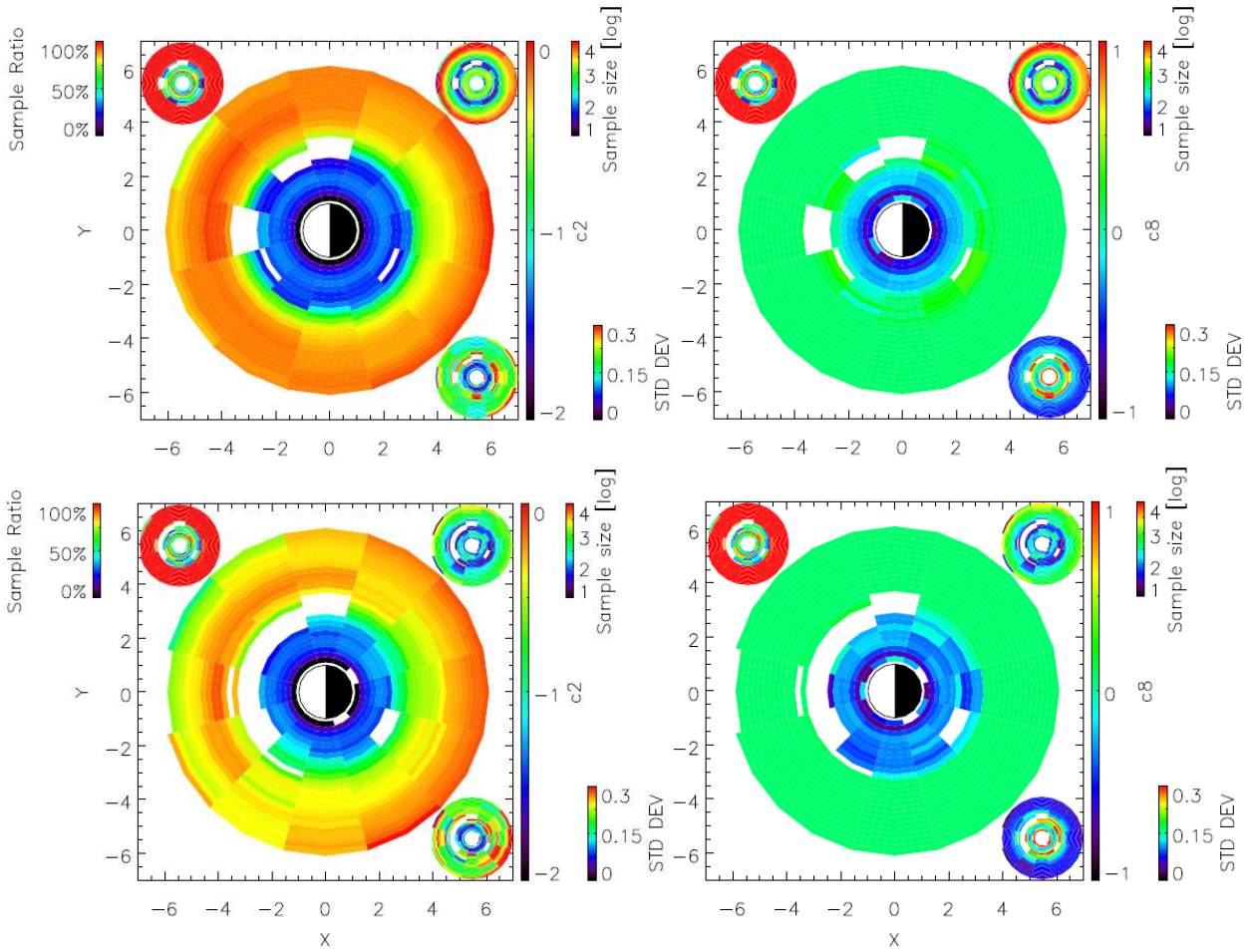

Figure A.4: Medians of (left) c_2 and (right) c_8 as a function of L and MLT for ~460 keV electrons during quiet times (Dst > -20 nT, top panels) and disturbed times (-20 nT > Dst > -50 nT, bottom panels). The ratios of good fits to total PADs are shown on the top left corner, and the sample sizes are shown on the top right corner. The standard deviations are also shown in the bottom right corner of each panel.

Figure A.5 shows the averaged PADs of ~105, 235, and 460 keV electrons as a function of L shell and MLT in the inner radiation belt, reconstructed from the empirical model of relativistic electron PADs during quiet geomagnetic activities (Dst > -20 nT). Note that in the inner belt, as expected, the averaged PADs have no dependence on MLT, indicating an azimuthally symmetric geomagnetic field (dipole field) in the low L region. The newly unveiled 90 °minimum PADs are clearly shown in the Figure A.5 for different energy electrons. It is clear from Figure A.5 that for electrons with higher energies the minimum at 90 °PA tends to be more

significant. At L=1.4 and 1.6, the minima at 90 °PA are very clear; while as the L shell becomes higher, the minima at 90 °gradually disappear. Though not shown here, during storm times with Dst < -20 nT, the averaged PADs in the inner belt have more significant minima at 90 °PA. This is consistent with the observations shown in Chapter 5. The wave-particle interaction of fast magnetosonic waves is suggested as a possible mechanism responsible for the formation of this PAD type, though the actual causes are still under debate. In Chapter 5 I showed some detailed observations in the slot region, indicating the disappearance of such type of PADs can be

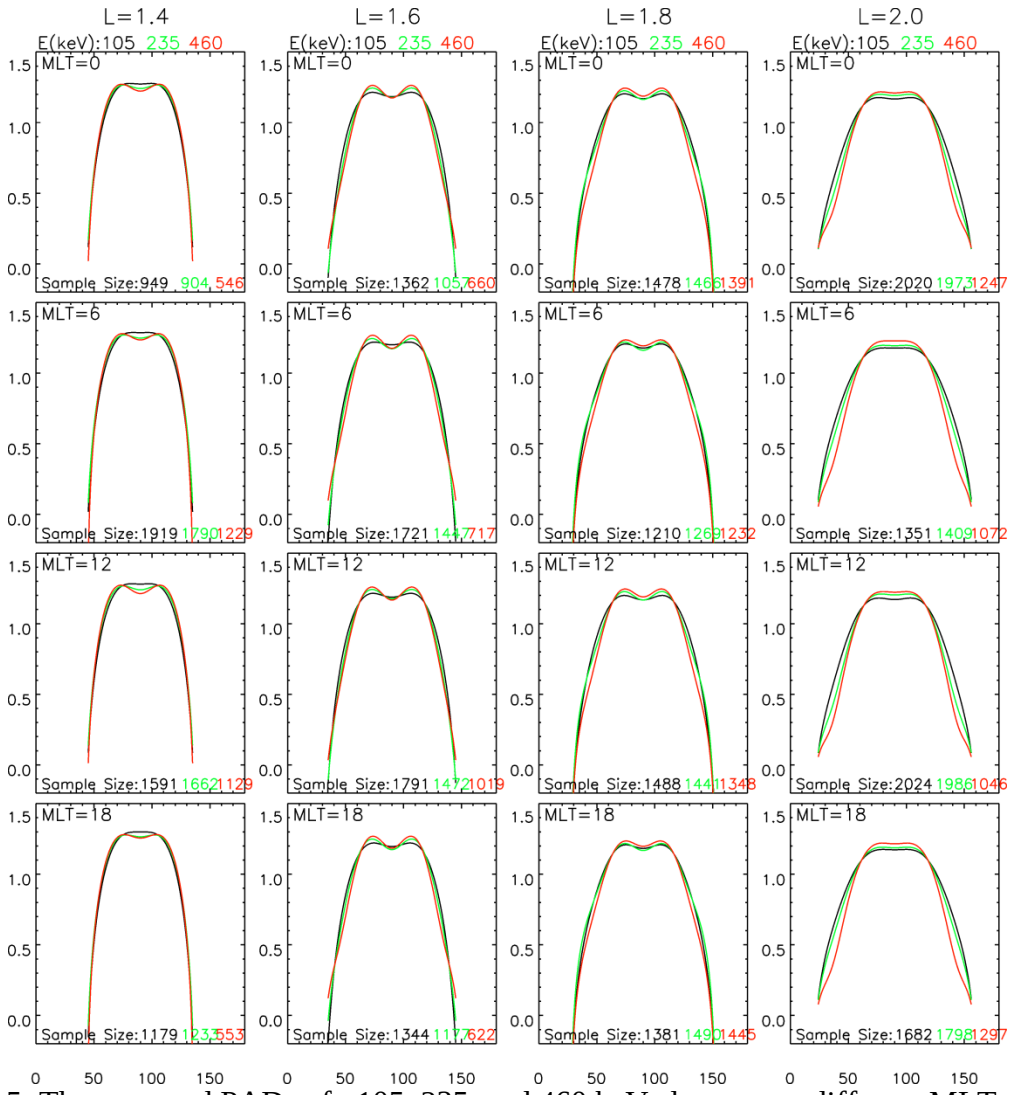

Figure A.5: The averaged PADs of ~105, 235, and 460 keV electrons at different MLTs in the inner radiation belt, reconstructed from the empirical model of relativistic electron PADs during geomagnetic quiet times (Dst > -20 nT).

attributed to the hiss wave scattering. Our model results also support this hypothesis, which shows that as the cap PADs appear (indicating the presence of hiss wave scattering) the minima at 90 °PA in electron PADs disappear (as can be seen in Figure A.6).

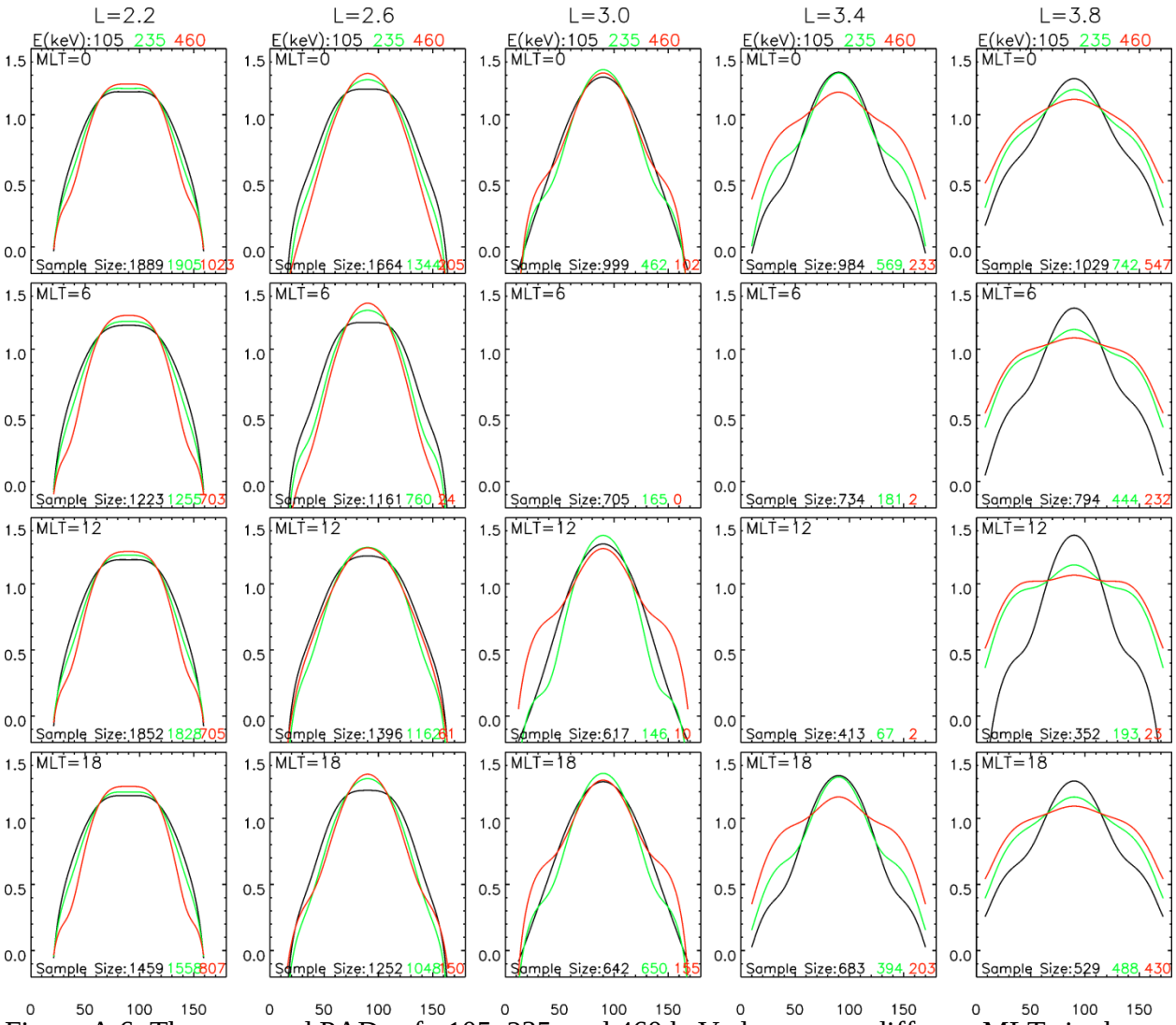

Figure A.6: The averaged PADs of ~105, 235, and 460 keV electrons at different MLTs in the slot region, reconstructed from the empirical model of relativistic electron PADs during geomagnetic quiet times (Dst > -20 nT).

Figure A.6 shows the averaged PADs of ~105, 235, and 460 keV electrons as a function of L shell and MLT in the slot region measured by MagEIS instruments during quiet geomagnetic activities (Dst > -20 nT). Similarly, no MLT dependence is observed in the slot region either. The cap PADs clearly show up in Figure A.6. At L=2.2, the cap PADs are only

present for ~460 keV electrons, while for ~105 and 235 keV electrons the PADs are more like pancake PADs. As L shell increases, the cap PADs can be observed for all energy electrons shown here, but the size of "cap" in pitch angle extent is smaller for higher energy electrons and larger for lower energy electrons. This is consistent with the theoretically predicted PADs caused by plasmaspheric hiss wave scattering [e.g., Lyons et al., 1972]. It is also worth to mention that during geomagnetic active times (-50 nT < Dst < -20 nT) the averaged PADs at lower L shells of slot region (L<~3) are mostly 90 °minimum PADs, but at higher L shells of slot region (~3<L<~4) the averaged PADs are mostly pancake PADs. This may indicate during active times other physical processes, e.g., inward radial diffusion and wave heating, play more important roles on relativistic electron dynamics than hiss wave scattering in the outer slot region.

A.5 Conclusions

Using data from MagEIS instruments, an empirical model of 100s of keV electron PADs in the inner radiation belt and slot region is constructed. It is shown that during geomagnetic quiet times, the 90 °minimum PADs in the inner belt are always observed, and the minima at 90 ° PA are more prominent for electrons with higher energies; while during geomagnetic disturbed times, the 90 °minimum PADs extend to the slot region. In the slot region, the cap PADs are generally observed during quiet times and the dependence of the PAD shape on electron energy and L shell is consistent with the theoretical prediction [e.g., Lyons et al., 1972]. However, during geomagnetic disturbed times, instead of cap PADs, the pancake PADs are commonly observed in the L range of ~3-4, which may indicate the more important roles of other physical mechanisms, e.g., inward radial diffusion and wave heating, than the hiss wave scattering during geomagnetic storm times in the outer slot region.

Appendix B

Additional Details from the Ring Current Study

B.1 Additional Details Concerning the Influence of MLT Asymmetry to Ring Current Energy Content Calculation

As discussed in Chapter 6, the ring current is MLT asymmetric during the main phases and early recovery phases of the storms, especially for low energy ions [e.g., Ebihara et al., 2002; Perez et al., 2012]. Thus the assumption of symmetric ring current we used in the ring current energy content calculation may have influence on the results. Here I show some detailed calculations regarding the influence of MLT asymmetry to ring current energy content calculations as mentioned in Section 6.3.2.

To investigate the MLT asymmetry of low energy ring current ion distribution, the 22.5-67.5 keV ion intensity distribution inferred from ENA observations from Perez et al. [2012] during the main phase of a moderate storm is used. One panel of Figure 5b from Perez et al. [2012] is shown in Figure B.1, which shows the de-convolved equatorial 22.5-67.5 keV ion intensities at the main phase of July 2009 moderate storm based on ENA images from TWINS1. To calculate the influence of MLT asymmetry to the total ring current energy content during the March 29 storm, we use similar distribution pattern to the one shown in Figure B.1 and fit the energy densities calculated from Van Allen Probe data during the main phase of the storm to this distribution pattern. The results are shown in Figure B.2, and the energy densities calculated using data from Van Allen Probe – A during one orbit at the storm main phase are also plotted. Then, using these fitted energy densities, the total energy content of ring current ions is calculated.

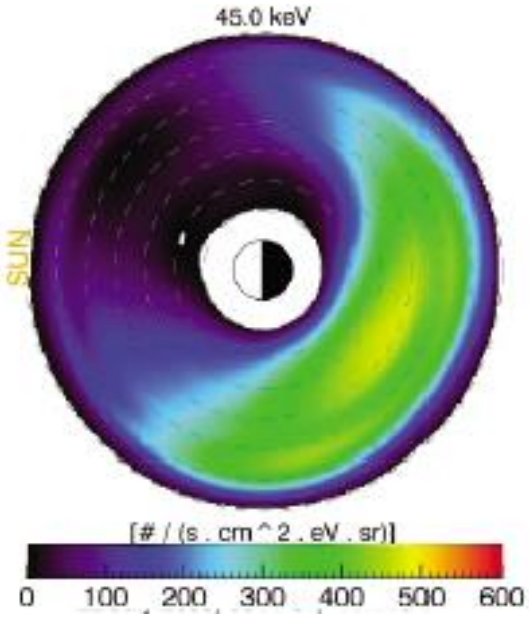

Figure B.1: (One panel of Figure 5b of Perez et al. [2012]) De-convolved equatorial ion intensities for energy band of 22.5-67.5 keV at the main phase of July 2009 storm, which is a moderate storm with minimum Dst of ~-80 nT, using ENA images from TWINS1.

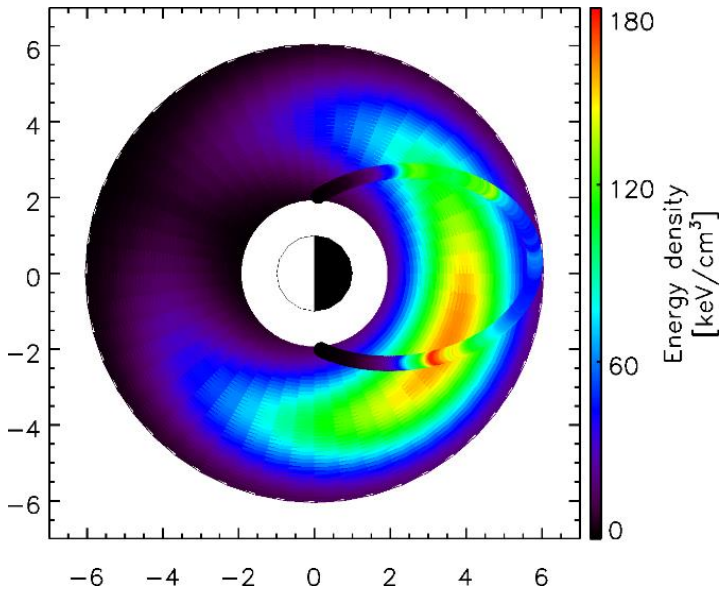

Figure B.2: Energy densities used in this study to calculate the asymmetric ring current energy content, derived based on the distribution pattern shown in Figure B.1 and the energy densities calculated using Van Allen Probe - A data of one pass during the main phase of the 29 March 2013 storm (also plotted).

As can be seen from Figure B.1 and Figure B.2, the low energy ring current ion distribution used in the calculation is very asymmetric. Even though it is highly asymmetric, the

total ring current energy content calculated using this asymmetric ring current model just decreased by ~30% comparing to the MLT-symmetry assumption. And for higher energy ions, the distribution should be more isotropic. Lui [2003], using ~1 keV – 4 MeV ion data from AMPTE/CCE, actually showed that even during active times (Kp > 3+) the asymmetry of the ring current proton pressure is not as significant. The differences between Lui [2003] and other studies (e.g., Ebihara et al. [2002]) could indicate that the high energy ion distribution is much more symmetric than that of low energy ions, and in terms of total ion energy density distribution, the asymmetry is probably not as significant as shown in Figure B.1 and Figure B.2. Thus we conclude that the influence of ring current MLT asymmetry to the calculated ring current energy content should not be very significant.

B.2 Additional Details Concerning the Influence of Using Spin-Averaged Fluxes Instead of Pitch-Angle-Resolved Fluxes to the Ring Current Energy Content Calculation

B.2.1 Derivation of the Equation for Ring Current Energy Content Calculation Using Pitch-Angle-Resolved Fluxes

As we have discussed in Section 6.3.2, we evaluate the error introduced by using isotropic pitch angle distribution assumption in the calculation of energy content. Using pitch-angle-resolved fluxes, the energy density at a specific location can be calculated as

$$\varepsilon = \int Efdv^3 = 2\pi \int_0^{\infty} v^2 Edv \int_0^{\pi} f sin\alpha d\alpha = 4\pi \int_0^{\infty} v^2 Edv \int_0^{\alpha_m} f(\alpha_0) \frac{B}{B_0} \frac{\sin\alpha_0 \cos\alpha_0}{\sqrt{1-\frac{B}{B_0}\sin^2\alpha_0}} d\alpha_0$$

where m, v and E are the mass, velocity and energy of particles, B and B_0 are the local and equatorial magnetic field strength, α and α_0 are the local pitch angle and equatorial pitch angle and $\frac{sin^2\alpha}{B} = \frac{sin^2\alpha_0}{B_0}$, and $\alpha_m = \sin^{-1}(\sqrt{\frac{B_0}{B}})$. Assuming dipole magnetic field only, the energy density is a function of (L, λ) where λ is the magnetic latitude.

With the assumption that the ring current energy density is azimuthally symmetric (MLT symmetric), the energy content calculation can be simplified as

$$E = \int \varepsilon dx^3 = \sum_{L=2}^{6} \bar{\varepsilon} \Delta V(L)$$

where $\bar{\varepsilon}$ is the flux-tube-averaged energy density, and $\Delta V(L)$ is the volume of thin L shell with ΔL=0.1 in a dipole field. The flux-tube-averaged energy density can be calculated as

$$\bar{\varepsilon} = \frac{E_{FT}}{V_{FT}}$$

where E_{FT} and V_{FT} are the total kinetic energy contained within a flux tube and the volume of a flux tube respectively.

The volume of a flux tube can be calculated as

$$V_{FT} = \int dV = \int A dl = \int A_0 \frac{B_0}{B} dl$$

where A is the cross-section area and B is the magnetic field, 0 denote the values at the magnetic equator, and $dl = r_0 \cos\lambda \, (1 + 3\, sin^2\, \lambda)^{\frac{1}{2}} d\lambda$ is the length element of the flux tube. Since we have $\frac{B_0}{B} = \frac{cos^6 \lambda}{\sqrt{1+3sin^2 \lambda}}$, the flux tube volume can be calculated as

$$V_{FT} = \int A_0 r_0 cos^7 \lambda d\lambda = 2 \int_0^{\lambda_m} A_0 r_0 cos^7 \lambda d\lambda$$

where λ_m is the magnetic latitude of the point that field line intercept with the Earth's surface and $\lambda_m = \cos^{-1}(\sqrt{\frac{1}{L}})$.

The total kinetic energy of particles contained within a flux tube can be calculated as

$$\begin{aligned} E_{FT}(L) = \int \varepsilon dV &= 2 \int_0^{\lambda_m} \varepsilon(L, \lambda) A_0 r_0 cos^7 \lambda d\lambda \\ &= 8\pi A_0 r_0 \int_0^{\infty} v^2 E dv \int_0^{\lambda_m} cos\, \lambda \, (1 \\ &+ 3\, sin^2\, \lambda)^{\frac{1}{2}} d\lambda \int_0^{\alpha_m} f(\alpha_0) \frac{sin\, \alpha_0\, cos\, \alpha_0}{\sqrt{1 - \frac{B}{B_0} sin^2\, \alpha_0}} d\alpha_0 \end{aligned}$$

Since $\int_0^{\lambda_m} \int_0^{\alpha_m} d\alpha_0 d\lambda \approx \int_0^{\frac{\pi}{2}} \int_0^{\lambda_{mir}(\alpha_0)} d\lambda d\alpha_0$, where $\lambda_{mir}(\alpha_0)$ is the mirroring magnetic latitude of particles with pitch angle α_0, we have

$$E = 8\pi A_0 r_0 \int_0^{\infty} v^2 E dv \int_0^{\frac{\pi}{2}} f(\alpha_0) \sin\alpha_0 \cos\alpha_0 \, d\alpha_0 \int_0^{\lambda_{mir}(\alpha_0)} \frac{\cos\lambda \, (1+3\sin^2\lambda)^{\frac{1}{2}}}{\sqrt{1-\frac{(1+3\sin^2\lambda)^{\frac{1}{2}}}{\cos^6\lambda}\sin^2\alpha_0}} d\lambda$$

Using the approximate value of integral $\int_0^{\lambda_{mir}(\alpha_0)} \frac{\cos\lambda(1+3\sin^2\lambda)^{\frac{1}{2}}}{\sqrt{1-\frac{(1+3\sin^2\lambda)^{\frac{1}{2}}}{\cos^6\lambda}\sin^2\alpha_0}} d\lambda \approx 1.30 - 0.56\sin\alpha_0$ [Roederer, 1970], the equation can be simplified as

$$E_{FT} = 8\pi A_0 r_0 \int_0^{\infty} v^2 E dv \int_0^{\frac{\pi}{2}} f(\alpha_0) \sin\alpha_0 \cos\alpha_0 \, (1.30 - 0.56\sin\alpha_0) d\alpha_0$$

$$f(\alpha_0) = \frac{m}{v^2} j(\alpha_0)$$

Assuming $j(\alpha_0) = j_0 \sin^n \alpha_0 \quad (n \geq 0)$, the equation can be further simplified as

$$E_{FT} = 8\pi A_0 r_0 \int_0^{\infty} \sqrt{\frac{mE}{2}} dE \int_0^{\frac{\pi}{2}} j_0 \sin^n \alpha_0 \, sin\,\alpha_0 \, cos\,\alpha_0 \, (1.30 - 0.56\, sin\,\alpha_0) d\alpha_0$$

$$= 8\pi A_0 r_0 \int_0^{\infty} (\frac{1.30}{n+2} - \frac{0.56}{n+3}) j_0 \sqrt{\frac{mE}{2}} dE$$

Then we have

$$\bar{\varepsilon} = \frac{E_{FT}}{V_{FT}} = \frac{4\pi \int_0^{\infty} (\frac{1.30}{n+2} - \frac{0.56}{n+3}) j_0 \sqrt{\frac{mE}{2}} dE}{\int_0^{\cos^{-1}\sqrt{1/L}} cos^7\lambda d\lambda}$$

B.2.2 Differences in Energy Density Calculations Using Spin-Averaged Fluxes versus Pitch-Angle-Resolved Fluxes

Using the equation shown above, the differences in energy density and content calculation using spin-averaged fluxes versus pitch-angle-resolved fluxes are calculated. The results show that during the storm main phase, using pitch-angle-resolved data does not change the results significantly. One example of a single pass of Van Allen Probes at the main phase of the March 29 storm is shown in Figure B.3. The energy densities of 60-1000 keV protons are calculated using MagEIS spin-averaged proton fluxes ("FPSA") and pitch-angle-resolved proton fluxes ("FPDU") respectively. And it can be seen from Figure B.3 that the difference between

the two during the storm main phase is fairly small especially at higher L shells, and the total energy content only differ by ~10%. Such small differences would be almost invisible in Figure 6.3 since the range of y axis of Figure 6.3 is much larger than that in Figure B.3. And as discussed in Section 6.3.2, for ions with lower energies, the pitch angle distributions are more isotropic, thus the influence of using spin-averaged fluxes on the ring current energy content calculation should be even smaller. Thus, we conclude that using spin-averaged fluxes instead of pitch-angle-resolved fluxes does not affect the ring current energy content calculation significantly.

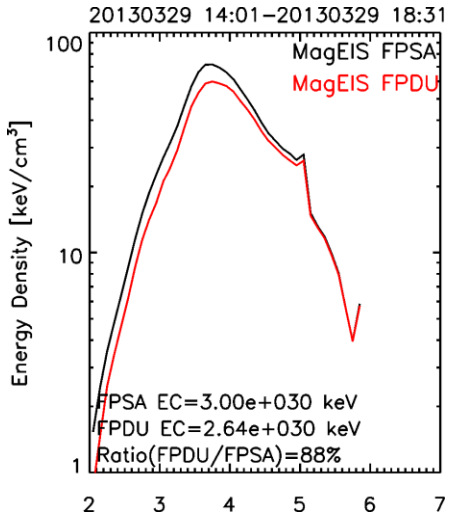

Figure B.3: The energy densities of ~60-1000 keV protons using MagEIS spin-averaged fluxes (FPSA) and pitch-angle-resolved fluxes (FPDU) respectively of one pass at the main phase of March 29 storm. The total energy content (EC) calculated by using two different dataset and the ratio between the two are also shown at the bottom of the figure.